Elaboration and Optimization of Tellurite-based Materials for Raman Gain Application

Guillaume Guéry

THÈSE

PRÉSENTÉE A

L'UNIVERSITÉ BORDEAUX 1

ÉCOLE DOCTORALE DES SCIENCES CHIMIQUES

Par **Guillaume GUERY**

POUR OBTENIR LE GRADE DE

DOCTEUR

SPÉCIALITÉ : Physique et Chimie de la Matière Condensée

Elaboration and Optimization of Tellurite-based Materials for Raman Gain Application

Directeurs de recherche: M. Thierry CARDINAL, M. Vincent RODRIGUEZ, Mme Kathleen RICHARDSON

Soutenue le: 28 Juin 2013

Devant la commission d'examen formée de:

M. SIMON, Patrick	Directeur de recherche – CEMHTI - CNRS	Rapporteur
M. MAGLIONE, Mario	Directeur de recherche- ICMCB – CNRS	Président
Mme. RIVERO, Clara	Chargée de recherche - Lockheed	Examinateur
M. SUNDARAM, S.K	Professeur – Alfred University	Examinateur
Mme. RICHARDSON, Kathleen	Professeur – University of Central Florida	Examinateur
M. RODRIGUEZ, Vincent	Professeur - ISM - Université Bordeaux 1	Examinateur
M. CARDINAL, Thierry	Directeur de recherche – ICMCB - CNRS	Membre invité

THÈSE

PRÉSENTÉE A

L'UNIVERSITÉ BORDEAUX 1

ÉCOLE DOCTORALE DES SCIENCES CHIMIQUES

Par **Guillaume GUERY**

POUR OBTENIR LE GRADE DE

DOCTEUR

SPÉCIALITÉ : Physique et Chimie de la Matière Condensée

Elaboration and Optimization of Tellurite-based Materials for Raman Gain Application

Directeurs de recherche: M. Thierry CARDINAL, M. Vincent RODRIGUEZ, Mme Kathleen RICHARDSON

Soutenue le: 28 Juin 2013

Devant la commission d'examen formée de:

M. SIMON, Patrick	Directeur de recherche – CEMHTI - CNRS	Rapporteur
M. MAGLIONE, Mario	Directeur de recherche- ICMCB – CNRS	Président
Mme. RIVERO, Clara	Chargée de recherche - Lockheed	Examinateur
M. SUNDARAM, S.K	Professeur – Alfred University	Examinateur
Mme. RICHARDSON, Kathleen	Professeur – University of Central Florida	Examinateur
M. RODRIGUEZ, Vincent	Professeur - ISM - Université Bordeaux 1	Examinateur
M. CARDINAL, Thierry	Directeur de recherche – ICMCB - CNRS	Membre invité

ABSTRACT

Tellurite-based oxide glasses have been investigated as promising materials for Raman gain applications, due to their good linear and nonlinear optical properties and their wide transparency windows in the near- and midwave infrared spectral region. Furthermore, their interesting thermal properties, i.e. low glass transition temperature and ability to be drawn into optical fibers, make tellurite-based glasses excellent candidates for optical fiber amplifiers. The estimation of the strength and spectral distribution of Raman gain in materials is commonly approximated from the spontaneous Raman scattering cross-section measurement. For development of tellurite-based glasses as Raman amplifiers, understanding the relationship between glass structure, vibrational response, and nonlinear optical properties (NLO) represents a key point. This dissertation provides an answer to the fundamental question of the PhD study: *"What is the impact of the glass structure on Raman gain properties of tellurite glasses?"*

This dissertation summarizes findings on different tellurite-based glass families: the TeO_2-$TaO_{5/2}$-ZnO, TeO_2-$BiO_{3/2}$-ZnO and TeO_2-$NbO_{5/2}$ glass networks. The influence of glass modifiers has been shown on the glass' properties. Introduction of tantalum oxide or zinc oxide has been shown to increase the glass' stability against crystallization, quantified by ΔT, where $\Delta T = T_x - T_g$. Added to the variation of the glass viscosity, this attribute is critical in fabricating optical fibers and for the use of these materials in fiber-based Raman gain applications. The role of ZnO in the tellurite network and the mechanism for structural modification has been determined. This addition results in not

only the largest ΔT reported for these highly nonlinear glasses to date, but coincides with a commensurate decrease of the refractive index. A hydroxyl purification has been developed that when employed, resulted in high purity preform materials exhibiting a limited absorption in the transmission bandwidth in the near infrared (NIR). A reduction of 90 % in the OH content in candidate glasses was realized and core-only optical fiber drawn from this glass exhibited optical losses lower than 10 dB/m (either at 1.55 μm or 2.0 μm). This optical attenuation in a high Raman gain material represents a first in the design of both material attributes.

The role of the glass modifiers on the glass structure has been investigated by a combination of vibrational spectroscopic methods, including IR absorption, as well as Raman and hyper-Raman scatterings. Following examination of fundamental vibrations present in the paratellurite crystal α-TeO_2, these results were extended to interpret the structure of multi-component tellurite glasses. It has been verified that the transformation of the tellurite entities $TeO_4 \rightarrow TeO_{3+1} \rightarrow TeO_3$ is directly related to the percentage and type of glass modifiers present in the various tellurite glass matrix. The dramatic disruption in the continuity of Te-O linkages in the tellurite glass backbone's chains during the introduction of the modifier zinc oxide, leads to a systematic reduction in glass network connectivity. This structural change is accompanied by a significant change in the glass' normalized polarization curve ($I_{\Psi V}/I_{HV}$), a paramter which quantifies directly the depolymerization ratio (DR). This metric provides direct correlation with a reduction in the ternary glass' polarizability/hyperpolarizability and a decrease in the glass' nonlinear optical properties, specifically its Raman gain response. These results have validated and

extended our understanding of the important role of Te-O-Te content and short, medium and longer-scale organization of the tellurite glass network and the corresponding impact on linear and nonlinear optical response and properties. Such fundamental knowledge of the relationship between vibrational response and structure, correlated to linear and nonlinear optical properties, allows the extension of this know-how to the development of customized optical components enabled by novel glass and glass ceramic optical materials.

RESUME

L'expansion de nouvelles technologies et la demande incéssante d'une transmission d'informations plus rapide font que les systèmes de télécommunications nécessitent plus de débit sur de plus longues distances. L'amplification optique et notamment l'amplification optique par effet Raman représente une intéressante possibilité à repousser les limites de distance et de debit.

Les verres à base d'oxyde de tellure sont des matériaux prometteurs pour les applications d'amplification optique par effet Raman; en particulier grâce à leurs fortes propriétés optiques linéaires et non linéaires, leurs fenêtres de transparence allant dans le proche et milieu infra-rouge du spectre de transmission. De plus, leurs propriétés thermiques et en particulier leurs faibles temperatures de transition vitreuse permettent une facilité de fibrage. L'estimation de l'intensité du gain Raman et sa zone spectrale mise en jeu sont généralement approchées à partir du spectre de diffusion Raman spontanée du matériaux. La compréhension des relations existantes entre la structure vitreuse, la réponse vibrationnelle et les propriétés d'optique non linéaire, représente un point clé au développement et à l'optimisation des verres de tellure pour l'amplification Raman. Cette dissertation apporte une réponse détaillée à la question fondamentale de l'étude doctorale: *"Quel est l'impact de la structure vitreuse sur les propriétés d'amplification Raman dans les verres d'oxyde de tellure?"*

L'essai résume les découvertes faites sur trois différentes familles de verres de tellure: TeO_2-$TaO_{5/2}$-ZnO, TeO_2-$BiO_{3/2}$-ZnO et TeO_2-$NbO_{5/2}$. L'influence des

modificateurs de réseau sur le propriétés du verre a été démontrée. L'introduction de l'oxyde de tantale provoque une augmentation de la stabilité vitreuse, quantifiée par ΔT, où $\Delta T = T_x - T_g$. Ce paramètre est critique à la fabrication de fibres optiques et pour l'utilisation de ces matériaux en tant que fibres optiques amplificatrices par effet Raman. Le rôle de l'oxyde de zinc dans le réseau tellure et dans le mécanisme de modification structurale, a été determiné. Cet ajout n'est pas seulement representatif d'une augmentation de la stabilité vitreuse, mais aussi d'une drastique décroissance de l'indice de refraction.

Une voie de reduction des groupements hydroxyles a été développée et employée, resultant dans la synthèse de verres de tellure ne proposant qu'une absorption limitée dans la fenêtre de transmission dans le proche infra-rouge. Une diminution de 90 % des groupes OH a été observée et a permis de mesurer des atténuations otiques de l'ordre de 10 dB/m (entre 1.55 μm et 2.0 μm). Ces pertes relativement basses sont prometteuses et peuvent être facilement améliorées par l'élaboration de fibres core-clad.

Le rôle des modificateurs de réseau dans la structure du verre a été regardé en combinant différentes méthodes de spectroscopies vibrationnelles, incluant l'absorption IR, et les diffusions Raman et hyper-Raman. Ces études ont été préalablement réalissées sur un cristal de paratellurite permettant l'obtention des vibrations fondamentales dans les matériaux tellurites. Ces résultats ont pu ensuite être extrapolés pour l'interprétation des structures multi-composants que sont les verres. La transition en géométrie des unités structurales élémentaires suivant $TeO_4 \rightarrow TeO_{3+1} \rightarrow TeO_3$ a été vérifiée et directement

reliée au pourcentage et au type de modificateurs présents dans le réseau tellure. L'importante rupture des chaînes de tellure Te-O-Te due à l'introduction du zinc dans la matrice vitreuse, conduit à une reduction systèmatique de la connectivité du réseau vitreux. Ces changements structuraux s'accompagnent d'une significante variation de la courbe de polarization normalisée ($I_{\Psi V}/I_{HV}$), permettant de directement quantifier le coefficient de dépolymérisation. Cette analyse apporte une corrélation entre la réduction de la polarisabilité/hyperpolarisabilité du système ternaire et la décroissance des propriétés d'optique non linéaire du verre avec en particulier la réponse du gain Raman.

Ces résultats ont validé et étendu notre compréhension sur l'importance du rôle des chaînes Te-O-Te mais aussi surl'impact de l'organisation à courte, moyenne et longue échelle du réseau vitreux de tellure sur les réponses optiques linéaires et non linéaires. De telles connaissances fondamentales sur les relations structure – réponse vibrationnelle corrélées aux propriétés d'optique linéaire et non linéaire, nous autorisent à étendre l'étude sur de nouveaux matériaux optiques type verre et verre céramique.

ACKNOWLEDGMENTS

Cette étude doctorale a été réalisée dans plusieurs laboratoires partenaires de ce projet, je souhaite remercier le directeur de l'Institut de Chimie de la Matière Condensée de Bordeaux, Monsieur Mario Maglione, le directeur de l'Institut des Sciences Moléculaires de Bordeaux, Monsieur Philippe Garrigue et le directeur du département Materials Science and Engineering de Clemson University, Monsieur Igor Luzinov. De plus je tiens à remercier une deuxième fois Monsieur Mario Maglione pour m'avoir fait l'honneur de présider ce jury de thèse.

J'adresse mes plus vifs remerciements à messieurs les rapporteurs, messieurs Bruno Bureau de l'Université de Rennes de l'équipe Verres et Céramiques, et Patrick Simon de l'Université d'Orléans; pour avoir juger ce travail.

Je souhaite remercier profondément mes trois encadrants de thèse, le professeur Kathleen Richardson, le professeur Vincent Rodriguez et le Docteur. Thierry Cardinal. Un immense merci à ces trois personnes qui ont su me diriger pendant ces trois années de doctorat. Merci pour votre disponibilité, votre enthousiasme et votre soutien infaillible, notamment sur la fin… Ce fût un réel plaisir d'évoluer et d'apprendre à vos côtés, nos échanges m'ont toujours énormément apporté.

J'aimerais ensuite remercier des personnes spéciales qui ont fait de cette thèse un plaisir quotidien. Tout d'abord la Team America avec mon groupe de recherche du Glass Processing and Characterization Laboratoray de Clemson. Un grand bravo à tous avec en particulier Benn Gleason, Cody Reynolds, Pete Wachtel et Baptiste Giroire. Vous m'avez

découvrir les USA et ses traditions comme jamais je n'aurais pu imaginer, des moments inoubliables. Deuxièmement je voudrais remercier l'équipe de l'ISM avec tout le groupe Spectroscopie, mais en particulier messieurs Frederic Adamietz et Marc Dussauze. Qui aurait cru que passer des journées entières dans le noir avec deux hommes pouvait être si amusant. Merci à vous deux pour avoir pris du temps pour m'expliquer la science hyper marrante et merci à Marc pour la session bateau à Saint-Malo et les bières d'après conférences. En troisième, j'aimerais remercier toutes les personnes de l'ICMCB que j'ai pu cotoyer. Tout d'abord mon groupe de recherche avec gros Aurélien Delestre, gros Kévin Bourhis et grAlex Fragues, un immense merci à mon binôme Sébastien Thomas qui fût mon cobureau, coloc et mon cocave pour la rédaction. Merci aux supers nanas Lucile Cornu, Noor Makria et Marion Dubernet, Patron avait raison, il ne faut jamais laisser trois filles dans le même bureau. Merci à Hélène Vigouroux, Evelyne Fargin, Alain Garcia, Yannick Petit, Véronique Jubéra, Benoît Glorieux; je regrette déjà nos discussions aux pauses café et toutes les journées passées à vos côtés. Un très grand merci à notre doyen Gilles le Flem, je souhaiterais que tous les groupes de recherche et surtout les doctorants puissent un jour rencontrer une personne comme Gilles. Merci de prendre soin de nous et de nous faire partager toutes vos histoires.

Une très amicable pensée va à un groupe de personnes qui ont su faire avancer humainement cette thèse, Stéphane Toulin, Carole Malburet, Sandrine Quillateau, Armand Decourt et Bob Owen.

Je devrais utiliser une centaine de pages pour exprimer ma gratitude à toutes les autres personnes du laboratoire. Je vous dirai simplement merci, vous m'avez tellement apporté pendant ces trois années que je ne trouverais pas les mots pour expliquer votre contribution à cette réussite.

Un immense merci à mes amis d'enfance, ma famille et ma Marion. Merci pour leur soutien quotidien, leur enthousiasme et leur amour sans faille.

TABLE OF CONTENTS

Page

ABSTRACT i

ACKNOWLEDGMENTS vii

LIST OF TABLES xiii

LIST OF FIGURES xvi

INTRODUCTION 1

Introduction – References 6

CHAPTER

I. NONLINEAR OPTICAL MATERIALS AND TECHNIQUES OF SIGNAL AMPLIFICATION 7

1. Principle of signal amplification 9
   1.1 Rare-earth doped fiber amplifiers 10
   1.2 Raman amplifiers 10
2. Fundamentals of Nonlinear Optics 14
3. Materials for Nonlinear Optics 20
   3.1 Fundamentals of glass formation 21
   3.2 Optical fibers for mid-IR applications 25
   3.3 Glasses for third-order nonlinear optical application 28
      3.3.1 Halide compounds 30
      3.3.2 Chalcogenide non-oxide glasses 31
      3.3.3 Tellurite oxide glasses 31
4. Relationship between tellurite glass compositions, nonlinearity and Raman gain 34
5. Conclusion 39

Chapter 1 – References 41

II. TELLURITE GLASS SYNTHESIS AND PROPERTIES 46

1. Multi-component tellurite glasses 47
2. Tellurite glass synthesis 48

Table of Contents (Continued)

Page

3. Glass properties in the TeO_2-$TaO_{5/2}$-ZnO, TeO_2-$NbO_{5/2}$, TeO_2-$BiO_{3/2}$-Z ZnO glass networks 50
3.1 Characterization tools 50
3.1.1 Differential Scanning Calorimetry – DSC 50
3.1.2 Density measurement – Archimede's principle 51
3.1.3 Microhardness measurement – Vickers' method 54
3.1.4 Linear refractive index – Brewster's angle 55
3.2 TeO_2-$TaO_{5/2}$-ZnO glass network 59
3.2.1 Results 59
3.2.2 Discussion 61
3.3 TeO_2-$NbO_{5/2}$ glass network 64
3.3.1 Results 64
3.3.2 Discussion 65
3.4 TeO_2-$BiO_{3/2}$-ZnO glass network 66
3.4.1 Results 66
3.4.2 Discussion 68
4. Tellurite glass purification process - Influence of OH content on tellurite glass properties 70
5. Fabrication of tellurite optical fiber 85
5.1 Optical losses measurements 89
6. Effect of crystallization in TeO_2-Bi_2O_3-ZnO glass network 93
6.1 α-$Bi_2Te_4O_{11}$ monoclinic phase 98
6.2 β-$Bi_2Te_4O_{11}$ cubic metastable phase 102
7. Conclusion 105
Chapter 2 – References 107

III. VIBRATIONAL SPECTROSCOPY ANALYSES 113

1. Introduction 114
2. Principles and experimental details of IR, Raman and hyper-Raman scattering techniques 116
2.1 Optical modes in materials 116
2.2 Infra-red (IR) reflectivity 119
2.2.1 Principles 119
2.2.2 Experimental use of infrared (IR) spectroscopy in the present work 123
2.3 Raman scattering (RS) 124
2.3.1 Principles 124
2.3.2 Experimental use of Raman spectroscopy in the present work 129

Table of Contents (Continued)

Page

2.4 Hyper-Raman scattering (HRS) 130
2.4.1 Hyper-Raman scattering principles 130
2.4.2 Experimental use of hyper-Raman/hyper-Rayleigh spectroscopy in the present work 133
3. Vibrational studies of Tellurite materials 137
3.1 TeO_2 crystal 138
3.1.1 Paratellurite α-TeO_2 138
3.1.2 Tellurite β-TeO_2 140
3.1.3 Tellurite γ-TeO_2 143
3.1.4 Tellurite δ-TeO_2 144
3.2 Vibrational insights in paratellurite α-TeO_2: a Raman and hyper-Raman study 144
3.2.1 Symmetry properties of paratellurite 147
3.2.2 Results of Raman and hyper-Raman scatterings on paratellurite crystal 151
3.2.2.1 Raman scattering of paratellurite 152
3.2.2.2 Hyper-Raman scattering of paratellurite crystal 161
4. Extended vibrational studies (IR, RS and HRS) of TeO_2-$TaO_{5/2}$-ZnO glass network 165
5. Raman and hyper-Raman complementary studies of TeO_2-$NbO_{5/2}$ glass network 180
6. Raman scattering study of TeO_2-$BiO_{3/2}$-ZnO glass network 186
7. Conclusion 188
Chapter 3 – References 191

IV. NONLINEAR OPTICAL PROPERTIES IN TELLURITE-BASED GLASS 199

1. Experimental techniques 200
1.1 Raman gain measurement 200
1.2 Raman gain estimation from spontaneous Raman scattering cross section measurements 208
1.3 Dispersion effect on Spontaneous Raman cross-section 214
1.4 Spontaneous Raman scattering cross-section measurements 216
1.5 Hyper-Rayleigh Scattering of glasses: principles 217
2. Results…… 222
2.1 Raman gain measurement: TeO_2-$TaO_{5/2}$-ZnO, TeO_2-$NbO_{5/2}$, TeO_2-$BiO_{3/2}$-ZnO 222
2.2 Hyper-Rayleigh Scattering measurements 231

Table of Contents (Continued)

Page

3. Relationship between hyperpolarizability and Raman gain in TeO_2-$TaO_{5/2}$-ZnO glasses 236
4. Conclusion 240
Chapter 4 – References 242

CONCLUSION AND FUTURE WORK 245

LIST OF TABLES

Table		Page
1.1	Spectral bands forming the electro-magnetic spectrum	9
1.2	Geometry of different types of molecules according to VSEPR rule	33
2.1	Evolution of characteristic temperatures (glass transition temperature T_g, onset of crystallization T_x, crystallization temperature T_p and glass stability ΔT), volumetric weights ρ and linear refractive index measured at 752 nm, in the TeO_2-$TaO_{5/2}$-ZnO glass network	60
2.2	Evolution of characteristic temperatures (glass transition temperature T_g, onset of crystallization T_x, crystallization temperature T_p and glass stability ΔT), volumetric weights ρ and linear refractive index measured at 752 nm, in the TeO_2-$NbO_{5/2}$ glass network	65
2.3	Evolution of characteristic temperatures (glass transition temperature T_g, onset of crystallization T_x, crystallization temperature T_p and glass stability ΔT), volumetric weights ρ in the TeO_2-Bi_2O_3-ZnO glass network	67
2.4	Volumetric weight, molar density and hydroxyl content in $80TeO_2$-$20Nb_2O_5$ and $70TeO_2$-$10Bi_2O_3$-20 ZnO glass compositions, melted or not in an air dried glove box	74
2.5	Evolution of characteristic temperatures, glass stability, volumetric weight, micro-hardness and cut off energy	83
2.6	Parameters for glass fiber fabrication in the $80TeO_2$-$10TaO_{5/2}$-10ZnO glass composition (Δ=130 ^oC)	89
2.7	Unit cell refinement results for β-$Bi_2Te_4O_{11}$ crystal phase	97
3.1	Raman spectroscopy - wavenumber assignments (cm^{-1}) [$\pm$ 2 cm^{-1}] for paratellurite crystal	160
3.2	Hyper Raman spectroscopy - wavenumber assignments (cm^{-1}) [$\pm$ 2 cm^{-1}] of paratellurite crystal	165

List of Tables (Continued)

Table Page

3.3 Summary of the spectral deconvolution for VV polarized Raman and hyperRaman spectra using normalized Gaussian function for TeO_2-$TaO_{5/2}$-ZnO glasses 171

3.4 Summary of the band desummation for VV polarized Raman and hyper-Raman spectra using normalized Gaussian function for $90TeO_2$-$10NbO_{5/2}$ glass. Results obtained with $90TeO_2$-$10NbO_{5/2}$ glass taken from Table 3.3 are reported here for comparison purpose 182

4.1 n linear refractive indices, number density of Te atoms, area of relative Raman gain peak and relative Raman gain as a function of $TaO_{5/2}$ and ZnO contents 224

4.2 n linear refractive index and relative Raman gain as function of $NbO_{5/2}$ content 226

4.3 Evolution of the Raman gain coefficient of $74TeO_2$-$12Bi_2O_3$-14ZnO as function of the crystallization (crystal volume fraction and average crystal size) 228

4.4 HRS intensity $|\beta_{HRS}|^2$, dipolar and octupolar β_J values (in atomic units) and anisotropic parameters (r_{AP}) deduced from HRS measurements. Measured refractive indices at optical frequencies ω and 2ω as well as volumetric weight of TeO_2-$TaO_{5/2}$-ZnO glasses are reported 233

LIST OF FIGURES

Figure		Page
1.1	Standard telecommunication using optical fiber	7
1.2	Telecommunication window for amplifiers	8
1.3	Raman gain - physical principle	12
1.4	Raman amplification of silica glass, with a pump at 1450 nm. Here the gain bandwidth is defined as 40 nm by the full width at half maximum (FWHM)	13
1.5	Effect of pump juxtaposition on Raman gain	14
1.6	Induced polarization, effect of an electric field on the electronic cloud	15
1.7	a) energy conservation rule and b) momentum conservation rule	19
1.8	Effect of temperature on the enthalpy of a glass melt	22
1.9	Principle of Optical fibers	26
1.10	Fiber cross section and refractive index profile of single-mode fiber	28
1.11	Order of magnitude of nonlinear refractive index in different glass families	30
1.12	Structural entities in TeO_2 glass: TeO_4 trigonal bipyramidal unit (tbp), TeO_{3+1} transition step unit and TeO_3 trigonal pyramidal unit (tp)	36
2.1	Melting process of tellurite oxide based glasses	49
2.2	DSC measurement with determination of glass transition temperature T_g, the onset of crystallization T_x and the crystallization temperature T_p	51
2.3	Measure of density by Archimede's method	52
2.4	Process to calculate the Vickers Hardness	54

List of Figures (Continued)

Figure Page

2.5 Reflection and transmission of an electromagnetic wave between two mediums 56

2.6 Evolution of the polarizability $\chi(1)$ as function of the introduction of ZnO into the glass matrix 69

2.7 Dried-air purged glove box with humidity<1%. 72

2.8 Measured and calculated IR spectra of orthotelluric acid H_6TeO_6 76

2.9 IR spectra evolution of $80TeO_2$-$20Nb_2O_5$ glass composition melted in ambient furnace conditions or within an humidity-controlled glove box 78

2.10 IR spectral evolution of $70TeO_2$-$10Bi_2O_3$-$20ZnO$ glass composition melted in ambient furnace conditions or within an humidity controlled glove box 79

2.11 Brass mold, diameter = 1 cm, length = 10 cm 86

2.12 Tellurite-based glass rods with (a) and without (b) bubbles in the following glass composition $70TeO_2$-$10Bi_2O_3$-$20ZnO$ 87

2.13 Drawing tower facilities at Institut Carnot de Bourgogne, University of Dijon, France – Prof. Frédéric SMEKTALA 88

2.14 Optical losses measurements on tellurite-based glasses 92

2.15 XRD patterns in situ high temperature of TBZ glass network and optical microscopy focusing on the β-$Bi_2Te_4O_{11}$ crystallization 95

2.16 XRD pattern of β-$Bi_2Te_4O_{11}$ crystal phase into $74TeO_2$-$12Bi_2O_3$-$14ZnO$ amorphous matrix 96

2.17 Different tellurium oxide geometry in the α-$Bi_2Te_4O_{11}$ crystal structure 99

2.18 Chain-like structure in α-$Bi_2Te_4O_{11}$ crystal 100

2.19 $Bi_2Te_4O_{11}$ crystal phase detailed as $Bi_2Te_2O_7$ crystal between TeO_2 crystal layers 101

List of Figures (Continued)

Figure Page

2.20 Ordering process of Te and Bi on the [111] in the CaF_2 fluorite structure during the $\beta \rightarrow \alpha$ crystal phase transition. Only one possible configuration of the Bi-Te ordering is presented as an example 102

2.21 Structure of β-$Bi_2Te_4O_{11}$ crystal phase 104

3.1 Fundamental IR absorption (left) in the mid-IR and harmonic absorption (right) in the near-IR 119

3.2 Principle of Raman spectroscopy..... 124

3.3 Relationship between the wave vectors of the exciting K_i and scattered K_s radiation and a wave vector Δk in the medium..... 126

3.4 Sketch of the 90^o Raman scattering geometry with different linear vertical (V) and horizontal (H) polarization for the incident and scattered beams 127

3.5 Energy level diagrams for Raman and hyper-Raman scatterings (Stokes lines)..... 131

3.6 (Top) 90^o scattering geometry for Raman scattering, hyper-Raman/hyper-Rayleigh scattering. For both processes, the collected signal corresponds to the Stokes lines in the green-red visible range. (Bottom): Schematic of the experimental setup for hyper-Raman in the right angle scattering geometry..... 134

3.7 Sketch of the disphenoid unit TeO_4E trigonal bipyramid; the arrow visualizes the direction of the lone pair E (a). Projection in the xOy plane of the structure of paratellurite (b) 138

3.8 Projection of the crystal structure β-TeO_2 in the xOy frame (a), 3D projection of a leaf of β-TeO_2 parallel to (100) plane (b)..... 142

3.9 Tridimensional projection of the γ-TeO_2 crystal 143

3.10 Helicoidal chain structure in γ-TeO_2 corresponding to the shaded regions part in Figure 3.9 144

3.11 Oxyz frame to Ox'y'z frame 150

List of Figures (Continued)

Figure Page

3.12 Polarized Raman spectra of paratellurite crystal in the backscattering geometry (Raman intensity in log scale) 153

3.13 Polarized Raman spectra of paratellurite crystal in the right angle geometry (Raman intensity in log scale) 156

3.14 Polarized Raman spectra of paratellurite crystal in the backscattering geometry (Raman intensity in log scale) 159

3.15 Polarized hyper Raman spectra of paratellurite crystal in the right angle geometry 162

3.16 Infrared (ε'') (left), Raman (middle) and hyper-Raman (right) spectra of bulk glasses in the systems $(100\text{-}x)TeO_2\text{-}xTaO_{5/2}$ in (top) and $80TeO_2\text{-}(20\text{-}x)TaO_{5/2}\text{-}xZnO$ in (bottom). Intensities are in arbitrary units 168

3.17 RS (top) and HRS (bottom) polarized spectra of $90TeO_2\text{-}10TaO_{5/2}$ 170

3.18 RS (top) and HRS (bottom) polarized spectra of $80TeO_2\text{-}20TaO_{5/2}$ 175

3.19 RS (top) and HRS (bottom) polarized spectra of $80TeO_2\text{-}5TaO_{5/2}\text{-}15ZnO$ 176

3.20 Potential mechanism of molecular arrangement during tantalum/zinc oxide introduction 178

3.21 RS (top) and HRS (bottom) polarized spectra of $90TeO_2\text{-}10NbO_{5/2}$ 181

3.22 Raman scattering of $(100\text{-}x)TeO_2\text{-}xNbO_{5/2}$ glass network 184

3.23 Position of the Raman band assigned to the Nb-O bond as function of the distortion Δ of NbO_6 octahedron, where ○ (Oh without non-bridging oxygen O_{nb}, without oxygen tri or tetra-coordinated O_t), ● (Oh with O_t, without O_{nb}), Δ (Oh with O_{nb}, without O_t) and ▲(Oh with O_{nb} and O_t) 185

3.24 Raman spectra of $TeO_2\text{-}BiO_{3/2}\text{-}ZnO$ glass system 187

4.1 Schematic representation of the Raman gain process 200

List of Figures (Continued)

Figure Page

4.2 Raman gain curve obtained from spontaneous Raman measurement and Raman gain Coefficient obtained by using pump on the glass composition $59.5TeO_2$–$25.5TlO_{1/2}$–15PbO 213

4.3 VV Polarized Experimental Spontaneous Raman Spectrum of samples $85TeO_2$-$15WO_3$ and $85TeO_2$-$10Nb_2O_5$-5MgO, normalized to SiO_2 measured at different wavelength (left) and Relative Raman gain coefficient calculated at $665cm^{-1}$ versus the wavelength (right) 215

4.4 Sketch of the HRS experimental setup with different polarization capabilities: $\psi = 0$, 90 degree corresponding respectively to a horizontal (H) and linear vertical (V) incident polarization; and $\psi = \pm 45$ degree correspond to left and right circular polarization 219

4.5 Raman spectra of bulk glass systems (100-x)TeO_2-x$TaO_{5/2}$ in (A) and $80TeO_2$-(20-x)$TaO_{5/2}$-xZnO in (B) depicted in the form of relative Raman gain using pure SiO_2 as reference 223

4.6 Raman spectra of bulk glass systems (100-x)TeO_2-x$NbO_{5/2}$ depicted in the form of relative Raman gain using pure SiO_2 as reference 225

4.7 Raman spectra of bulk glass and glass ceramic systems $66TeO_2$-$21BiO_{3/2}$-13ZnO depicted in the form of relative Raman gain using pure SiO_2 as Reference 229

4.8 Left: Quadratic dependence of the HRS scattered intensity in $90TeO_2$-$10TaO_{5/2}$ (90Te10Ta) glass and acetonitrile (MeCN). Right: Experimental (circles) polarization curve of $90TeO_2$-$10TaO_{5/2}$ and best fit (solid line) according to Eq. 4.34 232

4.9 Evolution of the second-order intensity $|\beta_{HRS}|^2$ with Tellurium content. Dotted lines are guide for the eye 234

4.10 Experimental Normalized polarization curve $I_{\psi V}/I_{HV}$ of $90TeO_2$-$10TaO_{5/2}$ and $90TeO_2$-$10NbO_{5/2}$ 235

List of Figures (Continued)

Figure Page

4.11 Evolution of the relative Raman gain to $Si0_2$ (red squares and full circles) and the linear optical intensity $|\chi^{(1)}|^2$ at 1064 nm (blue squares and full circles) with Tellurium content. Full lines are guide for the eye.....237

4.12 Relative Raman gain and first-order intensity versus second-order intensity$|\beta_{HRS}|^2$. Solid lines are guide for the eye.....238

INTRODUCTION

Drinking water, oil, ores, lot of reserves begin to be missing on our planet and the human being knows this tragedy. But another indispensable resource is over exploited in some cases: the hertzian spectrum. Due to its invisibility and immateriality, the medium wanes with a total disregard, but overused, many technologies would be paralyzed and would drastically turn upside down our style life. Indeed, internet, television, radio, mobile phone, GPS, but also radar systems for air traffic, military applications, space observation, directly rely on the bandwidth provided by the electro-magnetic (EM) spectrum. Theoretically, it is composed of an infinite number of frequencies, but actually available spectral bands are limited and over-used, risking signal interference. The rapid expansion of new wireless technologies bottle-necks bandwidth capabilities of our society, leading to incredible data traffic in a narrow telecommunication window.

From this demand for high speed communication and the overload of data traffic, optical transmission systems and the spectral regions where they function, are changing. In 1950, scientists discovered the laser, which has been the root of a new domain of research. Indeed, the laser, and more specifically the photon, has become the medium of information translation. This new way of transmission uses the photon rather than the electron, which allows transfer of more information with a higher speed. During the 60's, Charles K. Kao and George A. Hockham from the Standard Telephones and Cables company promoted the idea of a reduction of the attenuation in optical fibers below 20 dB/km. From this time, optical fibers have become a practical medium for

communication **[Hecht 1999]**. Since that time, the scientific community has continued to explore the fiber as the medium of light propagation. This discovery and its future expansion are the motivations for research, particularly in the field of new materials, capable of being drawn and used as an optical fiber.

Actual technology for optical fiber has been demonstrated **[Hecht 2002]**, but the never-ceasing demand of high speed transmission and the volume of data exchanged show the limits of the present system, especially with the bandwidth of telecommunication window and its losses due to the distortion/absorption of the signal.

The focus of this research effort is made in this context, and the core thesis of the research is to evaluate how new glass materials may solve the actual issues through expansion of the spectral regimes available for data transmission. Raman amplification is a nonlinear optical mechanism that when utilized in broadly transmitting optical glass fibers, provide a means to expand this bandwidth for data transmission.

Recent efforts in exploring new compositions that possess broad bandwidth in both optical transmission and Raman gain have shown promise in correlating glass chemistry with resulting nonlinear optical properties. This combination of glass science and optical engineering know-how is critical to the goal of engineering new materials capable of exploiting the nonlinear process needed for amplification. Further know-how is required to optimize glass materials and their stability in fabrication and use to approach requisite low optical loss targets while maintaining high gain in the longer wave (lower frequency) spectral regions desired."

Working with inorganic glasses has been proved to be an excellent solution, thanks to a relatively low cost and straight-forward way to synthesis and compositionally tailor the variation of glass properties by composition modulation. Tellurite-based glasses TeO_2 exhibit high nonlinearity useful for Raman amplification application **[Berthereau 2005][Petit 2002][Rivero 2004]** and forms the basis of the present effort.

This PhD dissertation aims to address the following issues and will make the necessary breakthrough in term of understanding of the suitability of tellurite glasses for Raman gain applications:

1. *What is the impact of the glass structure on the Raman gain response*?

   Accordingly to available data, the Raman response of the tellurite glass is attributed to the vibrations associated with the Tellurium oxide network. Addition of modifiers or intermediate ions can drastically modify the Raman response and especially the magnitude of the signal. It is not clear to date, what the key role and impact of the modifier or intermediate species on the tellurite network is that gives rise to its Raman response.

2. *What is the influence of the short and intermediate-range glass orders on the Raman gain response?*

   The network structure of tellurite glass strongly affects the Raman response. The polymerization of the TeO_n units seems to be an important factor in realizing a glass' strong Raman cross section. A systematic study of well-chosen

compositions is necessary for answering these questions and links the glass structure to the resulting polarizability and hyperpolarizability of the material. Tellurite glass ceramic could lead to the increase of the magnitude of the Raman response. The benefit of such materials will to be evaluated.

During this PhD, the following two points will be specifically examined to provide fundamental understanding of optical glass science and engineering required to answer the above questions:

i. Approximate the best trade-off in term of Raman gain response, glass thermal stability, damage threshold resistance, and hydroxyl content in the scope of fiber fabrication of the glass.
ii. Investigate and evaluate the possible benefits of using controlled crystallization to form optical glass ceramics for Raman gain application.

Thus, this effort will develop and assess the use of heavy metal oxide (HMO) multi-component tellurite glass compositions with high glass stability, good laser damage resistance and low optical loss, for their use in Raman gain and novel mid-infrared fiber applications.

This PhD has been initiated following a successful MILMI-Atlantis dual Masters exchange program between Clemson University (USA) and University of Bordeaux (France). The dual PhD program/co-tutelle offers the opportunity to obtain an international recognized dual degree from the United States of America and from Europe. This study has been successfully completed in three different laboratories: i) the Glass

Processing and Characterization Laboratory (GPCL) within COMSET (Center of Optical Materials Science and Engineering Technologies) and the Department of Materials Science and Engineering at Clemson University, Clemson, South Carolina; ii) the ICMCB laboratory (Institut de Chimie de la Matière Condensée de Bordeaux) at Bordeaux, France and iii) the ISM laboratory (Institut des Sciences Moléculaires) at the University of Bordeaux, France. Additional components of the effort have been performed in partner laboratories through collaborations, specifically with the ICB laboratory (laboratoire Interdisciplinaire Camot de Bourgogne) at Dijon, France; SPCTS laboratory (Science des Procédés Céramiques et de Traitements de Surface) at Limoges, France; LOMA laboratory (Laboratoire Ondes et Matières Aquitaine) at Bordeaux, France, and CREOL laboratory (Center for Research and Education in Optics and Lasers) at the University of Central Florida, Orlando, Florida.

Introduction – References

Berthereau 1995: A Berthereau, PhD thesis "Matériaux vitreux pour l'optique non linéaire" (1995) University of Bordeaux, France.

Hecht 1999: J. Hecht, "City of Light: The Story of Fiber Optics", Oxford University Press (1999) ISBN 0195108183.

Hecht 2002: E. Hecht, "Optics", Pearson Education, ISBN 0-8053-8566-5.

Petit 2002: L. Petit, PhD thesis "Amplification optique dans des verres borophosphate de niobium et tellurite dopes aux ions de terres rares présentant un indice optique non linéaire élevé" (2002) University of Bordeaux, France.

Rivero 2005: C. Rivero, PhD thesis "High gain/Broadband oxide glasses for next generation Raman amplifiers" (2005) University of Central Florida, USA/University of Bordeaux, France.

CHAPTER 1

NONLINEAR OPTICAL MATERIALS AND TECHNIQUES OF SIGNAL AMPLIFICATION

Due to the expansion of new technologies, telecommunication systems require a higher data capacity. Optical amplification represents the main technique that enables a trade-off of transmission versus data attenuation. A traditional telecommunication system using optical fiber can be represented as shown in Figure 1.1.

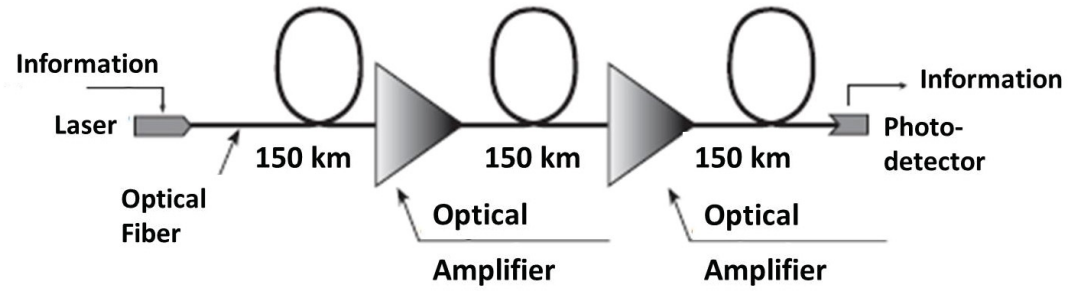

Figure 1.1 Standard telecommunication using optical fiber. Figure taken from [Chluda].

In the schematic, a laser emits light which is modulated in magnitude to obtain a binary code (extinction=0, ignition=1). In the optical fiber, the modulated light is propagated through the network and analyzed by a photo-detector to translate the information into an electronic signal. Optical fiber for telecommunication are based on silica glasses (SiO_2), which possess a minimum of optical losses / signal attenuation for a specific wavelength, $\lambda = 1.55$ μm without dispersion effect. This wavelength is used for the telecommunication systems to transmit light of this wavelength/frequency. Signals in regular silica optical

fiber can cover an average distance of about 150 km without amplification as explained by Chluda **[Chluda].** To be capable to surpass those limits, signals have to be amplified every 150 km.

High speed telecommunication and the expansion to the volume of data transmission require an extension of the telecom spectral window in order to support data traffic. For achieving this goal, enhanced fiber transmission window is needed as well as appropriate amplifications to reduce the problem of optical losses. As shown in Figure 1.2, improvements in the fiber optic industry have been achieved and optical transmission over the entire telecom window of 1260 nm to 1675 nm can be obtained by reducing the amount of hydroxyls impurities (Figure 1.2) **[Refi 1999].**

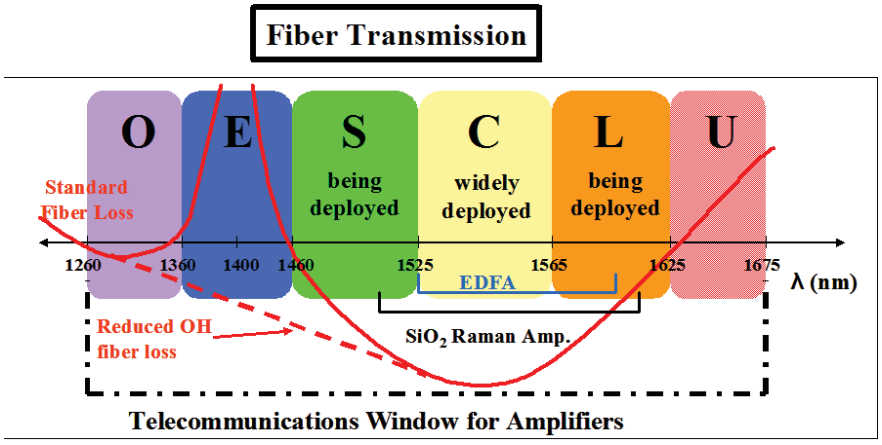

Figure 1.2 Telecommunication window for amplifiers [Rivero 2005].

The challenge is now to discover the best materials for amplification in order to exploit this large transmission window that could be compatible for long-haul communications or for local area networks.

The different bands present in the telecommunication windows (Figure 1.2) are summarized in Table 1.1.

Band	Descriptor	Spectral window (nm)
O band	Original	1260 to 1360
E band	Extended	1360 to 1460
S band	Short wavelength	1460 to 1530
C band	Conventional	1530 to 1565
L band	Long wavelength	1565 to 1625
U band	Ultra-long wavelength	1625 to 1675

Table 1.1 Spectral bands forming the electro-magnetic spectrum.

1 Principle of signal amplification

During the transmission of information in the optical fiber, the data signal becomes depleted due to intrinsic losses in the transmission medium. Thus, an amplification tool becomes necessary to improve the intensity of the signal in the network. Indeed, an optical amplifier does not regenerate a signal; it will amplify its intensity (as well as the noise present) in the optical domain. The following sections briefly review the different techniques commonly employed to optically amplify a signal, specifically:

- Rare-earth doped fiber amplifiers,
- Raman amplifiers.

1.1 Rare-earth doped fiber amplifiers

Rare-earth (RE) doped fiber amplifiers are related to RE doped fiber lasers by the same process of inversion of electronic population. In this kind of fiber, the signal is amplified through interaction with dopant ions, previously excited by a pump laser. Different doping ions can be considered and yield specific response in the target communication spectral bands shown in Table 1.1. Thulium ions are suitable in the S-band (1460-1530 nm), while Praseodymium ions could be used in the O-band (1260-1360 nm). Erbium-doped fiber amplifiers (EDFA) are the most common rare earth fiber amplifiers because of their amplification in the window 1525 nm – 1565 nm, the C-band, widely used for telecommunication in silica glasses. The L band (1570 – 1610 nm) can be also accessible using erbium ions as dopants. The main disadvantage of rare-earth doped fiber amplifier is associated with the available window of amplification which is determined by the energy level of the rare earth ions. Even if other rare-earth ions have been investigated in order to expand the spectral bandwidth (especially for Thulium), it remains difficult to cover the entire available spectral window.

1.2 Raman amplifiers

Despite the fact that Raman amplification requires high pump powers (typically >100 mW), the technology represents the only way to amplify a signal on a tunable telecommunication window without doping the fiber materials. Specifically, in this system one can amplify a given signal, regardless of its (excitation) wavelength, through a Raman Gain medium. The limitation of the gain medium in the context of Raman

amplification is its spectral transmission window, which dictates the ultimate breadth of the electro-magnetic spectrum that can be amplified. For these reasons, Raman amplification becomes an excellent method for optical amplification if the fundamental materials limitations, can be addressed. Silica glass is the most often used material for optical fibers due to its superb transparency; however, as a candidate oxide glass for Raman amplification, it has a low (by comparison to newer gain media discussed in subsequent sections) Raman cross section; with a Raman gain magnitude of g_R=0.89x10^{-13} m/W at 1 μm, it possesses a limited usable bandwidth of 5 THz **[Rivero 2005]**.

Silica is the most accessible material thanks to its low optical losses which lead to an acceptable figure of merit ($\frac{Gain \times Bandwidth}{Optical\ Loss}$) **[Seo 2000]**. Heavy metal glasses (especially tellurite and chalcogenide) have a great potential for being new candidates for Raman gain thanks to their transparency in visible and mid infra-red range, and to their high intrinsic optical nonlinearity (Gain=50-100x SiO_2), if low loss materials can be realized and high power handling structures, can be fabricated (Loss=1000x SiO_2).

Raman gain is a nonlinear optical process based on Raman scattering and stimulated emission. Raman amplification is based on the combination of pump beam excitation $h\omega_{pump}$, signal beam excitation $h\omega_{signal}$ which is in resonance with the vibration mode of the materials, as shown in Figure 1.3.

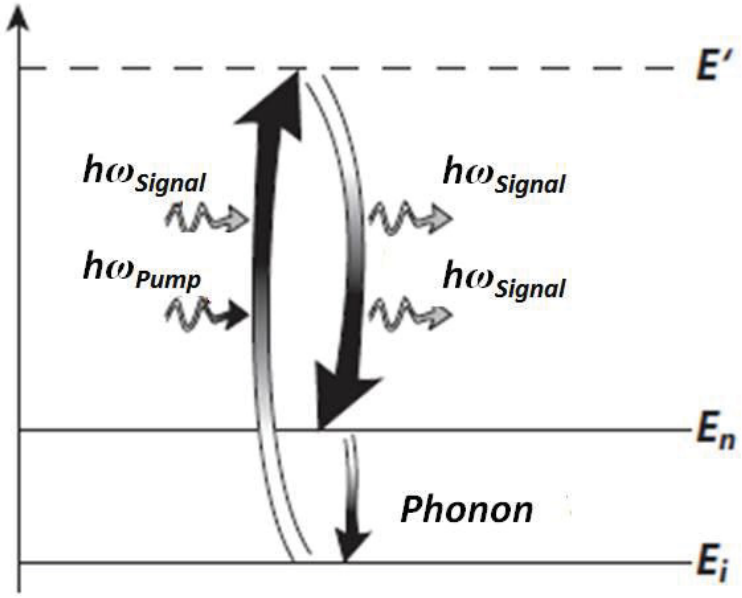

Figure 1.3 Raman gain - physical principle [Chluda].

Raman gain is based on the stimulated emission of a photon at a frequency that is down-shifted by the vibrational modes of a medium thanks to the stimulated Raman scattering mechanism. The phenomena can be described by the excitation of an electron to an intermediate state by an incident photon (pump beam), and the stimulated emission of a photon giving rise to a Stokes transition.

Through Raman scattering processes, the interaction between a signal photon and a pump photon will result in two photons at the signal wavelength; this leads to a "photon duplication" at the signal wavelength, yielding amplification, as shown in Figure 1.3.

The gain magnitude depends on the pump wavelength and on the material properties (Stokes shift and Raman spectra intensity), as shown with the example of SiO_2 in Figure 1.4.

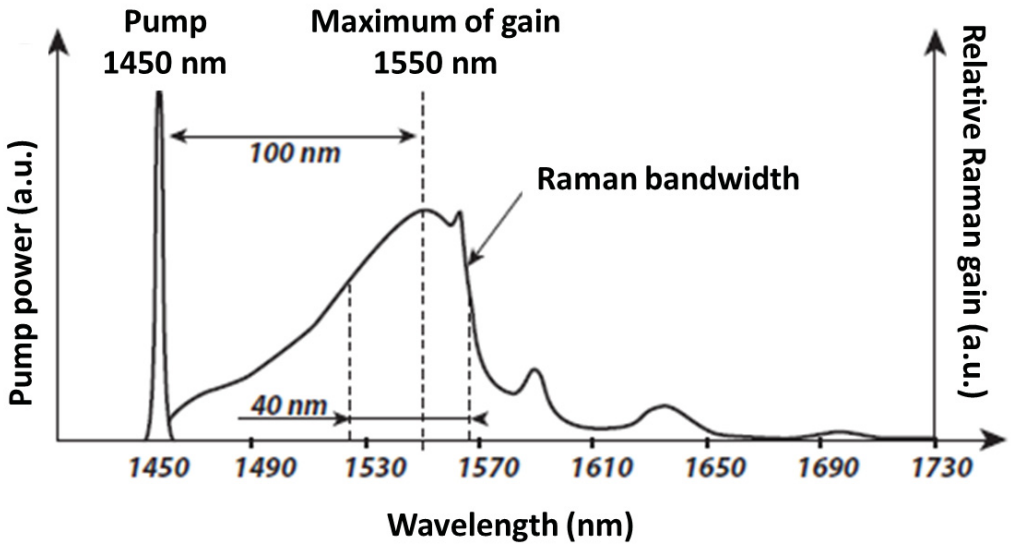

Figure 1.4 Raman gain spectra of silica glass, with a pump at 1450 nm [Chluda]. Here the gain bandwidth is defined as 40 nm by the full width at half maximum (FWHM).

The maximum of the material's gain or amplification can be seen to be shifted 100 nm from the pump wavelength, and the spectral Raman bandwidth is close to 40 nm. As Raman gain is a scattering amplification, maximizing this bandwidth is possible by combining laser pumps at different wavelengths in the same materials, as shown in Figure 1.5 or, tailoring the glass material's chemistry to enhance the Raman peaks bandwidth.

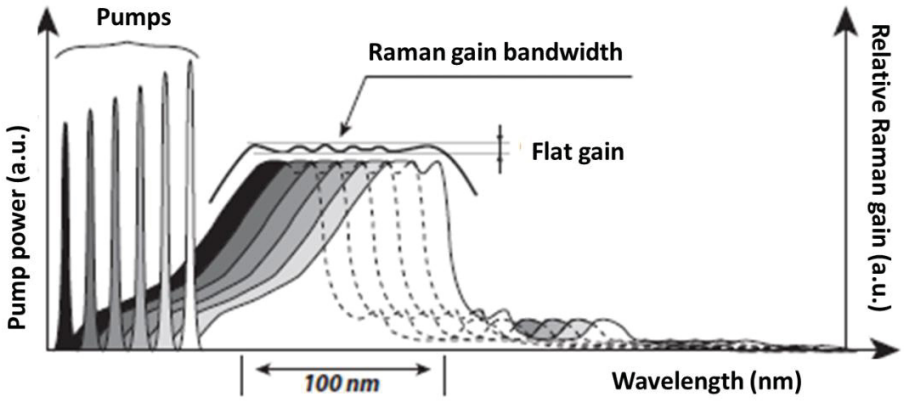

Figure 1.5 Effect of pump juxtaposition on Raman gain [Chluda].

The juxtaposition of multiple pumps at different wavelength permits to obtain amplification with a high flat gain and an important Raman gain bandwidth. While possible, this is a costly approach that could be alleviated were there to be suitably broad-band glass materials which enabled larger potential shifts from a single pump.

2 Fundamentals of Nonlinear Optics

Nonlinear optics is the study of phenomena linked to the modification of the optical properties when the material is subjected to a high-intensity light source (i.e. laser) as compared to 'linear' material response of a material under low-intensity illumination. During the light-matter interaction, the incident electric field deforms the electronic cloud and creates an induced polarization or induced dipole, as shown in Figure 1.6.

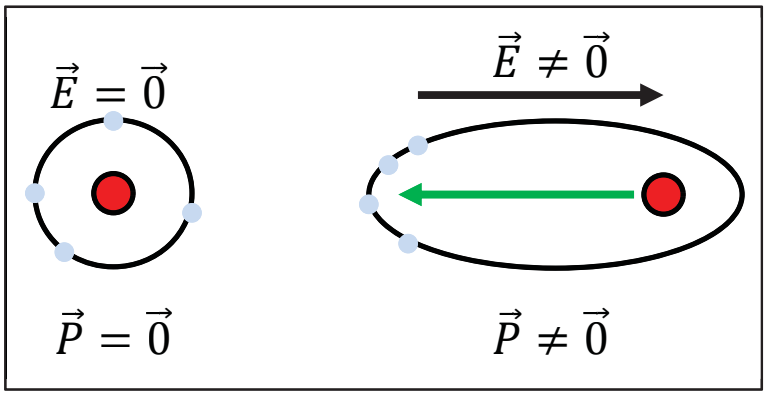

Figure 1.6 Induced polarization, effect of an electric field on the electronic cloud.

During the interaction with an electric field, positive charges within a material move in the direction parallel to the applied electric field whereas negative charges (electrons) are shifted in the opposite direction. Considering the Born Oppenheimer approximation, and comparing the mass of electrons and nucleus, only the negative charges are moving.

The induced dielectric polarization P is the response of the electric field E of the light and is expanded in a Taylor series in terms of the total applied electric field **[Shen 1984]**:

$$P = P^{(0)} + P^{(1)} + P^{(2)} + P^{(3)} + \cdots + P^{(n)} = P_0 + \varepsilon_0 \chi^{(1)} E(\omega) + \varepsilon_0 \chi^{(2)} E(\omega) E(\omega) + \varepsilon_0 \chi^{(3)} E(\omega) E(\omega) E(\omega) + \cdots \quad \textbf{Eq. 1.1}$$

Where P_0 is the permanent polarization, ε_0 is the permittivity of free space and $\chi^{(n)}$ is a tensor of n rank and represents the complex of dielectric susceptibility linked to the microscopic structure of the material.

The electromagnetic field essentially impacts the electronic cloud; a microscopic polarization μ appears and is defined such as:

$$\vec{\mu} = \vec{\mu}^{(0)} + \vec{\mu}^{(linear)} + \vec{\mu}^{(nonlinear)} = \vec{\mu}^{(0)} + \varepsilon_0 \alpha \vec{E}(\omega) + \varepsilon_0 \left[\frac{1}{2} \beta \vec{E}(\omega) \vec{E}(\omega) + \frac{1}{6} \gamma \vec{E}(\omega) \vec{E}(\omega) \vec{E}(\omega) + \cdots \right] \quad \textbf{Eq. 1.2}$$

Where $\mu^{(0)}$ is the permanent polarization, $\mu^{(linear)}$ is the induced linear polarization, $\mu^{(nonlinear)}$ is the induced nonlinear polarization, E is the applied electric field, α represents the polarizability, β and γ are the 2nd and 3rd order of hyper-polarizability, and ω is the frequency.

In regular conditions of illumination (meaning ambient, low intensity light levels), the intensity is weak enough to considerer the polarization proportional to the electric field; the response of the material is linear.

On the other hand, as the light intensity increases (electric field closing 10^6 V/m), the polarization becomes a function of increasing the electric field E, so called nonlinear optics.

- For the first order, the polarization can be written as:

$$P^{(1)}(\omega) = \varepsilon_0 \chi^{(1)}(\omega) E(\omega) \qquad \textbf{Eq. 1.3}$$

Where ω is the signal frequency. The 1st order of polarization refers to the linear susceptibility $\chi^{(1)}$. The real and the imaginary parts of the $\chi^{(1)}$are respectively linked to the linear refractive index and to the absorption of the material.

- For the second order, the polarization can be written as:

$$P^{(2)}(\omega_1 + \omega_2) = \varepsilon_0 \chi^{(2)}(\omega_1, \omega_2) E(\omega_1)(E\omega_2) \qquad \textbf{Eq. 1.4}$$

The 2nd order describes the quadratic nonlinearity. This order of susceptibility is function of the symmetry of the material. $\chi^{(2)}$ is null in isotropic (and centrosymmetric) material such as vitreous material due to the symmetries (Neumann's principle). The second order is responsible to i) the Pockels effect, i.e. linear fluctuation of the refractive index as function of applied electric field; and ii) the second harmonic generation (SHG), used in particular for doubling the frequency w.

- For the third order, the polarization can be written as:

$$P^{(3)}(\omega_1 + \omega_2 + \omega_3) = \varepsilon_0 \chi^{(3)}(\omega_1, \omega_2, \omega_3) E(\omega_1)(E\omega_2) E(\omega_3) \qquad \textbf{Eq. 1.5}$$

The 3rd order of polarization describes the cubic non linearity, 4-electric field waves mixing (3 excitation and 1 response), and the main four effects investigated are the general 4 wave mixing $\chi^{(3)}(-\omega_4,\omega_1,\omega_2,\omega_3)$, the third harmonic generation $\chi^{(3)}(-3\omega,\omega,\omega,\omega)$, the Raman gain $\chi^{(3)}(-\omega_s,\omega_p,-\omega_s,\omega_p)$, and the Kerr effect $\chi^{(3)}(-\omega,\omega,-\omega,\omega)$ responsible for the fast refractive index variation function of the light intensity **[Chemla 1981][Boyd 1992]**

In general, four wave mixing process, the polarization can be written as:

$$P(\omega_4) = \varepsilon_0 \chi^{(3)}(-\omega_4, \omega_1, \omega_2, \omega_3) E(\omega_1) E(\omega_2) E(\omega_3) \qquad \textbf{Eq. 1.6}$$

These materials are capable to obtain a frequency ω_4 different than excitation light frequencies ω_1, ω_2, ω_3. Energy conservation rule ($E = \frac{h\omega}{2\pi}$ where h is the Planck constant) and momentum conservation rule ($p = \frac{hk}{2\pi}$ where k is the wave vector) have to be respected, as shown in Figure 1.7 a) and b).

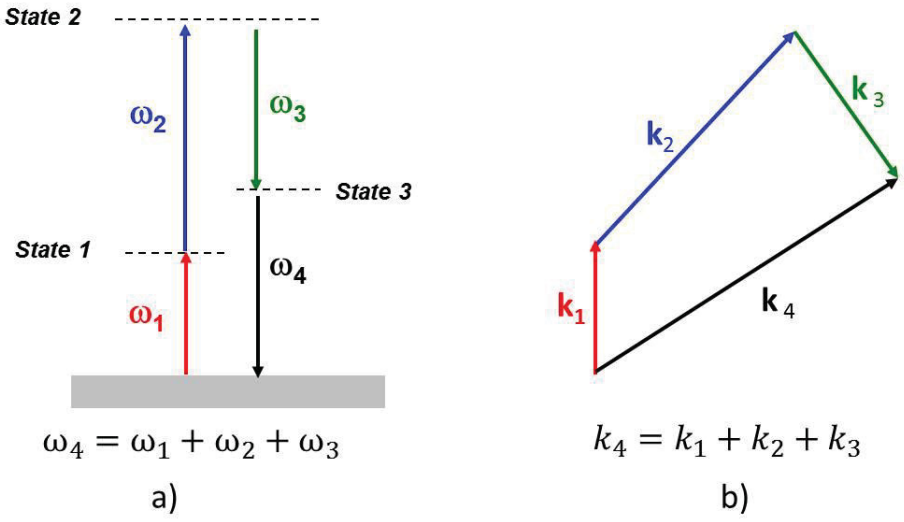

Figure 1.7 a) energy conservation rule and b) momentum conservation rule.

In the case of the Raman gain, the third-order term can be written as:

$$P(\omega_s) = \varepsilon_0 \chi^{(3)}(-\omega_s, \omega_p, -\omega_s, \omega_p) E(\omega_p) E(-\omega_s) E(\omega_p) \qquad \textbf{Eq. 1.7}$$

These different nonlinear optical phenomena may occur in a medium depending on its threshold for where nonlinear optical processes 'turn on' and the material's intrinsic laser damage threshold. Materials able to support high pump power for the nonlinear optical processes are presented in the next session.

3 Materials for Nonlinear Optics

Nonlinear optical (NLO) phenomena has been observed and exploited thanks to the expansion of laser science in the early 1960's, first studied in crystals (BaB_2O_4, $KTiOPO_4$, KH_2PO_4, $LiNbO_3$, etc.) **[Nie 1993].** In glasses, the first investigated effect under intense laser irradiation is the Kerr effect. This effect is at the origin of the refractive index changes or modification of a material which occurs to an extent related to the intensity of light. In the case of a Gaussian laser beam propagating through a material for instance, this change in refractive index can lead to the formation of a photo-induced lens, induced through the self-focusing effect. If large enough, such high intensity self-focusing can lead to laser damage, inevitably leading to the loss of the transmission efficiency. In most materials the change is reversible, reverting back to the original condition upon removal of the light; however in some materials a permanent change can result whereby the light modifies permanently the material's bonding.

In the 1980's, pulsed lasers appeared, enabling high intensity pulses of energy realized over a very short time period. Glasses became interesting candidates for investigation of NLO properties due to their advantages of low(er) cost (as compared to slow-growth crystalline materials), compositional and synthesis process flexibility, material properties, etc. Pulsed lasers allow the possibility for obtaining locally, an electric field high enough for taking advantage of the NLO response in glass materials. Within this context, third-order nonlinearities of glasses become accessible. They have been explored since the 90's to offer a general survey of the relationship structure – glass NLO properties

[Berthereau 1995][Cardinal 1995][Nazabal 1999][Kang 2002][Noguera 2003][O'Donnell 2004][Stegeman 2006-1][Anne 2007][Delestre 2010].

3.1 Fundamentals of glass formation

Since the study of glasses started, many definitions have been given to these materials. The first definition, having its origin in the process of formation, defines a glass as a supercooled liquid. This definition does not serve to differentiate an inorganic glass from a polymeric glass. Furthermore, some glasses can be formed without having ever been in a liquid state. Two alternative definitions can be: "a solid that does not show long range order" or "a liquid that has lost its ability to flow" **[Carter 2007]**. A glass can thus be defined as an amorphous (non-crystalline) solid lacking long-range order, exhibiting a glass transition temperature T_g. Indeed, glasses are disordered materials that lack the periodicity of crystals but behave mechanically like solids **[Debenedetti 2001].**

Understanding quantitatively the viscous slow-down that goes with supercooling and glass formation is a key challenge for glass scientists **[Abderson 1995]**. Debenedetti et al. focused attention on the liquid's energy landscape to relate the complex phenomenology to the molecular-scale events; namely the multidimensional surface generated by the system's potential energy as function of molecular coordinates. Debenedetti only used the dynamics and thermodynamics of viscous liquids above and close the glass transition temperature T_g to obtain the best definition of a glass.

The glass transformation behaviour, observed in glasses, is often discussed in terms of enthalpy variation during the glass formation. A plot of enthalpy (or volume) as a function of temperature can be illustrated, as shown in Figure 1.8.

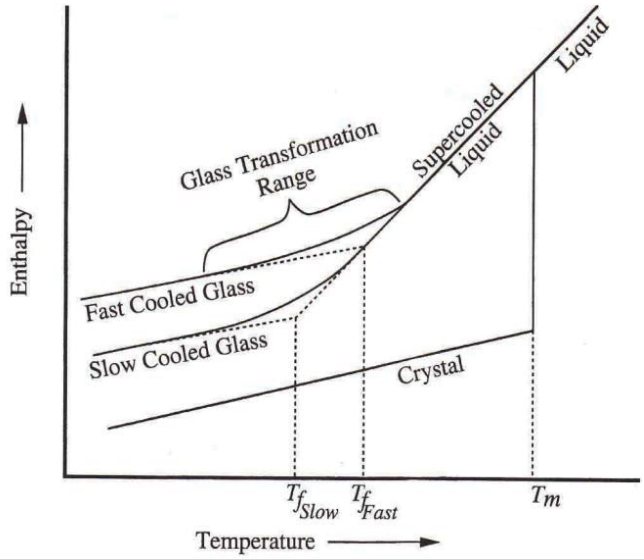

Figure 1.8 Effect of temperature on the enthalpy of a glass melt. [Shelby 2005].

Figure 1.8 shows the difference of enthalpy depending about the rate of the thermal quench. One can notice that faster is the thermal quench (i.e. transition liquid solid), higher is the enthalpy of the medium. If the liquid state has enough time for decreasing its enthalpy, molecular arrangement will occur, leading to a long-rang arrangement, namely crystallization.

One can envision a glass-melt at a temperature well above the melting temperature and cooled down at various cooling rates. For melts cooled at a slow rate, the enthalpy decreases linearly with temperature following the "liquid" line and then decreases rapidly at $T = T_m$ without entering the supercooled liquid region. This abrupt change in volume and enthalpy corresponds to the formation of a crystal, giving rise to fully crystallized materials having long-range order and periodic atomic arrangement. The change in enthalpy results in a phase change between the liquid state and the solid crystal. This phenomenon typically occurs at the melting temperature, T_m, of the corresponding crystal.

When the cooling rate is fast enough to avoid crystallization, the liquid reaches a state called a *"supercooled liquid"*. The atoms in the liquid will rearrange in a continuous fashion, leading to slow changes in enthalpy, until the viscosity of the liquid reaches a value that inhibits further rearrangement. When the rearrangement of the atoms in the supercooled liquid slows down, the enthalpy starts to deviate from the equilibrium line leading to a decrease in the slope of the graph (see Figure 1.8). In other words, the viscosity of the supercooled liquid is such that the atoms can no longer rearrange and this leads to formation of a solid with no long-range order. The region in which the slope of the enthalpy/temperature curve changes in the diagram is referred as to *"the transformation range"*, corresponding to the temperature range at which the supercooled liquid becomes a glass. The intercept between the supercooled liquid line and the glass line is commonly referred as to *"the fictive temperature"* T_f **[Shelby 2005]**. The intersection of the liquid and vitreous portions of the enthalpy (volume) versus

temperature curve provides one division of T_f occurring usually at $\frac{2}{3}T_m$. This temperature is an ideal temperature at which the (solid) glass would possess the exact same structure as that of the supercooled liquid. Keeping the same structure does not involve a discontinuous change in any physical property, leading to characterize this region as a fictive phase transition **[Debenedetti 2001].**

Practically, T_f is complicated to measure. From a thermodynamic point of view, if we assume a liquid cooled with an extremely slow cooling rate (i.e. the cooling rate tends to 0), the entropy of the supercooled liquid should have the same value as that of the crystal by extrapolation of the entropy curve. It is impossible to have an amorphous material with an entropy equal to that of the equivalent crystal, and this phenomenon is called the *"Kauzmann's paradox"* **[Kauzmann 1948]**. The only physically reasonable explanation of this phenomenon is a change of physical state below T_f. This "region" of glass transformation is called the *"glass transition temperature"* or glass transformation region. Through thermal analysis, it is possible to define the glass transition temperature (T_g) corresponding to the temperature range where bonds between atoms start to break and rearrange. T_g is not an intrinsic property of the glass since it varies with the heating rate applied to the sample **[Shelby 2005]**. It is also defined as a temperature at which the shear viscosity reaches 10^{12} Pa.s (viscosity is highly sensitive close to the glass transition temperature). It has been observed that the viscous slow-down is more pronounced close to T_g, over 2 to 4 orders of magnitude in viscosity by the Vogel-Tamman-Fulcher equation **[Angel 2000][Vogel 1921][Tamman 1926]][Fulcher 1925]**, suggesting a relationship between kinetics and thermodynamics **[Wolynes 1988]** and can be described

as done by Gibbs et al.: *"The thermodynamic viewpoint that emerges from this analysis considers the laboratory glass transition as a kinetically controlled manifestation of an underlying thermodynamic transition to an ideal glass with a unique configuration"* **[Gibbs 1958]**. From Adam and Gibbs' point of view, the viscous slow-down at T_g is from the decrease in the number of possible configurations that the system is capable of realizing **[Adam 1965]**. These fundamentals of glass formation are important for a good understanding of the material, leading to facilitate the comprehension of the properties ensued from the glass structure. Indeed, the conception of the glass medium is not an easy task compared to a crystal and the question of the "real" definition is still opened.

The relationship between the structure of the medium and its properties represents the key point of this study. With the existence of a glass transition temperature, it is possible to control the viscosity of the material without modifying the initial structure, only by controlling the thermodynamic and kinetic parameters. This capability to change the viscosity and so on the physical state of the glass permits to obtain easily and quickly new shapes such as fibres for telecommunication applications.

3.2 Optical fibers for mid-IR applications

An electric signal is transformed into light signal thanks to a transceiver. A transceiver uses a LED (Light Emitting Diode) or a laser for producing light. An optical fiber transmits this signal in its core thanks to the total internal reflection. This physical phenomenon occurs if the refractive index of the core n_{core} is higher than the refractive index of the surrounding cladding layer, n_{clad}, and if the incident angle of the light, α is

higher than limit reflection angle α_{crit} defined by $\sin(\alpha_{crit}) = \frac{n_{clad}}{n_{core}}$ as shown in Figure 1.9.

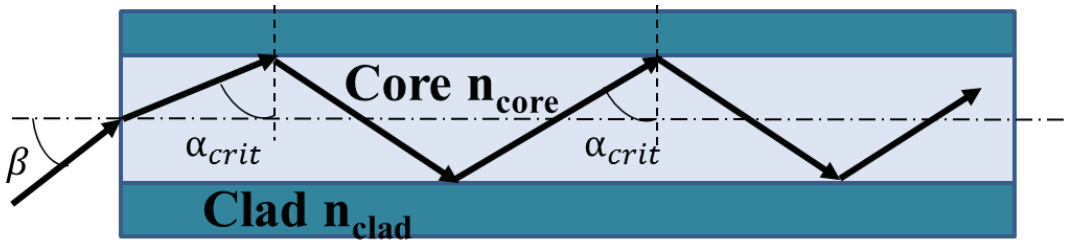

Figure 1.9 Principle of Optical fibers.

If $n_{core} > n_{clad}$, the light is trapped in the glass core and propagates through the fiber core as long as losses do not lead to attenuation of the signal. The light can be coupled in the fiber if the beam is introduced with an angle lower than a specific angle β, defined by:

$$\sin\beta = \frac{1}{n_0}\sqrt{n_{core}^2 - n_{clad}^2} \qquad \textbf{Eq. 1.8}$$

Where $(n_0 \sin\beta)$ represents the numerical aperture NA.

An optical fiber allows the light to have numerous propagation modes m, determined as function of its numerical aperture NA, the diameter d of the fiber and the wavelength λ of the used light. The number of modes, m, can be calculated by:

$$m \approx \left(\frac{NA*d}{\lambda}\right)^2 \qquad \textbf{Eq. 1.9}$$

Based on this equation, different types of fibers exist: multi-mode fibers and single-mode fibers. Multi-mode fibers (MMF) are able to transport multi-light paths. Due to this inter-modal dispersion (which is a phenomenon corresponding to the existence of different possible speeds for wave propagation), a signal spread with time, proportional to the fiber length, is observed. This dispersion limits the use of MMF to low data rate (quantity of data transfer) and/or short-distance applications. For these reasons, multi-mode fibers do not represent a judicious candidate for long-haul applications. Discussed below are short descriptions of various types of fibers where their use in different applications is presented.

Single-mode fiber (SMF)

Single-mode fibers (SMF) are optimized for long-haul/high data rate applications. The small size of SMF core thus can only admit one mode for propagation, the most direct as possible which means along the axis of the fiber. Optical losses are minimized because there is less reflection at the core/clad interface. These mono-mode lines are perfectly adapted for high data rate/long-haul applications. To avoid any dispersion (signal distortion due to the variation of different mode propagation rates), signals which are not parallel or fairly parallel to the fiber axis, have to be eliminated by using a relative large diameter of the clad (~50 to 100 μm), compared to the diameter of the core (~1 μm), as described in Figure 1.10.

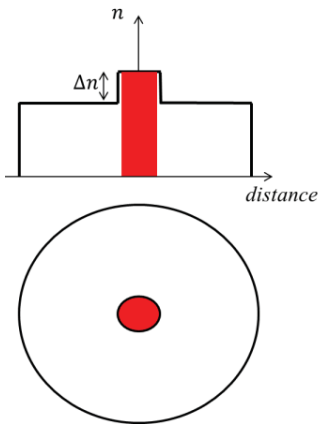

Figure 1.10 Fiber cross section and refractive index profile of single-mode fiber.

Based on this review of fiber geometry, one can now consider the attributes of the glass matrix that are important for Raman amplifiers based on glass fibers.

3.3 Glasses for third-order nonlinear optical application

Results obtained during Rivero's PhD work indicate a correlation in the evolution of Raman gain and the non-resonant Kerr effect. As discussed ealier, the optical Kerr effect has been extensively studied in glasses. The Kerr effect is a nonlinear effect, which is described by the nonlinear refractive index n_2, found in:

$$n = n_0 + n_2 I \qquad \textbf{Eq. 1.10}$$

Where n is the refractive index, n_0 is the linear refractive index, n_2 is the nonlinear coefficient called nonlinear index and I represents the light intensity. The n_2 can have different contributions **[Adair 1989][Vogel 1991]:**

$$n_2 = n_2^{electronic} + n_2^{nuclear} + n_2^{electrostrictive} + n_2^{thermal} \qquad \textbf{Eq. 1.11}$$

These four major quantities form the total nonlinear response.

The electronic response originates from the distortion of the electronic orbitals under an applied electric field. This distortion concerns essentially the external orbitals from the nucleus. The nuclear response can come from different origins, such as the molecular redistribution, molecular reorientation, or vibrational phenomena. The electrostrictive response occurs if the material is subject to shape deformation. The thermal response takes place during the material absorption of the electromagnetic wave, leading to a heated up area and intrinsically to a variation of the refractive index.

In term of response time, only two first contributions exhibit a fast response ($<10^{-9}$ s) (electronic ~ 10^{-15} s, nuclear ~ 10^{-13} s, electrostrictive ~ 10^{-9} s, thermal ~ 10^{-6} s) **[Kang 1996]**. The evolution of the tendency of nonlinear refractive indices measured in the non-resonant regime have been investigated for different glass families, as summarized in Figure 1.11 **[Adair 1987][Vogel 1991][Jeansannetas 1999][Cardinal 1999][Fargin 1999]**.

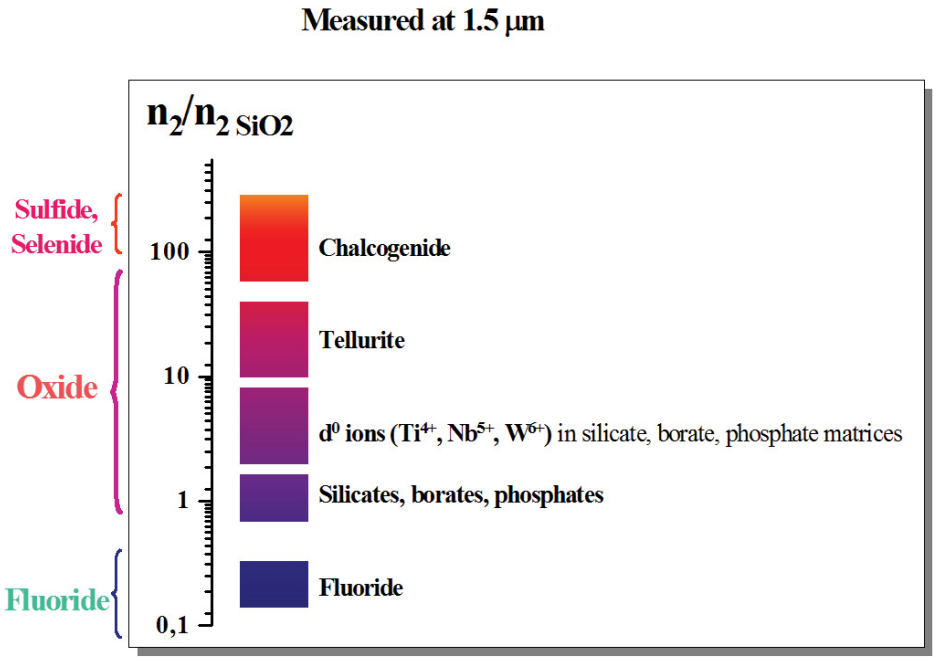

Figure 1.11 Order of magnitude of nonlinear refractive index in different glass families [Fargin 1999].

In a first approach, it can be seen that the Kerr effect follows the polarizability of anions ($F^{-}<O^{2-}S^{2-}<Se^{2-}$).

Discussed below are details associated with each of these glass families and the attributes that are important to their consideration as Raman gain materials.

3.3.1 Halide compounds

As shown in Figure 1.11, fluoride glasses exhibit the lowest nonlinear refractive index. These weak values are related to the low polarizability of fluorine and the large electronic band gaps, characteristic to fluoride materials.

3.3.2 Chalcogenide non-oxide glasses

In most of the chalcogenide glasses (ChGs) when the band-gap is small, the measure of the nonlinear refractive index has to be done in the non-resonant regime to avoid permanent, photo-induced structural modification. This, for most ChGs means measurements need to be made at wavelengths above 2 μm. This glass family exhibits the highest nonlinearity but is hardly compatible for telecommunication applications at 1.5 μm due to the occurrence of nonlinear multiphoton absorption. The optical nonlinearity of As_2S_3 for instance is 80 times higher than the silica one (e.g. $As_2S_3 \approx 80 \times SiO_2$) for a measurement in the near IR (1.06 μm). This high optical nonlinearity is essentially due to the higher hyperpolarizability of sulphur/selenium, as compared to matrices dominated by the oxygen anion, and to the small electronic band gap **[Hall 1989][Cardinal 1999].** The laser damage threshold of chalcogenide glass can be low (<10 GW/cm^2) **[Stegeman 2006-2]** as compared to oxide glasses and as discussed herein, this in some compositions could limit ChGs use as Raman gain media.

3.3.3 Tellurite oxide glasses

In these materials, the optical nonlinearity is more than 50 times of silica mainly thanks to the ns^2 lone pair of electrons **[Jeansannetas 1999]**. Tellurite oxide-based glasses are excellent candidates for Raman gain applications due to their theoretical broad transmission range [0.3 – 5 μm], their large optical nonlinearity and their high Raman cross section as compared to silica **[Hampton 1988]**. They represent one of the best

trade-off between optical nonlinearity and laser damage threshold among possible inorganic glass systems **[Hampton 1988]**.

Different structural configurations and hence, atomic positions or sites for tellurium ions, have been observed in glass and those sites have been shown to yield a different impact on the optical nonlinearity. The Valence Shell Electron Pairs Repulsion (VSEPR) rules allow understanding those types of sites.

The VSEPR rules, also called Gillespie or Nyholm-Gillespie theory, are a model which enables prediction of the geometry of a molecule; it is based on the electronic repulsion on the valence band.

Those rules are established from assumptions about types of bonds between atoms, such as:

- Electron pairs are used to link atoms in a molecule,
- Two atoms can be linked by at least one electron pairs,
- Atoms can own lone-pair electrons, not used to create a bond,
- Electrons apply a repulsive electric field on each other,
- Multiple bonds use more room than single bond,
- Lone electron pairs use more room than regular electron pairs.

The AXE method is a technique permitting to apply the VSEPR rules, where A represents the central atom; X is the number of sigma bonds between atoms and E the

number of lone electron pairs surrounding the central atom. By this noting way, it is possible to register all different molecule geometries (Table 1.2).

Molecule Type	Geometry	Example
$\mathbf{AX_1}$	Linear	HF
$\mathbf{AX_2}$	Linear	CO_2
$\mathbf{AX_2E}$	Bent	SO_2
$\mathbf{AX_2E_2}$	Bent	H_2O
$\mathbf{AX_2E_3}$	Linear	$XeCl_2$
$\mathbf{AX_3}$	Trigonal planar	SO_3
$\mathbf{AX_3E}$	Trigonal pyramidal	NH_3
$\mathbf{AX_3E_2}$	T-shaped	BrF_3
$\mathbf{AX_4}$	Tetrahedral	CH_4
$\mathbf{AX_4E}$	Trigonal bipyramidal	SF_4
$\mathbf{AX_4E_2}$	Square planar	XeF_4
$\mathbf{AX_5}$	Trigoanl bipyramidal	PCl_5
$\mathbf{AX_5E}$	Square pyramidal	BrF_5
$\mathbf{AX_5E_2}$	Pentagonal planar	XeF_5^-
$\mathbf{AX_6}$	Octahedral	SF_6
$\mathbf{AX_6E}$	Pentagonal pyramidal	$XeOF_5^-$
$\mathbf{AX_7}$	Pentagoanl bipyramidal	IF_7
$\mathbf{AX_8}$	Square antiprismatic	IF_8^-
$\mathbf{AX_9}$	Tricapped trigonal prismatic	ReH_9^{2-}

Table 1.2 Geometry of different types of molecules according to VSEPR rules

The combination of the VSEPR rules with the localized molecular orbital theory permits to associate the understanding of molecule geometry with the impact of lone electron pairs on a material structure. TeO_4 molecular units are an AX_4E molecule type. The molecular entity's lone pair of electron $5s^2$ induces a strong deformation of the molecular entities, and is not totally free because of hybridization with the 2p orbitals of oxygen. Furthermore, for all TeO_n entities, Berthereau et al. showed by ab ignition calculation,

that the $5s^2$ and the 5p are hybridized together and form a molecular orbital with a high polarizability, leading to a highly polarizable and hyperpolarizable material **[Bertherau 1995]**. The lone pair of electron is very sensitive to an electromagnetic field, leading to low electronic band gap characteristic to the ns-np transition. The higher optical nonlinearities have been obtained when TeO_2 is associated with another ion having a lone pair electron such as Tl^+, Pb^{2+}, Bi^{3+}… **[Dutreilh 2003][Fargin 1996]**. Berthereau shows that the evolution of the nonlinear refractive index is both linked to the tellurite content and to the nature of the glass modifier introduced into the glass matrix. Depending on the glass modifier different $\chi^{(3)}$ values can e observed with the following evolution $d^{10} < ns^2np^6 < d^0 < ns^2$ **[Berthereau 1995].**

Based on the superb properties of tellurite glasses, the present PhD study has focused on optimizing the bulk glass materials for use as optical fibers for Raman applications. The important attributes of these materials and their prior investigation as candidate Raman gain media, are discussed in the next section.

4 Relationship between tellurite glass compositions, nonlinearity and Raman gain

Oxide glasses based on TeO_2 for nonlinearity applications were intensively studied between 1989 and 1998 by Japanese research teams (MITI, STA, Monbusto) and by national companies (Ube, Sumitomo, Asahi glass…). These research teams were the first to invest more than 500 millions of yen for developing the TeO_2-based glasses

[Kilidjian 1994]. Tellurite oxide based glasses possess a large Raman gain coefficient measured to around 50 times that of fused silica ($0.89x10^{-13}$ $m.W^{-1}$). Furthermore, glasses containing a high TeO_2 content present really interesting thermal and physical properties, which make possible the manufacture of fibers and waveguides **[Savelii 2011].**

An 'ideal' Raman gain material would possess the following attributes:

1) Broadband optical transparency over the spectral range of interest;
2) Low intrinsic and extrinsic absorption over pump wavelengths and signal transmission wavelengths;
3) High spontaneous Raman cross-section across a broad spectral window;
4) High optical nonlinearity for high Raman gain;
5) High laser damage resistance to enable the maximum power handling during pumping.

Hence, material composition and bonding as well as other attributes that dictate thermal, mechanical and optical properties all are important contributors to the overall resulting material optical performance. Discussed next are the relationship between glass chemistry and structure, as this structure dictates all resulting physical properties.

Pure TeO_2 glass is impossible to prepare, requiring minor (a few mol%) additions of modifiers to avoid crystallization. Previous investigations have shown that the introduction of d^0-transition ions (W^{6+}, Nb^{5+}, Ta^{5+},Ti^{4+},etc.) or ions with a lone pair of electrons such as Tl^+ or Pb^{2+} to the TeO_2 glass network former, allows one to maintain

high optical nonlinearity, high Raman gain and to improve the processing conditions required to make high quality glass **[Stegeman 2005][Kim 1995][Rivero 2007]**.

TeO_2 glasses with concentration of TeO_2 above 95 mol% are mainly formed by *trigonal bipyramids* TeO_4. When a glass modifier is introduced in the TeO_2 matrix, distortions appear, transforming TeO_4 trigonal bipyramids to TeO_{3+1} molecular units with long Te-O bonds (usually forming chains); further additions lead to TeO_3 *trigonal pyramids*. This evolution of molecular species with modifier addition is shown below in Figure 1.12.

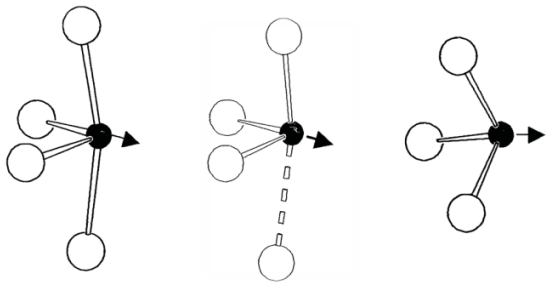

Figure 1.12 Structural entities in TeO_2 glass: TeO_4 trigonal bipyramidal unit (tbp), TeO_{3+1} transition step unit and TeO_3 trigonal pyramidal unit (tp)

In the literature, the structural role of alkali- or alkaline-earth oxide in TeO_2 glass has been discussed previously **[Sekiya 1994][Sekiya 1992][Himei 1994][Heo 1992][Duverger 1997]**, and these authors agree that the conversion of TeO_4 toTeO_3 through the introduction of divalent cation and high basicity oxygen anion into TeO_2 glass, can be confirmed. These findings have been reported in Raman spectra of TeO_2-MO glasses **[Sekiya 1994][Himei 1994][Heo 1992].**

Several TeO_2-based glass systems, such as TeO_2-Nb_2O_5, TeO_2-ZnO, and TeO_2-Nb_2O_5-PbO, have also been shown to have excellent thermal and optical performances **[Komatsu 1991][Kim 1995][Ren 2002]**. In these systems, it is reported that ZnO and Nb_2O_5 can improve optical nonlinearity, resistance to crystallization, chemical durability and thermal stability of the glasses.

According to Soulis et al. **[Soulis 2008][Udovic 2009]**, the introduction of d^0 element such as Nb leads to the formation of six-coordinated Nb^{5+} ions (NbO_6) that are preferentially connected with neighboring TeO_4 units. The simultaneous incorporation of $[NbO6]^{7-}$ and M^{2+} (M=Zn, Mg, Ca, Sr, Ba) is expected to stabilize TeO_4 units, followed by the cleavage of the Te^{IV}–$_{eq}O_{ax}$–Te^{IV} connection. This mechanism is significantly different from that seen in the case of the single doping of M^{2+} ions to TeO_2 glass that brings about TeO_4 → TeO_3 conversion as a result of the cleavage of Te^{IV}–$_{eq}O_{ax}$–Te^{IV} connection **[Hayakawa 2010].**

Introduction of a metal oxide such as ZnO and/or an alkali or alkaline earth has also been shown to lead to suitable glasses for optical fiber fabrication **[Savelii 2011][Manning 2012].** Zinc ions, within the tellurite network occupy a tetrahedrally coordinated site.

As explained by Jeansannetas et al. **[Jeansannetas 1999]**, the largest nonlinear response is generated by heavy cations having ns^2 electron pairs such as Te^{4+}, Bi^{3+}, Pb^{2+} or also Tl^{+} ions. It has been described by Linda et al. **[Linda 2013]** that the addition of Tl_2O in the

tellurite glass matrix leads to high magnitude of optical nonlinearity **[Jeansannetas 1999][Dutreilh-Colas 2003]** but is at the expense of depolymerization of the glass network and a reduction to the glass' stability **[Noguera 2004][Sekiya 1992].**

Recently, Xu et al. showed that the Bi_2O_3 content leads to a high $\chi(3)$ value which is attributed to the presence of BiO_6 octahedral units in a TeO_2-Bi_2O_3-BaO glass system **[Xu 2011]**. Heavy metal barium, added as a modifier BaO in the tellurite system has been reported to exhibit good potential in resulting fiber fabrication **[Hill 2007]** and Raman gain **[Jackson 2009]** applications. Udovic et al. and Durand et al., proved that the addition of Bi_2O_3 strongly modifies the glass framework by giving rise to the island-like $[Te_nO_m]^{2(m-2n)-}$ complexed tellurite anions, thus causing depolymerization of the tellurite glass in the TeO_2-Bi_2O_3-TiO_2 system. **[Udovic 2006][Durand 2006].**

Of special importance to our overall goal of drawing fiber with low levels of crystallization and thus low scatter losses, the effect of crystallization on the optical properties is also an interesting phenomenon to consider. Literature on this glass system has been previously summarized by Massera et al. who carried out an analysis on the crystallization of tellurite bismuth zinc-based oxide glass materials **[Massera 2009]**.

While crystallization (and scatter) is usually undesirable in glasses, controlled crystallization of a glass that can result in unique morphology, i.e. a nano-composite or glass ceramic, can yield materials with unique properties and functionality.

5 Conclusion

To summarize, tellurite-based materials will be studied as Raman gain candidates in this thesis due to their remarkable optical properties, good thermal stability, chemical durability, broad homogeneity range, and modestly low melting temperatures **[El-Mallawany 2002]**. Tellurite oxide-based glasses are excellent candidates as gain media meeting many of the criteria listed earlier, namely their broad transmission range [0.3 – 5 μm] and their high Raman cross section as compared to existing commercial silica fibers materials **[Hampton 1988]**. With previously measured Raman gain coefficients to around 58 times that of fused silica previously reported for *bulk* glasses **[Stegeman 2005]** further material optimization to make these matrices suitable for fiber formation (i.e. with enhance crystallization stability during fiberization) will extend their potential. TeO_2-$TaO_{5/2}$-ZnO, TeO_2-$NbO_{5/2}$ and TeO_2-$BiO_{3/2}$-ZnO glass systems have been chosen in this study to probe the effect of glass modifiers on the structural response and on Raman gain and to enhance this stability required for fiber formation.

For many optical applications, optical fibers are desired. This target requires the development of high purity materials exhibiting limited or no absorption in the transmission bandwidth in the near infrared (NIR). Hydroxyl groups are among the impurities which can dramatically decrease the transmission window in the near infrared (NIR). Indeed, in tellurite glasses, impurities such as hydroxyl groups are common and exhibit a strong absorption in the spectral range around 3 μm with harmonics at around 1.4 μm and 1μm **[Shultz 1974][Sanghera 1998]**. An effort has been conducted in the

present work on the purification of material, able to reduce the strong OH absorption. Glass properties will be compared in term of structural, optical and physical changes between a “purified” glass and a “non-purified” glass.

Regarding the Raman gain performance of tellurite, the underlying issue of the influence of the tellurite glass network on the resulting Raman response is a major issue not fully understood. A limited number of studies have been conducted to relate the glass composition and the glass structure to the vibrational response in terms of magnitude and spectral width response. In this PhD, an effort will be done to understand the influence of different glass modifiers on both glass structures and nonlinear optical response as well as glass stability. Systematic spectroscopic vibrational analyses will be investigated on tellurite crystal and tellurite-based glasses to probe the vibrational signature and the impact of the short-range order and intermediate-range order on the nonlinear optical glass properties. The relationship between the polarity, the polarizability and the hyperpolarizability will be evaluated to relate the impact of the short-range order on the nonlinear optical properties in relation with the numerous experimental and theoretical investigations conducted on different tellurite glass systems. Fiber fabrication will be also presented for the most promising glass composition.

Chapter 1 – References

Abderson 1995: P.W. Abderson, Science 267 (1995) 1615.

Adair 1987: R. Adair, L.L. Chase, S.A. Payne, Journal of the Optical Society of America B 4 (1987) 875-881.

Adair 1989: R. Adair, L.L. Chase, S.A. Payne, Physical Review B 39 (1989) 3337-3350.

Adam 1965: G. Adam, J.H. Gibbs, Journal of Chemical Physics 43 (1965) 139-146.

Angel 2000: C.A. Angel, K.L. Ngai, G.B. McKenna, P.F. McMillan, S.W. Martin, Journal of Applied Physics 88 (2000) 3113-3157.

Anne 2007: M.L. Anne, PhD thesis "Guides d'ondes en verres de chalcogénures pour la détection infrarouge d'espèces (bio)chimiques" (2007) University of Rennes, France.

Berthereau 1995: A. Berthereau, PhD thesis "Matériaux vitreux pour l'optique non linéaire" (1995) University of Bordeaux, France.

Blanchandin 2002: S. Blanchandin, P. Thomas, P. Marchet, J.C. Champarnaud-Mesjard, B. Frit, Journal of Alloys and Compounds 347 (2002) 206–212.

Boyd 1992:R. W. Boyd, "Nonlinear optics", Academic Press (1992) ISBN 0-12-121680-2.

Cardinal 1995: T. Cardinal, PhD thesis "Propriétés optiques non linéaires des verres borophosphatés de titane ou de niobium" (1995) University of Bordeaux, France.

Cardinal 1996: T. Cardinal, E. Fargin, G. Le Flem, M. Couzi, L. Canioni, P. Segonds, L. Sarger, A. Ducasse, F. Adamietz, European Journal of Solid State and Inorganic Chemistry 33 (1996) 597.

Cardinal 1999: T. Cardinal, K. Richardson, H. Shim, G. Stegeman, A. Schulte, R. Beathy, K. Le Foulgoc, C. Meneghini, J.F. Viens, A. Villeneuve, Journal of Non-Crystalline Solids 256-257 (1999) 353.

Carter 2007: C. B. Carter, M. G. Norton, "Ceramic Materials", Springer (2007).

Chemla 1981: D. Chemla, J. L. Oudar, J. Zyss, "L'echo des recherches", 103 (1981) 3.

Chluda:https://www2.lirmm.fr/lirmm/interne/BIBLI/CDROM/ROB/2006/Doctiss_2006/articles/07.pdf.

Debenedetti 2001: P.G. Debenedetti, F.H. Stillinger, Nature 410 (2001) 259.

Delestre 2010: A. Delestre, PhD thesis "Polarisation thermique et microstructuration planaire de propriétés optiques non linéaires du second ordre dans des matériaux vitreux: Etude des verres $NaPO_3$-$Na_2B_4O_7$-Nb_2O_5" (2010) University of Bordeaux, France.

Durand 2006: O. Durand, PhD thesis "Propriétés structurales et vibrationnelles des phases désordonnées dans le système TeO_2-Bi_2O_3"(2006) University of Limoges, France.

Dutreilh 2003: M. Dutreilh-Colas, P. Thomas, J.C. Champarnaud-Mesjard, E. Fargin, Physics and Chemistry of Glasses 44 (2003) 349.

Duverger 1997: C. Duverger, M. Bouazaoui, S. Turrell, Journal of Non-Crystalline Solids 220 (1997) 169.

El-Mallawany 2002: R.A.F. El-Mallawany, Tellurite Glasses Handbook: Properties and Data, CRC Press, Boca Raton, FL, (2002).

Fargin 1996: E. Fargin, A. Berthereau, T. Cardinal, G. Le Flem, L. Ducasse, L. Canioni, P. Segonds, L. Sarger, A. Ducasse, Journal of Non-Crystalline Solids 203 (1996) 96.

Fargin 1999: E. Fargin, Phosphorus Research Bulletin 10 (1999) 490.

Fulcher 1925: G.S. Fulcher, Journal of the American Ceramic Society 8 (1925) 339.

Gibbs 1958: J.H. Gibbs, E.A. DiMazio, Journal of Chemical Physics 28 (1958) 373-38.

Hall 1989: D.W. Hall, M.A. Newhouse, N.F. Borelli, W.H. Dumbaugh, D.L. Weidman, Applied Physics Letters 54 (1989) 1293.

Hampton 1988: R.N. Hampton, W. Hang, G.A. Saunders, R.A. El-Mallawany, Physics and Chemistry of Glasses 29 (1988) 100.

Hayakawa 2010: T. Hayakawa, M. Hayakawa, M. Nogami, P. Thomas, Optical Materials 32 (2010) 448-455.

Heo 1992: J. Heo, D. Lam, G.H. Sigel, E.A. Mendoza, D.A. Hensley, Journal of the American Ceramic Society 75 (1992) 277.

Hill 2007: J. Hill, A. Jha, Journal of Non-Crystalline Solids 353 (2007) 1372

Himei 1994: Y. Himei, A. Osaka, T. Nanba, Y. Miura, Journal of Non-Crystalline Solids 177 (1994) 164.

Jackson 2009: J. Jackson, C. Smith, J. Massera, C. Rivero-Baleine, C. Bungay, L. Petit, K. Richardson, Optics Express 17 (2009) 9071.

Jeansannetas 1999: B. Jeansannetas, S. Blanchandin, P. Thomas, P. Marchet, J.C. Champarnaud, T. Merle, B. Frit, V. Nazabal, E. Fargin, G. Le Flem, M.O. Martin, B. Bousquet, L. Canioni, S. Le Boiteux, P. Segonds, L. Sarger, Journal of Solid State Chemistry 146 (1999) 329.

Kang 1996*:* I. Kang, S. Smolorz, T. Krauss, F. Wise, B.G. Aitken, N.F. Borelli, Physical Review B 54 (1996) 12641.

Kang 2002: Y. Kang, PhD thesis "Calculations and measurements of Raman gain coefficients of different fiber types" (2002) Faculty of the Virginia Polytechnic Institute and State University, USA.

Kauzmann 1948: W. Kauzmann, Chemical Reviews, 43 (1948) 219.

Kilidjian 1994: G. Kilidjian, Service pour la science et la technologie, Bulletin de l'Ambassade de France au Japon, Mai-Octobre (1994) 3.

Kim 1995: S. Kim, T. Yoko, Journal of the American Ceramic Society 78 (1995) 1061.

Komatsu 1991: T. Komatsu, H. Tawarayama, H. Mohri, Journal of Non-Crystalline Solids 135 (1991) 105.

Linda 2013: D. Linda, J.R. Duclere, T. Hayakawa, M. Dutreilh-Colas, T. Cardinal, A. Mirgorodsky, A. Kabadou, P. Thomas, Journal of Alloys and Compounds 561 (2013) 151-160.

Manning 2012: S. Manning, H. Ebendorff-Heidepriem, T. M. Monro, Optical Material Express 2 (2012) 140-152.

Massera 2009: J. Massera, PhD thesis "Nucleation and growth behavior of tellurite-based glasses suitable for mid-infrared applications" (2009) Clemson University, USA.

Murugan 2005: G.S. Murugan, Y. Ohishi, Journal of Non-Crystalline Solids 351 (2005) 364-371.

Nazabal 1999: V. Nazabal PhD thesis "Génération de second harmonique dans des verres oxydes polarisés thermiquement" (1999) University of Bordeaux, France.

Nie 1993: W. Nie, Advanced Materials 5 (1993) 520-545.

Noguera 2003: O. Noguera, PhD thesis "Propriétés structurales, vibrationnelles et diélectriques de matériaux à base d'oxyde de tellure" (2003) University of Limoges, France.

Noguera 2004: O. Noguera, T. Merle-Mejean, A.P. Mirgorodsky, P. Thomas, J.C. Champarnaud-Mesjard, Journal of Physics and Chemistry of Solids 65 (2004) 981.

O'Donnell 2004: M. O'Donnell, PhD thesis "Tellurite and fluorotellurite glasses for active and passive fibreoptic waveguides" (2004) University of Nottingham, United Kingdom.

Petit 2002: L. Petit, PhD thesis "Amplification optique dans des verres borophosphate de niobium et tellurite dopes aux ions de terres rares présentant un indice optique non linéaire élevé" (2002), University of Bordeaux, France.

Refi 1999: J.J. Refi, Bell Labs Technical Journal, 246-261, January-March (1999).

Ren 2002: J. Ren, W. Huang, J. Lin, Journal of Optoelectronic Laser 13 (2002) 590.

Rivero 2005: C. Rivero, PhD thesis "High gain/Broadband oxide glasses for next generation Raman amplifiers" (2005) University of Central Florida, USA/University of Bordeaux, France.

Rivero 2007: C. Rivero, R. Stegeman, K. Richardson, G. Stegeman, G. Turri, M. Bass, P. Thomas, M. Udovic, T. Cardinal, E. Fargin, M. Couzi, H. Jain, and A. Miller, Journal of Applied Physics 101 (2007) 023526.

Sanghera 1998: L.S. Sanghera, I.D. Aggarwal, "Infrared Fiber Optics", CRS Press, New York (1998).

Savelii 2011: I. Savelii, J.C. Jules, G. Gadret, B. Kibler, J. Fatome, M. El-Amraoui, N. Manikandan, X. Zheng, F. Desevedavy, J.M. Dudley, J. Troles, G. Renversez, F. Smektala, Optical Materials 33 (2011) 1661-1666.

Sekiya 1992: T. Sekiya, N. Mochida, A. Ohtsuka, M. Tonokawa, Journal of Non-Crystalline Solids 144 (1992) 128.

Sekiya 1994: T. Sekiya, N. Mochida, A. Ohtsuka, Journal of Non-Crystalline Solids 168 (1994) 106.

Seo 2000: H.S. Seo, K.Oh, Optics Communications 181 (2000) 145-151.

Shelby 2005: J.E. Shelby, "Introduction to Glass Science", 2nd Edition, RS.C (2005).

Shen 1984*:* Y. R. Shen, "The principles of nonlinear optics", Wiley – Interscience, New York (1984) ISBN 0471-88998-9.

Shultz 1974: P.C. Shultz, Journal of the American Ceramic Society 57 (1974) 309-313.

Soulis 2008: M. Soulis, A.P. Mirgorodsky, T. Merle-Méjean, O. Masson, P. Thomas, M. Udovic, Journal of Non-Crystalline Solids 354 (2008) 143.

Stegeman 2005: R. Stegeman, C. Rivero, K. Richardson, G. Stegeman, P. Delfyett, Y. Guo, A. Pope, A. Schulte, T. Cardinal, P. Thomas, J.C. Champarnaud-Mesjard, Optics Express 13 (2005) 1144-1149.

Stegeman 2006-1: R. Stegeman, PhD thesis "Direct nonlinear optics measurements of Raman gain in bulk glasses and estimates of fiber performance" (2006) University of Central Florida, USA.

Stegeman 2006-2: R. Stegeman, G. Stegeman, P. Delfyett, L. Petit, N. Carlie, K. Richardson, M. Couzi, Optics Express 14 (2006) 11702.

Tamman 1926: G. Tamman, W. Hesse, Zeitschrift fur Anorganische und Allgemeine Chemie 156 (1926) 245-257.

Udovic 2006: M. Udovic, P. Thomas, A. Mirgorodsky, O. Durand, M. Soulis, O. Masson, T. Merle-Mejean, J.C. Champarnaud-Mesjard, Journal of Solid State Chemistry 179 (2006) 3252–3259.

Udovic 2009: M. Udovic, P. Thomas, A.P. Mirgorodsky, O. Masson, T. Merle-Méjean, C. Lasbrugnas, J.C. Champarnaud-Mesjard, T. Hayakawa, Material Research Bulletin 44 (2009) 248.

Vogel 1921: H. Vogel, Zeitschrift fur Physik 22 (1921) 645-646.

Vogel 1991: E.M. Vogel, M.J. Weber, D.M. Krol, Physics and Chemistry of Glasses, 32 (1991) 231.

Wolynes 1988: P.G. Wolynes, AIP Conference Proceedings 180 (1988) 39-65.

Xu 2011: T. Xu, F. Chen, S. Dai, X. Shen, X. Wang, Q. Nie, C. Liu, K. Xu, J. Heo, Journal of Non-Crystalline Solids 357 (2011) 2219-2222.

CHAPTER 2

TELLURITE GLASS SYNTHESIS AND PROPERTIES

Chapter 1 introduced the key aspects on nonlinear optics as applied to optical glasses and discussed how and why tellurite glasses modified with heavy metal oxide species, are good potential candidates for Raman gain applications. When these glasses are formed into fiber, the glass is required to have superb crystallization stability so as to minimize scatter loss while preserving high gain. Previous investigations reported in Chapter 1, typically looked at these issues separately, not deliberately optimizing glass compositions for high gain with excellent crystallization stability. This dissertation aims to establish such a correlation based on structure/property optimization that has evaluated the glass chemistry, structure, and optical property correlation within a multi-component tellurite glass system.

This chapter discusses the impact of different glass modifiers present into TeO_2-$TaO_{5/2}$-ZnO, TeO_2-$NbO_{5/2}$ and TeO_2-$BiO_{3/2}$-ZnO glass matrices on thermal, physical and optical properties. Furthermore, another way to synthesis tellurite-based glasses in order to reduce the water content is explored with an investigation on potential change of properties between a regular and purified tellurite-based glass. Crystallization in TeO_2-$BiO_{3/2}$-ZnO glass matrix is examined as a means to form glass ceramic (GC), as a means of possibly enhancing the material's nonlinear optic. Finally, the process of fiber fabrication will be explained with measure of the optical losses and gain for the most promising glass composition.

1 Multi-component tellurite glasses

Tellurite-based glasses containing different glass modifiers such as Nb_2O_5, Ta_2O_5, Bi_2O_3 and/or ZnO have been elaborated. Three glass systems have been investigated:

- TeO_2-$TaO_{5/2}$-ZnO,
- TeO_2-$NbO_{5/2}$,
- TeO_2-$BiO_{3/2}$-ZnO.

As explained in the Chapter 1, d^0-ions represent a good glass modifier for nonlinear optical applications. Ta^{5+} and Nb^{5+} ions have been chosen, they propose a similar chemistry and we were interested in evaluating and comparing two pentavalent species, especially since the niobium ion possesses two oxidation states (+3 and +5) while the tantalum ion maintains a single oxidation state +5. ZnO has proven its compatibility with and assistance in fiber fabrication. Finally the bismuth tellurite-based glass has been chosen in order to look at the crystallization behavior of this glass and understand potential improvement in terms of its nonlinear optical response.

After the description of the glass preparation methods used, the physical and chemical properties of the three families of tellurite glass are discussed and the purification processes used to ensure the resulting Raman gain materials possess low absorption loss, is presented.

The crystallization phenomena of the TeO_2- $BiO_{3/2}$-ZnO glass system exhibiting a single crystalline phase has been studied previously but these glasses showed only moderate resistance to crystallization upon drawing into fiber. Additionally, these glasses exhibited higher losses in fiber form, than in their bulk glass counterpart, despite purification efforts to remove hydroxyl impurities. In the present effort, a change to the type of modifier has been carried out, to enable improved crystallization stability while maintaining good Raman gain performance.

2 Tellurite glass synthesis

Tellurite-based glasses in the host systems TeO_2-$TaO_{5/2}$-ZnO, TeO_2-$NbO_{5/2}$ and TeO_2- $BiO_{3/2}$-ZnO are prepared in 7-10 g batches by weighing exact quantity m_x of raw materials:

$$m_x = a_x * \frac{m_{glass}}{M_{glass}} * M_x \qquad \textbf{Eq. 2.1}$$

Where a_x is the stoichiometric coefficient, m_x is the mass of one raw material, m_{glass} the mass of the glass, M_{glass} the molecular weight of the glass and M_x the molecular weight of the raw materials. The glasses are prepared from (TeO_2 99.99% (Alfa Aesar), Ta_2O_5 99.993% (Alfa Aesar), Nb_2O_5 99.5% (Alfa Aesar) Bi_2O_3 (Alfa Aesar, 99%) and ZnO 99.0% (Alfa Aesar)). Before melting, raw materials are pre-heated at 200, 300 and

400 °C to eliminate or minimize components such as water, hydroxyl and carbonyl groups, respectively, already present in the raw materials.

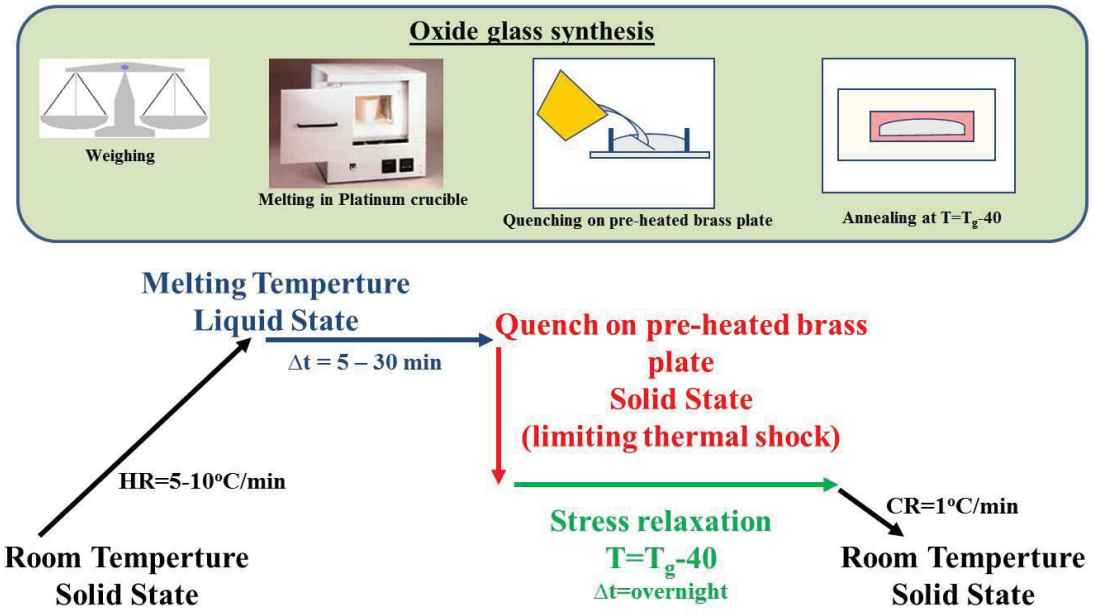

Figure 2.1 Melting process of tellurite oxide based glasses

As described in Figure 2.1, the batch mixtures are melted in a platinum crucible at a temperature between 800 and 1000 °C, depending on the glass composition, for 15 minutes to prevent volatilization and limit the interaction with the platinum crucible, which could lead to partial reduction of TeO_2. Indeed, tellurite oxide melts at 732 °C and boils at 1245 °C, but black smoke appears at 1000 °C, due to vaporization of TeO_2, leading to a change of glass composition. The melts are quenched on a pre-heated brass plate and the resulting glasses are annealed overnight at a temperature 40 °C below the glass transition temperature (T_g) to avoid glass fracture.

3 Glass properties in the TeO_2-$TaO_{5/2}$-ZnO, TeO_2-$NbO_{5/2}$, TeO_2-$BiO_{3/2}$-ZnO glass networks

3.1 Characterization tools

3.1.1 Differential Scanning Calorimetry - DSC

In a typical differential scanning calorimetry (DSC) experiment, a sample and a reference are both subject to a linear heating ramp. The calorimeter records the temperature difference between the sample and the reference and then converts that information into a measure of the heat flow that goes into and out of the sample. The supplied energy difference is recorded as a function of the temperature. Thermal events appear as deviations from the baseline. Thus DSC measures temperatures and heat flows variation associated with thermal transitions (phase transition, heat capacity change) in the material. In case of a glass, one can measure the glass transition temperature (T_g), the onset of crystallization (T_x), the crystallization temperature (T_p) and melting temperature (T_m). Additional informations such as heat capacity, melting enthalpy or apparent activation energy can be calculated from DSC patterns. In this study, the thermal properties of the investigated glasses are measured using a disc-type differential scanning calorimeter, DSC 2920 of TA instruments. The measurements are carried out in a hermetically sealed aluminium pan. The glass transition temperature (T_g), the onset of crystallization (T_x) and the crystallization temperature (T_p) are determined at a heating rate of 10 °C/min. The glass transition temperature (T_g) is measured at the onset of the

change of heat capacity and the crystallization temperature (T_p) at the maximum of the exothermic peak as illustrated below in Figure 2.2.

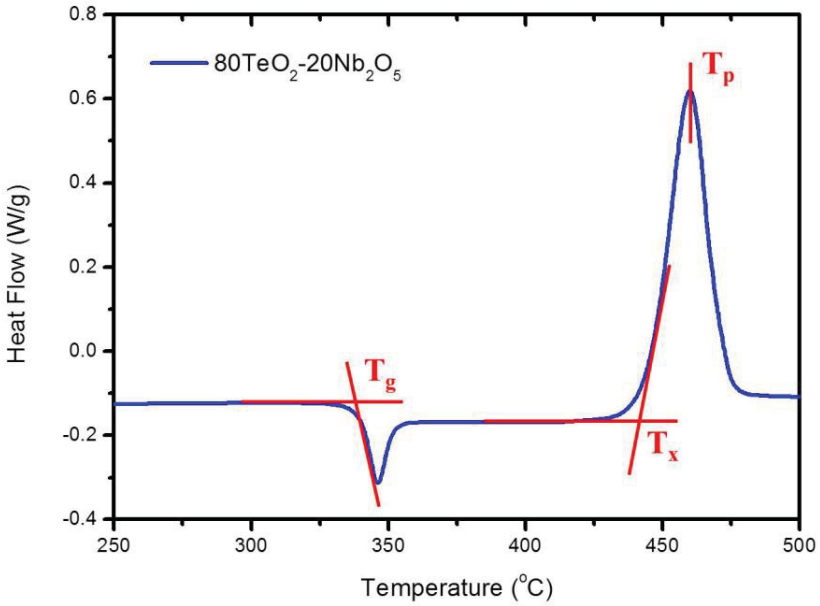

Figure 2.2 DSC measurement with determination of glass transition temperature T_g, the onset of crystallization T_x and the crystallization temperature T_p

The accuracy of the measurement is estimated to be ±2 °C. The difference between the glass transition temperature and the onset of crystallization ($\Delta T=T_x-T_g$) represents the glass stability against the crystallization.

3.1.2 Density measurement – Archimede's principle

Density is defined as the mass of the substance per unit of volume (g/cm^3). In this study, the density of bulk glass materials was measured by Archimedes' principle using

diethylphtalate liquid with a known density as a function of temperature. The measurements were performed on polished samples. The accuracy was better than 0.02g/cm^3. The density measurement apparatus is represented in Figure 2.3. **[Massera 2009]**.

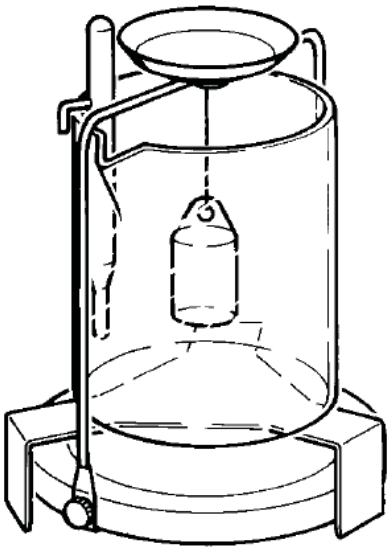

Figure 2.3 Measure of density by Archimede's method

The polished glass is first weighed in air, and then while immersed in the oil. From these two weightings, density of the glass is calculated as follows:

$$\vec{P}_{liq} = \vec{P}_{air} + \vec{F}_{Archimedes} \qquad \textbf{Eq. 2.2}$$

Where $\vec{P}_{liq}$: is the force measured when the sample is immersed in the diethylphtalate liquid, $\vec{P}_{air}$ is the force due to the gravity of the sample in the air and $\vec{F}_{Archimedes}$:the Archimedes' force. The above expression can be re-written as follows:

$$m_{liq} \times g = m_{air} \times g - V \times \rho_0 \times g \qquad \textbf{Eq. 2.3}$$

With $V = \frac{m_{air}}{\rho_{sample}}$, the volume of the sample, g is the gravitational constant), m_{air} is the weight of sample in air, and m_{liq} is the weight of sample (g) when immersed in the diethylphtalate liquid (g), ρ_0 is the density of the diethylphtalate liquid at a given temperature (g/cm^3), ρ_{sample} defined as the density of the solid body (g/cm^3),

Hence,

$$\rho_{sample} = \rho_0 \frac{m_{air}}{m_{air} - m_{liq}} \qquad \textbf{Eq. 2.4}$$

The volumetric weight has been measured by Archimedes' method using diethylphtalate liquid and offers accuracy expected at ±0.01 g.cm^{-3}.

3.1.3 Microhardness measurement – Vickers' indentation method

Hardness is a measure of the amount of force required to plastically deform material. It can be measured using multiple methods such as Brinell method, Rockwell method, Knoop method and Vickers method, and provides insight into the physical durability and robustness of the resulting optical component after fabrication.

In this study, a Shimadzu DUH-211S Microhardness tester was used. The Vickers method uses a diamond tip indenter with a square base and an angle of 136 degrees between opposite faces as shown below in Figure 2.4.

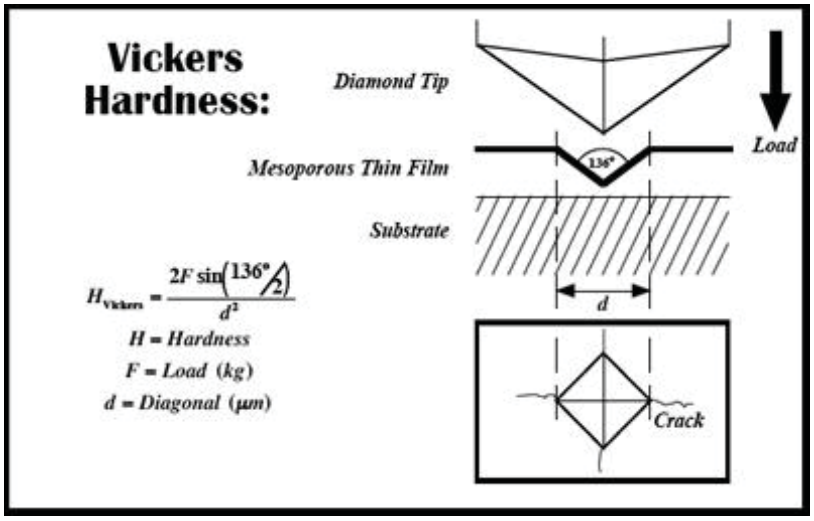

Figure 2.4 Process to calculate the Vickers Hardness [Vickers]

A static load of 2000 mN was used for the experiments and the reported microhardness values obtained are the average of fifteen tests. This load was selected as the max load

without cracking to yield largest diagonal. The diagonal length of indentation is measured after the test and the microhardness is then calculated. Errors for microhardness, H_v values obtained are typically ±3%, by measuring 15 times the hardness of the material **[Lopez 2004]**.

3.1.4 Linear refractive index – Brewster's angle

At a dissimilar material (including air-solid) interface, a fraction of the incident light will be reflected. By applying reflection laws one can estimate with good accuracy, linear refractive indices. The electric field associated with the incident light on the interface $\sum$ between two mediums with different refractive indices n_1 and n_2, can be decomposed into two components with two polarization respectively perpendicular $E_{\perp}$ and parallel $E_{//}$ to the incident plane (XZ), as shown in Figure 2.5.

In this case, the light is reflected and transmitted. The incident plan (XZ) is defined as the plane including the incident light and the perpendicular to the surface, called normal. The angle of incidence θ_i is the angle between the incident light and the normal. Reflection angle θ_r and transmission angle θ_t are the angles between the normal and the reflected beam and the transmitted beam respectively.

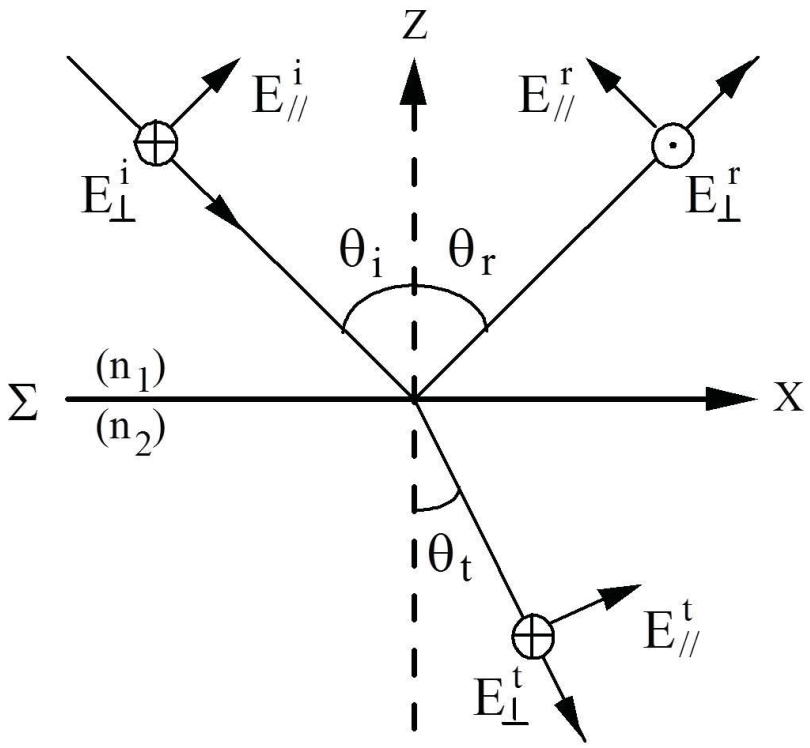

Figure 2.5 Reflection and transmission of an electromagnetic wave between two mediums

The conservation of moment's transfert of the vector leads to the Snell-Descartes laws for the refraction and reflection:

- Incident, transmitted and reflected beams are in the incident plane,
- Reflection angle is equal to the incident angle, namely $\theta_i=\theta_r$,
- Incident and transmitted angles are measured from the normal and can be described as:

$$n_1 \sin(\theta_i) = n_2 sin(\theta_t) \qquad \textbf{Eq. 2.5}$$

The conservation of the energy at the interface ∑ leads to define the Fresnel's coefficients which represent the links between the magnitude of the reflected and transmitted waves compared to the magnitude of the incident wave:

$$r = \frac{E_r}{E_i} \qquad \textbf{Eq. 2.6}$$

and

$$t = \frac{E_t}{E_i} \qquad \textbf{Eq. 2.7}$$

Where r is the coefficient of the magnitude of the reflected wave, t is the coefficient of the magnitude of the transmitted wave, E_i, E_r and E_t are the magnitude linked to the incident, reflected and transmitted electric field respectively. In term of intensity, both reflected and transmitted wave are described as the square of the coefficient: $R = r^2$ and $T = t^2$.

For a plane interface, it is necessary to differentiate parallel and perpendicular polarizations.

For a polarization perpendicular to the incident plane, called R_s or TE (Transverse Electric), the coefficients of reflection and transmission in magnitude are:

$$r_{(\perp)} = \frac{n_1 cos(\theta_i) - n_2 cos(\theta_t)}{n_1 cos(\theta_i) + n_2 cos(\theta_t)} \qquad \textbf{Eq. 2.8}$$

and

$$t_{(\perp)} = \frac{2n_1 cos(\theta_i)}{n_1 cos(\theta_i)+n_2 cos(\theta_t)} \quad \textbf{Eq. 2.9}$$

For a polarization parallel to the incident plane, called R_p or TM (Transvers Magnetic), the Fresnel coefficients are:

$$r_{(//)} = \frac{n_2 cos(\theta_i)-n_1 cos(\theta_t)}{n_2 cos(\theta_i)+n_1 cos(\theta_t)} \quad \textbf{Eq. 2.10}$$

and

$$t_{(//)} = \frac{2n_1 cos(\theta_i)}{n_1 cos(\theta_i)+n_2 cos(\theta_t)} \quad \textbf{Eq. 2.11}$$

Fresnel's coefficients give information about magnitude and intensity of the reflected and transmitted waves. Snell-Descartes' laws permit one to determine the direction of the reflected and transmitted waves.

The parallel polarization can be null for one specific angle, the Brewster's angle θ_B .Brewster's law permits to obtain the Brewster's angle θ_B based on Fresnel's equations, predicting that polarized light (same polarization between the incident ray and the surface normal) is not reflected at: $\theta_B = \arctan(\frac{n_2}{n_1})$. This specific angle is obtained at $r_{(//)} = 0$. So from Snell-Descartes' law $(n_1 sin\theta_i = n_2 sin\theta_t)$, we can obtain the refractive index by:

$$n_2 = n_1 \frac{sin\theta_B}{cos\theta_B} = n_1 tan\theta_B \qquad \textbf{Eq. 2.12}$$

For all samples, linear refractive indices have been measured using the Brewster angle reflection method at a wavelength of 752 nm. The glass sample is placed on a rotational support, permitting to measure the reflected intensity in the [-80°, +80°] angular range with step of 1° and 3 seconds of collection time. The obtained angular scan is then treated by tensor described by Rodriguez et al. **[Rodriguez 2002]**. The experimental error has been found to be ±0.01 refractive index units (RIU). Using this principal, samples in this study had their linear index measured at 752 nm and 1.5 μm.

3.2 TeO_2-$TaO_{5/2}$-ZnO glass network

3.2.1 Results

Glasses in the (100-x)TeO_2-x$TaO_{5/2}$, 80TeO_2-(20-x)$TaO_{5/2}$-xZnO glass families were prepared using the process protocols discussed above and their physical properties have been quantified. To our knowledge and as explained by Murugan et al. **[Murugan 2005],** there is no report in the literature of either the Raman characteristics or on the glass formation of ternary Ta_2O_5 containing tellurite glasses. This study has evaluated the impact of this modifying compound on both the physical and optical properties of the glass, with varying levels of Ta_2O_5. Table 2.1 summarizes the various thermal characteristic temperatures as well as density and refractive indices, for each glass composition.

Glass Composition (mol%)	T_g [± 2 °C]	T_x [± 2 °C]	T_p [± 2 °C]	$\Delta T = T_x - T_g$	ρ [± 0.01 g.cm^{-3}]	n (752 nm) [± 0.01]
$90TeO_2$-$10TaO_{5/2}$	351	430	465	79	5.81	2.15
$85TeO_2$-$15TaO_{5/2}$	370	489	516	119	5.91	2.15
$80TeO_2$-$20TaO_{5/2}$	387	502	505	115	5.99	2.14
$80TeO_2$-$15TaO_{5/2}$-5ZnO	360	496	537	136	5.89	2.12
$80TeO_2$-$10TaO_{5/2}$-10ZnO	350	478	526	128	5.78	2.08
$80TeO_2$-$5TaO_{5/2}$-15ZnO	335	468	498	133	5.67	2.06

Table 2.1 Evolution of characteristic temperatures (glass transition temperature T_g, onset of crystallization T_x, crystallization temperature T_p and glass stability ΔT), volumetric weights ρ and linear refractive index measured at 752 nm, in the TeO_2-$TaO_{5/2}$-ZnO glass network

As can be seen by the property data shown, in the binary **TeO_2-$TaO_{5/2}$** glass network, the introduction of a glass modifier ($TaO_{5/2}$) leads to an increase of the characteristic temperatures (T_g, T_x, T_p). Nevertheless, a slight decrease in the crystallization temperature T_p occurs in the (80:20) glass composition. Additionally, the stability of the glass against crystallization is normally evaluated by the gap between the glass transition temperature and the onset of crystallization ($\Delta T = T_x - T_g$). This property also exhibits a slight reduction in the (80:20) composition. For fiber fabrication, glasses with a higher value of ΔT ($\Delta T > 100$ °C) represents ideal candidates to prepare a crystal-free fiber (with minimal scattering loss) **[Soufiane 1993]**. Thus using this threshold, the binary TeO_2-

$TaO_{5/2}$ glass compositions (85:15) and (80:20) represent excellent candidates for good quality fibers, in term of their glass stability. During the introduction of tantalum oxide, the volumetric weight increases. Within the accuracy of the measurement, the linear refractive indices track the sample density, and are not influenced by the exchange TeO_2 with $TaO_{5/2}$.

With the addition of an additional modifier, ZnO, we can observe the role of its addition on the **TeO_2-$TaO_{5/2}$ -ZnO** ternary glass network. As can be seen, the addition of ZnO results in a decrease of the characteristic temperatures (T_g, T_x and T_p) through the replacement of tantalum ions by zinc ions. Despite these trends, the introduction of ZnO in the glass matrix leads to a sizeable (~25% or more) improvement in glass stability, ΔT, as compared to that seen in the binary TeO_2-$TaO_{5/2}$ glasses. The volumetric weight and the refractive index decrease with the addition of zinc oxide, as the modifier slightly depolymerizes the glass network and has a lower polarizability than the Ta ion it is replacing.

3.2.2 Discussion

TeO_2-Ta_2O_5 binary system

The difference in bonding energies of the glass network former or modifier, directly defines the evolution of characteristic temperatures. Tellurium-oxygen (Te-O) bonds have a bond energy of 376.1 $kJ.mol^{-1}$, requiring this much energy to be broken; tantalum-oxygen (Ta-O) bonds are much stronger, needing 799.1 $kJ.mol^{-1}$ to be severed. The introduction of tantalum oxide into the tellurite glass network produces an

enhancement of the average bond energy, leading to an increase of the glass transition temperature. As discussed by Berthereau, the refractory nature of the glass modifiers is responsible for the increase in the characteristic temperatures due to a possible creation of bond-bridging R-O-Te species, (where R could be Ta, Nb, W, Al) **[Berthereau 1995]**. This evolution of temperatures is in accordance with the results observed by Murugan et al. **[Murugan 2005]** who found that the glass transition temperature, T_g, the onset of crystallization, T_x and the crystallization temperature, T_p could be monitored by the amount of Ta_2O_5 in the tellurite glass matrix. It can be seen that further addition (to 20 mol%) leads to a lower value of the crystallization temperature for the (80:20) glass composition. This composition is localized at the limit of the vitrification, with additional tantalum oxide addition leading to a crystalline result. The same phenomenon has been observed by Berthereau in the TeO_2-Nb_2O_5 glass system, indicative of a characteristically abrupt change of the local glass structure **[Berthereau 1995]**.

The increase of the volumetric weight, noticed during the introduction of tantalum oxide, is related to the difference of molar mass of the elements ($M[TeO_2] = 159.60$ g.mol^{-1} and $M[TaO_{5/2}] = 220.93$ g.mol^{-1}).

The constant value of the refractive index is essentially governed by the high value of the refractive index of the tellurite glass network and the similar levels of polarizability of the constituent ions. Murugan et al. showed a refractive index dependence with the Ta_2O_5 content in a TeO_2-BaO-SrO-Ta_2O_5 glass network. Here, he increased the Ta_2O_5 content from 2 to 12 mol% and showed a decrease in the linear refractive index of the glass from

2.17 to 2.14 **[Murugan 2005]**. In our case no variation has been noticed with the levels of tantalum oxide content examined.

TeO_2-Ta_2O_5-ZnO ternary system

As shown above for the binary system TeO_2-$TaO_{5/2}$, the evolution of the characteristic temperatures is mostly due to the difference of difference in bonding energies between the Te-O bonds (376.1 kJ.mol^{-1}), Ta-O (E_{Ta-O}=799.1 kJ.mol^{-1}). In the ternary system an additional bond type is present, that created by the addition of ZnO. In the present study ZnO addition ranged from 5-15 mol%., and the modifier possesses a lower M-O bond strength, (E_{Zn-O}=159.0 kJ.mol^{-1}) to that of the other (Te-O) or modifier (Ta-O) bonds. It is observed that the replacement of Ta-O bonds with the much weaker Zn-O results in an overall decrease of average bond energy within the glass matrix, resulting in a decrease of the glass transition temperature. Despite this decrease, the presence of these weaker bonds does not appreciably decrease glass stability (reduction of ΔT by < 10 ^oC). The addition of the modifier zinc oxide moves the glass composition away from the limit of vitrification thus improving the glass-forming range. Introduction of metal oxide such as ZnO and/or alkali an alkaline earth have been well studied as leading to suitable glasses for optical fiber fabrication **[Savelii 2011][Manning 2012]**.

The decrease of the volumetric weight is essentially due to the molar mass of the zinc (M[ZnO]=81.37 g.mol^{-1}) compared to tantalum one (M[$TaO_{5/2}$] = 220.93 g.mol^{-1}). The results are in accordance with the data published by Burger et al. **[Burger 1992]**. The

decrease of volumetric weight comes with a visible decrease of the refractive index, impacted again, by the reduced polarizability of the Zn ion as compared to that of the Ta ion it is replacing.

3.3 TeO_2-$NbO_{5/2}$ glass network

3.3.1 Results

The binary (100-x)TeO_2-x$NbO_{5/2}$ glass system has been well studied for its nonlinear optical properties **[Hoon 1991][Komatsu 1991][Komatsu 1993][Shioya 1995][Berthereau 1995][Berthereau 1996][Murugan 2004-1][Jose 2006].** In the current effort, we extend these findings towards evaluation of the glass' Raman gain behavior as well as its resistance to crystallization needed for fiber fabrication.

Table 2.2 summarizes the same physical property data for the binary TeO_2-$NbO_{5/2}$ system where the $NbO_{5/2}$ content ranges from 10-30 mol%. As can be seen, the characteristic temperatures T_g, T_x and T_p all increase with the addition of niobium oxide. This addition results in a large range of glass stability, ΔT, most notably for the glass composition 80TeO_2-20$NbO_{5/2}$. One can note an increase in the volumetric weight with niobium oxide content, while the refractive index stays fairly constant.

Glass Composition (mol %)	T_g [± 2 °C]	T_x [± 2 °C]	T_p [± 2 °C]	$\Delta T = T_x - T_g$	ρ [± 0.01 g.cm^{-3}]	n (752 nm) [± 0.01]
$90TeO_2$-$10NbO_{5/2}$	342	433	452	91	5.27	2.14
$85TeO_2$-$15NbO_{5/2}$	354	469	496	115	5.44	2.15
$80TeO_2$-$20NbO_{5/2}$	371	510	535	139	5.52	2.13
$75TeO_2$-$25NbO_{5/2}$	384	508	535	124	5.58	2.16
$70TeO_2$-$30NbO_{5/2}$	405	517	539	112	5.60	2.16

Table 2.2 Evolution of characteristic temperatures (glass transition temperature Tg, onset of crystallization Tx, crystallization temperature Tp and glass stability ΔT), volumetric weights ρ and linear refractive index measured at 752 nm, in the TeO_2-$NbO_{5/2}$ glass network

3.3.2 Discussion

From data presented in Table 2.2 and in accordance with prior literature for this system, the introduction of a glass modifier ($NbO_{5/2}$) leads to an increase of characteristic temperatures **[Berthereau 1995]**. This effect is related to the fact that a niobium-oxygen bond Nb-O (E_{Nb-O}=771.5 kJ.mol^{-1}) is again, stronger than the Te-O bond (E_{Te-O}=376.1 kJ.mol^{-1}) it is replacing. As seen for the addition of tantalum oxide, the introduction of niobium oxide into the tellurite glass network enhances the average bonding energy. Murugan et al. and Jose et al. show the same evolution within a TeO_2-SrO-BaO-Nb_2O_5 glass system, that the glass transition temperature T_g and the onset of crystallization T_x increases with the niobium oxide content **[Murugan 2004-1][Jose 2006]**. The evolution of the glass transition temperature with the Nb_2O_5 content is also accordance with

observation in a ternary glass system TeO_2-Nb_2O_5-Bi_2O_3 **[Blanchandin 2002]**. Tellurite-niobium oxide glasses have remarkably good glass stability suggesting they are amenable to fiber fabrication.

The increase of the volumetric weight is due to the difference of molar mass ($M[TeO_2]$ = 159.60 $g.mol^{-1}$ and $M[NbO_{5/2}]$ = 132.88 $g.mol^{-1}$), in accordance with results published by Villegas et al. in TeO_2-TiO_2-Nb_2O_5 glass system **[Villegas 2007]**.

Linear refractive indices are not affected by the exchange TeO_2 → $NbO_{5/2}$. This suggests that the relative molar refractivity and corresponding polarizability associated with the two species, is similar. This result is similar to that of Murugan et al. and Jose et al. in the TeO_2-BaO-SrO-Nb_2O_5 (with BaO:SrO:Nb_2O_5=1:3:8 series) despite their introduction of clearly less polarizable, alkaline earth oxides.

3.4 TeO_2-$BiO_{3/2}$-ZnO glass network

3.4.1 Results

As noted previously, theTeO_2-$BiO_{3/2}$-ZnO glass network has been intensively studied for its capability to obtain a homogeneous glass material with attractive thermal, physical and structural properties **[Blanchandin 2002][Udovic 2006][Massera 2010]**. Additionally, the composition (with molar ratio 66:21:13) it has been shown that it is possible to crystallize a unique cubic crystalline phase **[Hu 2011]**, enabling the formation of glass ceramics with tailored microstructures and properties. Glasses in the ternary system have been prepared and analyzed, keeping the relative fraction of $BiO_{3/2}$ constant

(at 18 mol%) and varying the relative amounts of TeO_2 and ZnO. This was done to examine the effect of modifier content, with another highly polarizable (like Tantalum) modifier oxide. Table 2.3 illustrates the impact of these compositional variations on the $(82\text{-}x)TeO_2\text{-}18BiO_{3/2}\text{-}xZnO$ glass series' properties.

Glass Composition (mol%)	**T_g [± 2 °C]**	**T_{x1} [± 2 °C]**	**T_{p1} [± 2 °C]**	**T_{x2} [± 2 °C]**	**T_{p2} [± 2 °C]**	**$\Delta T = T_x - T_g$**	**ρ [± 0.005 g.cm^{-3}]**	**n (1.5 µm) [± 0.01]**
$68TeO_2$-$18BiO_{3/2}$-14ZnO	330	381	405	414	444	51	6.18	2.11
$66TeO_2$-$18BiO_{3/2}$-16ZnO	333	-	-	476	512	143	6.17	2.09
$64TeO_2$-$18BiO_{3/2}$-18ZnO	337	-	-	463	490	126	6.16	2.08
$60TeO_2$-$18BiO_{3/2}$-22ZnO	337	376	404	424	457	39	6.15	2.05

Table 2.3 Evolution of characteristic temperatures (glass transition temperature Tg, onset of crystallization Tx, crystallization temperature Tp and glass stability ΔT), volumetric weights ρ in the TeO_2-Bi_2O_3-ZnO glass network. Taken from [Massera 2009]

As discussed in the original work **[Hu 2012]**, introduction of zinc oxide leads to a small increase in the glass transition temperature, T_g, but the onset of crystallization T_x and the crystallization temperature T_p fluctuate largely. This has been attributed to the presence of multiple crystalline phases which can form across this composition space. During the exchange of TeO_2 for ZnO, it can be seen that the two extreme glass compositions (68:18:14) and (60:18:22) exhibit (at least) two possible phases of crystallization while the two intermediate glass compositions exhibit a single crystallization peak. It is also observed that the two glasses on the extremities exhibit low glass stability, ΔT, (due in

part to the possibility for multiple phase formation) while the two intermediate glass compositions exhibit a glass stability higher than 100 ^{o}C. Addition of zinc oxide in the tellurite glass matrix leads to a slight decrease of the volumetric weight and of the refractive index for the same reasons discussed previously in the tantalum-zinc-tellurite ternary system.

3.4.2 Discussion

As explained previously for the both TeO_2-$TaO_{5/2}$-ZnO and TeO_2-$NbO_{5/2}$ glass systems, when TeO_2 is replaced by ZnO in the glass as El-Mallawany reports, the ZnO has a network-former behavior and strongly modifies the tellurite properties including the glass transition temperature or the refractive index **[El-Mallawany 2000][Chagraoui 2007][Bürger 1992]**. The presence of two crystallization peaks for the extreme glass compositions and the fluctuation of the onset of crystallization T_x and the crystallization temperature T_p are related to their potential proximity to the vitrification limits.

Concerning the volumetric weight, a decrease is seen during the TeO_2 → ZnO atomic exchange due to the difference between the molar mass of each components (M[TeO_2] = 159.60 g.mol^{-1} and M[ZnO] = 81.37 g.mol^{-1}). The difference of atomic weight of each component is at the origin of the slight decrease of the glass volumetric weight. As explained previously, the refractive index of the glass is mostly directed by the refractive index of TeO_2 and $BiO_{3/2}$ both being polarizable species; thus the reduction of the tellurite content, leads to a reduction of the refractive index.

For the different glass systems, the progressive introduction of zinc oxide leads to the decrease of the linear refractive index. As shown in Figure 2.6, the increase of the zinc to tellurium ratio induces the drop of the linear susceptibility. While direct compositional analogs were not studied due to limits in the glass-forming region, similar Zn/Te ratios across the two systems (Ta-containing and Bi-containing glasses) clearly illustrate the role of the highly polarizable heavy metal ions Bi and Ta.

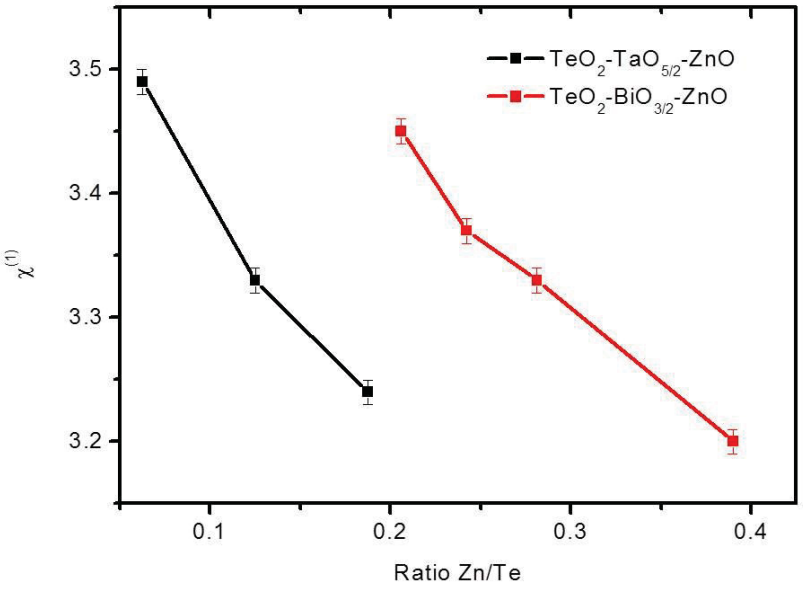

Figure 2.6 Evolution of the polarizability $\chi^{(1)}$ as function of the introduction of ZnO into the glass matrix

As noted, it appears that the behavior observed in optical properties is similar for the TeO_2-$TaO_{5/2}$-ZnO and the TeO_2-$BiO_{3/2}$-ZnO glass systems. An increase of the ratio Zn/Te gives rise to a variation of the linear susceptibility in the same order of magnitude.

Such an effect is not visible in the case of the binary TeO_2-$TaO_{5/2}$ glass system. As both the oxide Ta_2O_5 or ZnO have similar refractive index (n_{Ta2O5} = 2.2, n_{ZnO} = 2.1), one can conclude the role of each in the network and thus, the resulting index, is not only related to the polarizability of the modifier. Such an effect has to be related to a change of the tellurite glass network that accompanies the introduction of the zinc oxide. This structural role, on the intermediate scale length, will be probed by various spectroscopic techniques as discussed in Chapter 3.

4 Tellurite glass purification process - Influence of OH content on tellurite glass properties

The majority of optical losses in glasses and optical fibers are due to the impurity absorption such as trace metallic species, hydroxyl groups and other contaminants or inhomogeneities. Optical performance within the telecommunication window requires the use of high purity starting materials exhibiting very low absorption in the transmission bandwidth in the near infrared (NIR). For silica glasses, the minimum of optical losses (0.15 dB/km) occurs at 1.55 μm and this low loss is realized through the use of high purity, gas-based precursors in the processes used to prepare the fiber preform. This type of processing is not easily employed in tellurites and hence, special attention to the quality (level of trace impurities) and contaminants (from crucible materials and the melting environment) need therefore, to be strictly controlled and minimized.

Hydroxyl groups are among the impurities which decreases the transmission in this region and when the present, can render loss in fibers, unacceptably high. Tellurite glasses are intrinsically hygroscopic and thus impurities such as hydroxyl groups are commonly found as impurities in as-received raw materials. The strongly bound OH^- anion exhibits a strong absorption in the spectral range around 3 μm with harmonics at around 1.4 μm and 1μm **[Shultz 1974][Sanghera 1998]** and is extremely challenging to remove completely.

Despite the recent interest in tellurite glasses, literature on purification of such glass compositions is limited. Massera et al. used a pre-heat treatment of the raw materials with NH_4-HF for reducing the hydroxyls group content by formation of HF **[Massera 2011]**. This technique has not been studied in this PhD thesis due to the complexity in controlling precisely the fluorine content present in the final glass. Presence of fluorine in Massera's effort was shown to reduce the glass' crystallization stability upon fiberization, a negative for the goals of this study. Another alternative is to melt the tellurite batch under control-atmosphere. Moiseev et al. showed that melting in a hermetic chamber in purified oxygen atmosphere and using initial high-purity starting ingredients enables production of TeO_2-ZnO-Na_2O-Bi_2O_3 and TeO_2-WO_3-La_2O_3-MoO_3 glasses **[Moiseev 2011]**. The synthesis of tellurite-based glass systems TeO_2-$NbO_{5/2}$ (following molar composition 80:20) and TeO_2-Bi_2O_3-ZnO (following molar composition 70:10:20) have been specifically investigated in this study with the intent of quantifying the impact of the OH content on the glass property. We hypothesize that these compositions should exhibit better crystallization stability (than the previously referenced

fluorination approach to purification of tellurite raw materials) thus making the possibility of high gain, low absorption fibers, a reality.

Ternary, high purity telluriteglasses were prepared using the following oxide raw materials: TeO_2 99.99% (Alfa Aesar), Nb_2O_5 99.9985% (Alfa Aesar), ZnO 99.0% (Alfa Aesar), Bi_2O_3 99.9995% (Alfa Aesar). To compare the influence of the melting atmosphere on the OH content, glasses of the same composition were weighed, batched and melted outside and inside a dried-air purged glove box (relative humidity <1%), as shown in Figure 2.7.

Figure 2.7 Dried-air purged glove box with humidity<1%

Before melting, raw materials were pre-heated at 200, 300 and 400 ^{o}C to eliminate organic components or impurities such as water, hydroxyl and carbonyl groups, already present in raw materials. The batch mixtures were melted in a platinum crucible at a temperature between 800 and 1000 ^{o}C, depending on the glass composition, for 15

minutes. The glasses were then quenched on a pre-heated brass plate and annealed overnight at a temperature 40 ^{o}C below their glass transition temperatures (T_g) **[Anheier 2011]**.

The absorption spectra of the glass samples were recorded at room temperature; UV-Vis-NIR absorption spectra were recorded using a dual beam UV-Vis-NIR Perkin Elmer Lambda 900 spectrophotometer on 1.5 mm thick optically polished samples. Absorbance in the infrared region was measured using Magna-IR 560 Fourier Transformed Infrared Spectrometer (FTIR) from Nicolet. The system was purged with N_2 to remove atmospheric water and CO_2 in the sample chamber prior to measurement. The amount of hydroxyl content present in the glass network can be approximated by:

$$N_{OH} = \frac{N_A}{L\varepsilon} \ln\left(\frac{1}{T}\right) \qquad \textbf{Eq. 2.13}$$

Where N_A is the Avogadro constant (6.022×10^{23} mol^{-1}) , L the sample thickness (cm), T the transmission and ε the molar absorptivity of the OH entity using reference data from silica glass (49.1×10^{3} cm^{2}.mol^{-1}) extrapolated for tellurite glasses **[Davis 1996]**. Precautions have to be taken since the absorptivity of hydroxyls has not been measured in tellurites glass network.

The concentration of hydroxyl groups can also be estimated in part per million (ppm) using the equation reported by **[Chida 1982]**.

$$C_{OH} = \frac{N_{OH} * W_{OH}}{N_{OH} * W_{OH} + N_{Glass} * W_{Glass}}$$ **Eq. 2.14**

where N_{OH} and N_{Glass} are the concentration (mol.cm^{-3}) of OH units and glass units, respectively. W_{OH} and W_{Glass} are the molecular weight of OH and glass, respectively.

Glass composition	Volumetric Weight (g/cm^3) [±0.02g/cm^3]	Molar Density (10^{22} mol/m^3) [±0.001 mol/m^3]	OH (10^{19} ions/cm^3) [±0.01 ions/cm^3]
80TeO_2–20Nb_2O_5	5.49	1.828	6. 13 (315 ppm)
80TeO_2–20Nb_2O_5 Glove Box	5.48	1.825	0.66 (34 ppm)
70TeO_2–10Bi_2O_3–20ZnO	6.21	2.142	7.18 (326 ppm)
70TeO_2–10Bi_2O_3–20ZnO Glove Box	6.20	2.138	1.58 (72 ppm)

Table 2.4 Volumetric weight, molar density and hydroxyl content in 80TeO_2-20Nb_2O_5 and 70TeO_2-10Bi_2O_3-20 ZnO glass compositions, melted or not in an air-dried glove box

The identification of absorption bands in glassy materials is not trivial. Regarding the signature of hydroxyls, the infrared absorption spectrum of the orthotelluric acid H_6TeO_6, reported in the Figure 2.8 brings relevant information for the band assignments. The infrared absorption spectrum has been measured thanks to our partnerships with P. Thomas and J. Cornette from the Laboratoire Science des Procédés Céramiques et de Traitements de Surface (SPCTS-CNRS) of Limoges University. IR spectroscopy shows

vibrations of water H_2O occurring at 3300 cm^{-1} (i.e. weakly hydrogen-bonded OH and free OH), the band localized between 1500 and 1000 cm^{-1} is attributed to δ (TeOH), and several intense bands below 1000 cm^{-1} are due to the coordinated tellurite entities **[Levason 1995]**.

Theoretical calculations have been conducted in order to look closer at the band vibration assignments and bring new information for the band attribution in the case of the glass studied. The geometry optimization of orthotelluric acid was calculated by Gaussian 09 program (1) at the density functional theory level using the CAM-B3LYP functional which is the hybrid B3LYP functional corrected by the Coulomb attenuation method in order to better take into account the long distance forces. The used basis set was, for the O and H atoms, the Gaussian Pople base 6-311++G** with polarization functions **[Frisch 2009]** and diffuse functions (+) and the LanL2DZ basis for the Te atom. The vibrational spectra were calculated in the harmonic approximation. For comparison to experiment, the calculated intensities were converted to Lorentzian bands with half-width of 7 cm^{-1} and the vibrational frequencies were multiplied by the 0.96 factor in the 0 - 2000 cm^{-1} range and by the 0.91 factor in the 2000 – 4000 cm^{-1} range for taking into account the anharmonic effect.

The calculated IR spectrum of the orthotelluric acid, accordingly to the crystal structure parameters proposed by Mullica et al., is reported in Figure 2.8 **[Mullica 1980]**.

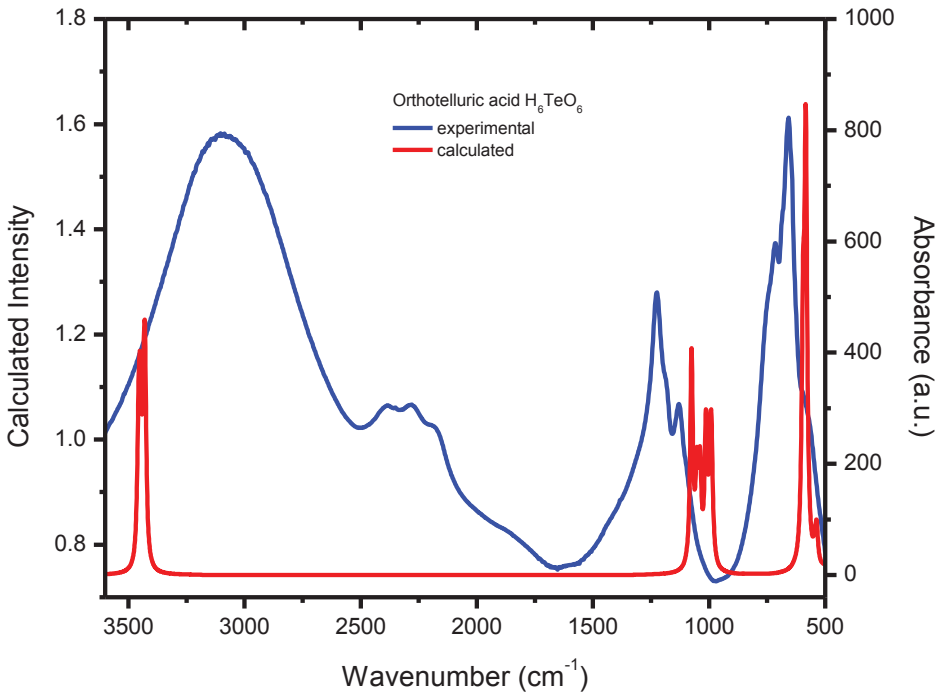

Figure 2.8 Measured and calculated IR spectra of orthotelluric acid H_6TeO_6

In the first approach, one can observe that the bands below 1500 cm^{-1} are shifted to lower wavenumber while the band about 3500 cm^{-1} is shifted to higher wavenumber. This shift is due to difference of site environment. Indeed, the calculated spectrum evaluates a unique molecular entity without its regular surrounding, i.e. the local change due to the charge compensation and/or site environment is not taken fully into account in the calculation. As explained previously, the calculated IR spectrum is obtained by a harmonic approximation, which permits to obtain the theoretical vibration of a single molecule without any interaction with the molecular environment. At high frequency, the tendency is to go down to lower frequencies due to coupling valences with the

environment. This trend is inversely proportional to the one at low frequencies which are shifted to higher frequencies due to the deformation of the network with the interaction with the environment.

In the calculated IR spectrum, we can observe vibration features in 3 spectral domains, localized in the 4000 – 3500 cm^{-1}, 1200 – 800 cm^{-1} and 700 – 500 cm^{-1} wavenumber ranges. In each spectral domain, the spectrum is formed by 6 vibrational contributions (symmetric or antisymmetric vibrations).

- **In the 4000 – 3500 cm^{-1} range,** the 6 contributions cannot be easily observed due to their overlapping and lead to the presence of two broad bands related to the stretching of the Te-O-H bonds [ν (TeOH)].
- **In the 1200 – 800 cm^{-1} range,** the 6 contributions lead to the presence of 5 distinguished bands assigned to symmetric and antisymmetric bending of the Te-O-H bonds [δ (TeOH)].
- **In the 700 – 500 cm^{-1} range,** the 6 contributions lead to the presence of 3 broad bands, related to the symmetric and antisymmetric of the Te-O bonds.

The calculation gives access to the fundamental vibrations of the IR spectra. The absence of the bands between 2500 and 2000 cm^{-1} in the calculated spectrum indicates that the vibration observed in the experimental spectrum is due to harmonics of fundamental vibrations. The absorption spectra of the tellurite glasses $80TeO_2$-$20Nb_2O_5$ and $70TeO_2$-$10Bi_2O_3$-20ZnO, elaborated in air and under a controlled dried atmosphere, are reported in Figures 2.9 and 2.10.

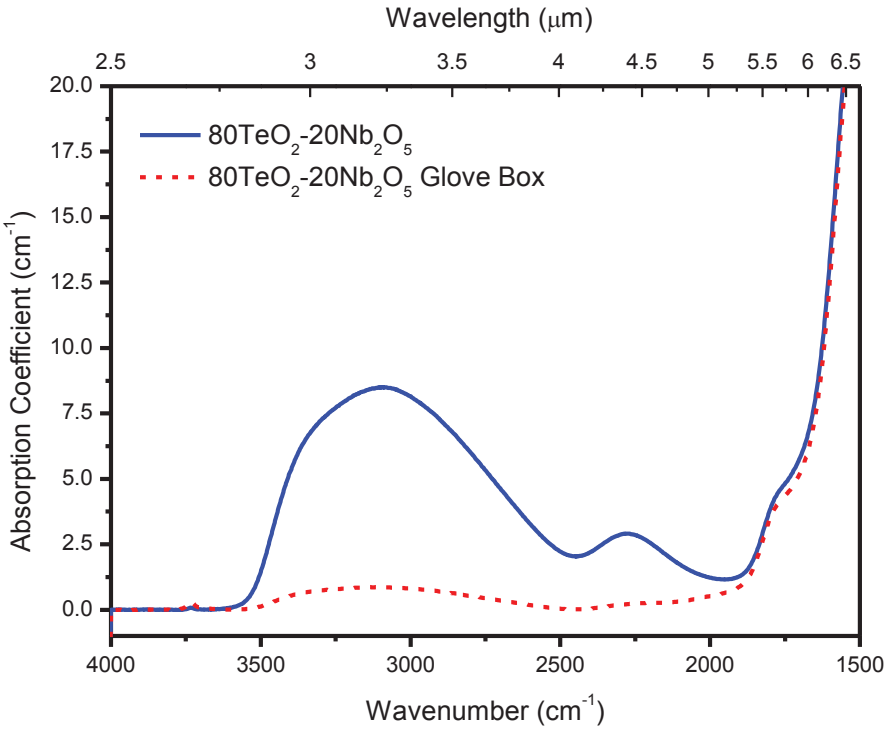

Figure 2.9 IR spectra evolution of $80TeO_2$-$20Nb_2O_5$ glass composition melted in ambient furnace conditions or within an humidity-controlled glove box

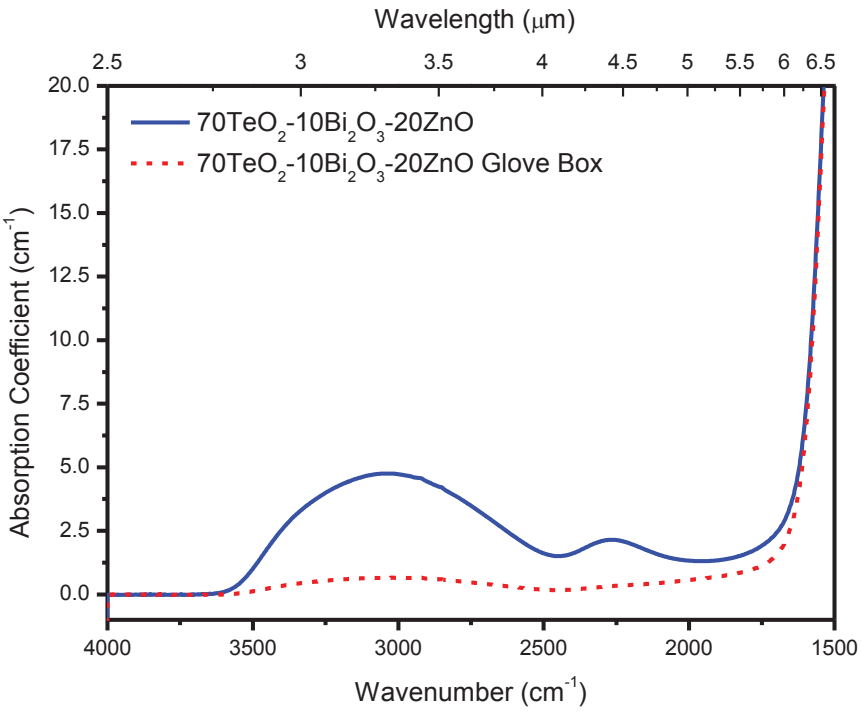

Figure 2.10 IR spectral evolution of $70TeO_2$-$10Bi_2O_3$-20ZnO glass composition melted in ambient furnace conditions or within an humidity controlled glove box

Both spectra show two broad bands centered at about 3000 cm^{-1} and 2250 cm^{-1} and a strong edge below 1700 cm^{-1}. For glasses elaborated into glove box the band intensities around 3000 cm^{-1} and 2250 cm^{-1} decrease drastically while the band edge below 1700 cm^{-1} is not affected. Bands at 3000 cm^{-1} and 2250 cm^{-1} are clearly correlated to the presence of OH in the glass structure. The last band at 1700 cm^{-1} is assigned to the multiphonon vibration edge characteristic of the glass network. Accordingly to previous investigations and results obtained on orthotelluric acid **[Mullica 1980]**, the band at around 3000 cm^{-1} is attributed to weakly hydrogen-bonded OH and free OH. Regarding

the band at around 2250 cm^{-1} the attribution is not clear in the literature. Feng et al. has assigned this vibration to a very strong hydrogen-bonded OH **[Feng 2001]** according to previous works on silicates **[Scholze 1959][Adams 1961][Scholze 1966][Scholze 1980]**. The attribution to strong hydrogen-bonded OH makes sense in silica glasses but cannot be directly extrapolated to tellurite glass network. The calculation on orthotelluric acid seems to rule out the attribution of the band at 2250 cm^{-1} to strong hydrogen-bonded OH. This vibration is more likely attributed to the 1st harmonic of the fundamental vibration δ (TeOH). Fusion and quenching have an important influence on the OH content in tellurite glass. The peak absorption for $80TeO_2$-$20Nb_2O_5$ at 3000 cm^{-1} (3.3 μm) reduces from around 8.5 cm^{-1} to 0.9 cm^{-1} (a reduction of 89 %) and the peak at 2250 cm^{-1} (4.4 μm) reduces from 2.9 cm^{-1} to 0.3 cm^{-1} which represents a reduction of 90 %. In the $70TeO_2$-$10Bi_2O_3$-20ZnO glass composition, the peak at around 3000 cm^{-1} (3.3 μm) decreases from 4.8 cm^{-1} to 0.7 cm^{-1} (85% reduction) and the peak at 2250 cm^{-1} (4.4 μm) reduces from 2.2 cm^{-1} to 0.3 cm^{-1} which represents a reduction of 86 %. Accordingly to the precision of the measurements and the extraction of the signal attributed to hydroxyls at around 3000 cm^{-1} and 2250 cm^{-1}, the correlation between both peaks is clearly observed in both glass networks.

Most publications related to hydroxyl glass purification have been carried out on silicate and phosphate glasses **[Shelby 1976][Bartholomew 1982][Brow 1990][Gomez 1997].** Nd-doped phosphate glass (such as LHG-5 and LG770 made by Hoya and Schott respectively) serve as laser gain material for the National Ignition Facilities (NIF) and Megajoule laser (LMJ) systems. It was shown early in the laser glass development

process in the 1980's that hydroxyl content can dramatically impact gain, as it changes not only the NIR absorption where the primary Nd^{+} absorption/excitation occurs, but also that at the wavelengths (UV) where the 3ω frequency converted higher energy beam, transmits. As explained by Davis **[Davis 1996-2]**, in phosphate glasses, low residual water exists entirely in the form of hydroxyl OH groups and can represents a content of $2x10^3$ ppm. In silica glasses, this OH groups are considered as glass modifier like alkali and alkaline earth metal ions and lead to change of glass structure by terminating the polymeric chains of the glass network **[Shelby 1976]**. Those observations have been made on high OH-containing glasses **[Shelby 1976][Bartholomew 1982][Abe 1983][Tomozawa 1985][Toratani 1987].** The influence of OH on glass properties in a low OH content glasses [50-800 ppm] have been looked by Arriagada et al. and Karmakar et al. **[Arriagada 1987][Karmakar 1999]** in phosphate glass matrices, and observed that hydroxyl content in glass can have a profound effect on its properties, and especially on the thermal and physical properties, with a proportional dependence of the glass transition temperature, the density and the refractive index with the OH content.

Karmarkar et al. **[Karmakar 1999]** show in a calcium metaphosphate glass in the range 50-800 ppm of OH content that the dehydroxylation causes a conversion of non-bridging oxygen of the H-bonded OH groups into bridging oxygen, leading to a rearrangement of the structural units investigated by magic angle spinning nuclear magnetic resonance (MAS-NMR) analysis **[Brow 1990]**. This effect of non-bridging oxygen changing the

glass structure has also been observed in sodium trisilicate **[Shelby 1976][Tomozawa 1983]**.

In most case, infra-red absorption spectroscopy is used to probe the eventual structural change, such as Davis et al. in silica glasses **[Davis 1995][Davis 1996-2]**, Karmakar et al. in phosphate glasses **[Karmakar 1999]** or Dorofeev et al. in tellurite glasses **[Dorofeev 2011]**. Nuclear magnetic resonance has also been used in phosphate glasses by Mercier et al. and Karmakar et al. **[Mercier 1998][Karmakar 1999]**. To understand the potential structural changes created during purification in tellurite-based glasses, Raman spectroscopy has been used, as done by Davis et al. in silica glasses **[Davis 1995][Davis 1996-2]**. Raman spectra in the spectral range of the Raman spectrum exhibiting vibrations attributed to the tellurite glass network between 200 cm-1 to 900 cm-1 are obtained using a Senterra (Bruker Optik) micro Raman system employing a 785 nm excitation with 10 mW incident power at the sample. No changes of the glass structure are observed by repeating the analysis on the same area twice in a row for each measurement. The reduction of OH content has no significant influence on the vibrations attributed to the tellurite glass network, in agreement with results previously reported by Massera et al. **[Massera 2011]**. In phosphate glasses, structural changes are seen during the purification because of the important gap of hydroxryl content before and after purification. In our case, OH content is initially low in tellurite glasses; structural changes are so not seen.

The impact of OH has been on the thermal and the physical properties (density, hardness and absorption cut off in UV) have been investigated in the tellurite glasses studied in the present work and these data are summarized in Table 2.5.

Glass composition	T_g [± 2 °C]	T_x [± 2 °C]	T_p [± 2 °C]	ΔT	ρ ($g.cm^{-3}$) [± 0.02]	H_v (kg/mm^2) [± 3%]	Cut off energy (eV)
$80TeO_2$-$20Nb_2O_5$	340	445	458	105	5.49	320	3.22
$80TeO_2$-$20Nb_2O_5$ Glove box	344	450	467	106	5.48	333	3.22
$70TeO_2$-$10Bi_2O_3$-20ZnO	340	444	460	104	6.21	294	3.06
$70TeO_2$-$10Bi_2O_3$-20ZnO Glove box	344	450	468	106	6.20	305	3.06

Table 2.5 Evolution of characteristic temperatures, glass stability, volumetric weight, micro-hardness and cut off energy

The transparency domain of the glass represents the limits of the amplification in a spectral window with low optical losses as discussed in the listing previously of the attributes of an 'ideal' Raman gain material. This information is given by measuring the UV cutoff edge. For both glasses, the UV cutoff edge is identical and no difference can be observed between the as-prepared and dried glasses indicating that there is no clear influence of the hydroxyl species in this spectral region. By comparison, Arrigada et al., Karmakar et al. **[Arriagada 1987][Karmakar 1999]** have observed a dependence of UV cutoff on the OH content of the phosphate glasses, due to the structural changes.

Karmarkar et al. **[Karmakar 1999]** report also a densification of the glass structure during the reduction of hydroxyl content in phosphate glasses, from 2.63 $g.cm^{-3}$ with 770 ppm of OH to 2.76 $g.cm^{-3}$ with 60 ppm of OH. In our case, such an effect is not observed; for similar OH content variation the glass density values remains all within the error bars of the measurement.

Purification of metaphosphate glasses have shown that the hydroxyl content can have a dramatic effect on the thermal and physical properties of glass, with a proportional dependence with OH content on the glass transition temperatures from T_g=490 ^oC (OH content picked at 770 ppm) to T_g=565 ^oC (OH content picked at 60 ppm) **[Karmakar 1999]**. Indeed the dependence of glass transition temperature T_g on the OH content reflects the structural changes due to the non-bridging/bridging oxygen content into the phosphate matrix, as explained earlier.

Closely examining the thermal properties summarized in Table 2.5, it can be seen that our measurements show, for both glass systems, that the reduction of OH content does not significantly affect the glass transition temperature T_g, which remains within the error bars of our measurement (± 2 ^oC). Concerning the dry glasses, an increase of the onset crystallization temperature is barely observed for both glass compositions, suggesting that the presence of OH groups is affecting the inhomogeneous crystallization kinetics by a probable weakening of the glass network. This is consistent with data shown for the glass' mechanical properties as illustrated by the measured Vickers hardness data. Our results show a higher hardness for both dried glasses, with measured hardness values well

(~ 4%), above the error. We thus confirm that the decrease of OH content increases the average bonding energy of the network system. Thus, a purified, dry material is slightly more mechanically robust than a material synthesized in ambient air atmosphere with no particular precaution. Such an effect can be associated with the reduced extent of polymerization of the network when hydroxyls are present, due to the increase of the number non-bridging oxygen atoms that can form with the OH^- anion **[Brow 1990]**. Such species can also induce a reduction in stability against crystallization. This statement is substantiated in this data, as the removal of moisture serves to enhance (increase) $\Delta T = T_x - T_g$.

These results show that it is not possible to extrapolate results from silica glasses and/or phosphate glasses to tellurite glasses, even for the same OH loading. Melting and quenching tellurite glasses in dried air atmosphere can clearly constitute a viable route to obtain purified materials with enhanced optical and mechanical properties. This method is used to obtain purified fiber glass for fiberization, in efforts to enhance Raman gain performance.

5 Fabrication of tellurite optical fiber

One of the goals of the PhD is to propose 'fiberizable' candidate glass systems for Raman gain applications. Drawing fibers represents the ultimate step which permits to compare the calculated Raman gain with the experimental one. Glass fibers in the present

study have been drawn from a 7 cm long glass rod with a diameter of 1 to 1.5 cm. The preform is obtained from a 60 g glass quench into a brass mold as shown in Figure 2.11.

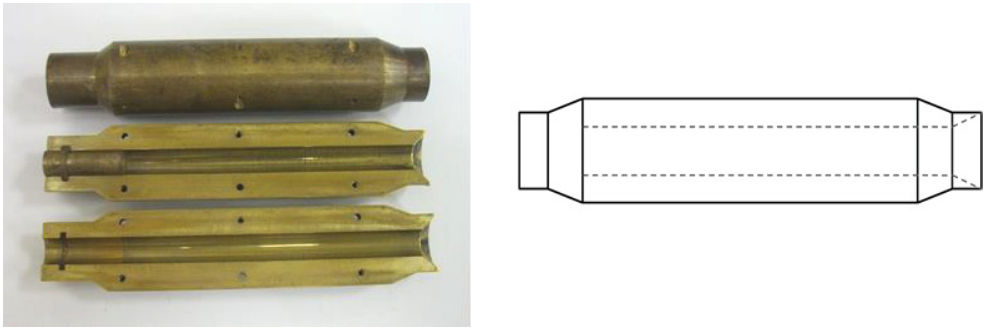

Figure 2.11 Brass mold, diameter = 1 cm, length = 10 cm

After the stress relaxation step, brass mold can be opened to be able to extract a solid rod glass, as shown in Figure 2.12.

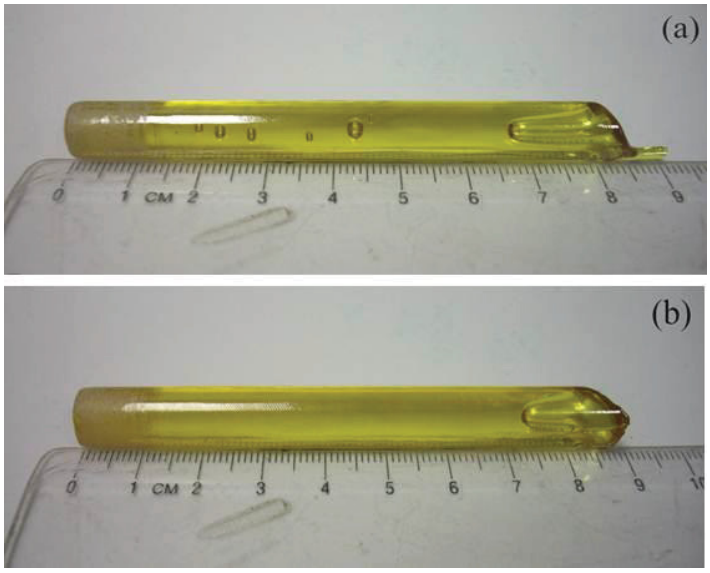

Figure 2.12 Tellurite-based glass rods with (a) and without (b) bubbles in the following glass composition $70TeO_2$-$10Bi_2O_3$-$20ZnO$

Glass science can represent a hard task in term of quenching glass, especially to obtain a homogeneous glass namely neither bubbles nor inclusions Figure 2.12 (b). The drawing tower is described on Figure 2.13.

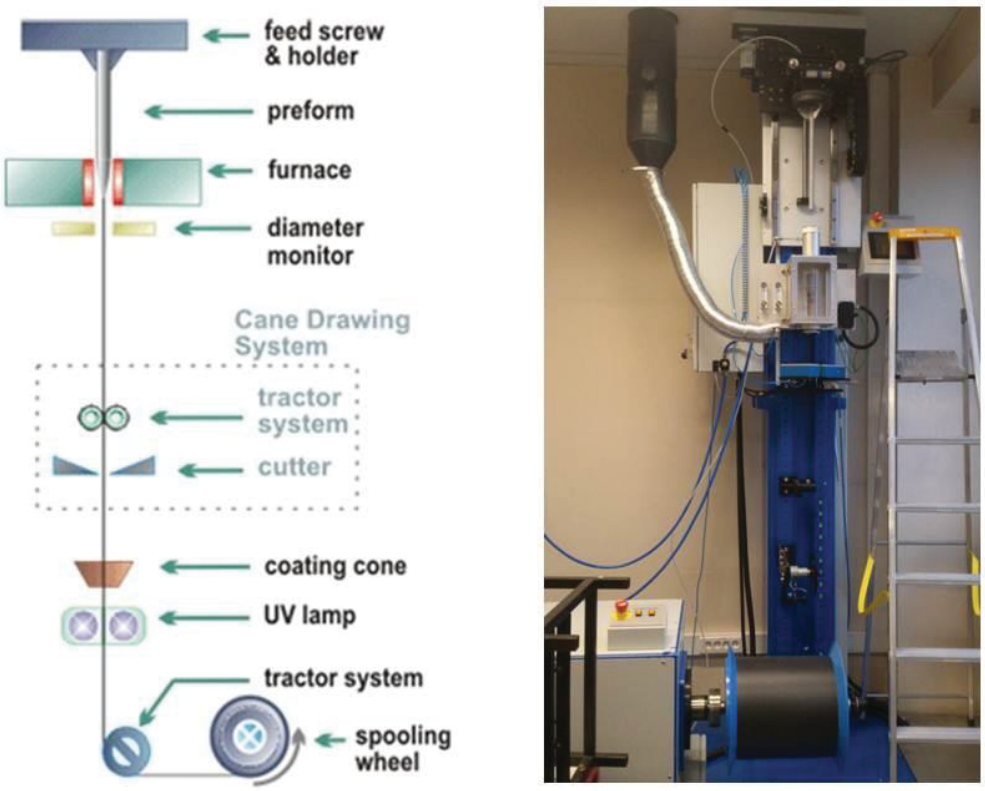

Figure 2.13 Drawing tower facilities at Institut Carnot de Bourgogne, University of Dijon, France – Prof. Frédéric SMEKTALA

This glass rod is placed at the top and is introduced slowly in the furnace. The glass rod is heated up to a temperature corresponding to a log of the viscosity at 5 Pa.s. This enclosure is scanned by a neutral gas as nitrogen and helium during few hours until heating up to reduce any presence of moisture (Helium debit: 3 L/min in the furnace, Nitrogen debit: 2 L/min as gas shutter)

Furthermore, the gas owns an excellent thermal conductivity, leading to enhance the homogeneity in temperature.

Controlling different parameters such as speed of rod descent or the rate of the fiber spindle permits to obtain the desired size of fiber materials (diameter and length). Parameters are explained it Table 2.6.

Preform rod glass length	7 cm
Preform rod glass diameter	1.5 cm
Temperature for the 1st glass drop	685 – 695 °C
Drawing temperature	720 °C
Descent speed rate	0.5 mm/min
Tension	10 g
Optical fibre diameter	130 µm
Optical fibre length	< 100 m

Table 2.6 Parameters for glass fiber fabrication in the $80TeO_2$-$10TaO_{5/2}$-10ZnO glass composition (Δ=130 °C)

The stability of the glass against crystallization is normally evaluated by the gap between the glass transition temperature and the onset of crystallization ($\Delta T=T_x-T_g$). For fiber fabrication, glasses with the higher value of ΔT ($\Delta T>100$ °C) represents ideal candidates to prepare a crystal-free fiber (minimal scattering loss from crystallites) **[Soufiane 1993].**

5.1 Optical losses measurements

In an optical fiber, signal attenuations are intrinsic to the material. Indeed, electronic absorptions, multiphonon absorption, Rayeigh scattering, crystal content, inclusions are at the origin of the signal reduction. In tellurite oxide glasses (but also true for any IR transparent materials such as chalcogenide glasses), humidity present in the

furnace during the melting process and purity of the raw materials represent the main source of optical losses. Indeed, due to the hygroscopic behavior of the tellurium, its tendency to form TeOH entities is exacerbated in a non-dried atmosphere. As explained previously, the fundamental stretching resonance of OH is centered between 2.7 and 3μm, but the position of the OH absorption band depends greatly on the glass composition. Hydroxyl groups present in glass, lead to optical losses at 1380 nm. The OH vibrational mode is slightly anharmonic, which leads to oscillation components at overtone frequencies. In the case of silicate glasses, loss minima occur at 1.3 and 1.55 μm with ~0.15dB/km **[Grattan 1998]**. In tellurite based glasses, optical losses have been calculated to be around $3.6x10^{-3}$ dB/km at 3.02 μm **[Wang 1994]**, and have been experimentally measured from 1000 dB/m to 0.02 dB/m at 1.55 μm depending about both purity of the glass and glass composition. Massera et al. show a decrease of the optical losses at 1.55 μm in the TeO_2-Bi_2O_3-ZnO glass system from 23 dB/m to 9 dB/m by using an O_2- atmosphere during the glass melting process **[Massera 2011]**. Those results are in accordance with Moiseev et al. in the TeO_2-WO_3-La_2O_3-MoO_3 where optical losses decrease from 100 dB/m to 0.074 dB/m at 1.56 μm, by using purified oxygen atmosphere during the glass melt **[Moiseev 2011]**. Ebendorff-Heidepriem et al. remark that in TeO_2-ZnO-Na_2O-La_2O_3, using a smaller batch, melting for a longer time with larger numbers of melt swirling in a dried-air atmosphere permit to reduce the OH content and so on the optical losses from 600 dB/m to 0.8 dB/m at 2.0 μm **[Ebendorff 2012]**. The TeO_2-ZnO-Na_2O glass network has been intensively investigated by Prasad et al, Savelii et al. and Lin et al. proposing a value of optical losses at 1.55 μm of 1.3 dB/m, 6.3 dB/m and 0.24

dB/m respectively **[Prasad 2006][Savelii 2011][Lin 2009]**. This gap of values is essentially due to the glass quality in term of free-bubbles, free-crystals, and/or free-OH content. The minimum of optical losses at 1.55 μm found in tellurite glasses, has been reported by Ohishi et al. in TeO_2-Bi_2O_3-ZnO-Na_2O, and represents 0.02 dB/m **[Qin 2007][Cheng 2012]**.

The cutback method has been used to characterize the optical losses in fibers, allowing to both neglect losses due to reflection at the extremities of the fiber and losses due to connection between the fiber and the source **[Kaminow 1978**]. To measure optical losses, 1 meter long in size fiber is used in a spectrophotometer FTIR Nicolet 6700 with an InSb detector. Transmission spectrum is measured on this initial length L_1. On the same fiber with a reduced length L_2 ($L_2<L_1$) and by keeping the same light injection parameters, a second transmission spectrum is collected, as shown in Figure 2.14.

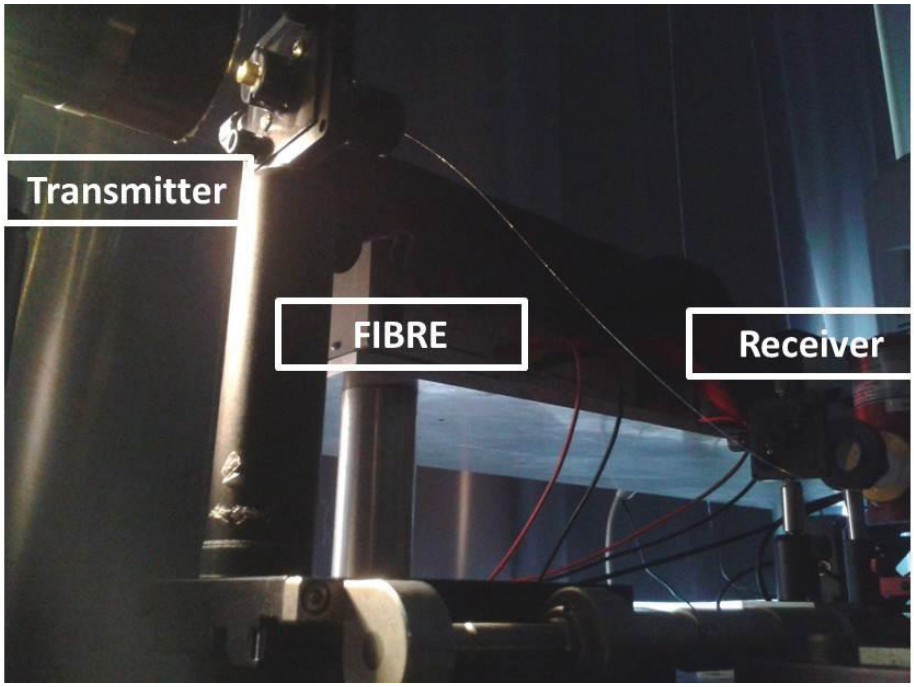

Figure 2.14 Optical losses measurements on tellurite-based glasses

For each wavelength, optical losses α in a fiber (dB/m) are calculated by:

$$\alpha = \frac{10}{L_1 - L_2} \log \frac{I_2}{I_1} \qquad \textbf{Eq. 2.16}$$

Where I_1 and I_2 are the spectra intensities of the fiber at a L_1 and L_2 length respectively.

The cutback method has been used on $80TeO_2$-$10TaO_{5/2}$-10ZnO optical fiber. The propagation losses at 1.55 µm and 2.00 µm for the core fiber are measured at 8.22 dB/m and 6.87 dB/m. Optical losses are important compared to those of Ohishi **[Qin**

2007][Cheng 2012] due to to the fact that the optical fiber is a mono component fiber, with only one refractive index (i.e. no core-clad fiber), as explained by Savelii et al. **[Savelii 2011].**

6 Effect of crystallization in TeO_2-Bi_2O_3-ZnO glass network

As noted previously, some tellurite systems studied by our group **[Massera 2009]** have exhibited poor crystallization stability (for fiberization) but unique formation of crystalline phases of interest for either glass ceramic applications or possible nonlinear applications. A component of the present effort is to examine in more detail, the evolution of second phase(s) in the TeO_2-Bi_2O_3-ZnO glass system for use in fabricating (either in bulk, or post-draw in fiber) glasses with unique second phase microstructures that enhance mechanical or optical properties. Glass ceramics (GCs) have been widely studied and shown to often enhance the mechanical properties and durability over that seen in the based glass. The impact of the second (crystalline) phase in tellurite glasses on the resulting optical properties has not been widely studied. To our knowledge, the effect of a second phase yielding a GC on Raman Gain behavior has not been studied previously.

In the section, the impact of the short-range order on glass properties will be investigated as function of a specific crystal phase. Burger et al. and Ozdabova et al. show that depending about the quenching rate, there is a potential formation of solidus

present in the liquidus, leading to the crystallization of $ZnTeO_3$, $Zn_2Te_3O_8$ or $Bi_2Te_4O_{11}$ **[Ozdabova 2007][Burger 1992][Udovic 2006]**. As shown by Massera et al., TBZ materials often propose different crystal phases such as $Bi_2O_3 + Zn_2TeO_3O_8$, $Bi_2Te_4O_{11}$ or also $Bi_2Te_2O_7 + TeO_2$, depending mostly about the studied glass matrix **[Massera 2010]**. Our effort is based on one specific glass composition, TeO_2:Bi_2O_3:ZnO 74:12:14, due to the possibility to obtain a single crystal phase after a specific heat treatment **[Murugan 2004-2]**. As shown by Murugan et al. the multi crystal phase $Bi_2TeO_5 + Bi_{3.2}Te_{0.8}O_{6.4}$ is reduced to a single crystal phase $Bi_2Te_4O_{11}$.

The study of the crystal structure present in the tellurite based glass has been studied. X-ray diffraction experiments are carried out using Cu *K*α (1.5418 Å) radiation to identify the crystal phases produced. XRD patterns are shown in Figure 2.15.

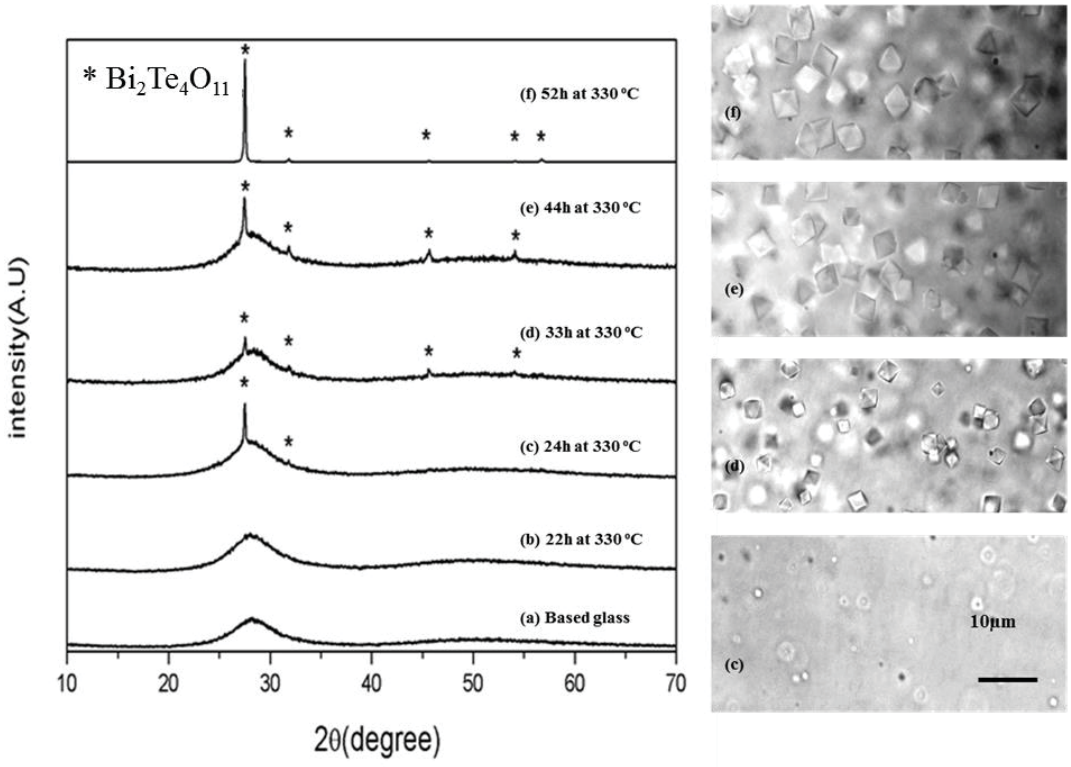

Figure 2.15 XRD patterns in situ high temperature of TBZ glass network and optical microscopy focusing on the β-$Bi_2Te_4O_{11}$ crystallization

The presence of broad line proves the amorphous state of the material. Then, a XRD analysis in situ at high temperature has been done to observe the apparition of this unique crystal phase, seen by optical microscopy. After 24h of heat treatment, apparition of peaks characteristic of crystallization occurs. After 52h, high density of crystalline phase is obtained, leading to a clear XRD pattern assigned to the β-$Bi_2Te_4O_{11}$ crystal phase, as shown in Figure 2.16.

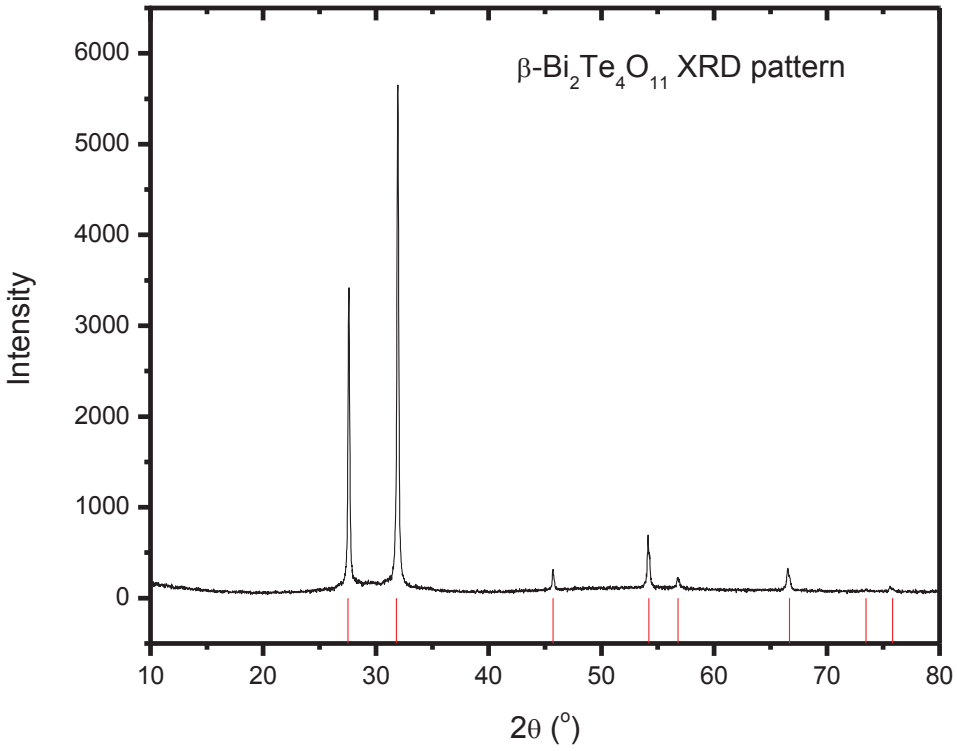

Figure 2.16 XRD pattern of β-$Bi_2Te_4O_{11}$ crystal phase into 74TeO_2-12Bi_2O_3-14ZnO amorphous matrix

XRD patterns are compared to ICDD data files and literatures sources to identify the crystalline phases present into the material. It is checked that the crystal phase obtained in the glass ceramic is the β-$Bi_2Te_4O_{11}$ phase with characteristic crystal parameters summarized in Table 2.7.

n	h	k	l	d_{obs}	$2\theta_{(obs)}$
1	1	1	1	3.246	27.53
2	2	0	0	2.814	31.83
3	2	2	0	1.984	45.7
4	3	1	1	1.692	54.22
5	2	2	2	1.621	56.8
6	4	0	0	1.403	66.7
7	3	3	1	1.289	73.46
8	4	2	0	1.255	75.84

Table 2.7 Unit cell refinement results for β-$Bi_2Te_4O_{11}$ crystal phase

The calculated parameter of the cubic phase – a = 5.6125 Å is close to the parameter reported for β-$Bi_2Te_4O_{11}$ by Szaller et al. a = 5.6397Å **[Szaller 1996]**, with a linear refractive index n = 2.22.

The chemical reaction between Bi_2O_3 and TeO_2 believed to be responsible for the formation of the phase is described by:

$$\frac{(1-x)}{2} Bi_2O_3 + xTeO_2 = Bi_{1-x}Te_xO_{\frac{3+x}{2}} \qquad \textbf{Eq. 2.15}$$

$Bi_2Te_4O_{11}$ crystal ($x = 0.667$) represents the first crystal phase formed in the solid reaction of Bi_2O_3 and TeO_2. $Bi_2Te_4O_{11}$ is a polymorph exhibiting two allotropic phases, a stable α-$Bi_2Te_4O_{11}$ monoclinic phase and a metastable β-$Bi_2Te_4O_{11}$ cubic structure **[Szaller 1996][Demina 1984][Frit 1972][Rossel 1992]**. To well-understand the metastable crystal structure, descriptions of the stable α-$Bi_2Te_4O_{11}$ monoclinic phase is

compared to the metastable β-$Bi_2Te_4O_{11}$ cubic phase. Clear differences are observed between α and β phase at the intermediate range order.

6.1 α-$Bi_2Te_4O_{11}$ monoclinic phase

This monoclinic symmetry $P_{2_1/n}$ (ICDD-JCPDS database **[ICDD-JCPDS 1601-1][ICDD-JCPDS 1601-2**] is related to the fluorite structure, anion-deficient superstructure of fluorite composed of an ordered intergrowth of $Bi_2Te_2O_7$ (fluorite-type) and Te_2O_4 (rutile-type) layers. Figure 2.17 shows the different tellurite entities present in the crystal, while Figure 2.18 represents the $Bi_2Te_2O_7$ crystal unit cell

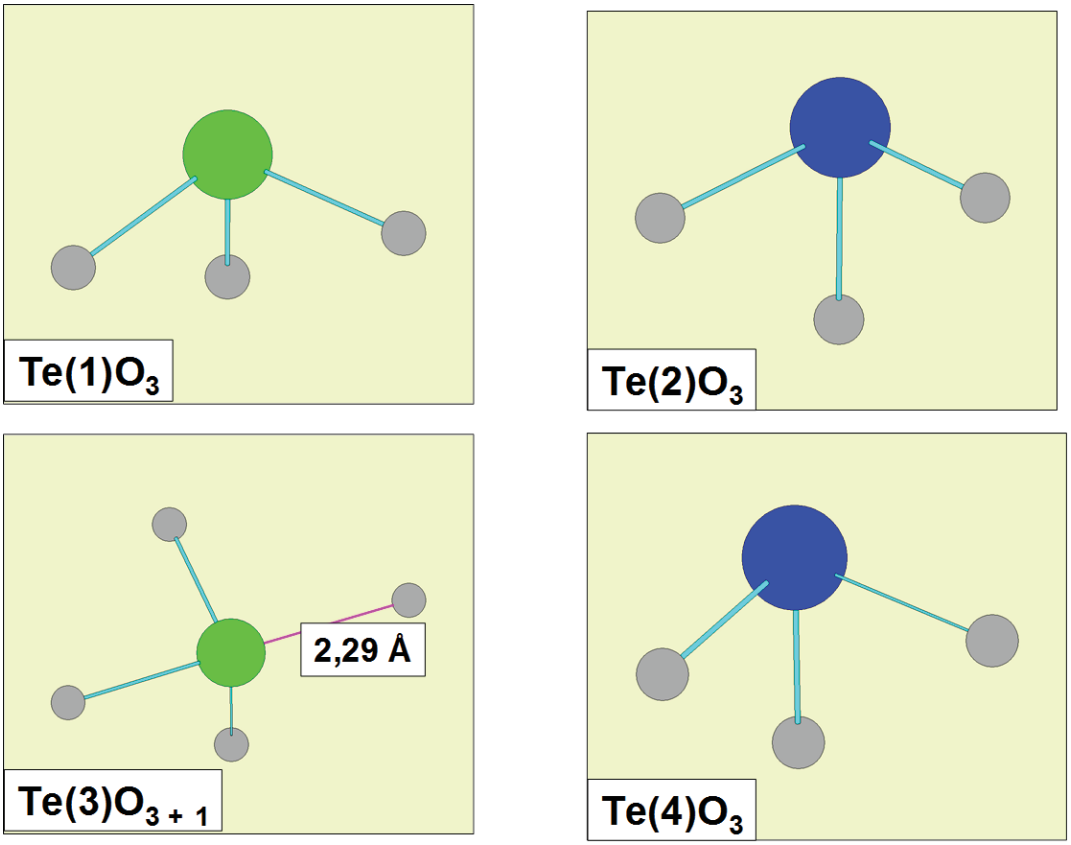

Figure 2.17 Different tellurium oxide geometry in the α-$Bi_2Te_4O_{11}$ crystal structure

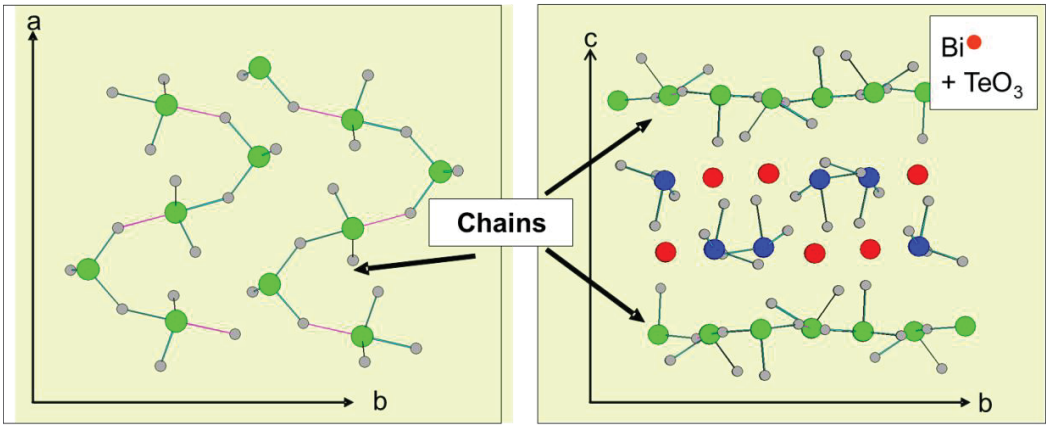

Figure 2.18 Chain-like structure in α-$Bi_2Te_4O_{11}$ crystal

This is an ordered sequence of tellurium-only layer and a mixed double layer containing equal numbers of Te and Bi atoms ($Bi_2Te_2O_7$). In the tellurium-only layer, TeO_3, TeO_{3+1} and TeO_4 are linked together by a single oxygen bridge to form parallel infinite long sinusoidal chains, as illustrated in Figure 2.18 and 2.19 **[Masson 2004]**.

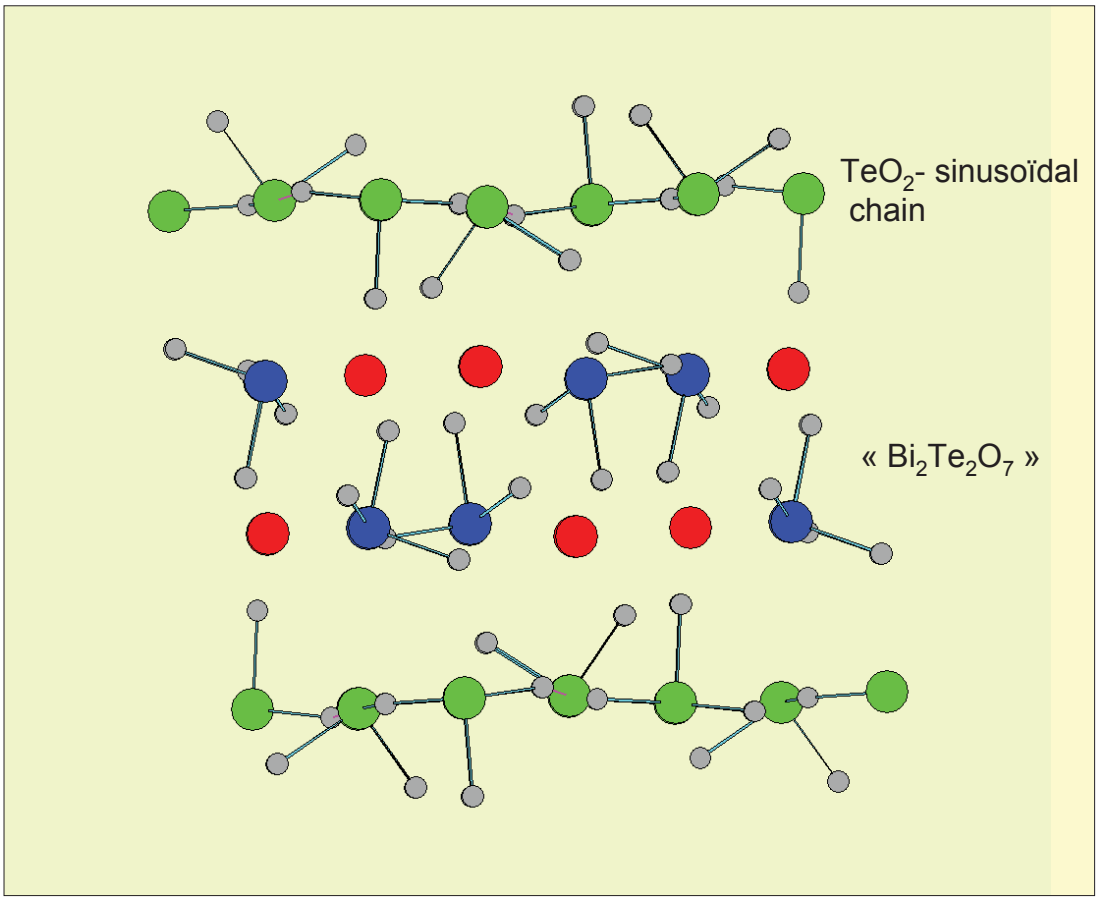

Figure 2.19 $Bi_2Te_4O_{11}$ crystal phase detailed as $Bi_2Te_2O_7$ crystal between TeO_2 crystal layers

The cubic to the monoclinic transition is the result of an ordering in one set of {111} planes. As a consequence of this ordering processes, the orthogonality of the [110] projection vanishes and the structure changes to the monoclinic structure, as shown in Figure 2.20.

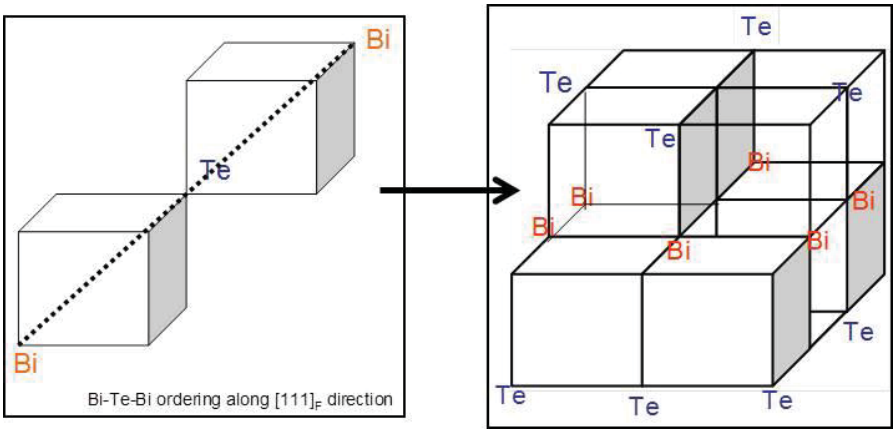

Figure 2.20 Ordering process of Te and Bi on the [111] in the CaF_2 fluorite structure during the β→α crystal phase transition. Only one possible configuration of the Bi-Te ordering is presented as an example

Szaller et al. show that the irreversible transition from the metastable β cubic phase to the stable α monoclinic crystal phase occurs at 443 ^{o}C **[Szaller 1996].**

6.2 β-$Bi_2Te_4O_{11}$ cubic metastable phase

The metastable cubic symmetry has a fluorite-type structure where each cation position is filled with bismuth and tellurium in 1/3 – 2/3 ratios, while the anion positions are occupied by oxygen in 11/12 site occupancy, representing a non-chemical ordering structure **[Lovas 1998]**. The identification and definition of the precise metastable crystal phase was a hard task because of some inconsistency in describing the actual structure by the fluoride model. To resolve this issue, we examine the work of O. Masson et al. who investigated the disordered metastable β-$Bi_2Te_4O_{11}$ phase using both neutron powder diffraction and Reverse Monte Carlo modeling (RMC) **[Masson 2004]**. In a Reverse Monte Carlo (RMC) study, O. Masson et al. described the β-phase as a local tellurium

environment made of TeO_3 and TeO_4 molecular units with 3:1 ratio; and proportions for bismuth atoms of 20%, 50% and 22% for respectively 8, 7 and 6 obtained coordination numbers. This phase is presented as having an apparent perfect oxygen – deficient fluorite type structure $F_{m\bar{3}m}$ (O_h^5). In fact it can be described as a short range ordering of the Bi and Te atoms along the [111] direction with several possible configurations and no long range ordering of the oxygen atoms in order to still have the typical tellurium oxygen polyhedral. This is an example of the coexistence of a cationic ordering and apparent anionic random distribution, as described in Figure 2.21 **[Masson 2004]**.

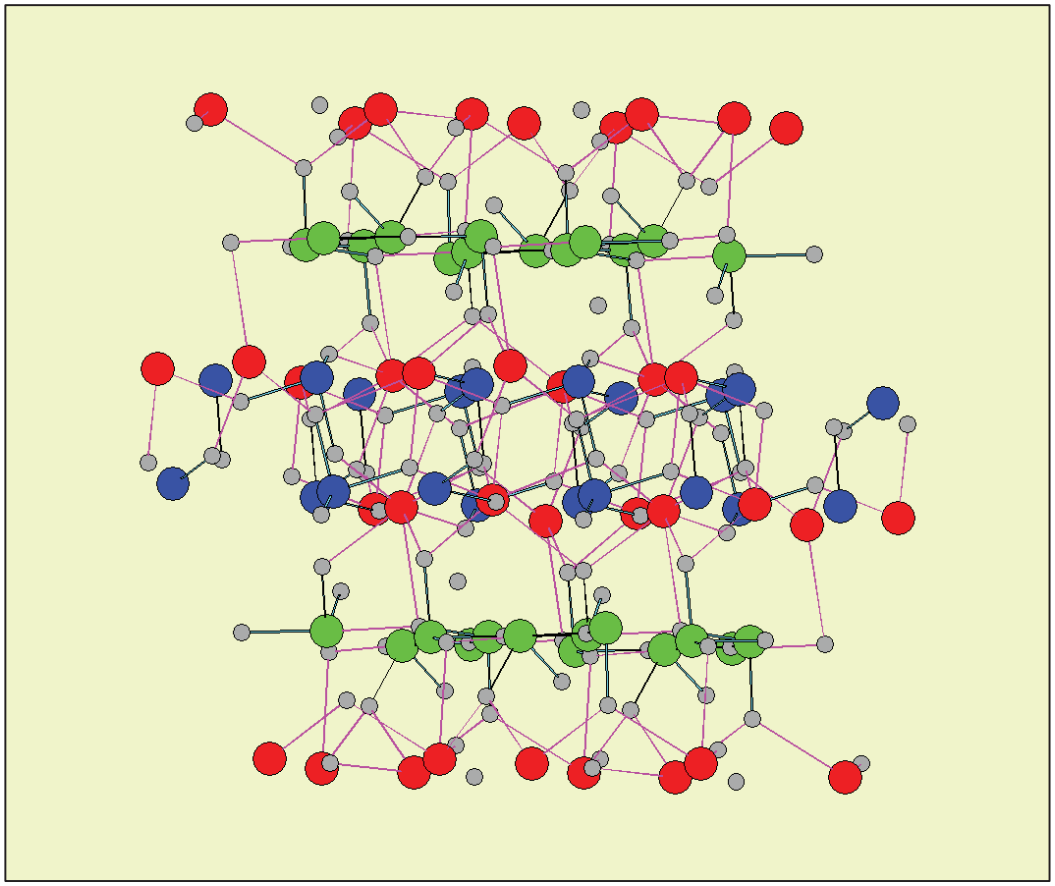

Figure 2.21 Structure of β-$Bi_2Te_4O_{11}$ crystal phase

To summarize the resulting phase formation in our tellurite glass system, the metastable β-$Bi_2Te_4O_{11}$ cubic forms under fast crystallization of the $Bi_2Te_4O_{11}$ melt **[El Farissi 1987][Astarf'ev 1989]**, and can be described as an intermediate state between the amorphous and crystalline states, namely having a short and medium range order similar to that of tellurite glasses and a premise of long range order among the cations only.

The cubic metastable phase and monoclinic stable crystal phase have a structural change in term of intermediate range order but own a structural analogy in general. Masson et al.

figure out this similarity by a total scattering analysis. An evident correlation is seen in the comparison between the total pair-correlation function from neutron measurement, i.e. Te-O and Bi-O bond lengths do not drastically change from β to α crystal phase. Finally the association of several fluorite - type cubes allows the construction of large Tellurium oxygen entities (chains or rings) close to that observed in several potassium tellurite crystals e.g. $K_2Te_4O_9$, $K_2Te_2O_5$. These can be seen as similar to the stable phase α-$Bi_2Te_4O_{11}$.

7 Conclusion

To summarize, in this chapter, three different glass networks have been investigated: TeO_2-$TaO_{5/2}$-ZnO, TeO_2-$NbO_{5/2}$ and TeO_2-$BiO_{3/2}$-ZnO. It has been shown that the introduction of tantalum oxide or zinc oxide allows increasing the glass stability toward crystallization. The introduction of ZnO into tellurite glass matrix permits to obtain the largest $\Delta T = T_x - T_g$. Concerning the refractive index, it has been observed in the different glass systems that the refractive index is mostly directed by TeO_2. Introduction of ZnO in the glass matrix induces an important decrease of the refractive index which has to be related with a glass network modification.

The crystallization of the TeO_2-Bi_2O_3-ZnO glass system with a specific glass composition (74:12:14) has been investigated. In this glass composition, it appears the formation of a unique crystal phase: $Bi_2Te_4O_{11}$. Heat treatments have been done below the temperature of crystal phase transition, and so, the metastable β-$Bi_2Te_4O_{11}$ cubic

phase is obtained. This cubic phase β-$Bi_2Te_4O_{11}$ can be described as an intermediate state between the amorphous and crystalline states.

An effort on the purification of tellurite-based glasses during the melting step has been done to propose a material with the lowest OH content. Melting and quenching under dried air atmosphere has been tested on two different tellurite-based glass systems TeO_2-Nb_2O_5 and TeO_2-Bi_2O_3-ZnO and shows a reduction of 90 % of the OH content in both materials. Improvements of the mechanical and thermal properties have been observed for the glasses with low OH content.

Optical glass fibers have been drawn from TeO_2-$TaO_{5/2}$-ZnO glass system with the specific composition (80:10:10). Optical losses have been measured on monolithic materials without core and cladding by using the cutoff method and represent 8.2 dB/m at 1.55 μm. The results obtained are promising for optical fiber fabrication.

Chapter 2 – References

Abe 1983: Y. Abe, "Topics in phosphorous chemistry", New York: John Wiley, 11 (1983) 20.

Adams 1961: R.V. Adams, Physics and Chemistry of Glasses 2 (1961) 39.

Anheier 2011: R. Anheier, NSF-International REU final report "Tellurite-based oxide glasses for novel MIR fibers applications with high Raman gain" (2011), Clemson University, USA.

Arriagada 1987: J.C. Arriagada, W. Burckhardt, A. Feltz, Journal of Non-Crystalline Solids 91 (1987) 375.

Astarf'ev 1989: S.A. Astarf'ev, A.A. Abdullaev, V.A. Dolgikh, B.A. Popovkin, Izvestiya Akademii Nauk SSSR Neorganik Mater. 5 (1989) 870.

Bartholomew 1982: R.F. Bartholomew "Treatise on materials science and technology", New York: Academic Press 22 (1982) 75.

Berthereau 1995: A. Berthereau, PhD thesis "Matériaux vitreux pour l'optique non linéaire" (1995) University of Bordeaux, France.

Berthereau 1996: A. Berthereau, E. Fargin, A. Villezusanne, R. Olazcuaga, G. Le Flem, L. Ducasse, Journal of Solid State Chemistry 126 (1996) 143-151.

Blanchandin 2002: S. Blanchandin, P. Thomas, P. Marchet, J.C. Champarnaud-Mesjard, B. Frit, Journal of Alloys and Compounds 347 (2002) 206-212.

Brow 1990: R.K. Brow, R.J. Kirkpatrick, G.L. Turner, Journal of Non-Crystalline Solids 116 (1990) 39.

Burger 1992: H. Burger, K. Kneipp, H. Hobert, W. Vogel, V. Kozhukharov, S. Neov, Journal of Non-Crystalline Solids 151 (1992) 134.

Chagraoui 2007: A. Chagraoui, A. Chakib, A. Mandil, A. Tairi, Z. Ramzi, S. Benmokhtar, Scripta Materialia, 56 (2007) 93.

Cheng 2007: T. Cheng, M. Lia, W. Gao, Z. Duan, T. Suzuki, Y. Ohishi, Optical Fiber Technology 18 (2012) 498-501.

Chida 1982: K. Chida, F. Hanawa, M. Nakahara, "Fabrication of OH-free multimode fiber by vapor phase axial deposition", IEEE Journal of Quantum Electronics, QE-18 (1982) 1883.

Davis 1995: K.M. Davis, M. Tomozawa, Journal of Non-Crystalline Solids 185 (1995) 203-220.

Davis 1996-1: K.M. Davis, A. Agarwal, M. Tomozawa, K. Hirao, Journal of Non-Crystalline Solids 203 (1996) 27-36.

Davis 1996-2: K.M. Davis, M. Tomozawa, Journal of Non-Crystalline Solids 201 (1996) 177.

Demina 1984: L.A. Demina, V.A. Dolgikh, Russian Journal of Organic Chemistry (Zh. Neorg. Khim.) 4 (1984) 949.

Dorofeev 2011: V.V. Dorofeev, A.N. Moiseev, M.F. Churbanov, T.V. Kotereva, A.V. Chilyasov, I.A. Kraev, V.G. Pimenov, L.A. Ketkova, E.M. Dianov, V.G. Plotnichenko, A.F. Kosolapov, V.V. Koltashev, Journal of Non-Crystalline Solids 357 (2011) 2366-2370.

Ebendorff 2012: H. Ebendorff-Heidepriem, K. Kuan, M.R. Oerman, K. Knight, T.M. Monro, Optical Materials Express 2 (2012) 432.

El-Farissi 1987: M. El Farissi, PhD thesis "Caractérisation structurale et propriétés électriques de nouveaux matériaux oxydes à base de Bi III, Te IV et Ln III" (1987) University of Limoges, France.

El-Mallawany 2000: R.A.H. El-Mallawany, Tellurite Glasses Handbook, CRC Press, 2000, pp. 113.

Feng 2001: X. Feng, S. Tanabe, T. Hanada, Journal of Non-Crystalline Solids 281 (2001) 48.

Frisch 2009: M.J. Frisch, G.W. Trucks, H.B. Schlegel, G.E. Scuseria, M.A. Robb, J.R. Cheeseman, G. Scalmani, V. Barone, B. Mennucci, G.A. Petersson, Gaussian 09, revision A.1, Gaussian Inc., Wallingford CT (2009)**.**

Frit 1972: B. Frit, M. Jaymes, Rev. Chim. Miner. 9 (1972) 837-844.

Gomez 1997: F. Gomez, P. Vast, Ph Llewellyn, F. Rouquerol, Journal of Non-Crystalline Solids 222 (1997) 415.

Grattan 1998: K.T.V. Grattan, B.T. Meggit, "Optical Fiber Sensor Technology: Fundamentals", Kluwer Academic Publishers Group, (1998).

Hoon 1991: K.S. Hoon, Y. Toshinobu, F. Miyaji, S. Sakka, Proceedings of the International Conference of Science and Technology of new glasses Tokyo 175 (1991) 187.

Hu 2011: X. Hu, G. Guery, J.D. Musgraves, D. VanDerveer, J. Boerstler, N. Carlie, P. Wachtel, S. Raffy, R. Stolen, K. Richardson, Journal of Non-Crystalline Solids 21 (2011) 3648-3653.

Hu 2012: X. Hu, G. Guery, J. Boerstler, J.D. Musgraves, D. VanDerveer, P. Wachtel, Journal of Non-Crystalline Solids 358 (2012) 952-958.

ICCD-JCPDS 1601-1: Powder Diffraction File PDF-1 ICDD-JCPDS 1601, Park Lane, Swarthmore, PA 19081 (1992).

ICCD-JCPDS 1601-2: Powder Diffraction File PDF-2 ICDD-JCPDS 1601, Park Lane, Swarthmore, PA 19081 (1993).

Jose 2006: R. Jose, T. Suzuki, Y. Ohishi, Journal of Non-Crystalline Solids 352 (2006) 5564-5571.

Karmakar 1999: B. Karmakar, P. Kundu, A.K. Chaudhuri, K. Annapurna, A. Kumar, R.N. Dwivedi, Bulletin of Material Science 22 (1999) 115-119.

Kaminow 1978: I. P. Kaminow, L. W. Stulz, Applied Physics Letters 33 (1978) 62.

Komatsu 1991: T. Komatsu, H. Tawarayama, H. Mohri, K. Matusita, Journal of Non-Crystalline Solids 135 (1991) 105.

Komatsu 1993: T. Komatsu, K. Shioya, K. Matusita, Journal of the American Ceramic Society 76 (1993) 2923.

Levason 1995: W. Levason, R. D. Oldroyd, Polyhedron 14 [8] (1995) 967-970.

Lin 2009: A. Lin, A. Zhang, E.J. Bushing, J. Toulouse, Optics Express 17 (2009) 16716.

Lopez 2004: C. Lopez, PhD thesis "Evaluation of the photo-induced structural mechanisms in chalcogenide glass materials" (2004) University of Central Florida, USA.

Lovas 1998: Gy. Lovas, I. Dodony, L. Poppl, Zs. Szaller, Journal of Solid State Chemistry 135 (1998) 175-181.

Manning 2012: S. Manning, H. Ebendorff-Heidepriem, T. M. Monro, Optical Material Express 2 [2] (2012) 140-152.

Massera 2009: J. Massera, PhD thesis "Nucleation and growth behavior of tellurite-based glasses suitable for mid-infrared applications" (2009) Clemson University, USA.

Massera 2010: J. Massera, J. Remond, J. Musgraves, M.J. Davis, S. Misture, L. Petit, K. Richardson, Journal of Non-Crystalline Solids 356 (2010) 2947-2955.

Massera 2011: J. Massera, A. Haldeman, J. Jackson, C. Rivero-Baleine, L.Petit, K. Richardson, Journal of the American Ceramic Society 94 [1] (2011) 130-136.

Masson 2004: O. Masson, P. Thomas, O. Durand, T. Hansen, J.C. Champarnaud, D. Mercurio, Journal of Solid State Chemistry 177 (2004) 2168-2176.

Mercier 1998: C. Mercier, L. Montagne, F. Sfihi, G. Palavit, J.C. Boivin, A.P. Legrand, Journal of Non-Crystalline Solids 224 (1998) 163-172.

Moiseev 2011: A.N. Moiseev, V.V. Dorofeev, A.V. Chilyasov, I.A. Kraev, M.F. Churbanov, T.V. Kotereva, V.G. Pimenov, G.E. Snopatin, A.A. Pushkin, V.V. Gerasimenko, A.F. Kosolapov, V.G. Plotnichenko, E.M. Dianov, Optical Materials 33 (2011) 1858-1861.

Mullica 1980: D.F. Mullica, J. D. Korp, W. O. Milligan, G. W. Beall, I. Bernal, Acta Crystallographica B36 (1980) 2565-2570.

Murugan 2004-1: G.S. Murugan, Y. Ohishi, Journal of Non-Crystalline Solids 341 (2004) 86-92.

Murugan 2004-2: G.S Murugan, E. Fargin, V. Rodriguez, F. Adamietz, M. Couzi, T. Buffeteau, P. Le Coustumer, Journal of Non-Crystalline Solids 344 (2004) 158-166.

Murugan 2005: G.S. Murugan, Y. Ohishi, Journal of Non-Cryst. Solids 351 (2005) 364-371.

Ozdabova 2007: J. Ozdabova, H. Ticha, L. Tichy, Journal of Non-Crystalline Solids 353 (2007) 2799-2802.

Prasad 2006: N.S. Prasad, J. Wang, R.K. Pattnaik, H. Jain, J. Toulouse, Journal of Non-Crystalline Solids 352 (2006) 519-523.

Qin 2007: G. Qin, A. Mori, Y. Ohishi, Optics Letters 32 (2007) 2179.

Rodriguez 2002: V. Rodriguez, C. Sourisseau, Journal of the Optical Society of America B 19 (2002) 2650.

Rossel 1992: H.J. Rossel, M. Leblanc, G. Ferey, D.J.M. Bevan, D.J. Simpson, M.R. Taylor, Australian Journal of Chemistry 45 (1992) 1415.

Sanghera 1998: L.S. Sanghera, I.D. Aggarwal, Infrared Fiber Optics, CRS Press, New York (1998).

Savelii 2011: I. Savelii, J.C. Jules, G. Gadret, B. Kibler, J. Fatome, M. El-Amraoui, N. Manikandan, X. Zheng, F. Desevedavy, J.M. Dudley, J. Troles, G. Renversez, F. Smektala, Optical Materials 33 (2011) 1661-1666.

Scholze 1959: H. Scholze, Glastechn. Ber. 32 (1959) 142.

Scholze 1966: H. Scholze, Glass Ind. 47 (1966) 622.

Scholze 1980: H. Scholze, "Le Verre: Nature, Structure et proprieties", Institut du Verre, Paris (1980) ISBN 2-85714-013-4.

Schultz 1974: P.C. Shultz, Journal of the American Ceramic Society 57 [7] (1974) 309-313.

Shelby 1976: J.E. Shelby, G. L. Mc Vay, Journal of Non-Crystalline Solids 20 (1976) 439.

Shioya 1995: K. Shioya, T. Komatsu, H.G. Kim, R. Sato, K. Matusita, Journal of Non-Crystalline Solids 189 (1995) 16-24.

Soufiane 1993: A. Soufiane; M. Poulain, "New fluorogallate glasses", Journal of Non-Crystalline Solids, 161 (1993) 206.

Szaller 1996: Zs. Szaller, L.Poppl, Gy. Lovas, I. Dodony, Journal of Solid State Chemistry 121 (1996) 251-261.

Tomozawa 1983: M. Tomozawa, M. Takata, J. Acocella, E.B. Watson, T. Takamori, Journal of Non-Crystalline Solids 56 (1983) 343.

Tomozawa 1985: M. Tomozawa, Journal of Non-Crystalline Solids 73 (1985) 197.

Toratani 1987: H. Toratani, H.E. Meissner, T. Izumitani, Journal of Non-Crystalline Solids 95-96 (1987) 701.

Udovic 2006: M. Udovic, P. Thomas, A. Mirgorodsky, O. Durand, M. Soulis, O. Masson, T. Merle-Mejean, J.C. Champarnaud-Mesjard, Journal of Solid State Chemistry 179 (2006) 3252-3259.

Vickers: http://eoin-brennan.com/Content/Images/Portfolio-VickersMed.jpg.

Villegas 2007: M.A. Villegas, J. M. Fernandez Navarro, Journal of the European Ceramic Society 27 (2007) 2715-2723.

Wang 1994: J.S. Wang, E.M. Vogel, E. Snitzer, Optical Materials 3 (1994) 187.

CHAPTER 3

VIBRATIONAL SPECTROSCOPY ANALYSES

Chapter 2 discussed the impact of different glass modifiers present in TeO_2-$TaO_{5/2}$-ZnO, TeO_2-$NbO_{5/2}$ and TeO_2-$BiO_{3/2}$-ZnO glass matrices on thermal, physical and optical properties. Additionally, a method for purifying these glasses to yield lower absorption low was defined and the effect of the purification process on those properties was presented. Furthermore, measurements of optical losses were measured on a promising glass candidate that were drawn into fiber.

In this chapter, we propose to probe the structural changes in these different glass systems in order to give an answer to: *"What is the impact of the different glass modifiers on the tellurite-based glass structure?"*. This investigation will be based on different vibrational spectroscopies such as infra-red, Raman and hyper-Raman spectroscopies. To be capable to understand the different parameters occurring in the modification of the glass structure, we propose to firstly probe the different vibrational contributions present in the paratellurite crystal. From the knowledge obtained on analysis of crystalline materials, we will be able to extend our investigation to isotropic tellurite materials: the glass. The role of glass modifiers on the structure will provide important information needed to understand the impact of those glass structures on the Raman gain response. It is envisioned that this structural know-how will permit the engineering of new materials with improved crystallization stability and tailored optical properties to yield enhanced Raman gain performance.

1. Introduction

Vibrational spectra of condensed media are studied widely because many physical properties of these media used practically in different areas of science and technology may be found from the spectra of vibrational excitations and their interactions. Today the simplest techniques for the study of vibrational spectra are infrared (IR) and Raman scattering (RS). Hyper-Raman scattering (HRS) is also one of the methods of vibrational spectroscopy and is an independent source of spectroscopic information.

In this part, fundamental aspects of different vibrational spectroscopic techniques will be introduced and the manner in which they are used for the structural understanding of materials, including glasses, will be discussed. This structural approach does relate to the fundamental questions: *"What is the impact of the glass structure on the Raman gain?"* Indeed, a detailed understanding of the glass structure will expose relationships with glass properties, specifically between glass chemistry, structure and the corresponding nonlinear optical properties. This approach is defined in the cgs system.

By looking at the molecular level total dipole moment $\vec{\mu}$, it is possible to separate each contribution to the overall dipole moment to gain a more complete description of the material response. Specifically, μ can be expressed as:

$$\vec{\mu} = \vec{\mu}^{(0)} + \varepsilon_0 \alpha \vec{E}(\omega) + \varepsilon_0 \left[\frac{1}{2} \beta \vec{E}(\omega)\vec{E}(\omega) + \frac{1}{6} \gamma \vec{E}(\omega)\vec{E}(\omega)\vec{E}(\omega) + \cdots \right] \quad \textbf{Eq. 3.1}$$

Where $\vec{\mu}^{(0)}$ is as the permanent dipole moment, ε_0 the vacuum permittivity, $\vec{E}(\omega)$ the applied electric field. α is defined as the molecular first-order polarizability (or linear polarizability) and β and γ are respectively the second- and third-order polarizability (or first- and second-nonlinear polarizability). Note that β is also called the first hyperpolarizability and γ the second-order hyperpolarizability and these terms provide information on the nonlinear polarizability. Vibrational optical techniques that have been used in this work are related to the dynamic induced dipole moment $\vec{\mu}$ modulated by the motion of nuclei with normal coordinate Q as follow:

$$\mu_i(Q) = \mu_{i\,(Q=0)} + \left(\frac{d\mu_i}{dQ}\right)_{Q=0} Q + \cdots \qquad \textbf{Eq. 3.2}$$

Where

$$\left(\frac{d\mu_i}{dQ}\right)_{Q=0} = \left(\frac{d\mu_i^{(0)}}{dQ}\right)_{Q=0} + \varepsilon_0 \left[\frac{d\alpha_{ij}}{dQ}_{Q=0} E_j(\omega) + \frac{1}{2}\left(\frac{d\beta_{ijk}}{dQ}\right)_{Q=0} E_j(\omega)E_k(\omega) + \cdots\right] \textbf{Eq. 3.3}$$

Where $\mu^{(0)}$ is the permanent polarization, E is the applied electric field, α represents the polarizability, β and γ are the 2nd and 3rd order of hyper-polarizability, and ω is the frequency. IR absorption spectroscopy is concerned with the first term $\left(\frac{d\mu_i^{(0)}}{dQ}\right)_{Q=0}$. Raman and hyper-Raman scattering techniques are related to the second $\frac{d\alpha_{ij}}{dQ}_{Q=0}$ and third $\left(\frac{d\beta_{ijk}}{dQ}\right)_{Q=0}$ terms which involve, respectively, the linear and the second-order nonlinear induced dipole moment.

When probing a material, the different molecular quantities previously defined are replaced by macroscopic quantities. The total dipole moment density response $\vec{P}$ is defined as the sum of individual contributions $\vec{\mu}$ in the elementary volume δV and the different polarizabilities are replaced with their corresponding dielectric susceptibility $\chi^{(n)}$ where n stands for the order of the polarizability. Note that the first-order susceptibility $\chi^{(1)}$ is related to the dielectric constant $\varepsilon = 1 + \chi^{(1)}$ (in SI unit)

2. Principles and experimental details of IR, Raman and hyper-Raman scattering techniques

2.1. Optical modes in materials

In the more general description **[Turrel 1972]**, the dielectric constant ε of a medium is defined from the electric field $\vec{E}$ and the polarization $\vec{P}$, the density of polarization as previously defined. The basic relation that defines the dielectric constant is:

$$\vec{D} = \varepsilon_0 \vec{E} + \vec{P} = \varepsilon_0 \varepsilon \vec{E} \qquad \textbf{Eq. 3.4}$$

Where $\vec{D}$ is the electric displacement. In an isotropic medium non-magnetic and electrically neutral, the wave propagation equation for electromagnetic waves is:

$$\frac{d^2\vec{D}}{dt^2} = c^2 \nabla^2 \vec{E} \qquad \textbf{Eq. 3.5}$$

Solutions are (monochromatic) plane-waves in the form of:

$$\vec{E} = \overrightarrow{E_0}.exp\left[i\left(\vec{K}.\vec{r} - \omega t\right)\right] \qquad \textbf{Eq. 3.6}$$

Where $\left|\vec{K}\right| = N\frac{\omega}{c}$ is the wave vector and N is the complex index of refraction of the medium and $i = \sqrt{-1}$. Solving thus Maxwell's equations we obtain:

$$-\left(\vec{K}.\vec{E}\right).\vec{K} + \left(\vec{K}.\vec{K}\right).\vec{E} = \frac{\omega^2}{c^2}\varepsilon.\vec{E} \qquad \textbf{Eq. 3.7}$$

With $\varepsilon = \varepsilon' + i\frac{4\pi\sigma}{\omega} = \varepsilon' + i\varepsilon''$ and where σ is the electrical conductivity. By taking the scalar product of the wave vector $\vec{K}$ with Eq. 3.7 it is found that:

$$\left(\frac{\omega^2\varepsilon}{c^2}\right)\vec{K}.\vec{E} = 0 \qquad \textbf{Eq. 3.8}$$

So that either $\vec{K}.\vec{E} = 0$ or $\varepsilon = 0$. Ordinary $\varepsilon \neq 0$, and the resulting condition, $\vec{K}.\vec{E} = 0$, describes a transverse wave, that is, a wave in which the electric field is perpendicular to the propagation direction. With $\vec{K}.\vec{E} = 0$, Eq. 3.7 becomes:

$$K^2 = \frac{\omega^2}{c^2}\varepsilon \qquad \textbf{Eq. 3.9}$$

Taking Eq. 3.4 and 3.9, we obtain for the transverse optical (TO) modes:

$$\overrightarrow{E_T} = \frac{4\pi\omega^2}{K^2c^2-\omega^2}\overrightarrow{P_T} \qquad \textbf{Eq. 3.10}$$

The condition represented by Eq. 3.8 can be satisfied in an alternative way, namely, $\varepsilon = 0$. In this case the electric field $\vec{E}$ is necessarily perpendicular to the wave vector $\vec{K}$ and the wave has a longitudinal component. In that case, from Eq. 3.4 we obtain for the longitudinal optical (LO) mode:

$$\overrightarrow{E_L} = -4\pi\overrightarrow{P_L} \qquad \textbf{Eq. 3.11}$$

In practice, dipolar modes induce modifications of the dipole moment of the medium, and thus create long-range Coulomb interactions that are superimposed to local interatomic force fields, resulting in more or less pronounced TO-LO splitting of normal modes. Vibrational spectroscopies that will be able to observe dipolar modes have the potential to reveal the TO-LO splitting of these modes. This applies not only to (ionic) crystals but also to any isotropic materials such as silica glass **[Payne 1984]**, or in very thin layers of material. In particular, in iono-covalent materials, the long-range Coulomb interactions due to dipolar modes act as an ordering force and may overcome the effects of the

disorder in isotropic material to produce well defined longitudinal and transverse optical vibrational modes.

2.2. Infra-red (IR) reflectivity

2.2.1 Principles

The infrared domain can be split in 3 regions, near-mid and far-infrared depending on the wavenumber (cm^{-1}) window. From 0.8 to 2.5 μm (12500 to 4000 cm^{-1}), the region is called near-IR where harmonic and overtones vibrations occur. The mid-IR ranges from 2.5 to 25 μm (4000 to 400 cm^{-1}) where fundamental vibrations occur, as shown in Figure 3.1. Finally the 25 to 1000 μm (400 to 10 cm^{-1}) range constitutes the far-IR (also called THz frequency domain) where for example molecular rotations are observed.

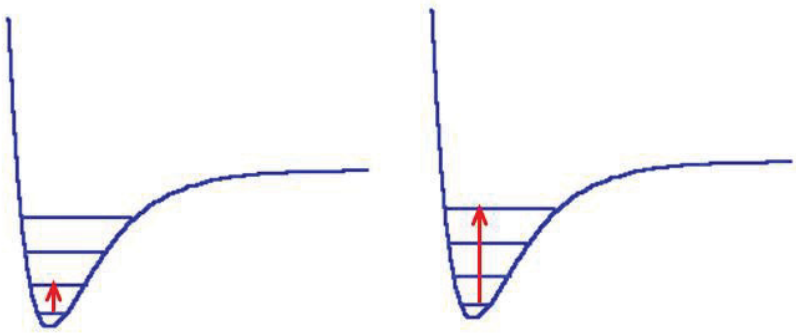

Figure 3.1 Fundamental IR absorption (left) in the mid-IR and harmonic absorption (right) in the near-IR

The mid-infrared region is currently used for the study of molecules or materials. For example, infra-red absorption spectroscopy permits to directly obtain molecular structural information, since we expect in this frequency domain stretching modes, which are characteristic of each bond A-B, bending modes, that come from angular oscillations of A-B-C moieties, and also deformation modes which are characteristics of an oscillating twist between two planes defined by a four atoms A-B-C-D unit. The vibrational selection rule of IR spectroscopy can be simply expressed as follow. A given normal vibration of a molecule may appear in the IR spectrum is at least one component $\mu^{(0)}$ of the permanent electric dipole moment of the molecule change during this vibration, i.e. when the value of a dipole moment derivative, taken at the equilibrium, differs from zero: $\left(\frac{d\mu^{(0)}}{dQ_k}\right)_0 \neq 0$, where Q_k is the kth normal coordinate associated with vibration of wavenumber ν_k; the subscript 0 refer to derivatives taken at the equilibrium configuration. This description and selection rule can be extended to any material including glass materials and IR active modes are intrinsically called dipolar modes. In the general case of dense matter, vibrations modes can couple and the resulting spectrum is much more complex to interpret as we will see later on in this chapter. As far as we are concerned with optical vibrational techniques, the optical constants fully describe the optical behavior of a material. The optical constants are the real, $n(\nu)$, and imaginary, $k(\nu)$, parts of the complex refractive index $\bar{n}(\nu) = n(\nu) + ik(\nu)$. They are thus important fundamental properties of matter whatever the domain frequency range. The result of any IR optical measurement can be calculated if the optical constants of the sample are known at all wavenumber of interest and the experimental configuration can

be described mathematically. Conversely, the optical constants of a sample can be calculated from any well-defined optical measurement. Under some circumstances one of these measurements can be replaced by the Kramers-Kronig relations, which as described below, allow the $n(\nu)$ and the $k(\nu)$ spectra to be calculated, provided the measurements cover a sufficiently wide wavenumber range and *n* is known at one wavenumber close to that range. Hence, because of the strong IR absorption of all glasses, it is rather unrealistic to get directly the low frequency range spectrum, which is indicative of the glass structure, in the transmission mode since that measurement would require sample thickness less than 10 μm. In that case it is necessary first to record the IR spectra in the reflection mode and second to perform a Kramers-Kronig transformation.

In the Kramers-Kronig approach, the measured specular reflectivity $R(\nu)$ is modified to obtain the phase angle $\theta(\nu)$ between the incident wave and the reflected one **[Stern 1963]** by:

$$\theta(\nu) = \frac{2\nu}{\pi} P \int_0^{\infty} \frac{\ln r(\nu_i) - \ln r(\nu)}{\nu^2 - \nu_i^2} d\nu_i \qquad \textbf{Eq. 3.12}$$

Where $r(\nu) = \sqrt{R(\nu)}$ and P represents the Cauchy principal value (assignment values to improper integrals). From the phase angle $\theta(\nu)$ spectrum the real $n(\nu)$ and imaginary $k(\nu)$ parts are obtained on the basis of the Fresnel formulas for normal incident.

$$\begin{cases} n(\nu) = \frac{1-r^2(\nu)}{1+r^2(\nu)-2r(\nu)\cos\theta(\nu)} \\ k(\nu) = \frac{2r(\nu)\sin\theta(\nu)}{1+r^2(\nu)-2r(\nu)\cos\theta(\nu)} \end{cases}$$ **Eq. 3.13**

From the complex dielectric function $\bar{\varepsilon}(\nu) = \varepsilon'(\nu) + i\varepsilon''(\nu)$, the real $\varepsilon'(\nu)$ and imaginary $\varepsilon''(\nu)$ parts are directly used:

$$\begin{cases} \varepsilon'(\nu) = n^2(\nu) - k^2(\nu) \\ \varepsilon''(\nu) = 2n(\nu)k(\nu) \end{cases}$$ **Eq. 3.14**

By analogy with crystalline solids, the maxima of $\varepsilon''(\nu)$ correspond to the transversal optical frequencies. The maxima of the energy loss function $-Im(\frac{1}{\bar{\varepsilon}(\nu)})$ relate to the longitudinal optical frequencies **[Galeneer 1980]**. The Kramers-Kronig approach is used to analyse infrared reflectivity glass data **[Almeida 1990][Merzbacher 1991][Kamitsos 1993]**. In many cases, the results of the Kramers-Kronig analysis are expressed in terms of absorption coefficient spectrum, $\alpha(\nu)$ calculated from $\alpha(\nu) = 4\pi\nu k(\nu)$. However, it is also possible to express the IR spectra in term of the imaginary part of the dielectric constant ε'' calculated from the relationship $\varepsilon'' = 2nk$; this representation is preferred to compare the IR spectrum with the Raman spectra which is related to the dielectric susceptibility $\chi^{(1)}$.

2.2.2. Experimental use of infrared (IR) spectroscopy in the present work

In the present work, spectroscopic techniques based on the above principals were employed to examine the role and the impact of glass modifier on the structural vibrational response of the glasses under study. Specifically, these tools were used to understand the variation of polarity of the materials.

Glass samples were fabricated by polishing optically a piece of 1 mm thick piece of glass to obtain the specular reflection, and examined using infrared (IR) transmission and reflection.

The IR spectra were recorded on a Nexus 670 spectrophotometer (Thermo Optek) equipped with a DTGS detector and a germanium-coated KBr beam splitter or hybrid FIR beam splitter. A total of 200 scans were averaged with a resolution of 4 cm^{-1}. The spectrometer was purged with dry air to minimize atmospheric CO_2 and water vapor. Reflectance experiments were performed using an external reflection attachment (Graesby, Specac) at an angle of incidence of 12^o. The complex refractive index of each sample was obtained through Kramers-Krönig analysis of its specular reflectance spectrum **[Kamitsos 1996][Kamitsos 1997]**. The infrared spectra reported in this work were expressed in term of the imaginary part of the dielectric constant ε''.

2.3. Raman scattering (RS)

2.3.1. Principles

The possibility of light scattering with significant change of frequency was first predicted on theoretical grounds by Smekal **[Smekal 1923]** in 1923. The first observation of the phenomenon were made in liquids by Raman and Krishnan **[Raman 1928]**, then in crystals by Landsberg et al. **[Landsberg 1928]**, both in 1928. The first comprehensive treatise of the underlying theory was offered by Placzek **[Plazek 1934]** in 1934.

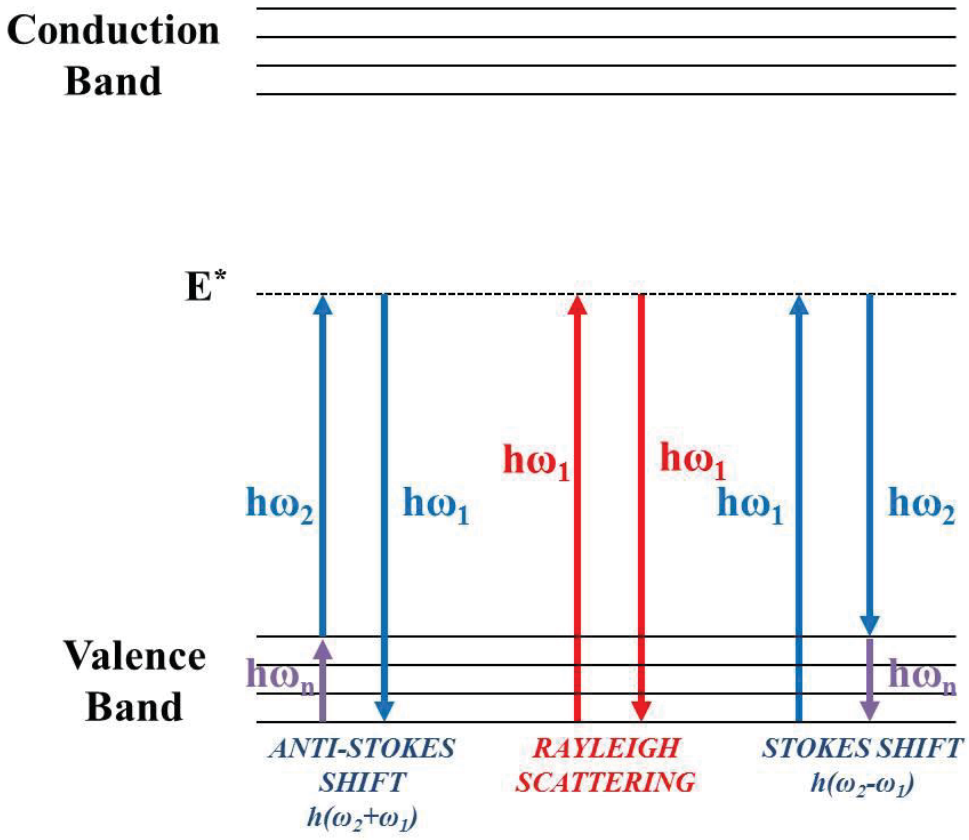

Figure 3.2 Principle of Raman spectroscopy

Raman scattering is a two-photon process in which a system is excited with one photon of frequency ω_i and emits one photon at the frequency $\omega_i \pm \omega$, where ω is the frequency of vibrational excitation of the medium (ω_n in Figure 3.2). Raman scattering is a very weak effect; it is always accompanied with Rayleigh scattering with intensity usually 3-5 order of magnitude greater (Figure 3.2). Note, however that Rayleigh scattering itself is only 10^{-4}-10^{-3} of the intensity of the incident exciting radiation. The new component appearing in the spectrum of the scattered radiation at shifted wavenumbers are termed Raman lines or Raman bands, and collectively they are referred to as the Raman spectrum. The Raman bands at wavenumbers less than the exciting wavenumber are referred to as Stokes lines, whereas those appearing at higher wavenumber as anti-Stokes lines. In practice, the Raman Stokes spectrum is used to analyze materials.

As is the case for IR spectroscopy, selections rules govern Raman activity. The classical radiation treatment we have invoked provides a basis for an answer to this important question. It is immediately clear that the induced dipoles responsible for Raman scattering associated with the molecular frequency ω will be zero unless at least one of the components of the derived polarizability tensor is non-zero: $\left(\frac{d\alpha_{ij}}{dQ}\right)_{Q=0} \neq 0$. This derivative is the ij component of the polarizability tensor with respect to the normal coordinate of vibration Q_k, taken at the equilibrium position. Thus, the condition for Raman activity is that, for at least one component of the polarizability tensor, a plot of that component against the normal coordinate must have a non-zero gradient at the equilibrium position.

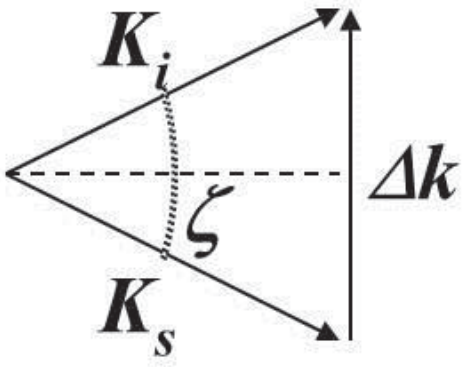

Figure 3.3 Relationship between the wave vectors of the exciting K_i and scattered K_s radiation and a wave vector Δk in the medium

In a material, the scattering processes can be analyzed by considering the geometry of the process as depicted in Figure 3.3. If K_i and K_s are, respectively, the wave vectors of the incident and the scattered radiation, and Δk is a wave vector of a given medium, the conservation of energy and momentum are assured by the relations $\omega_i = \omega_s + \omega_Q$ and $K_i = K_s + \Delta k$. Since $\omega_Q \ll \omega_i$, $K_i \approx K_s$ and the magnitude of the wave vector of the scattering process is given by $\Delta k = 2K_i \sin(\frac{\theta}{2})$. Raman scattering is usually at an angle of 90° with respect to the incident radiation, $\theta = 90^o$, and $\Delta k = K_i\sqrt{2}$. When considering Raman microscopy, the scattering is at an angle of 180° with respect to the incident radiation, $\theta = 180^o$, and $\Delta k = 2K_i$. For both case, note the Raman scattering process is inelastic and the corresponding phonon momentum K_Q is almost zero.

According to Placzek **[Plazek 1934]**, the Raman intensity I_{RS} collected in a solid angle $d\Omega$ can be expressed in the following general form:

$$I_{RS} = G.\nu_{laser}^4.I_{laser}.N.\left|\overrightarrow{E_s}\bar{\bar{\alpha}}\overrightarrow{E_i}\right|^2 d\Omega \qquad \textbf{Eq. 3.15}$$

Where G is a general instrumental constant, ν_{laser} is the frequency of the laser, I_{laser} is the laser power, N is the number density of scatterers, $\bar{\bar{\alpha}}$ is the Raman polarizability tensor, and $\overrightarrow{E_i}$ and $\overrightarrow{E_s}$ are the direction of the incident and scattered electric field (polarization), respectively, usually denoted as vertical (V) or horizontal (H) polarization with respect to the plane of incidence. This polarization orientation based on these assignements, is shown schematically in Figure 3.4.

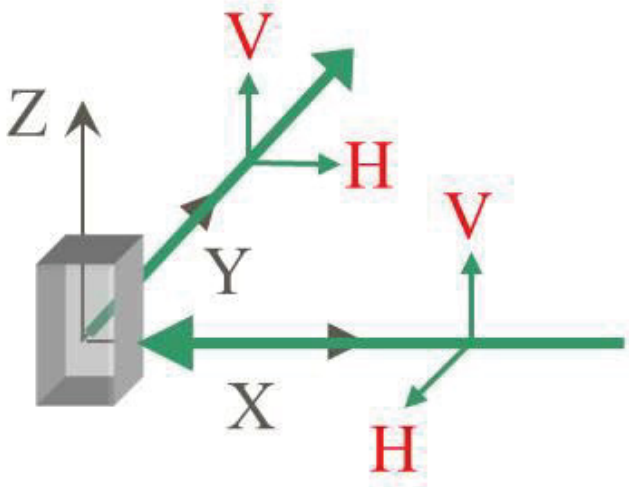

Figure 3.4 Sketch of the 90° Raman scattering geometry with different linear vertical (V) and horizontal (H) polarization for the incident and scattered beams

It is then useful to specify the different scattering geometries with the Porto's notation **[Damen 1966]**. Let the laser beam be directed along the X axis ($\boldsymbol{K_i}$ // X) and the scattered light is observed along the Y axis ($\boldsymbol{K_s}$ // Y) (figure 4). The $\boldsymbol{K_Q}$ vibrational wave vector will then be located in the XY plane. Porto's notation is expressed as $K_i(E_sE_i)K_s$. Following Figure 3.4, we are left with the four geometries of polarization as:

$$VV \rightarrow X(ZZ)Y$$

$$VH \rightarrow X(ZX)Y$$

$$HV \rightarrow X(YZ)Y$$

$$HH \rightarrow X(YX)Y \qquad \textbf{Eq. 3.16}$$

If the sample is an oriented single crystal aligned in such a way that its crystallographic directions (x, y, z) are aligned with the referenced lab frame (X, Y, Z), it is easy to show that the X(ZZ)Y scattering geometry with involve phonons modifying the α_{zz} Raman component. The X(ZX)Y scattering geometry with involve phonons modifying the $\alpha_{zx} = \alpha_{xz}$ Raman component, and so on.

If the sample is an isotropic medium like a liquid or a glass material, there are only two scattering geometries that gives non-equivalent spectra, namely the VV (or //) or VH = HV = HH (or $\perp$). In that case, no LO mode can be observed using Raman spectroscopy

since dipolar modes are Raman inactive in a centrosymmetric medium (by the mutual exclusion rule).

2.3.2. Experimental use of Raman spectroscopy in the present work

In the present part, Raman spectroscopic techniques based on the above principle were employed to examine the role and the impact of glass modifier on the structural vibrational response of the glasses under study. Specifically, these tools were used to understand the variation of polarizability of the materials.

In the present study, Raman spectra were recorded using two scattering geometries. The 90° scattering Raman scheme (Figure 4) is classical except that we have used a unique Raman/hyper-Raman spectrometer (see experimental details next paragraph). For Raman measurements in the different materials, the Raman setup works with a pulsed laser source operating at 532 nm by frequency doubling a fundamental IR radiation (60 picosecond pulses at 2kHz) using a NLO crystal in the phase matching condition. The fundamental beam at 1064 nm is rejected using a bandpass neutral density filter. Hence, we detect the Raman scattered light at the optical frequency $2\omega-\omega_Q$ (Stokes response) from an incident laser pulsed at 2ω, where ω_Q again denotes the frequency of a normal mode of vibration Q. Raman backscattering polarized experiments have also been performed using a micro-Raman HR-800 from Horiba/Jobin-Yvon coupled with a continuous laser source emitting at 532 nm. For both Raman configurations the spectral resolution was 4 cm^{-1}.

2.4. Hyper-Raman scattering (HRS)

2.4.1. Hyper-Raman scattering principles

The (vibrational) hyper-Raman phenomenon was theoretically predicted at the same time by several authors **[Kielich 1964][Li 1964][Akhmanov 1965]** and was first observed experimentally in 1965 by Terhune and co-workers **[Terhune 1965]**. It is a three-photon process in which the system is excited by two photons of frequency ω and emits one photon at the frequency $2\omega \pm \omega_Q$, with ω_Q the frequency associated with a vibrational transition (Figure 3.5) **[Kielich 1983][Denisov 1987][Long 2002]**. The HRS intensity is determined by the quadratic nonlinear susceptibility, in contrast to other nonlinear processes like coherent Stokes and anti-Stokes Raman spectroscopy, two-photon absorption which are determined by the cubic nonlinear susceptibility. It is therefore a nonlinear inelastic scattering phenomenon.

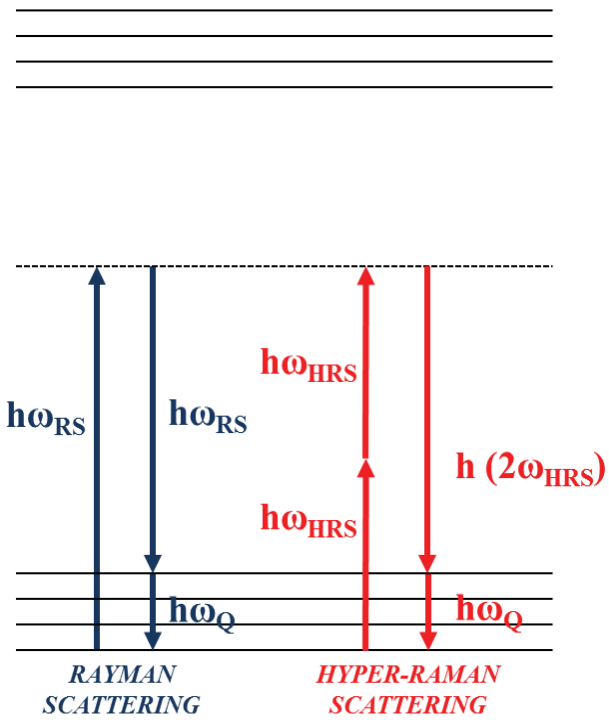

Figure 3.5 Energy level diagrams for Raman and hyper-Raman scatterings (Stokes lines)

Since the hyper-Raman scattering is ruled by different selection rules$\left(\left(\frac{d\beta_{ijk}}{dQ}\right)_{Q=0} \neq 0\right)$ from Raman scattering $\left(\left(\frac{d\alpha_{ij}}{dQ}\right)_{Q=0} \neq 0\right)$ and infrared absorption $\left(\left(\frac{d\mu^{(0)}}{dQ_k}\right)_0 \neq 0\right)$, the hyper-Raman spectroscopy is complementary to IR and Raman. In particular, it can provide information on low-frequency vibrational transitions, which are difficult to detect with the IR and Raman spectroscopies as well as to detect modes that are silent in both IR and Raman spectroscopies **[Cyvin 1965][Christie 1971]**. These peculiarities of HRS selection rules permit one to look at the activity of dipolar modes

(IR active) in any medium. This property is especially important for the study of centrosymmetric media where the dipole modes are forbidden in RS; or studying bulk vibrational polaritons and their effects in centrosymmetric media inaccessible by RS techniques, such as originally used to study bulk vibrational polaritons **[Denisov 1987]**.

HRS has been used for crystal studies of CsBr, CsI and RbI **[Vogt 1976][Vogt 1979]**, $SrTiO_5$ **[Vogt 1976][Inoue 1979][Inoue 1980][Inoue 1981-1][Inoue 1981-2][Vogt 1981]**, $NaNO_3$ **[Vogt 1978]**, NH4Cl **[Savage 1971][Dines 1976]**, NH_4Br **[Long 1979]**, $BaTiO_3$ **[Inoue 1981-2][Vogt 1982]**, NaCI, KC1, KBr, KI and RbI **[Vogt 1985]**, $CaCO_3$ **[Polivanov 1978][Polivanov 1981]**, ZnSe **[Presting 1985]**,CdS **[Polivanov 1979-1][Soobsch 1979][Polivanov 1979-2]**, $KTaO_3$ **[Vogt 1984]**, $KNbO_3$ **[Vogt 1986]**, KC1 and $LiTaO_3$ **[Agalzov 1985]** to obtain the silent modes. It was shown **[Vogt 1981]** that the HRS spectra enables one to define the dielectric function more precisely than from IR spectra because IR reflectivity data are very sensitive to the surface quality/treatment. In contrast, the HRS spectra give information from the volume of the sample negating such limitations. Experimental recording of hyper-Raman spectra in most materials has often been hampered by the weakness of the signal – as evidenced by the significant noise contained in many reported spectra; however recent improvements in the spectral detection and analysis of scattering processes within the last decade (spectrographs with high luminosity efficiencies including CCD detectors), have allowed experimentalists to overcome this intrinsic difficulty **[Rodriguez 2006][Quinet 2004][Quinet 2006][Guimbretière 2008]**. Recent experiments have been done where spontaneous hyper-Raman and Raman scattering together with harmonic light scattering techniques

have been combined to study isotropic materials following a multipolar description of the response of the media **[Rodriguez 2012]**. The observation of TO and LO polar modes using HRS spectroscopy has been described in the literature by Denisov et al. For example in the 90° scattering geometry, four different scattering geometries that only consider linear state of polarizations have been considered. Recently, four new additional scattering geometries that invoke a cross state of polarization (non-degenerate polarization) of the biphotonic excitation have been demonstrated **[Rodriguez 2012]**. These new TO-LO opportunities have been shown in analysis of NaCl crystal and also in silica glass. These techniques open the door to new possibilities in the study of various glass materials.

2.4.2. Experimental use of hyper-Raman/hyper-Rayleigh spectroscopy in the present work

In this section, hyper-Raman/hyper-Rayleigh spectroscopic techniques based on the above principals were employed to examine the role and the impact of glass modifier on the structural vibrational response of the glasses under study. Specifically, these tools were used to understand the variation of hyper-polarizability of the materials.

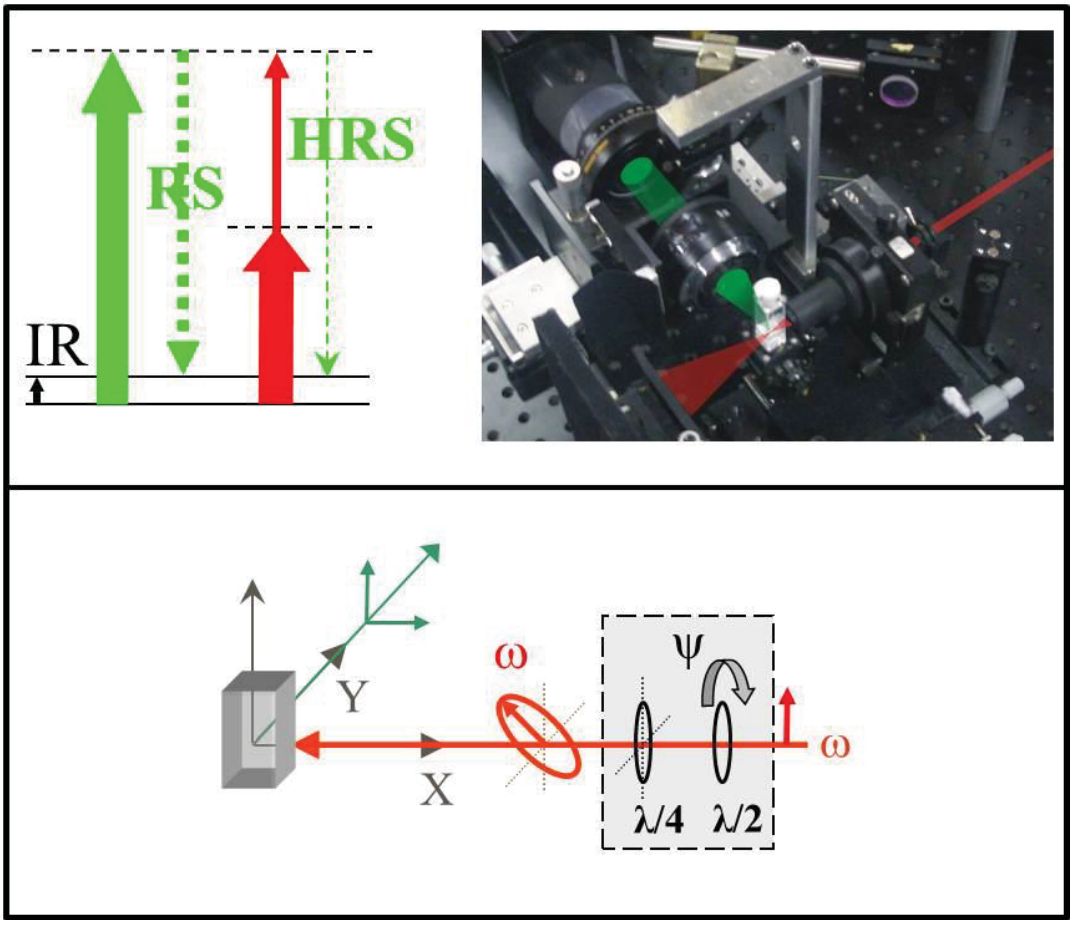

Figure 3.6 (Top) 90° scattering geometry for Raman scattering, hyper-Raman/hyper-Rayleigh scattering. For both processes, the collected signal corresponds to the Stokes lines in the green-red visible range. (Bottom): Schematic of the experimental setup for hyper-Raman in the right angle scattering geometry

The experimental setup discussed in the previous section is able to perform spontaneous Raman scattering (RS) and hyper-Raman/hyper-Rayleigh (HRS or also called harmonic light scattering or HLS) analysis in transparent materials (far from any resonance). Therefore, RS and HRS responses that we consider involve only fully symmetric tensors of normal modes **[Christie 1971]**. For that purpose, the experimental

setup employed in our study has been configured in a classical 90° scattering geometry both for RS and HRS/HLS detection (Figure 3.6 top) and is based on a previous setup **[Rodriguez 2006]** that has been upgraded to optimize the process of collection by using now a picosecond laser (previsouly nanonsecond laser) **[Rodriguez 2012]**. The incident radiation at 1064 nm is obtained from a passively mode-locked Nd:YVO_4 laser (EKSPLA) producing trains of 65 ps pulses, with $\leq 50\,\mu J$ per pulse at a repetition rate of 2 kHz.

In the hyper-Raman/hyper-Rayleigh scheme (Figure 3.6 bottom), we detect the scattered light at the optical frequency $2\omega-\omega_Q$ (Stokes response) from an intense incident laser pulsed at ω, where ω_Q denotes the frequency of a normal mode of vibration Q. Here the incident laser operates at $\lambda = 1064$ nm. The HLS signal, i.e. the quasielastic/elastic component where $\omega_Q \rightarrow 0$, is indicative of the structure of the molecules or elementary structural units (ESU) that constitute the material **[Verbiest 2009]** (in terms of intensity) and the dynamics of its orientation/position **[Maker 1970][Kaatz 1996]** (in terms of width and profile). The direction of the incident radiation is set along the X direction (Figure 3.6) and a rotating half-wave plate controls the rotation of the plane of the incident polarization, giving thus a vertical (V), horizontal (H) or 45° incident polarization. When necessary (only used for hyper-Rayleigh scattering seen in Chapter 4), the introduction of a fixed quarter-wave plate after the half-wave plate gives elliptical or circular states of polarization characterized by the angle ψ (Figure 3.6 bottom). This circular polarization is only useful for hyper-Rayleigh measurement. In hyper-Raman

spectroscopy, the two main polarizations are the parallel VV and the perpendicular HV which give access to the different vibrational responses. The polarized incident laser beam is then focused onto the sample using a 5X Mitutoyo Plan Apo NIR objective (infinity-corrected with NA=0.14) and positioned to pass at a distance of 1–2 mm from the inside of the sample side facing the collecting lens. The incident laser beam waist had a diameter of ca. 10 μm with a Rayleigh range ~200 μm. The scattered light is collected at 90° in the Y direction; it is analyzed either vertically or horizontally by means of a polarizer and then focused with *f* /1.7 optics into a Horiba spectrograph described elsewhere **[Rodriguez 2006]**. The entrance slits of the spectrograph were closed to fit the full beam waist image. The spectrally dispersed light (obtained using an 1800 grooves/mm grating) was detected by a nitrogen cooled CCD camera (2048×512 pixels) in a continuous acquisition mode, with a spectral resolution better than 5 cm^{-1}. Incident radiation with energy less than 5 μJ has been used to probe all samples in the present study since tellurite materials are very sensitive to strong energy pulse that may trigger self-focusing (optical Kerr effect) or laser induced damage, in the material. Hyper-Raman spectra were obtained with acquisition times of 120 s to 240s, depending on the scattering geometry, and repeated up to four times for averaging scans to improve the signal-to-noise ratio.

The scattering geometries used to collect the signal from the sample, as depicted above in Figure 3.6 bottom, are denoted by X(IJK)Y using the extended Porto's notation as defined in the Raman section (section 2.3.1). Here, (J,K) and I denote the polarization directions of the biphotonic excitation and of the scattered light, respectively. Hence, the HV 90°

scattering geometry will be noted X(ZYY)Y thus probing the β_{ZYY} HRS tensor component.

With the theoretical principles of the various spectroscopic techniques used in the present study discussed, and the experimental conditions under which samples were characterized, defined, the following section presents the findings of these experiments made on tellurite crystal and tellurite glass samples introduced in Chapter 2.

3. Vibrational studies of Tellurite materials

To probe the structural properties of a tellurite-based glass, it is first necessary to correctly understand the foundations, namely of the parent network, the crystal of TeO_2. The tellurite crystal is a polymorphic crystal, having four different allotropic phases: α, β, γ and δ **[Beyer 1967][Thomas 1988][Chagraoui 1996][Blanchandin 1999-1][Mirgorodsky 2000]** The difference between those phases has been intensively studied by Noguera **[Noguera 2003-1].** In the present study, we propose a more full evaluation of crystalline materials in the context of a description of the different configurations, to enventually extrapolate to our glassy materials, specific information in terms of structural arrangement.

3.1. TeO_2 crystal

3.1.1. Paratellurite α-TeO_2

The paratellurite phase, α-TeO_2 with space group $P_{4_1 2_1 2_1}$, is from a D_4 (i.e. D_4^4) crystalline class, lacking a center of inversion **[Thomas 1988][Nye 1957]**. The microscopic origin of the properties of paratellurite is not clear, but scientifics generally agree that they are related to the peculiarities in the short range atomic ordering around the tellurium atom. As depicted in the molecular schematic shown in Figure 3.7 (a), the tellurium atoms (blue) in paratellurite have four neighboring oxygen atoms (red) such that the ESU is a TeO_4 disphenoid.

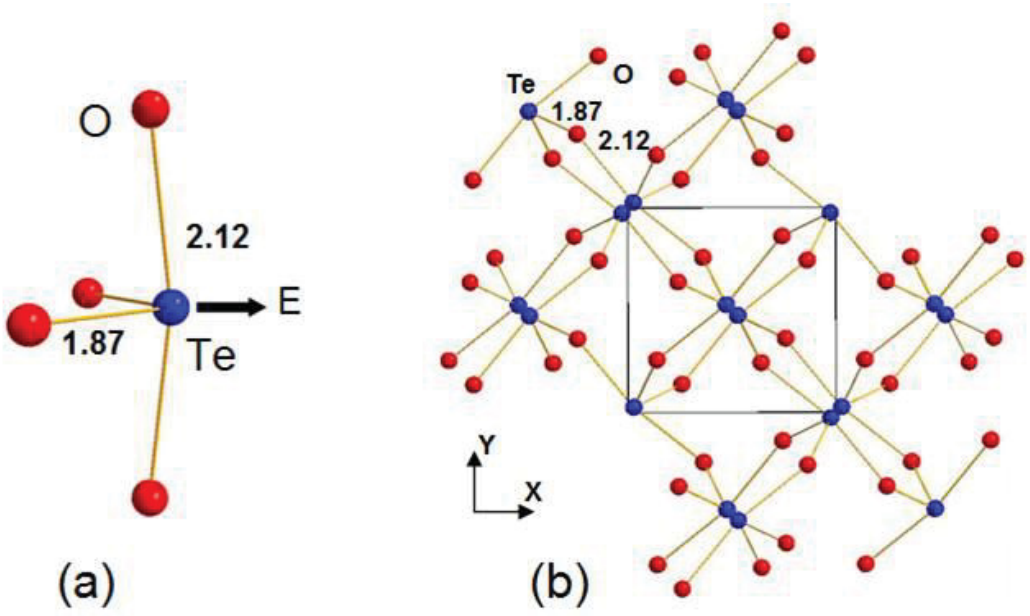

Figure 3.7 Sketch of the disphenoid unit TeO_4E trigonal bipyramid; the arrow visualizes the direction of the lone pair E (a). Projection in the xOy plane of the structure of paratellurite (b)

If we take into accounts the $5s^2$ lone pair of tellurium atom (E), a distorted TeO_4E trigonal bipyramid unit results. In this bipyramid, the two equatorial oxygen atoms O_{eq} are separated from Te by distances (1.878(1) Å) shorter than the sum of the covalent radii of O and Te atoms (2.08 Å), and the two axial oxygen atoms O_{ax} by distances (2.122(1) Å) longer than that value. The α-TeO_2 paratellurite structure thus, is built up from such TeO_4 units sharing corners, as shown in Figure 3.7 (b). This results in the existence of highly asymmetrical Te-$_{eq}O_{ax}$-Te bridges involving one short Te-O_{eq} bond and one long Te-O_{ax} bond, making bond angles of 138.67°. Remarkably, the isolated TeO_2 bent molecule with two Te=O double bonds and with C_{2v} symmetry has a geometry very close to that of the $TeO_{2(eq)}$ grouping in α–TeO_2 **[Thomas 1988][Muenow 1969]**. Hence, from the point of view of crystal chemistry, it can be considered that α–tellurite is a molecular crystal rather than a framework-like one. This point of view is strongly supported by valence force field calculations **[Mirgorodsky 2000][Noguera 2003-1]** and ab initio studies of the vibrational properties of α-TeO_2 **[Ceriotti 2006]**. Therefore, employing this description, the vibrational modes of paratellurite can be classified into internal modes of the TeO_2 "molecules" and "external modes" issued from the "external" rotational and translational degrees of freedom of these entities. The internal modes comprise the symmetric combination of Te-O_{eq} stretching (ν_1), the antisymmetric combination of Te-O_{eq} stretching (ν_3), and the bending mode (ν_2) of the O_{eq}-Te-O_{eq} angle. In the paratellurite unit cell that contains four such molecular units, these internal modes transform as:

$\nu_1: A_1 + B_2 + E$

$\nu_2: A_1 + B_2 + E$

$\nu_3: A_2 + B_1 + E$ **Eq. 3.17**

The calculations of the mode frequencies **[Mirgorodsky 2000][Noguera 2003-1][Ceriotti 2006]** also show that if this description is fully valid for the ν_1 and ν_3 stretching modes occurring in the 500-800 cm^{-1} wavenumber range, no pure ν_2 bending modes can be defined in the range 300-400 cm^{-1} where they are expected. In fact the ν_2 modes are strongly influenced by the Te-O_{ax} force constant and result in vibrations that rather characterize the Te-$_{eq}O_{ax}$-Te bridges **[Mirgorodsky 2000]**. The previously defined "external modes" include the optical modes corresponding to the translational and rotary vibrations of the $TeO_{2(eq)}$ groups with respect to each other, and they are expected to exist in the low wavenumber range below 300 cm^{-1} **[Mirgorodsky 2000][Noguera 2003-1][Ceriotti 2006].**

3.1.2. Tellurite β-TeO_2

The crystal phase β-TeO_2 with space group P_{bca} is from a D_{2h}^{15} crystalline class with cell parameters as a=12.035 Å, b=5.464 Å and c=5.607 Å **[Beyer 1967]**. As described in Figure 3.8 (a), the tellurium atom in the β-TeO_2 crystal is centered into a distorted trigonal bipyramidal unit. Compared to the crystalline geometry for

paratellurite, α-TeO_2, the TeO_4E entity in β-TeO_2 is changed by the absence of both symmetry and equatorial bond distances. Furthermore it is observed here, as an inequality in the two axial bond distances. This results in a different arrangement of the TeO_4E entities, alternatively corner and edge-shared, and so forms folding-leafs, parallel to (100) plane as depicted in (Figure 3.8 (b)). This alternating sequence of corner-sharing / edge-sharing units leads to the presence of both single Te-O-Te and dual $Te <^{O}_{O}> Te$ bond bridges.

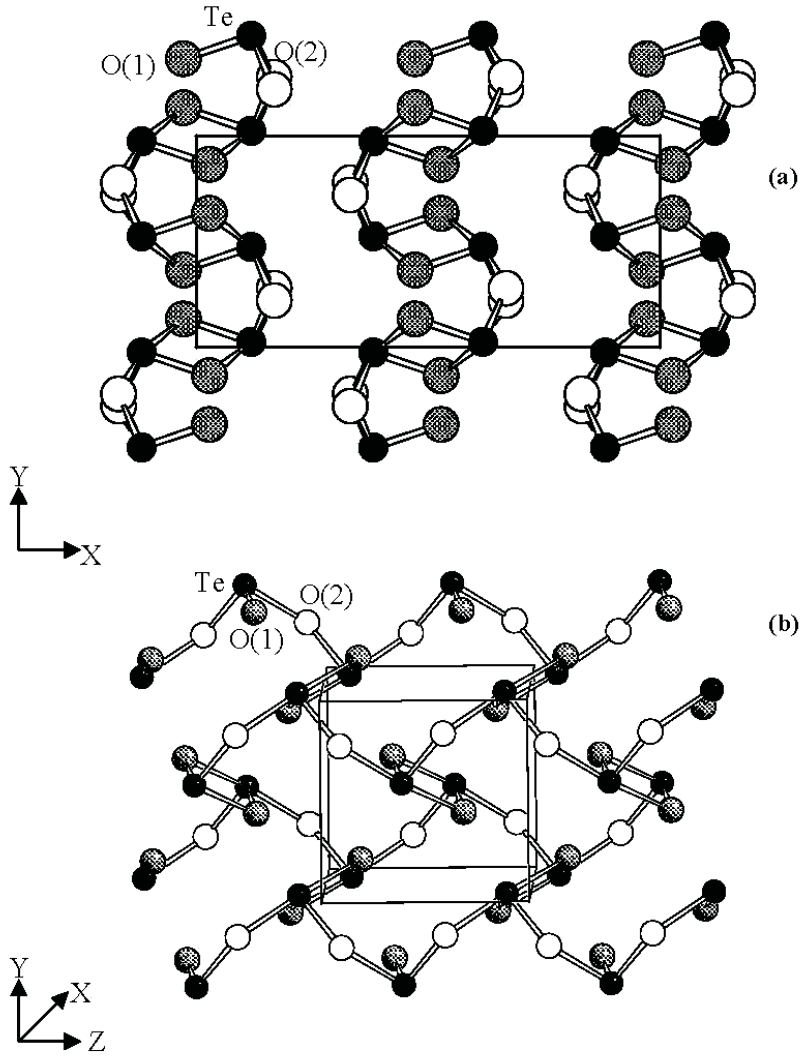

Figure 3.8 Projection of the crystal structure β-TeO_2 in the xOy frame (a), 3D projection of a leaf of β-TeO_2 parallel to (100) plane (b) taken from [Noguera 2003-1]

3.1.3. Tellurite γ-TeO_2

The γ-TeO_2 crystal phase is a metastable phase crystallizing in the orthorhombic system with a $P_{2_12_12_1}$ space group (a=4.898 Å, b=8.574 Å, c=4.351 Å) **[Blanchandin 1999-2][Champarnaud-Mesjard 2000][Blanchandin 1999-1][Blanchandin 2000]**. In this crystal phase, the tellurium atom is localized at the center of a distorded trigonal bipyramidal unit with two equatorial bonds (length, 1.86 Å and 1.94 Å) and two axial bonds (length, 2.02 Å and 2.20 Å). The TeO_4E corner-shared entities arrange in a tridimensional network which possess large pseudo-rectangular tube cavities with the tellurium lone-pair electron E directed to the center of those tubes. These cavities are shown in the shaded regions of the schematic of the γ-TeO_2 crystal, shown in Figure 3.9.

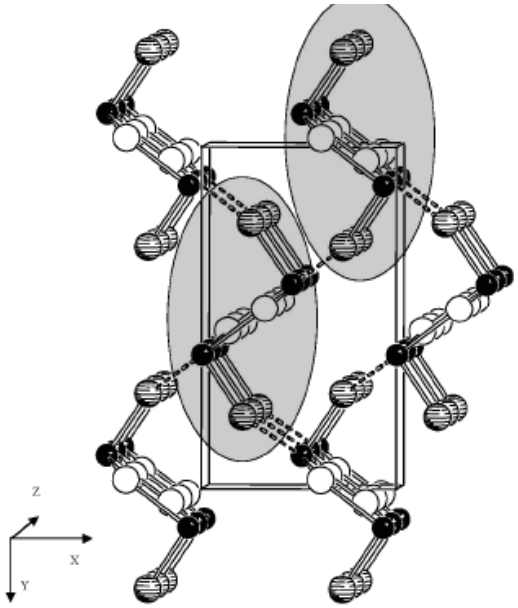

Figure 3.9 Tridimensional projection of the γ-TeO_2 crystal taken from [Noguera 2003-1]

As described by Noguera **[Noguera 2003-1]**, in the shaded regions of Figure 3.9, one of the four Te-O bonds has a distance of 2.20 Å, larger than that of the other three Te-O bonds and too large to be considered as a covalent bond. Thus, the polyhedral units of TeO_3E, are corner-shared and arrange to constitute a helicoidal chain, as show in Figure 3.10.

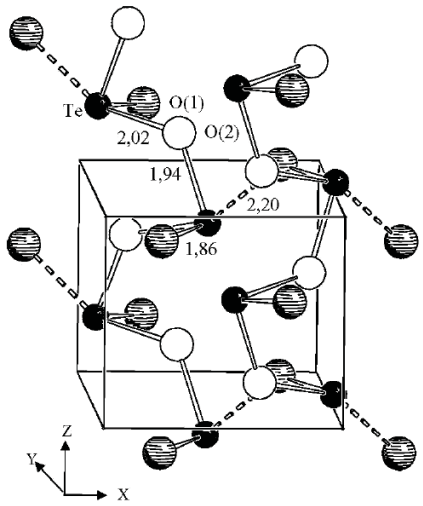

Figure 3.10 Helicoidal chain structure in γ-TeO_2 corresponding to the shaded regions part in Figure 3.9, taken from [Noguera 2003-1]

One can notice that α-TeO_2 and β-TeO_2 phases are built from quasi-similar entities, TeO_4E, where in both systems, these entities are linked by single Te-$_{eq}O_{ax}$-Te bond bridges. The analogy is not complete due to the difference in these bridges. α-TeO_2 possesses identical Te-$_{eq}O_{ax}$-Te bond bridges, while in the β-TeO_2, Te-$_{eq}O_{ax}$-Te bond bridges are both symmetric (1.94 – 2.02 Å) and antisymmetric (1.86 – 2.20 Å). The

formation of the network in β-TeO_2 is more irregular than in α-TeO_2, and this irregularity gives rise to the creation of the resulting helicoidal chains.

3.1.4. Tellurite δ-TeO_2

The δ-TeO_2 crystal phase has been found during investigations of Blanchandin et al. and the single crystalline phase that results from TeO_2-WO_3 and TeO_2-Nb_2O_5 glasses **[Blanchandin 1999-2][Champarnaud-Mesjard 2000][Blanchandin 1999-1][Blanchandin 2000]**. The δ phase has a fluorite-related structure, indexed in the $F_{m\bar{3}m}(O_h^5)$ cubic space group (a=5.691 Å, Z=4). Mirgorodsky et al. define this structure as an intermediate structure between the crystalline and glass states, existing as a superposition of domains of α, β and γ-crystalline phases **[Mirgorodsky 2000]**.

With this background of possible crystalline phases possible within a tellurite matrix, section 3.2 continues the discussion in the context of how these phases can provide insight into interpretation of Raman and hyper-Raman analysis of the candidate tellurite glasses being examined in this study as Raman gain materials.

3.2. Vibrational insights in paratellurite α-TeO_2: a Raman and hyper-Raman study

The paratellurite structure that belongs to the crystalline class D_4 lacks a center of inversion and has been reported to also be potentially optically active **[Nye 1957]**. The TeO_2 single crystals, grown by the Czochralski method using an [110] oriented seed, are

transparent in the entire visible-near infrared range and possess a high refractive index and strongly birefringence. Furthermore, the elastic constants of these single crystals result in an extremely slow [110] shear wave, at the origin of the high pressure phase transition. These characteristics lead to interesting piezoelectric, acousto-optic and nonlinear optical applications as discussed by numerous authors **[Arlt 1968][Schweppe 1970][Uchida 1970][Chemla 1970][Singj 1972].** In addition, as discussed in Chapter 1, TeO_2 is a glass former and tellurite-based glasses have been shown to be promising optical materials based on their structure. For instance their third-order nonlinear susceptibility ($\chi^{(3)}$) is amongst the highest ever obtained in oxide glasses (more than forty times higher than silica-based glasses measured in a non-resonant regime) **[Stegeman 2003].** Also, these glasses, they can be modified from their initial centrosymmetric state via thermal poling to become efficient frequency conversion (doublers) materials **[Lasbrugnas 2009]**. Infrared spectroscopy (IR) and Raman scattering (RS) have been widely used techniques to characterize the short-range and medium-range structure of amorphous materials **[Guery 2012]**, and in this context, the precise knowledge of the vibrational spectra of the related crystalline phases is a necessary prerequisite to model the structure and properties of the glassy state.

In the present case, only a few publications have investigated the IR and RS studies of α-TeO_2 single crystals **[Krauzman 1971][Ayrault 1972][Pine 1972][Korn 1973][Syrbu 1996]**. It has been found that discrepancies exist between the different authors in the assignment of the observed vibrational modes. On the one hand, the interpretation of the IR data depended on the accuracy of the reflectivity measurements

and also on the model of dielectric function adopted to fit the spectra. On the other hand, the Raman data were influenced by the strong optical activity of paratellurite **[Mamedov 2003]** that perturbed in an uncontrolled manner, the polarization properties of the incident and scattered lights, resulting in the observation of "anomalous polarization-selection-rules violations" **[Pine 1972]** that made insecure the interpretation of the spectra. For these reasons, the current effort chose to re-examine this material in an effort to have a firm basis on which to compare our tellurite based glass samples.

In this section, the Raman spectra of paratellurite are revisited. We show that it is possible to eliminate the influence of the optical activity in the plane perpendicular to the four fold axis, and to then correctly interpret the remaining pre-defined "anomalous polarization-selection-rules violations" due to the optical activity along the unique axis. Also, we present for the first time, results on the hyper-Raman scattering (HRS) spectra of paratellurite that complements the IR and RS data. These data have been used as reference for further measurements on the optical and spectroscopic properties of tellurite-based glasses.

3.2.1. Symmetry properties of paratellurite

As discussed in section 3.1.1., the paratellurite crystal (α-TeO_2) belongs to the $P4_12_12$ - D_4^4 space group. The primitive unit cell contains four formula units, with the tellurium atoms in positions 4(a) (x, x, 0) and the oxygen atoms in general positions 8(b) (x, y, z) **[Thomas 1988].** This results in 33 optical phonon branches with Γ-point

symmetries $4A_1 + 4A_2 + 5B_1 + 4B_2 + 8E$. The three acoustic modes of zero frequency at the zone-center belong to $A_2 + E$ symmetry. The singlet A_2 modes are infrared active in the extraordinary ray spectrum and the doublet E modes are infrared active in the ordinary ray spectrum. The A_1 ,B_1, B_2 and E modes are Raman active, while the A_2, B_1, B_2 and E modes are hyper-Raman active. Note that the A_2 and E polar modes exhibit TO-LO splitting in the close vicinity of the Brillouin zone center, which is probed by the IR, RS and HRS techniques. For the D_4 point group, the Raman and hyper-Raman tensors of the different symmetry types in the Oxyz frame (where Ox is parallel to the [100] crystallographic direction, Oy is parallel to [010] and Oz is parallel to [001]) are of the form expressed below **[Christie 1971][Cyvin 1965][Denisov 1987][Loudon 1964]:**

Raman tensor:

$$A_1:\begin{pmatrix}\alpha & 0 & 0\\ 0 & \alpha & 0\\ 0 & 0 & \beta\end{pmatrix},\quad B_1:\begin{pmatrix}\gamma & 0 & 0\\ 0 & -\gamma & 0\\ 0 & 0 & 0\end{pmatrix},\quad B_2:\begin{pmatrix}0 & \delta & 0\\ \delta & 0 & 0\\ 0 & 0 & 0\end{pmatrix}$$

$$E_x:\begin{pmatrix}0 & 0 & 0\\ 0 & 0 & \varepsilon\\ 0 & \varepsilon & 0\end{pmatrix},\quad E_y:\begin{pmatrix}0 & 0 & -\varepsilon\\ 0 & 0 & 0\\ -\varepsilon & 0 & 0\end{pmatrix} \qquad \textbf{Eq. 3.18}$$

Hyper-Raman tensor:

$$A_{2,z}:\begin{pmatrix}0&0&0&0&\beta&0\\0&0&0&\beta&0&0\\\beta&\beta&\alpha&0&0&0\end{pmatrix},\qquad B_1:\begin{pmatrix}0&0&0&\gamma&0&0\\0&0&0&0&\gamma&0\\0&0&0&0&0&\gamma\end{pmatrix}$$

$$B_2:\begin{pmatrix}0&0&0&0&\delta&0\\0&0&0&-\delta&0&0\\\delta&-\delta&0&0&0&0\end{pmatrix}\qquad \textbf{Eq. 3.19}$$

$$E_x:\begin{pmatrix}\varepsilon&\eta&\mu&0&0&0\\0&0&0&0&0&\eta\\0&0&0&0&\mu&0\end{pmatrix},\qquad E_y:\begin{pmatrix}0&0&0&0&0&\eta\\\eta&\varepsilon&\mu&0&0&0\\0&0&0&\mu&0&0\end{pmatrix}$$

The strong optical activity along the three principal crystallographic directions leads to an important perturbation in the polarization-selection-rules in Raman scattering experiments **[Pine 1972].** For crystal class 422 (D_4), the non-zero components of the spontaneous gyration pseudo-tensor are $g_{11} = g_{22}$ ($g_\perp$) and g_{33} ($g_{//}$) **[Nye 1957][Kopsky 1979]** and according to Mamedov *et al.* **[Mamedov 2003]** the absolute value of $g_{//}$ is twice as that of $g_\perp$, with $g_{//}$ positive and $g_\perp$ negative in α-TeO_2.

In order to minimize the effect of the optical activity in the Oxy plane, we have prepared a crystal in the form of a parallel-piped (9.0x6.5x6 mm^3) with surfaces polished and cut perpendicular to the crystallographic [110], $[1\bar{1}0]$ and [001] directions respectively, checked by a Laue analysis. It can be shown for the crystalline class D_4 that the [110] and $[1\bar{1}0]$ directions are very less sensitive in the Oxy plane **[Kaminsky 1993][Rodriguez 2008]**, so that no effective optical activity is expected for incident or scattered light

propagating in these directions. Under these conditions, we are left with the optical activity occurring along [001] related to g_{33}. So, in the new Ox'y'z frame (Ox' is set parallel to [110], Oy' parallel to $[1\bar{1}0]$ and Oz parallel to [001]) as shown in Figure 3.11.

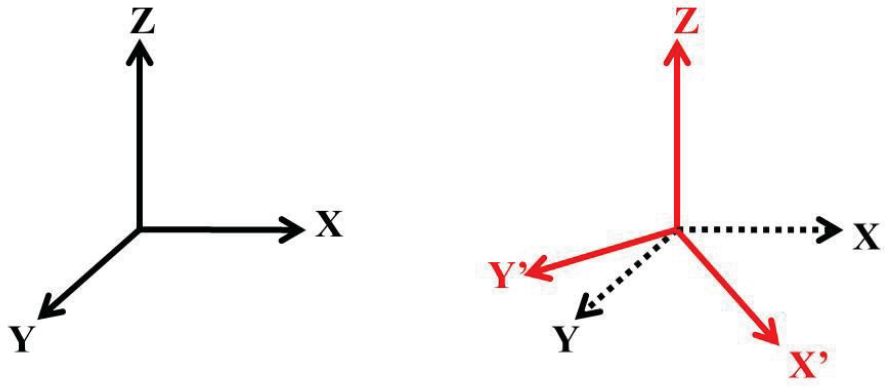

Figure 3.11 Oxyz frame to Ox'y'z frame

From this analysis, the Raman and hyper-Raman tensors become:

Raman tensor:

$$A_1:\begin{pmatrix}\alpha & 0 & 0\\ 0 & \alpha & 0\\ 0 & 0 & \beta\end{pmatrix},\qquad B_1:\begin{pmatrix}0 & -\gamma & 0\\ -\gamma & 0 & 0\\ 0 & 0 & 0\end{pmatrix},\quad B_2:\begin{pmatrix}\delta & 0 & 0\\ 0 & -\delta & 0\\ 0 & 0 & 0\end{pmatrix}$$

$$E_x:\frac{1}{\sqrt{2}}\begin{pmatrix}0 & 0 & \varepsilon\\ 0 & 0 & \varepsilon\\ \varepsilon & \varepsilon & 0\end{pmatrix},\qquad E_y:\frac{1}{\sqrt{2}}\begin{pmatrix}0 & 0 & -\varepsilon\\ 0 & 0 & \varepsilon\\ -\varepsilon & \varepsilon & 0\end{pmatrix} \qquad \textbf{Eq. 3.20}$$

Hyper-Raman tensor:

$$A_{2,z}:\begin{pmatrix}0&0&0&0&\beta&0\\0&0&0&\beta&0&0\\\beta&\beta&\alpha&0&0&0\end{pmatrix},\qquad B_1:\begin{pmatrix}0&0&0&0&\gamma&0\\0&0&0&-\gamma&0&0\\\gamma&-\gamma&0&0&0&0\end{pmatrix}$$

$$B_2:\begin{pmatrix}0&0&0&-\delta&0&0\\0&0&0&0&-\delta&0\\0&0&0&0&0&-\delta\end{pmatrix}$$

$$E_x:\frac{\sqrt{2}}{4}\begin{pmatrix}(\varepsilon+3\eta)&(\varepsilon-\eta)&2\mu&0&0&-(\varepsilon-\eta)\\-(\varepsilon-\eta)&-(\varepsilon+3\eta)&-2\mu&0&0&(\varepsilon-\eta)\\0&0&0&-2\mu&2\mu&0\end{pmatrix}$$

$$E_y:\frac{\sqrt{2}}{4}\begin{pmatrix}(\varepsilon+3\eta)&(\varepsilon-\eta)&2\mu&0&0&(\varepsilon-\eta)\\(\varepsilon-\eta)&(\varepsilon+3\eta)&2\mu&0&0&(\varepsilon-\eta)\\0&0&0&2\mu&2\mu&0\end{pmatrix}$$

Eq. 3.21

3.2.2. Results of Raman and hyper-Raman scatterings on paratellurite crystal

For the RS and HRS measurements, we have used different right angle and backscattering geometries so as to set the momentum transfer vector K_Q(i. e. the direction of propagation of the excited phonon modes) either parallel or perpendicular to the four-fold optical axis Oz. Under those conditions, we were able to observe and to discriminate the pure TO and LO components of the polar modes with A_2 and E symmetries. Note that we have adopted a logarithmic scale for the intensities of RS and HRS spectra in order to enhance the presence of low intensity but real signals.

3.2.2.1. Raman scattering of paratellurite

Raman spectra for paratellurite crystal are reported in Figures 3.12, 3.13 and 3.14; and band assignments for the crystal are summarized in Table 3.1.

Figure 3.12 shows the Raman spectra obtained in a back scattering geometry where the directions of the incident and scattered lights are both set parallel to X', so that the momentum transfer vector $\boldsymbol{K_Q}$ is set perpendicular to the Oz four-fold axis. The $X'(ZZ)\overline{X}'$ spectrum corresponds to the A_1 modes (α_{zz}), the $X'(Y'Y')\overline{X}'$ spectrum corresponds to the A_1 and B_2 modes ($\alpha_{y'y'}$) and the $X'(ZY')\overline{X}'$ spectrum corresponds to the E polar modes ($\alpha_{zy'}$). In the latter case, only the LO components are allowed **[Krauzman 1971][Porto 1966][Loudon 1964]**. Very clearly, these spectra do not show any significant polarization leakage. Three A_1 modes out of the four expected ones are observed at 148, 393 and 648 cm^{-1} on the $X'(ZZ)\overline{X}'$ spectrum.

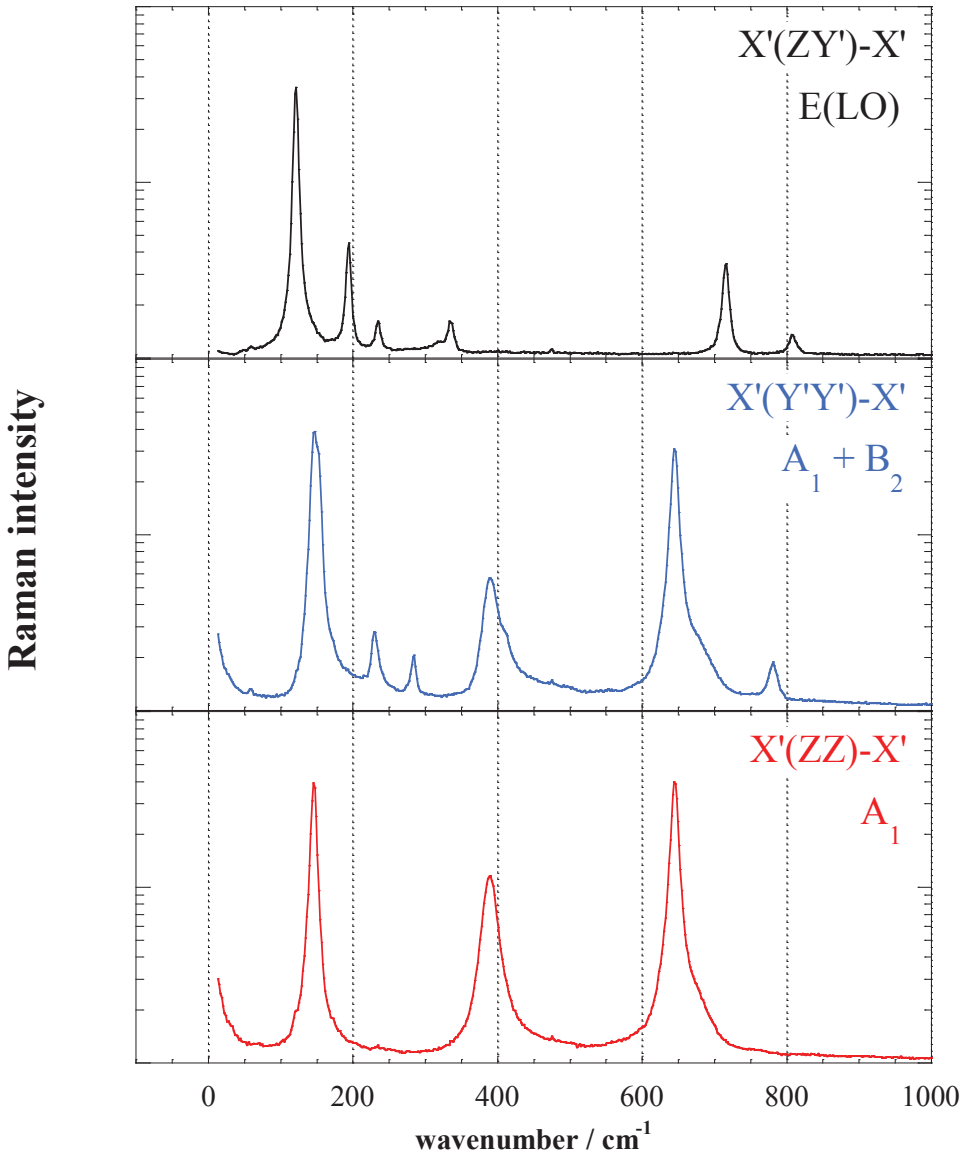

Figure 3.12 Polarized Raman spectra of paratellurite crystal in the backscattering geometry (Raman intensity in log scale)

According to section 3.2.1., the mode of highest wavenumber at 648 cm^{-1} is assigned to the A_1 component of the ν_1 mode of the $TeO_{2(eq)}$ groups (Eq. 3.15) and that at 393 cm^{-1} is assigned to a vibration of the Te-O-Te bridges assigned to ν_2. The remaining low wavenumber mode is then assigned to an external mode. On the $X'(Y'Y')\bar{X}'$ spectrum, in addition to the A_1 modes previously identified, four modes are clearly observed at 233, 287, 415 and 784 cm^{-1} together with an additional unresolved shoulder at *ca.* 150 cm^{-1} on the high wavenumber side of the strong A_1 mode at 148 cm^{-1}. We note that the 233 cm^{-1} line is already present as an extremely weak signal on the $X'(ZZ)\bar{X}'$ spectrum. So, in agreement with the *ab initio* calculations referred to earlier **[Ceriotti 2006]** and a previous Raman study of the crystal by Krauzman **[Krauzman 1971]**, we assign this line to the fourth expected A_1 mode corresponding to an external mode. The four remaining lines at 150 cm^{-1} (shoulder), 287, 415 and 784 cm^{-1} are assigned to the four expected B_2 modes. The mode of highest wavenumber (784 cm^{-1}) is assigned to the B_2 component of the ν_1 mode of the $TeO_{2(eq)}$ groups (Eq.3.15), that at 415 cm^{-1} is assigned to a vibration of the O-Te-O bridges issued from ν_2, and the two remaining low wavenumber modes are assigned to external vibrations. The $X'(ZY')\bar{X}'$ (Figure 3.12) and $X'(Y'Z)\bar{X}'$ (not shown) spectra are identical and display six E (LO) modes (out of the eight expected ones) at 122, 195, 235, 336, 717 and 809 cm^{-1}. The two modes of highest wavenumber (717 and 809 cm-1) are assigned to the two expected E (LO) components of the ν_1 and ν_3 modes of the $TeO_{2(eq)}$ groups, the mode at 336 cm^{-1} is assigned to a mode of the Te-O-Te bridges issued from ν_2 and the remaining three lines are assigned to external vibrations.

Figure 3.13 shows the Raman spectra obtained in a right angle scattering geometry where the direction of the 532 nm incident excitation light is set parallel to X' and that of the scattered light is set parallel to Y', so that the momentum transfer vector K_Q is set perpendicular to the Oz four-fold axis as in the previous geometry.

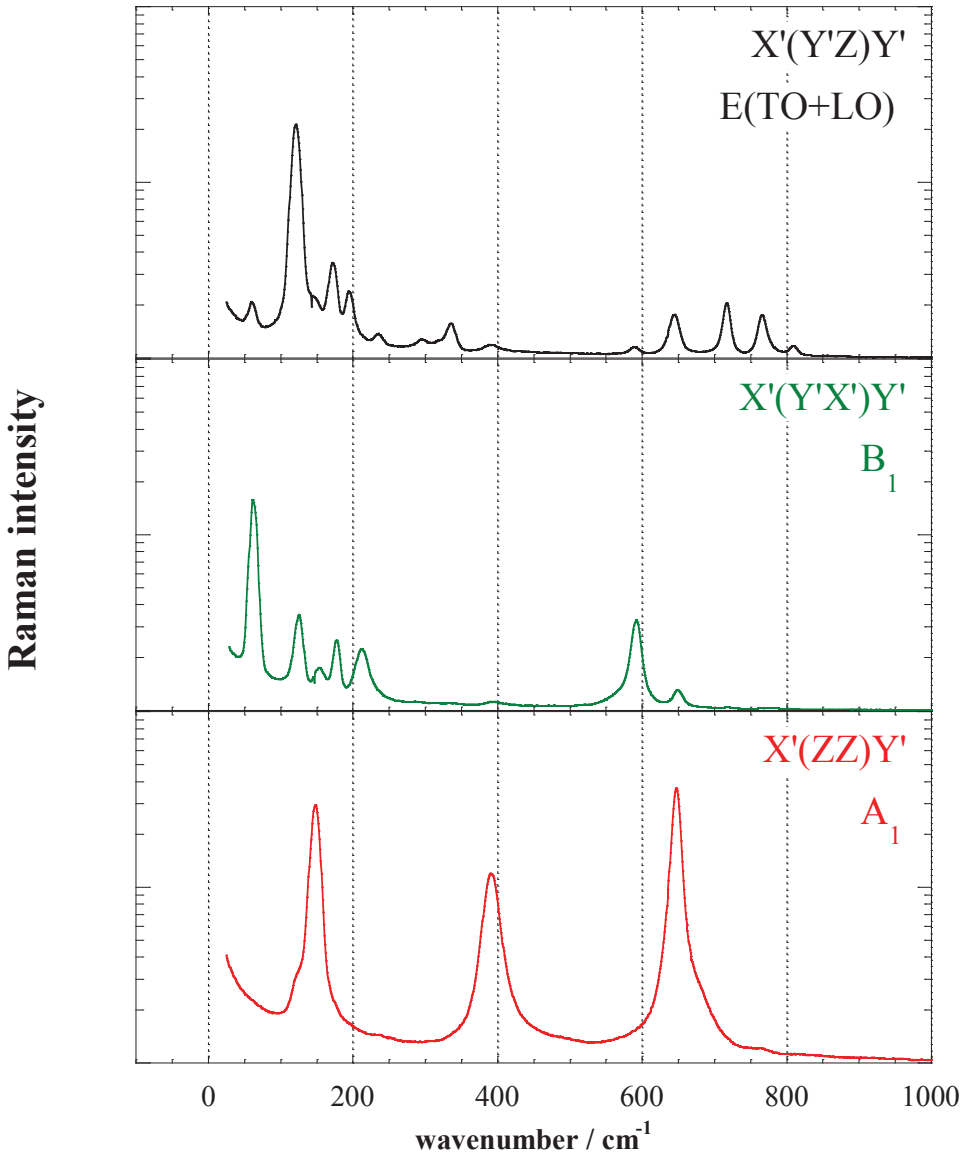

Figure 3.13 Polarized Raman spectra of paratellurite crystal in the right angle geometry (Raman intensity in log scale)

The $X'(ZZ)Y'$ spectrum corresponds to the A_1 modes (α_{zz}), the $X'(Y'X')Y'$ spectrum corresponds to the B_1 modes ($\alpha_{y'x'}$) and the $X'(ZY')Y'$ spectrum corresponds to the E polar modes ($\alpha_{y'z}$). In this configurations both TO and LO components of the E modes are now allowed. Again, the polarization leaks are very weak. As expected, the A_1 $X'(ZZ)Y'$ spectrum is identical to the $X'(ZZ)\bar{X}'$ spectrum previously described. The $X'(Y'X')Y'$ spectrum reveals the five expected B_1 modes, localized at 62, 125, 177, 210 and 590 cm^{-1}. This latter peak can be assigned to the B_1 component of the ν_3 mode of the $TeO_{2(eq)}$ groups (Eq. 3.15) and the other ones occurring at low wavenumber should be assigned to external vibrations. When comparing the $X'(Y'Z)Y'$ spectrum due to E (TO+LO) (Figure 3.13) with the E (LO) spectrum shown in Figure 3.12, we localize seven E (TO) modes (out of the eight expected ones) at 122, 173, 296, 336, 392, 646 and 767 cm^{-1}. Hence, the modes at 646 and 767 cm^{-1} are assigned to the E (TO) counterparts of the ν_1 and ν_3 E (LO) modes already observed at 717 and 809 cm^{-1} in back scattering geometry (Figure 3.12).

Figure 3.14 shows the Raman spectra obtained in a back scattering geometry where the direction of the incident and of the scattered lights are both set parallel to the Z axis, so that the K_Q vector is now directed parallel to the four-fold axis. The $Z(Y'X')\bar{Z}$ ($\equiv Z(X'Y')\bar{Z}$) spectrum is supposed to correspond to B_1 modes ($\alpha_{y'x'}$) (already shown in Figure 3.13) and the $Z(Y'Y')\bar{Z}$ ($\equiv Z(X'X')\bar{Z}$) spectrum is supposed to correspond to the $A_1 + B_2$ modes ($\alpha_{y'y'}$) (already shown in Figure 3.12 and reported also in Figure 3.14 for comparison). In fact, the $Z(Y'X')\bar{Z}$ and $Z(Y'Y')\bar{Z}$ spectra are identical within the limit of

experimental accuracy, due to quasi perfect mixing of polarizations owing to the strong optical activity of paratellurite acting on both the incident and scattered lights propagating along the four-fold axis, so resulting in a quasi-perfect mixing of the $A_1 + B_2$ ($\alpha_{y'y'}$) and B_1 ($\alpha_{x'y'}$) spectra.

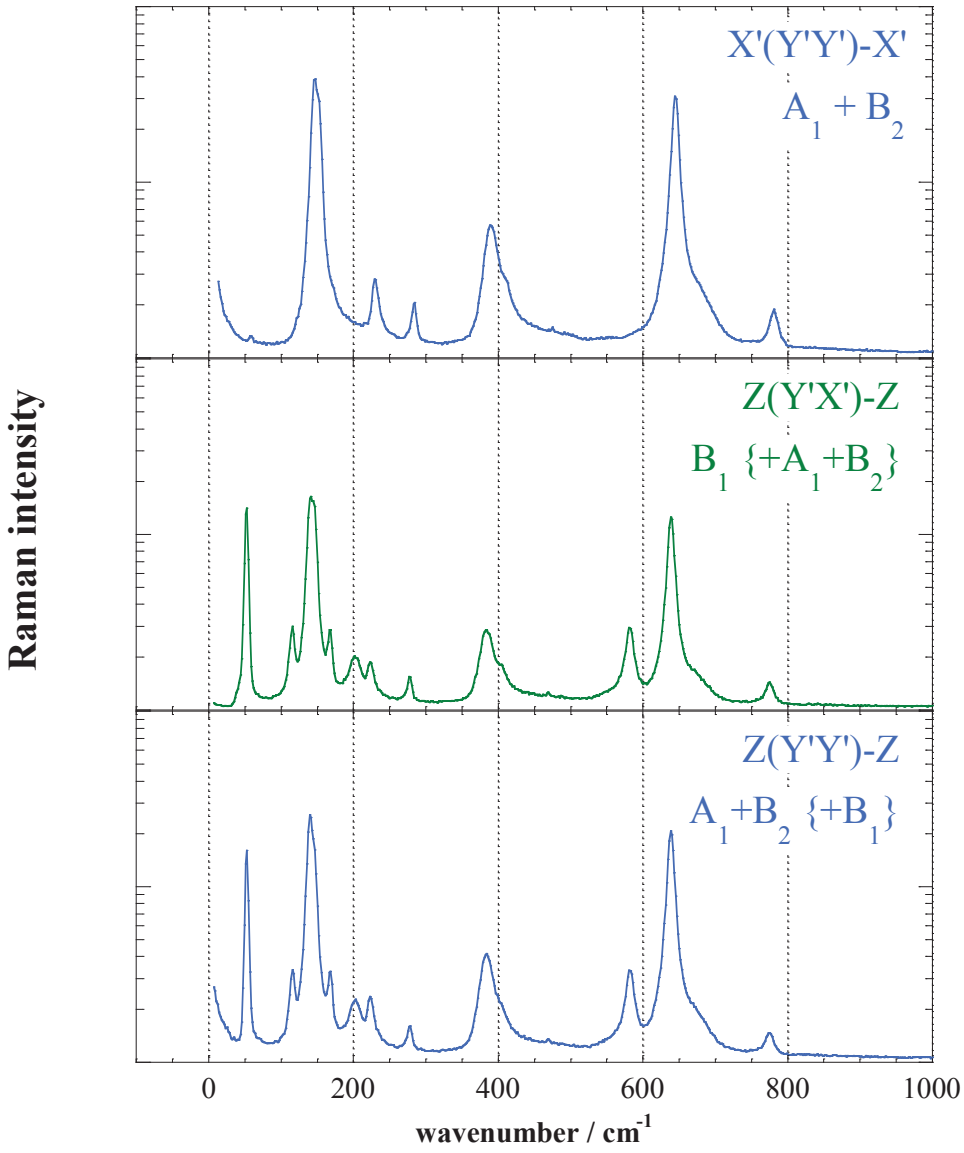

Figure 3.14 Polarized Raman spectra of paratellurite crystal in the backscattering geometry (Raman intensity in log scale)

To summarize our Raman data, all expected A_1, B_1 and B_2 modes have been clearly identified and also, seven E (TO) and six E (LO) modes have been assigned out of the eight expected pairs of E modes (Table 3.1). Note also that the *ab initio* calculations **[Ceriotti 2006]** generally fit nicely with our interpretation of the Raman spectra, with some minor differences in the peak positions.

	A_1 (3/4)	A_2 (TO) (4/4)	B_2 (4/4)	B_1 (5/5)	E (TO) (7/8)	E (LO) (7/8)
X'(ZZ)-X': A_1	148, 393, 648	-	-	-	-	-
X'(ZY')-X': E(LO)	-	-	-	-	-	122, 195, 235, 336, 717, 809
X'(Y'Y')-X': A_1 + B_2	148, 393, 648	-	233, 276, 415, 784	-	-	-
Z(Y'Y')-Z: A_1 + B_2 {+B_1}	148, 393, 648	-	233, 276, 415, 784	62, 125, 177, 210, 590	-	-
Z(Y'X')-Z: B_1 {+A_1 + B_2}	148, 393, 648	-	233, 276, 415, 784	62, 125, 177, 210, 590	-	-
X'(ZZ)Y': A_1	148, 393, 648	-	-	-	-	-
X'(Y'Z)Y': E (TO+LO)	-	-	-	-	122, 173, 296, 392, 646, 767	122, 196, 236, 337, 718, 811
X'(Y'X')Y': B_1	-	-	-	62, 125, 177, 212, 590	-	-
X'(ZX')Y': E (TO+LO)	-	-	-	-	122, 173, 297, 336, 392, 645, 766	122, 195, 235, 718, 809

Table 3.1 Raman spectroscopy - wavenumber assignments (cm^{-1}) [± 2 cm^{-1}] for paratellurite crystal

3.2.2.2. Hyper-Raman scattering of paratellurite crystal

To the best of our knowledge, no prior investigation on the hyper-Raman scattering of paratellurite crystal has been previously reported. We present in Figure 3.15 the first study on hyper-Raman scattering performed on paratellurite and corresponding band assignments from these spectra, have been summarized in Table 3.2.

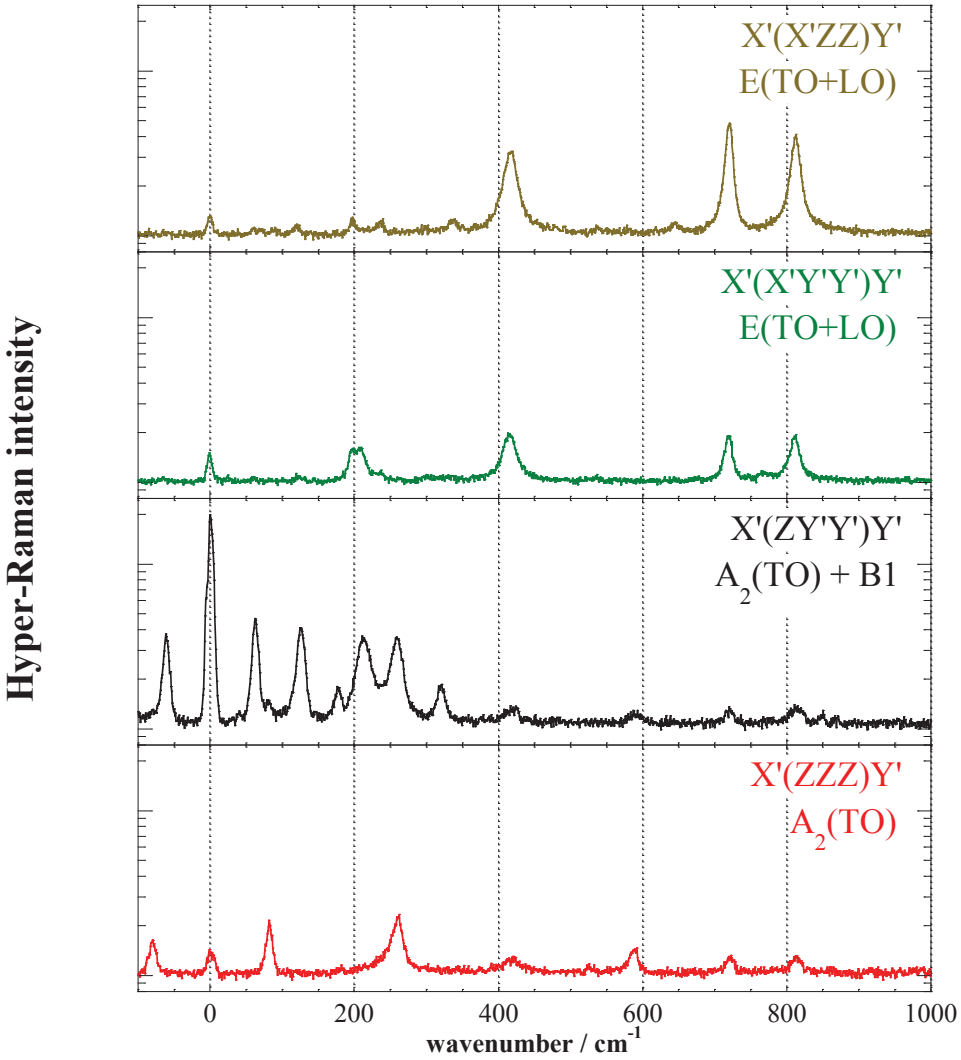

Figure 3.15 Polarized hyper Raman spectra of paratellurite crystal in the right angle geometry

As in previous Raman measurements, we have adopted a right angle scattering geometry where the direction of the incident λ= 1064 nm excitation light is set parallel to X' and that of the scattered light is set parallel to Y', so that the momentum transfer vector K_Q is set perpendicular to the Oz four-fold axis. Hence, the $X'(ZZZ)Y'$ spectrum corresponds

to the A_2 (TO) polar modes (β_{zzz}), the $X'(ZY'Y')Y'$ spectrum corresponds to the A_2 (TO) and B_1 modes ($\beta_{zy'y'}$) and the $X'(X'Y'Y')Y'$ and $X'(X'ZZ)Y'$ spectra both correspond to the E (TO + LO) modes ($\beta_{x'y'y'}$ and $\beta_{x'zz}$ respectively) **[Christie 1971][Cyvin 1965][Denisov 1987]**. Three A_2 (TO) modes are clearly identified on the $X'(ZZZ)Y'$ spectrum at 82, 262 and 592 cm^{-1} (Figure 3.15). All five B_1 modes already identified on the Raman spectra are observed on the $X'(ZY'Y')Y'$ spectrum and the fourth expected A_2 (TO) mode is also identified at 321 cm^{-1} on this spectrum (Figure 3.15). Following the arguments developed in section 2, the A_2 (TO) mode at 592 cm^{-1} is assigned to the expected A_2 component of the ν_3 mode of the $TeO_{2(eq)}$ groups (Eq. 3.15). The $X'(X'Y'Y')Y'$ and $X'(X'ZZ)Y'$ HRS spectra (Figure 3.13) reveal most of the E (TO) and E (LO) modes already identified on the RS spectra, but also exhibit two new lines at 207 and 418 cm^{-1} that cannot be seen on the RS spectra. According to published IR data **[Krauzman 1971][Ayrault 1972][Korn 1973][Syrbu 1996]**, the line at 207 cm^{-1} most likely corresponds to a TO mode and that at 418 cm^{-1} corresponds to a LO mode.

In the four hyper-Raman spectra reported in Figure 3.15 we observe a weak or strong (*X'(ZY'Y')Y'* spectrum) elastic contribution corresponding to harmonic light scattering. However, no HLS is expected under the Kleinman condition since all the components of the symmetric part for the A_1 symmetry are zero **[Christie 1971][Cyvin 1965]**.

To summarize our HRS data, all expected A_2 (TO) and B_1 modes have been detected and identified, and the combined RS and HRS spectra exhibit the eight expected E (TO) modes and seven E (LO) modes (Table 3.2). For the polar A_2 and E modes, there is good agreement between the wavenumbers determined by RS and HRS for the E modes, but we notice marked differences between our data and published IR data, which themselves do not agree. This can be explained by the fact that RS and HRS techniques provide direct response functions of the TO and LO modes, whereas this information must be extracted from the IR reflectivity spectrum via a Kramers-Kronig analysis (not used in the cited works) and/or by fitting the reflectivity data using phenomenological dielectric functions; thus, in this case, the wavenumbers and widths of the TO and LO modes are introduced as adjustable parameters. Note that additional hyper-Raman spectra have been performed at right angle geometry but with the four-fold axis in the plane of incidence (not shown). For both possible configurations, i.e. where the c axis is perpendicular either to the input (case 1) or output (case 2) side, we observed also perfect mixing of polarization, as observed in Raman scattering (Figure 3.14), owing to the strong optical rotation of light along the c axis at ω for case 1 and 2ω for case 2.

	A_1 (3/4)	A_2 (TO) (4/4)	B_2 (4/4)	B_1 (5/5)	E (TO) (7/8)	E (LO) (7/8)
X'(ZZZ)Y' : A_2(Z) TO	-	82, 262, 592	-	-	Leak of polarization	Leak of polarization
X'(ZY'Y') Y': A_2(Z) TO + B_1	HLS	82, 262, 321, 592	-	62, 125, 176, 212, 592	Leak of polarization	Leak of polarization
X'(X'ZZ) Y': E (TO+LO)	-	-	-	-	122, 645	122, 197, 239, 337, 418, 720, 812
X'(X'Y'Y')Y': E (TO+LO)	-	-	-	-	122, 207, 764	122, 197, 239 , 418, 720, 812

Table 3.2 Hyper Raman spectroscopy - wavenumber assignments (cm^{-1}) [± 2 cm^{-1}] of paratellurite crystal

Through this detailed Raman and hyper-Raman scattering study for paratellurite crystal, crystal vibrational modes can be related to vibrational modes present in the glassy state. These structural data discussed in section 3.2.2., are results to analyze the structural organization of the multicomponent tellurite glasses in our study. It is our objective to understand the role of this structural organization and how it directly relates to the observed linear and nonlinear optical properties of our glasses, to more fully understand the underlying origin of the observed Raman gain behavior.

4. Extended vibrational studies (IR, RS and HRS) of TeO_2-$TaO_{5/2}$-ZnO glass network

An extended vibrational analysis, combining the IR, RS and HRS spectroscopic techniques discussed above, will provide an opportunity to better understand the local

structure of the glass matrix. Hence, a goal is to be able to tune the glass composition to optimize its structure with respect to the desired optical property and eventual application.

Figure 3.16 illustrates the IR (a), RS (b) and HRS (c) spectra of the studied glasses. The vibrational features of all these different techniques are dominated by the structural features of the tellurite network but include influences on that structure, introduced through the addition of the modifiers, Ta and Zn. The two series of composition for the binary and ternary glasses, respectively, exhibit similar IR/HRS and RS spectra, with an intense (weaker) band present at 610 cm^{-1} in IR (HRS), a shoulder (intense band) at higher wavenumber (~720-830 cm^{-1}) seen in both IR and RS (HRS) and a large envelope and intense envelope at lower wavenumber with an apparent maximum at 300 cm^{-1} in IR (and also HRS) and 450 cm^{-1} in RS. The glass' IR spectra contain the contribution of dipolar modes (see section 2.2.1). HRS spectra for the glasses are also dominated by the dipolar contribution of vibrational modes, while their octupolar contribution seen to a lesser extent, in the spectra. Here, we have a perfect illustration of the respective activity of IR and HRS which provide the same spectral information but with quite different intensities of the resulting bands. The strongest IR band at ~610 cm^{-1} (Figure 3.16) is clearly weaker in the glass' HRS spectra (Figure 3.16 right). In contrast, the strongest HRS band at ~720-830 cm^{-1} appears as a mere shoulder in the material's IR spectra. In the HRS spectra (Figure 3.16), we can clearly see the strong effect of the glass modifiers which not only affects the global intensity of the spectra but also the relative intensities of the bands; the addition of Zn is extremely pronounced in the HRS spectra. As can be

observed, the IR spectra are clearly less affected by the modifiers, as shown in Figure 3.16. Note that IR reflectivity spectra are very sensitive to the quality of the interface that may modify the obtained IR intensity though the Kramers-Kronig treatment. The HRS and RS spectra are unaffected by surface effect since the signal comes from a volume inside the material.

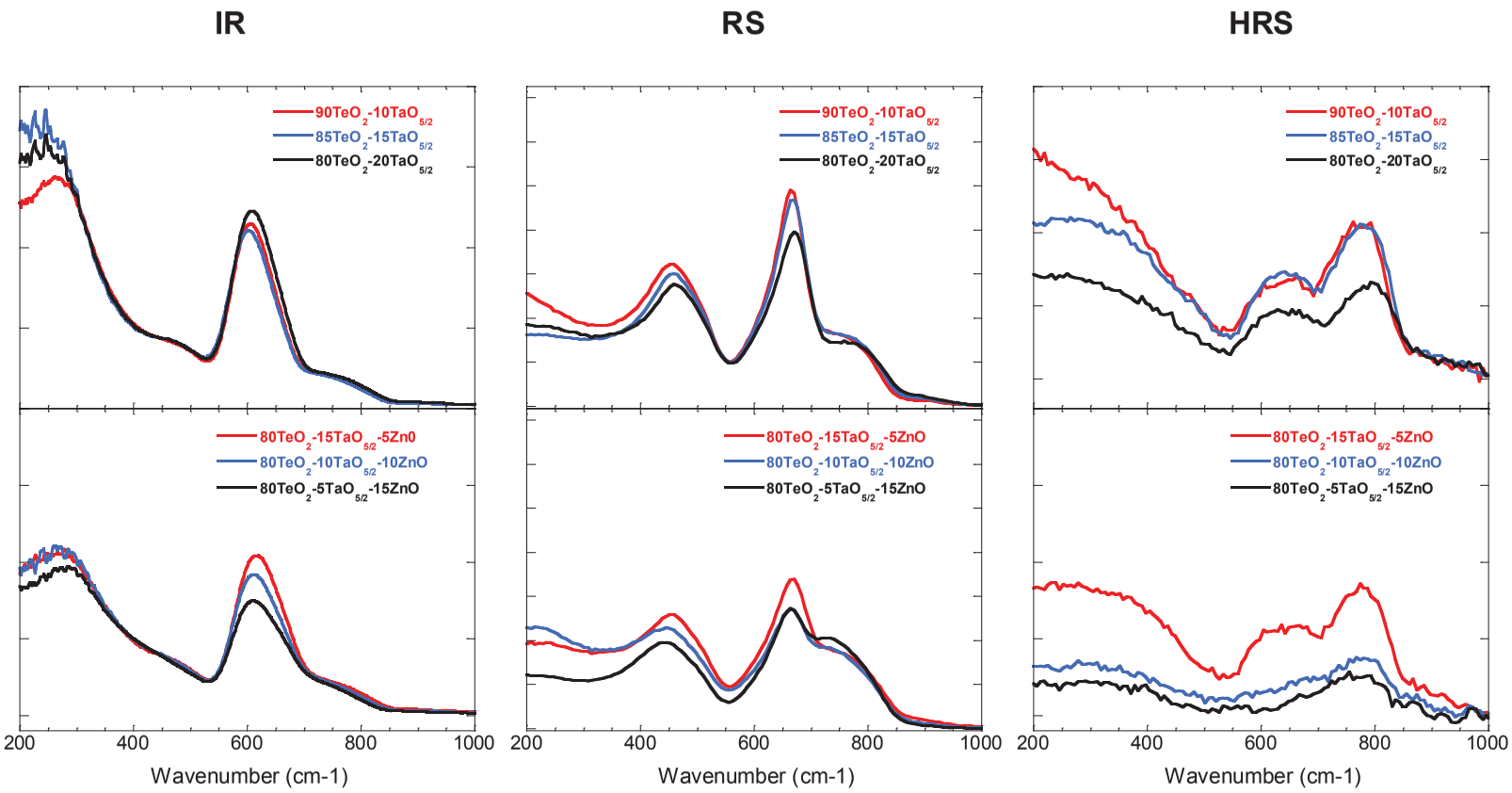

Figure 3.16 Infrared (ε'') (left), Raman (middle) and hyper-Raman (right) spectra of bulk glasses in the systems (100-x)TeO_2-x$TaO_{5/2}$ in (top) and 80TeO_2-(20-x)$TaO_{5/2}$-xZnO in (bottom). Intensities are in arbitrary units

A global assignment of the vibrational modes for the glasses can be made based on previous studies on pure TeO_2 crystalline phases (α-TeO_2, β-TeO_2 and γ-TeO_2) as reported in section 3.1 above, **[Pine 1972][Korn 1973][Migrorodsky 2000]** along with results from TeO_2 glasses and crystals containing various modifier oxides **[Manning 2012][Dexpert 1994][Sekiya 1992][Arnaudovv1982]**.

We have developed an original extended vibrational study of the TeO_2-$TaO_{5/2}$-ZnO glass network to better understand and quantify the structure-property relationships in this system. For that purpose, we have made a spectral decomposition into normalized Gaussian functions of the polarized VV and HV Raman and hyper-Raman for the three glass composition.

$$G(\bar{\upsilon}) = \frac{A}{2*HWHM}\sqrt{\frac{4\ln(2)}{\pi}}\exp(-4\ln(2)\left(\frac{\bar{\upsilon}-\overline{\upsilon_0}}{2*HWHM}\right)^2) \qquad \textbf{Eq. 3.22}$$

Where A is the Amplitude of the band, HWHM is the Half Width at Half Maximum and $\overline{\upsilon_0}$ is the band position. Eight bands have been necessary to fit/reproduce all the components of the polarized glass' spectra for the compositions $90TeO_2$-$10TaO_{5/2}$, $80TeO_2$-$20TaO_{5/2}$ to see the effect of Tantalum, and to track the effect of Zn in $80TeO_2$-$5TaO_{5/2}$15Zn0. All corresponding polarized spectral data obtained from the spectral deconvolution for these three compositions, are reported in Table 3.3.

Let us consider the first glass composition $90TeO_2$-$10TaO_{5/2}$ for which the four decomposed RS (VV and HV) and HRS (VV and HV) spectra are shown in Figure 3.17. The vibrational modes observed for that composition are thus assigned as follow:

Modes 1, 2, 4 and 4 are assigned to of TeO_4 units forming a continuous network as in α-TeO_2:

- Mode **4** at 611 cm^{-1} and mode **5** at 667 cm^{-1} are respectively anti-symmetric (ν_{as}) and symmetric (ν_s) Te-O-Te stretching of TeO_4 units. The symmetric Te-O-Te stretch (mode **5**) dominates the Raman VV spectrum whereas its intensity is weaker in the HRS spectrum, indicating clearly a strong isotropic (symmetric) but a weaker dipolar contribution of that band.

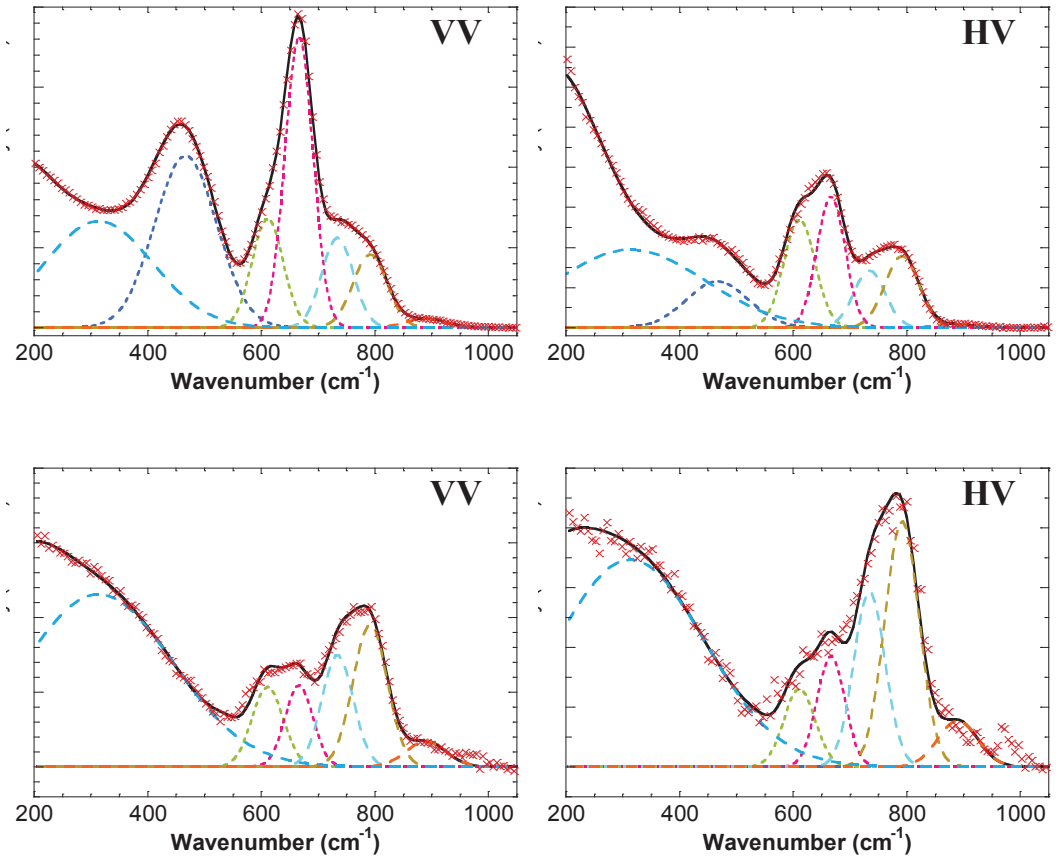

Figure 3.17 RS (top) and HRS (bottom) polarized spectra of $90TeO_2$-$10TaO_{5/2}$

mode	$90TeO_2 10TaO_{5/2}$				$80TeO_2 20TaO_{5/2}$				$80TeO_2 5TaO_{5/2} 15Zn0$			
	Band position (cm^{-1})	HWHM BandWidth (cm^{-1})	VV Intensity (%) RS	VV Intensity (%) HRS	Band position (cm^{-1})	HWHM BandWidth (cm^{-1})	VV Intensity (%) RS	VV Intensity (%) HRS	Band position (cm^{-1})	HWHM BandWidth (cm^{-1})	VV Intensity (%) RS	VV Intensity (%) HRS
1	**314**	135	0.29	0.64	**304**	135	0.33	0.53	**348**	135	0.29	0.52
2	**467**	77	0.27	0.00	**462**	77	0.25	0.06	**460**	77	0.21	0.00
3					**576**	32	0.02	0.04	**589**	32	0.03	0.02
4	**611**	39	0.09	0.06	**617**	39	0.09	0.07	**636**	39	0.10	0.01
5	**667**	35	0.21	0.06	**665**	34	0.17	0.06	**673**	34	0.12	0.07
6	**734**	39	0.07	0.09	**733**	39	0.06	0.08	**730**	39	0.13	0.14
7	**792**	42	0.06	0.12	**791**	42	0.06	0.13	**788**	42	0.10	0.19
8	**890**	49	0.01	0.03	**881**	49	0.02	0.04	**858**	49	0.01	0.05

Table 3.3 Summary of the spectral deconvolution for VV polarized Raman and hyper-Raman spectra using normalized Gaussian function for TeO_2-$TaO_{5/2}$-ZnO glasses

- Mode **2** at 467 cm^{-1} and mode **1** at 314 cm^{-1} are symmetric (δ_s) and antisymmetric (δ_{as}) highly coupled bending and stretching modes of continuous chains Te-O-Te of corner sharing TeO_4 polyhedra. The symmetric Te-O-Te bending (mode **2**: δ_s) clearly dominate the RS VV whereas it totally disappears in the HRS spectrum. Here the dipolar nature of that symmetric bending mode δ_s is none, much more than the ν_s mode at 667 cm^{-1}. This is consistent with the fact that the associated anti-symmetric bending mode is highly dipolar since it dominates the HRS spectrum. Note however that that effect here is artificially enhanced because we did not apply the temperature correction (Bose-Einstein correction) to RS and HRS spectra, so the low frequency range [0 - 400 cm^{-1}] intensity is temperature activated. The IR spectra are not affected by this effect and we can see in Figure 3.16 (left) that both the strongly dipolar anti-symmetric bands ν_{as} and δ_{as} dominate effectively the IR spectrum.

The high energy range of the spectra (720 - 850 cm^{-1}) contains two main contributions generally assigned to the stretching modes of TeO_{3+1} (or TeO_3) unit: mode **6** at 734 cm^{-1} and mode **7** at 792 cm^{-1} corresponds respectively to the symmetric ν_s and anti-symmetric ν_{as} stretch of TeO_{3+1}. These modes have a moderate intensity in Raman (VV and HV) whereas they dominate the HRS intensity spectrum VV and HV. Note here that we assign now the anti-symmetric mode ν_{as} at higher frequency than the symmetric one ν_s regarding the relative hierarchy of the HRS intensity of the bands: $I_{HRS}(\nu_{as})$=012 >

$I_{HRS}(\nu_s)$=0.09 (see Table 3.3). This result is actually not surprising when considering nearly three-fold TeO_{3+1} (or TeO_3) unit.

Lastly, TaO_6 vibrational contributions (stretching mode) are also expected at 890 cm^{-1} as previously reported by Wada **[Wada 2004]**.

From Figure 3.17, it can be seen that the information provided by Raman and hyper-Raman polarized spectra are very powerful and provide complementary vibrational information that allows one to elucidate the structure of glasses, specifically the effect of added modifiers on the tellurite network. The RS and HRS HV spectra give additional insight to consideration of the vibrational multipolar analyses (VMA) as reported elsewhere **[Guimbretiere 2008][Rodriguez 2012]**. However here it is not our purpose to go this way but we aim to demonstrate that considering RS and HRS VV spectra is strong enough to interpret straightforwardly and easily the effect of the glass modifiers Ta and Zn. One is reminded that the VV RS spectrum is strongly dominated by the isotropic contribution of the modes while the HRS VV spectrum is dominated by the dipolar contribution of the same modes.

The deconvolved RS and HRS polarized VV spectra of the two glass compositions $80TeO_2$-$20TaO_{5/2}$ and $80TeO_2$-$5TaO_{5/2}$-15ZnO are reported in Figures 3.18 and 3.19, respectively. The corresponding results are also gathered in Table 3.3. Increasing the amount of Tantalum to 20 mol% while decreasing in proportion the

Tellurium content does not affect the general feature of polarized VV RS and HRS spectra but we will see in detail in Chapter 4 the drastic decrease of the overall spectral intensities, notably the total Raman intensity which is related to the Raman gain. This "blank" relative spectral modification would indicate that the Tantalum does not really act as a glass modifier for the TeO_2 network that dominates the RS and HRS spectra. One can postulate that the only effect of Ta addition is more of a dilution effect, i.e. since the amount of Te decreases; specifically, the total spectral intensity decreases but no real spectral modification is evident. A new weak mode (**3**) at 576 cm^{-1} merges in between the intensity decreasing TeO_4 stretching and bending modes. By analogy, this mode could be assigned to a bending contribution of TeO_{3+1} (or TeO_3) units.

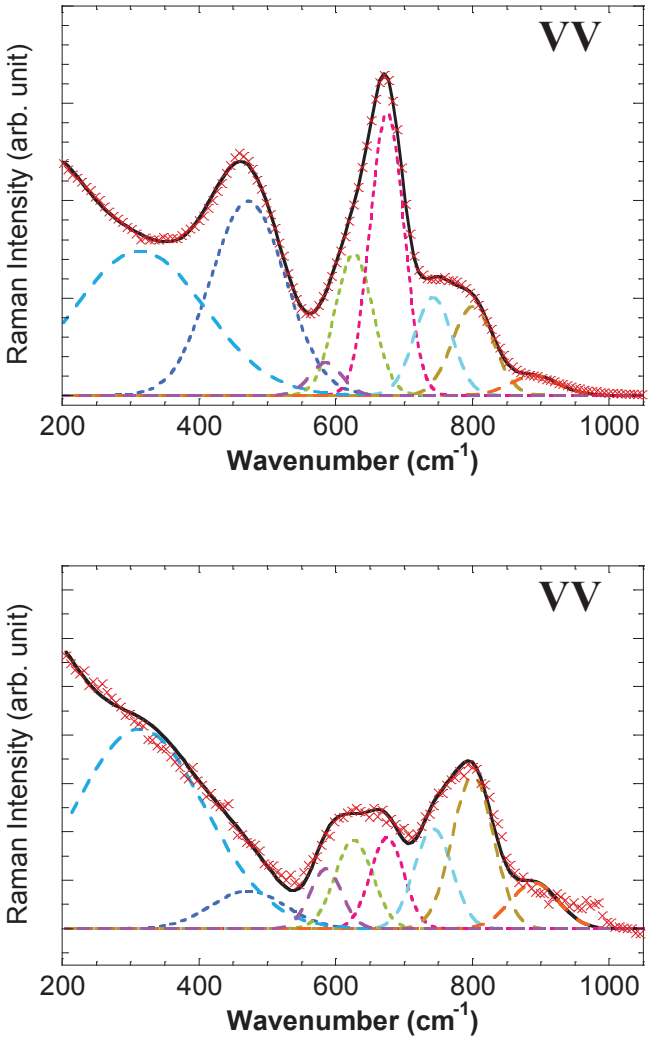

Figure 3.18 RS (top) and HRS (bottom) polarized spectra of $80TeO_2$-$20TaO_{5/2}$

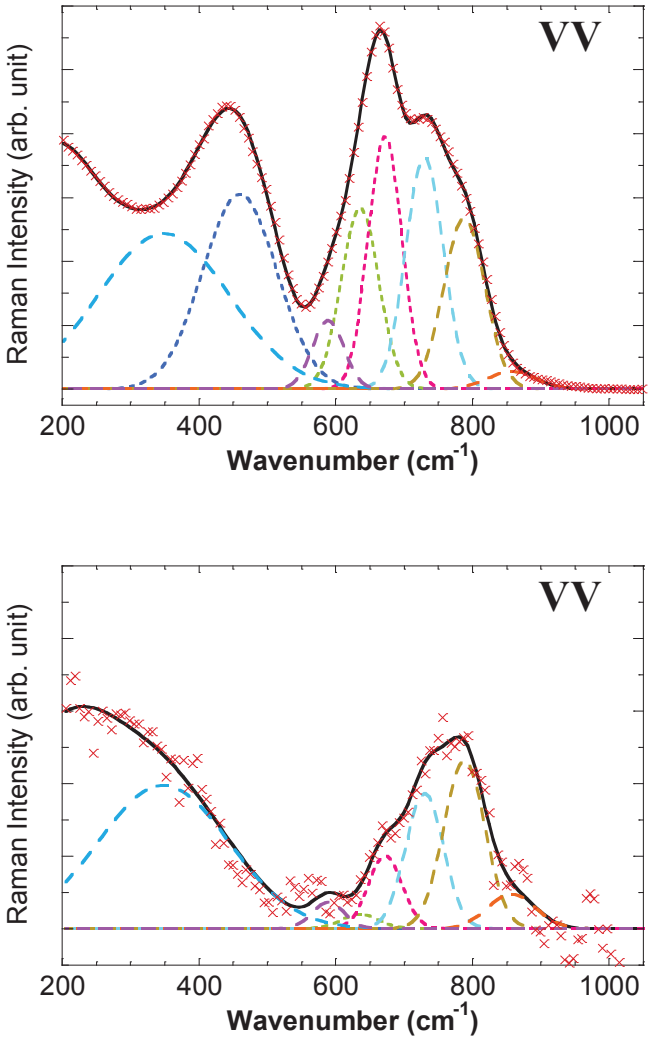

Figure 3.19 RS (top) and HRS (bottom) polarized spectra of $80TeO_2$-$5TaO_{5/2}$-15ZnO

In the ternary glasses, we have chosen to keep the tellurium content constant, but change the type of modifier present by substituting zinc for tantalum. As can be seen in Figure 3.19, this substitution does not result in the same effect. Here, the primary network unit balance has been changed from the TeO_4 seen in the prior samples without ZnO in favor of the TeO_{3+1} (or TeO_3) units in the Zn-containing materials: all the modes corresponding to TeO_4 units forming a continuous network have been seen to become less intense whereas the high frequency part of the spectra attributed to the highly (ending) distorted units now clearly dominate the HRS spectrum. Besides, the intensity of mode **3** at 589 cm^{-1} doesn't change when substituting Ta by Zn. The same observation can be seen for mode **8** at 858 cm^{-1} if considering the RS intensity, while the relative HRS intensity of that mode increases with the level of substitution (Ta then Ta/Zn) probably indicating an increasing asymmetric surrounding. However the intensity evolution of band **8** with the Ta content seems not to be well correlated. Since highly coupled bending and stretching modes of continuous chains Te-O-Te dominates both the RS and HRS spectra, it is not excluded that these strong coupled modes could be sufficiently anharmonic to give weak contributions in the HRS spectra at high frequency that coincides with mode **8** below 900 cm^{-1}: i.e. $2\delta_s$ or $\delta_{as}+\nu_{as}$ ….

One can observe that the introduction of the ZnO in the glass network affects both the polarizability (Raman part) and hyperpolarizability (hyper-Raman part) in the Te-O-Te, and TeO_4 trigonal bipyramidal units. Using a molecular approach, a hypothesis of the mechanism of the reaction can be illustrated as depicted in Figure 3.20.

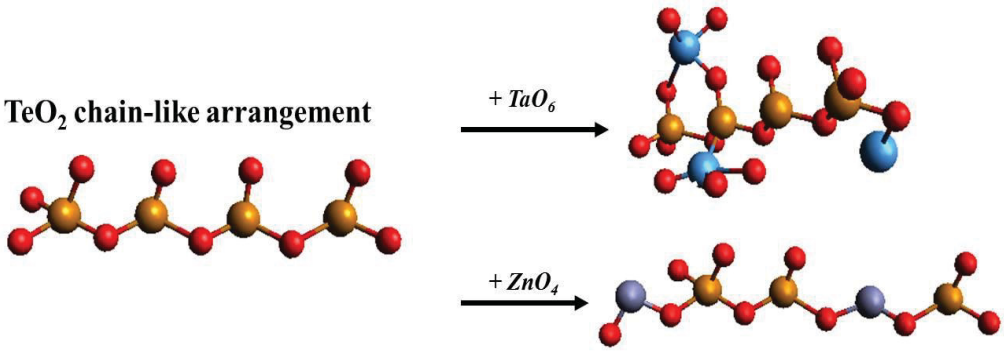

Figure 3.20 Potential mechanism of molecular arrangement during tantalum/zinc oxide introduction

From this molecular approach, we can imagine that tantalum oxide molecules will preferentially occur on the TeO_2 chains, while the zinc oxide will come into these tellurite chains, leading to a discontinuity of neighboring tellurium atoms within the networks' chain.

IR spectroscopy (Figure 3.16) has shown that the glass network owns a fairly constant quantity of tellurite entitites (Te-O-Te, TeO_4, TeO_3 and TeO_{3+1}), the short reduction of the polarizability and hyperpolarizability in TeO_2-$TaO_{5/2}$ network can be explained by an intercalation of the tantalum octahedral TaO_6 on the TeO_2 chains; whereas the drastic fall of the polarizability and hyperpolarizability in TeO_2-$TaO_{5/2}$-ZnO may be justified by an insertion of the ZnO into the TeO_2 chains. Intercalation of glass modifiers into the tellurite chains has been observed by Petit **[Petit 2004]** with a MAS ^{11}B NMR study in a TeO_2-$Na_2B_4O_7$ glass system. A change of the bore environment from BO_3 to BO_4 creates a partial depolymerization of the tellurite network when the $Na_2B_4O_7$ content increases.

Introduction of boron leads to the rupture of Te-O-Te bonds with the formation of Te-O-$BO_{2/2}$-O-Te entities. Those observations confirm the ab initio study of Mirgorodsky **[Mirgorodsky 2006]** related to the nonlinear optical susceptibility in TeO_2-based glasses. In his theoretical study, he defines the TeO_2-based glass structure as a $(TeO_2)_p$ polymer **[Noguera 2003-2]**, able to adopt different structural arrangements, examples such as: cycles formed by corner-sharing TeO_3 pyramids, chains formed by edge-sharing trigonal bipyramidals, rings formed by self-switching of these chains. Mirgorodsky et al. chose to use the density functional theory realized in Beck's three-parameter hybrid method (using the Lee-Yang-Parr correlation functional **[Becke 1993][Lee 1988]**). This method is capable of reproducing energies, geometries and vibrational spectra of many-electron systems, such as molecules containing several tellurium atoms, with an efficiency confirmed in different study on tellurium oxide molecules **[Noguera 2003-2][Noguera 20044][Uchino 1997][Nida 2001]**. Thanks to this method, they found that form all different possible geometries including, the TeO_2-chains Te-O-Te were energetically favorable; additionally, the calculations confirm that the most stable structure is an ensemble of corner-sharing TeO_4 units. Introduction of a glass modifier will lead to the molecular change TeO_4 → TeO_3, thus limiting the most favorable geometry as found by their calculations.

This extended IR, Raman and hyper-Raman studies in the TeO_2-$TaO_{5/2}$-ZnO glass system is in good agreement with the theoretical study of Mirgorodsky, and proves the hypothesis of an intercalation of the ZnO in the TeO_2 chains, leading to the reduction of the polarizability/hyper-polarizability responses. Such structural organization would be

expected to decrease the NLO contributions with increasing glass modifier concentration **[Mirgorodsky 2006].** This information allows us to understand the organization of the glass network upon addition of modifier and with modifier type variation. Through this understanding, it is possible to attempt a model of how such glass networks can give rise to their measured nonlinear optical response.

5. Raman and hyper-Raman complementary studies of TeO_2-$NbO_{5/2}$ glass network

Raman spectroscopy on niobium oxide has proved that the niobium ion, Nb^{5+} will adopt an octahedral geometry more or less distorted. It is also possible to find niobium in tetrahedral geometry as for instance in a rare-earth niobate $YNbO_4$ **[Blasse 1973]** and H-Nb_2O_5 **[Gatehouse 1964]**. However, the 5+ oxidation state of niobium is accompanied by a strong blue coloration of the material. In accordance with Berthereau **[Berthereau 1995]**, the octahedral geometry NbO_6 is clearly the only one adopted by the Nb^{5+} ion in the TeO_2-$NbO_{5/2}$ glass network. To confirm this point, let us first consider the glass composition $90TeO_2$-$10NbO_{5/2}$ for which the four decomposed RS (VV and HV) and HRS (VV and HV) spectra are reported in Figure 3.21. Peaks assigned to the vibrations of Nb-O in the octahedron NbO_6 take place on a large frequency domain [400 cm^{-1} – 1000 cm^{-1}] but due to the strong tellurite Raman and hyper-Raman cross section, only bands at high energy might be considered in term of i) bond length Nb-O, ii) octahedron distortion NbO_6 and iii) non-bridging oxygen content.

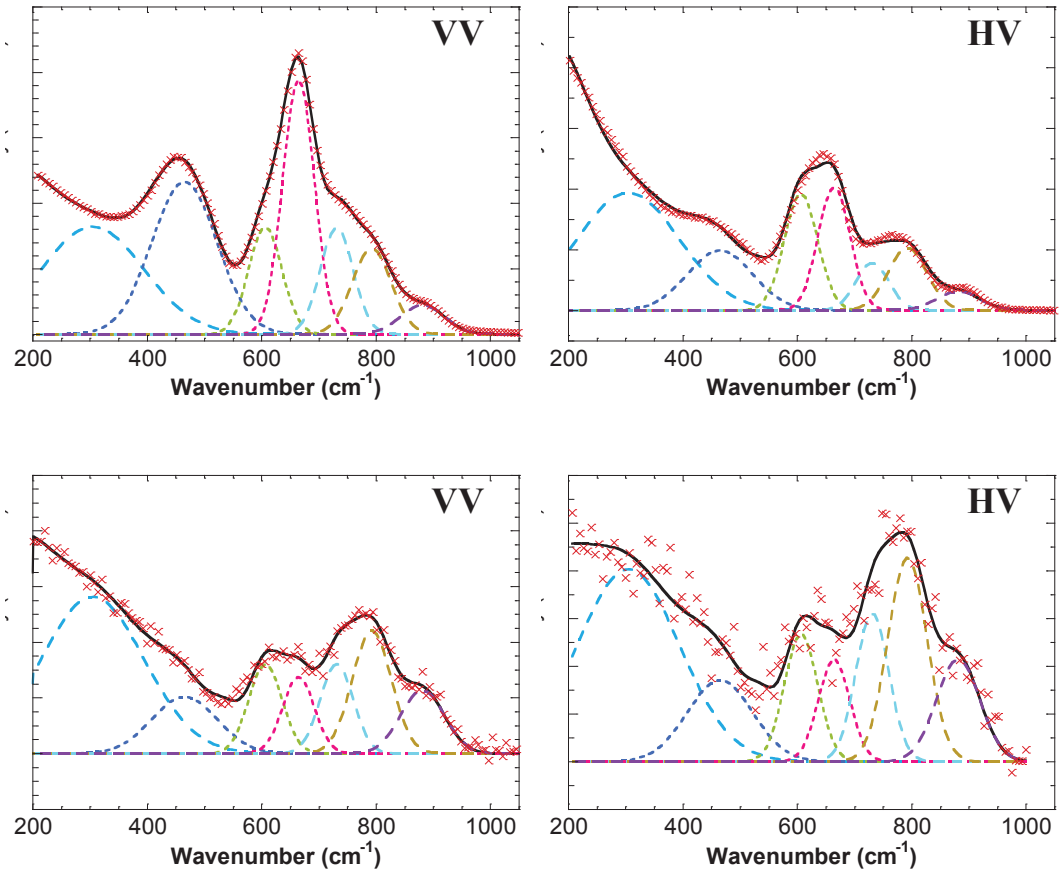

Figure 3.21 RS (top) and HRS (bottom) polarized spectra of $90TeO_2$-$10NbO_{5/2}$

A direct comparison of the substitution of Tantalum by Niobium can thus be made by comparing Figure 3.21 and Figure 3.17 that relates the composition $90TeO_2$-$10TaO_{5/2}$. The vibrational modes observed with that composition ($90TeO_2$-$10NbO_{5/2}$) are thus assigned as the TeO_2-$TaO_{5/2}$-ZnO system and are reported in Table 3.4.

	Mode assignment	$90TeO_2 10NbO_{5/2}$ Band position (cm^{-1})	HWHM BandWidth (cm^{-1})	VV Intensity (%) RS	VV Intensity (%) HRS	$90TeO_2 10TaO_{5/2}$ Band position (cm^{-1})	HWHM BandWidth (cm^{-1})	VV Intensity (%) RS	VV Intensity (%) HRS
1	$\delta_{as}(TeO_4)$	**304**	126	0.27	0.45	**314**	135	0.29	0.64
2	$\delta_{s}(TeO_4)$	**465**	80	0.24	0.10	**467**	77	0.27	0.00
3									
4	$\nu_{as}(TeO_4)$	**607**	41	0.09	0.08	**611**	39	0.09	0.06
5	$\nu_{s}(TeO_4)$	**665**	39	0.20	0.07	**667**	35	0.21	0.06
6	$\nu_{s}(TeO_{3+1})$	**731**	41	0.09	0.08	**734**	39	0.07	0.09
7	$\nu_{as}(TeO_{3+1})$	**793**	48	0.08	0.13	**792**	42	0.06	0.12
8	$\nu(TaO_n)$?					**890**	49	0.01	0.03
9	$\nu(NbO_6)$	**881**	54	0.03	0.08				

Table 3.4 Summary of the band desummation for VV polarized Raman and hyper-Raman spectra using normalized Gaussian function for $90TeO_2$-$10NbO_{5/2}$ glass. Results obtained with $90TeO_2$-$10NbO_{5/2}$ glass taken from Table 3.3 are reported here for comparison purpose

The VV polarized RS and HRS spectra of $90TeO_2$-$10NbO_{5/2}$ and $90TeO_2$-$10TaO_{5/2}$ glasses are quite similar. The only difference in the Raman VV spectrum comes from new mode **9** which is assigned to a stretching mode of distorted NbO_6 as we will detail a little bit further. This new mode is clearly more evidenced in the HRS VV spectrum at 881 cm^{-1}. Globally the HV polarized RS and HRS spectra show more pronounced differences than their VV homologues, indicating here that the continuous Te-O-Te network made of TeO_4 units is quite modified by the introduction of Niobium, in contrast with Tantalum. Another difference that we can see is in the VV HRS spectrum at low frequency. The symmetric bending mode **2** (δ_s) at 465 cm^{-1} which was initially 100% isotropic (no HRS VV contribution) with 10% Ta has now a marked dipolar contribution (10% signal in HRS VV) with 10%Nb. The same trend is observed in the HRS HV spectrum indicating that probably there is a global loss of even symmetry of the Te-O-Te network that introduce HRS (dipolar and octupolar) contributions.

Measurements of Raman spectra (VV) for other glass compositions with higher content of Niobium are reported in Figure 3.22. Again, globally, the Raman spectra do not show any feature changes since the VV Raman spectra are dominated by the tellurite cross-section (see Table 3.4), only global intensity effects like Raman gain are effective (see Chapter 4).

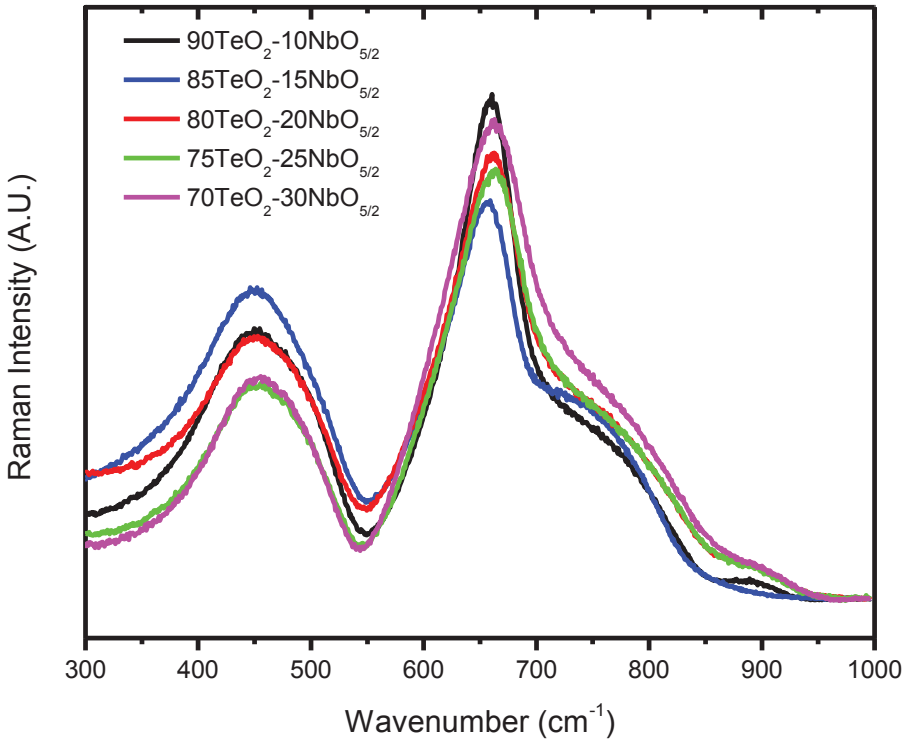

Figure 3.22 Raman scattering of (100-x)TeO_2-x$NbO_{5/2}$ glass network

Fukumi et al and Husson et al. attributed the band at around 900 cm^{-1} to a distorted niobium octahedron having a short non-bridging oxygen bond Nb-O (~ 1.70 Å) **[Fukumi 1988][Husson 1983]**. This change of Nb-O bond length leads to a distortion of the geometry of the unit. Shannon et al. **[Shannon 1976]** measured the frequency domain of the NbO_6 as function of its distortion in crystallized compounds, as shown in Figure 3.23. The degree of distortion Δ is described as $\Delta = \frac{1}{6}\sum\left(\frac{R_i - \langle R\rangle}{\langle R\rangle}\right)^2$ where R_i is a Nb-O bonding distance and $\langle R\rangle$ is the average Nb-O bonding distance. It can be noticed that the

more the octahedron is distorted, the more the vibrational band appears at high energy. The position of the (Raman) band of the Nb-O bonds in the octahedron NbO_6 probes the dimensionality of the network. **[Husson 1977-1][Husson 1977-2][Husson 1977-3]** found this band at 900 cm^{-1} in Columbite-like stucture [$(Fe,Mn)Nb_2O_6$], characteristic of bi-dimensional Niobium-Oxygen network. While in a tri-dimensional Niobium-Oxygen network (tungsten-bronze type $NaBa_2Nb_5O_{15}$ **[Burns 1969]**, Perovskite-like structure $LiNbO_3(BaNb_2O_6\text{-}SrNb_2O_6)$ **[Repelin 1979-1][Repelin 1979-2]**, the assigned Raman band will occur at a lower energy [600 cm^{-1} – 700 cm^{-1}].

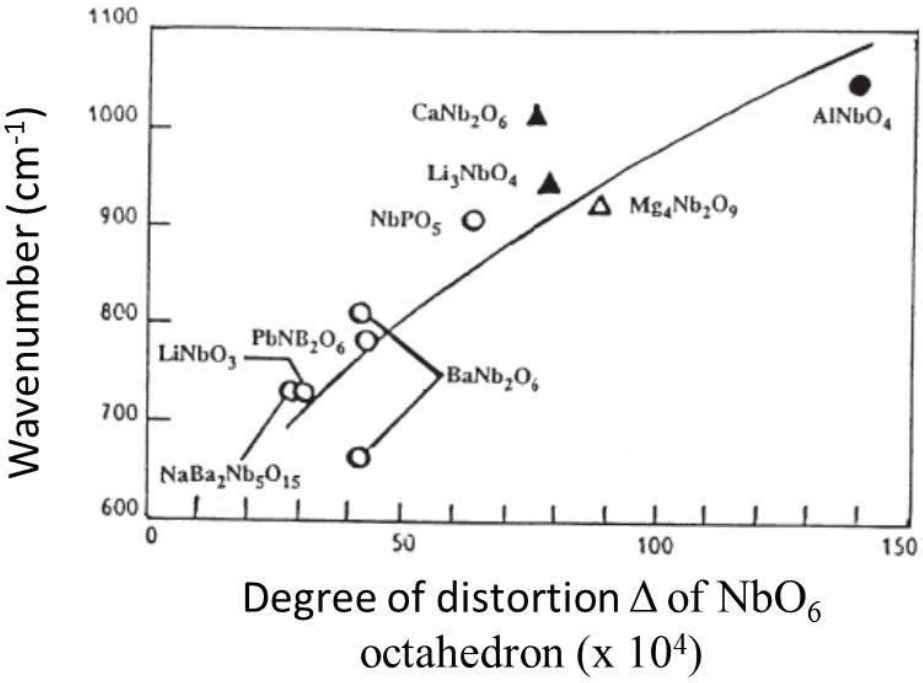

Figure 3.23 Position of the Raman band assigned to the Nb-O bond as function of the distortion Δ of NbO_6 octahedron, where ○ (Oh without non-bridging oxygen O_{nb}, without oxygen tri or tetra-coordinated O_t), ● (Oh with O_t, without O_{nb}), Δ (Oh with O_{nb}, without O_t) and ▲(Oh with O_{nb} and O_t) taken from [Shannon 1976]

In the (100-x)TeO_2-x$NbO_{5/2}$ glass system, it is observed that band assigned to the Nb-O in NbO_6 octahedron shifts to the lower energy when the niobium oxide content increases (Figure 3.22). From the degree of distortion investigated by Shannon **[Shannon 1976]**, at low niobium oxide content (10%), band **9** at 881 cm^{-1} (Table 3.4, Figure 3.21) is characteristic of a distorted octahedron with non-bridging oxygen that interacts strongly with the Te-O-Te chains and this is probably true down to 15% of Nb. At higher content of $NbO_{5/2}$ we may observe a shift of that mode to lower energies. This shift to lower energy has been observed by Fukumi et al. **[Fukumi 1988]** in a K_2O-SiO_2-Nb_2O_5 glass system but also by Berthereau **[Berthereau 1995]** in a TeO_2-Nb_2O_5 glass system.

6. Raman scattering study of TeO_2-$BiO_{3/2}$-ZnO glass network

As previously explained, when cation modifiers are introduced within the TeO_2 matrix, structural variations are interpreted by a progressive transformation of TeO_4 trigonal bipyramidal (tbp) units into TeO_3 trigonal pyramidal (tp) units, via the intermediate bonding state TeO_{3+1}. TeO_{3+1} corresponds to a distorted TeO_4 entity with one long Te-O bond, as found in TeO_2 crystals and some binary tellurite crystals **[Noguera 2003-3]**.

The Raman spectra (VV + HV) observed in Figure 3.24 are characteristic of a TeO_2 glass network strongly modified by Bismuth and Zinc. In fact, the spectral features

of the tellurite cross-section are more difficult to extract directly (see Figures 3.16 and 3.22).

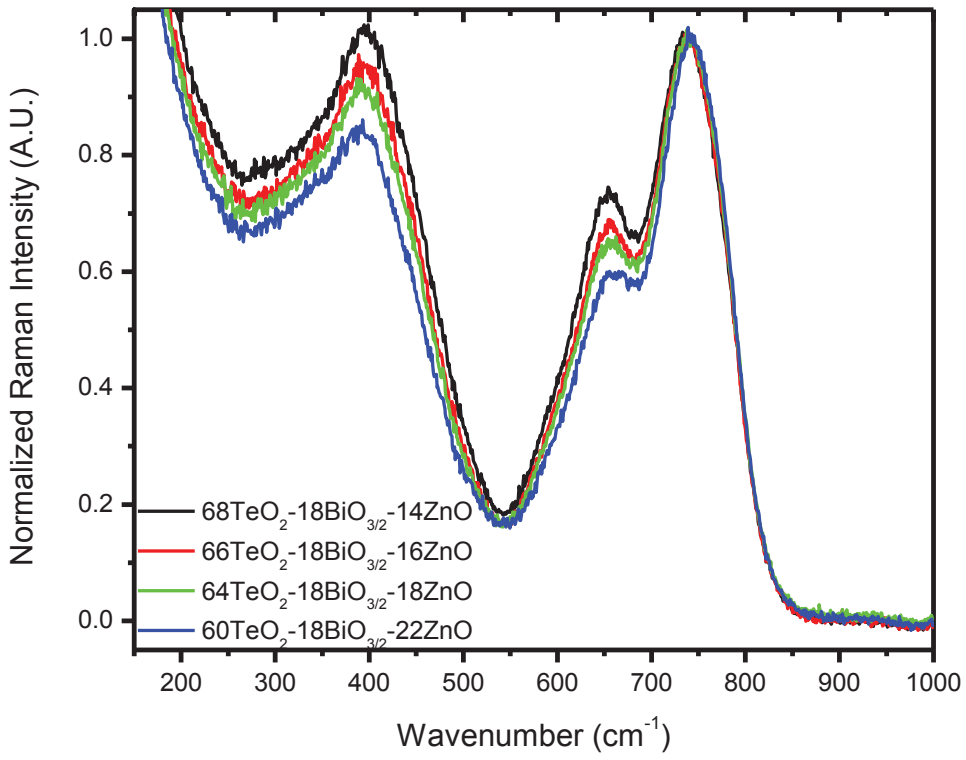

Figure 3.24 Raman spectra of TeO_2-$BiO_{3/2}$-ZnO glass system [Massera 2009]

Starting from the low frequency range, the band at 380 cm^{-1} is assigned to symmetric stretching anion motion of Bi-O-Bi in the [BiO_6] octahedral units **[Hazra 1997][Tincher 2010]**. The band at 350 - 400 cm^{-1} results from highly coupled bending and stretching modes of continuous chains Te-O-Te of corner sharing TeO_4 units (~ modes **1** and **2** in Table 3.3 for the composition $80TeO_2 5TaO_{5/2} 15ZnO$). Bands located at

640 cm^{-1} and 670 cm^{-1} originate respectively from anti-symmetric and symmetric stretching of TeO_4 units forming a continuous network (respectively, modes **4** and **5** in Table 3.3 for the composition $80TeO_25TaO_{5/2}15ZnO$). The high energy broad shoulder (720-830 cm^{-1}) is expected to contain the two stretching modes **6** and **7** of TeO_{3+1} and TeO_3 units.

The two first bands can also be modified by the Raman activity of ZnO because in amorphous ZnO, the broad bands are observed at around 400 cm^{-1} and 600 cm^{-1} **[Tzolov 2001]**. From the evolution of the Raman spectrum of TeO_2-Bi_2O_3-ZnO, we clearly observe a diminution of the TeO_4 units during the introduction of ZnO as in the TeTaZn system. It is explained by a trigonal bipyramids transformation into trigonal pyramids: $TeO_4 \rightarrow TeO_{3+1} \rightarrow TeO_3$. Ozdabova et al. announced **[Ozdabova 2007]** that this process may be due to a potential formation of entities such as $ZnTeO_3$, $Zn_2Te_3O_8$ and $Bi_2Te_4O_{11}$ **[Burger 1992][Udovic 2006]**. As shown in Chapter 2, it is observed the formation of a $Bi_2Te_4O_{11}$ crystal phase into this glass matrix. So the broadening of the Te-O-Te band into low frequency region reflects most probably the formation of following linkages O-Te-O **[Tzolov 2001]**, O-Te-Bi **[Udovic 2006]** and Bi-O-Bi **[Baia 2002]**.

7. Conclusion

Due to the characteristic electronic delocalization in glasses, vibrational spectra are constituted by broad bands covering large wavenumber windows, leading to complicated understanding of the structural properties. To delineate each structural contribution present into those bands, we have done a vibrational study on the TeO_2

crystal, strictly assigning contributions. Variations of the laser polarization and position (crystallographic positions) of the material lead to the assignment of 33 optical phonon branches in the paratellurite. By combining vibrational spectroscopies as infra-red absorption, Raman scattering and hyper-Raman scattering, and due to the different selection rules associated with the differing techniques, we have shown that it is possible to probe different vibrational modes, which are not available with a traditional single technique investigation.

This crystal knowledge has been extrapolated to tellurite glass systems, TeO_2-$TaO_{5/2}$-ZnO, TeO_2-$NbO_{5/2}$ and TeO_2-Bi_2O_3-ZnO, to probe and assign the different vibrational contributions present in those isotropic materials.

Specifically, vibrational analysis has confirmed existence of transformations of the tellurite entities $TeO_4 \rightarrow TeO_{3+1} \rightarrow TeO_3$ as function of the percentage of glass modifiers present into the various tellurite glass matrix. Furthermore, thanks to spectral deconvolutions done on the RS and HRS, we have been able to look at the evolutions of Raman and hyper-Raman cross sections, leading to information about the impact of the different glass modifiers on the tellurite glass structure (fluctuation of the polarity, polarizability and hyper-polarizability).

In TeO_2-$TaO_{5/2}$-ZnO and TeO_2-Bi_2O_3-ZnO glass systems, the effect of the zinc oxide has been demonstrated, drastically affecting the Te-O-Te chains and so, the polarizability of the material. The hypothesis consists to explain that zinc oxide does not intercalate between tellurite chains as for $TaO_{5/2}$, $NbO_{5/2}$ or $BiO_{3/2}$ entities; but at this opposite, it

will take place into Te-O-Te chains occurring to rupture of chain continuity. This decrease of chain connection implies a decrease of the glass polymerization. As explained in Chapter 2, ZnO represents an excellent candidate (in term of glass modifier) for fiber fabrication. This affirmation is now understandable thanks to our structural comprehension. From now on, the relationship between structural changes and nonlinear optical properties has to be elucidated.

In the next chapter, the relationship between nonlinear optical properties and glass structure will be the tackled and discussed. This new information will enable a 'best' trade-off in term of material for fiber amplifiers and finally offer a solid answer to the fundamental question of this study: *"What is the impact of the glass structure on the Raman gain?"*

Chapter 3 - References

Agalzov 1985: A.M. Agalzov, V.S. Gorelik, M.M. Suschinsky. Optika i Spectroskopiya 58 (1985) 386.

Almeida 1990: R.M. Almeida, T.A. Guiton, C.G. Pantano, Journal of Non-Crystalline Solids 121 (1990) 193.

Akhmanov 1965: S.A. Akhmanov, D.N. Klysho, Zh. Eksp. Teor. Fiz. Pis'ma 2 (1965) 171.

Arlt 1968: G. Arlt, H. Schweppe, Solid State Communications. 6 (1968) 783.

Arnaudov 1982: M. Arnaudov, V. Dimitrov, Y. Dimitriev, L. Markova, Materials Research Bulletin 17 (1982) 1121.

Ayrault 1972: B. Ayrault, E.A. Descamps, F. Abba, Y. Marqueton, M. Durand, Solid State Communications 11 (1972) 639.

Baia 2002: L. Baia, R. Stefan, W. Kiefer, J. Popp, S. Simon, Journal of Non-Crystalline Solids 303 (2002) 379.

Becke 1993: A. D. Becke, Journal of Chemical Physics 98 (1993) 1372.

Berthereau 1995: A. Berthereau, PhD thesis "Matériaux vitreux pour l'optique non linéaire" (1995) University of Bordeaux, France.

Beyer 1967: H. Beyer, Zeitschrift fuer Kristallgraphie, Kristallgeometrie, Kristallphysik, kristallchemie 123 (1967) 228-237.

Blanchandin 1999-1: S. Blanchandin, P. Thomas, P. Marchet, J.C. Champarnaud-Mesjard, B. Frit, Journal of Materials Chemistry 9 (1999) 1785.

Blanchandin 1999-2: S. Blanchandin, P. Marchet, P. Thomas, J.C. Champarnaud-Mesjard, B. Frit, A. Chagraoui, Journal of Materials Science 34 (1999) 4285-4292.

Blanchandin 2000: S. Blanchandin, PhD thesis "Etude cristallochimique de quelques phases cristallisées et vitreuses appartenant aux systèmes TeO_2-WO_3 et TeO_2-Nb_2O_5-Bi_2O_3 " (2000) University of Limoges, France.

Blasse 1973: G. Blasse, Journal of Solid State Chemistry 7 (1973) 169.

Burger 1992: H. Burger, K. Kneip, H. Hobert, W. Vogel, V. Kozhukharov, S. Neov, Journal of Non-Crystalline Solids 151 (1992) 134.

Burns 1969: G.Burns, J.D. Axe, D.F. O'Kane, Solid State Communications 7 (1969) 933.

Ceriotti 2006: M. Ceriotti, F. Pietrucci, M. Bernasconi, Physical Review B 73 (2006) 104304.

Chagraoui 1996: A. Chagraoui, PhD thesis "Matériaux cristallisés et amorphes appartenant au système Bi_2O_3-TeO_2-WO_3" (1996) University of Hassan II-Mohammedia, Marocco.

Champarnaud-Mesjard 2000: J.C. Champarnaud-Mesjard, S. Blanchandin, P. Thomas, A.P. Mirgorodsky, T. Merle-Mejean, B. Frit, Journal of Physics and Chemistry of Solids 61 (2000) 1499-1507.

Chemla 1970: D.S. Chemla, J. Jerphagnon, Applied Physics Letters 2 (1970) 222.

Christie 1971: J.H. Christie, D.J. Lockwood, Journal of Chemical Physics 54 (1971) 1141.

Cyvin 1965: S.J. Cyvin, J.E. Rauch, J.C. Decius, Journal of Chemical Physics 43 (1965) 4083.

Damen 1966: T.C. Damen, S.P.S. Porto, B. Tell, Physical Review 42 (1966) 570-574.

Denisov 1987: V.N. Denisov, B.N. Mavrin, V.B. Podobedov, Physics Report 151 (1987) 1-92.

Dexpert 1994: J. Dexpert-Ghys, B. Piriou, S. Rossignol, J.M. Réau, B. Tanguy, J.J. Videau, J. Portier, Journal of Non-Crystalline Solids 170 (1994) 167.

Dines 1976: T.J. Dines, M.J. French, R.J.B. Hall and D.A. Long, Proceedings of the Fifth International Conference on Raman Spectroscopy, Freiburg (1976).

Fukumi 1988: K. Fukumi. S. Sakka, Journal of Materials Science 23 (1988) 2819.

Galeneer 1980: F.L. Galeneer, G. Lucovsky, J.C. Mikkelsen, Physical Review B 22 (1980) 3983.

Gatehouse 1964: B.M. Gatehouse, A.D. Wadsley, Acta Crystallographica 17 (1964) 1545.

Guery 2012: G. Guery, A. Fargues, T. Cardinal, M. Dussauze, F. Adamietz, V. Rodriguez, J.D. Musgraves, K. Richardson, P. Thomas, Chemical Physics Letters 554 (2012) 123.

Guimbretiere 2008: G. Guimbretière, A. Bouchet, V. Rodriguez, M. Couzi, D. Talaga, T. Buffeteau, L. Canioni, Journal of Physical Chemistry C 112 (2008) 17906.

Hazra 1997: S. Hazra, S. Mandal, A. Gosh, Physical Review B 56 (1997) 8021-8025.

Husson 1977-1: E. Husson, Y. Repelin, N.Q. Dao, H. Brusset, Journal of Chemical Physics 66 (1977) 5173.

Husson 1977-2: E. Husson, Y. Repelin, N.Q. Dao, H. Brusset, Journal of Chemical Physics 67 (1977) 1157.

Husson 1977-3: E. Husson, Y. Repelin, N.Q. Dao, H. Brusset, Spectrochimica Acta 33A (1977) 995.

Husson 1983: E. Husson, Y. Repelin, Comptes Rendus de l'Académie des Sciences, Paris 296 (1983) 1405.

Inoue 1979: K. lnoue, T. Sameshima, Journal of Physical Society of Japan 47 (1979) 2037.

Inoue 1980: K. Inoue, N. Asai, T. Sameshima, Journal of Physical Society of Japan 48 (1980) 1787.

Inoue 1981-1: K. Inoue, N. Asai and T. Sameshima, Journal of Physical Society of Japan 50 (1981) 1291.

Inoue 1981-2: K. Inoue, N. Asai, Journal de Physique (Paris) colloque 42 (1981) C6-430.

Kaatz 1996: P. Kaatz, D. P. Shelton, Molecular Physics 88 (1996) 683.

Kaminsky 1993: W. Kaminsky, E. Hartmann, Z. Phys. B 90 (1993) 47.

Kamitsos 1993: E.I. Kamitsos, A.P. Patsis, G.D. Chryssikos, Journal of Non-Crystalline Solids 152 (1993) 246.

Kamitsos 1996: E. I. Kamitsos, Physical Review B 53 (1996) 14659.

Kamitsos 1997: E.I. Kamitsos, Y.D. Yiannopoulos, C.P. Varsamis, H. Jain, Journal of Non-Crystalline Solids 222 (1997) 59.

Kielich 1983: S. Kielich, "Progress in optics", edited by E. Wolf North-Holland, Amsterdam (1983).

Kielich 1964: S. Kielich, Physica 30 (1964) 1717.

Kopsky 1979: V. Kopsky, Acta Crystallographica A 35 (1979) 83.

Korn 1973: D.M. Korn, A.S. Pine, G. Dresselhaus, T.B. Reed, Physical Review B 8 (1973) 768.

Krauzman 1971: M. Krauzman, J.P. Mathieu, Comptes Rendus de l'Académie des Sciences, Paris 273B (1971) 342.

Landsberg 1928: G. Landsberg, L. Mandelstam, Naturwissenschaften 557 (1928) 772.

Lasbrugnas 2009: C. Lasbrugnas, P. Thomas, O. Masson, J.C. Champarnaud-Mesjard, E. Fargin, V. Rodriguez, M. Lahaye, Optical Materials 31 (2009) 775.

Lee 1988: C. Lee, W. Yang, R. G. Parr, Physical Review B 37 (1988) 785.

Li 1964: Y.Y. Li, Physical Sinica 20 (1964) 164.

Long 1979: D.A. Long, Proceedings of the 31st International Meeting of the Society de Chimie Physique, Elsevier, Amsterdam (1979).

Long 2002: D.A. Long, "The Raman Effect", Wiley, New York (2002).

Loudon 1964: R. Loudon, Advanced Physics 1964, 13, 423.

Maker 1970: P.D. Maker, Physical Review A 1 (1970) 923.

Manning 2012: S. Manning, H. Ebendorff-Heidepriem, T.M. Monro, Optical Materials Express 2 (2) (2012) 140.

Mamedov 2003: N. Mamedov, N. Yamamoto, Y. Shim, Y. Ninomiya, T. Takizawa, Japanese Journal of Applied Physics Part 1 42 (2003) 5145.

Massera 2009: J. Massera, PhD thesis "Nucleation and growth behavior of tellurite-based glasses suitable for mid-infrared applications" (2009) Clemson University, USA.

Merzbacher 1991: C.I. Merzbacher, W.B. White, Journal of Non-Crystalline Solids 130 (1991) 18.

Mirgorodsky 2000: A.P. Mirgorodsky, T. Merle-Mejean, J.C. Champarnaud, P. Thomas, B. Frit, Journal of physics and Chemistry of Solids 61 (2000) 501-509.

Mirgorodsky 2006: A.P. Mirgorodsky, M. Soulis, P. Thomas, T. Merle-Mejean, M. Smirnov, Physical Review B 73 (2006) 134206.

Muenow 1969: D.W. Muenow, J.W. Hastie, R. Hauge, R. Bautista, J.L. Margrave, Transactions of the Faraday Society 65 (1969) 3210.

Nida 2001: H. Nida, T. Uchino, J. Jin, S.-H. Kim, T. Fukunaga, T. Yoko, Journal of Chemical Physics 114 (2001) 459.

Noguera 2003-1: O. Noguera, PhD Thesis "Propriétés structurales, vibrationnelles et diélectriques de matériaux à base d'oxyde de tellure" (2003) University of Limoges, France.

Noguera 2003-2: O. Noguera, M. Smirnov, A. P. Migorodsky, T. Merle-Mejean, P. Thomas, and J. C. Champarnaud-Mesjard, Physical Review B 68, (2003) 094203.

Noguera 2003-3: O. Noguera, T. Merle-Mejean, A.P. Mirgorodsky, M.B. Smirnov, P. Thomas, J.C. Champarnaud-Mesjard, Journal of Non-Crystalline Solids 330 (2003)50-60.

Noguera 2004: O. Noguera, M. Smirnov, A. Mirgorodsky, T. Merle-Mejean, P. Thomas, and J. C. Champarnaud-Mesjard, Journal of Non-Crystalline Solids 345&346 (2004) 734.

Nye 1957: J.F. Nye, "Physical properties of crystals", Clarendon Press, Oxford (1957).

Ozdabova 2007: J. Ozdabova, H. Ticha, L. Tichy, Journal of Non-Crystalline Solids 353 (2007) 2799-2802.

Payne 1984: M.C. Payne, J.C. Inkson, Journal of Non-Crystalline Solids 68 (1984) 351.

Petit 2004: L. Petit, PhD thesis "Amplification optique dans des verres borophosphate de niobium et tellurite dopes aux ions de terres rares présentant un indice optique non linéaire élevé" (2004) University of Bordeaux, France.

Pine 1972: A.S. Pine, G. Dresselhaus, Physical Review B 5 (1972) 4087.

Plazek 1934: G. Plazek, "Rayleigh-Streuung and Raman-Effekt", in "Handbuch der Radiologie", Ed. E. marx, Akademische Verlag, Leipzig, Vol. VI, Part 2, 205-374 (1934).

Polivanov 1978: Y.N. Polivanov, R.Sh. Sayakhov, Fizika Tverdogo Tela 20 (1978) 2708.

Polivanov 1979-1: Y.N. Polivanov and R.Sh. Sayakhov, Journal of Experimental and Theoretical Physics (Zh. Eksp. Teor. Fiz. Pis'ma) 30 (1979) 617.

Polivanov 1979-2: Y.N. Polivanov and R.Sh. Sayakhov, Kvant Elektronika 6 (1979) 2485.

Polivanov 1981: Y.N. Polivanov and R.Sh. Sayakhov, Physica Status Solidi (b) 103 (1981) 89.

Porto 1966: S.P.S. Porto, J.A. Giordmaine, T.C. Damen, Physical Review 147 (1966) 608.

Presting 1985: H. Presting and H. Vogt, Proceedings of the 17th International Conference of the Physics of Semiconductors, Springer-Verlag (1985).

Quinet 2004: O. Quinet, B. Champagne, V. Rodriguez, Journal of Chemical Physics 121 (2004) 4705.

Quinet 2006: O. Quinet, B. Champagne, V. Rodriguez, Journal of Chemical Physics (2006) 244312.

Raman 1928: C.V. Raman, K.S. Krishnan, Nature 121 (1928) 501.

Repelin 1979-1: Y. Repelin, E. Husson, H. Brusset, Spectrochimica A35 (1979) 937.

Repelin 1979-2: Y. Repelin, E. Husson, H. Brusset, Spectrochimica A35 (1979) 1165.

Rodriguez 2006: V. Rodriguez, D. Talaga, F. Adamietz, J. L. Brunéel, M. Couzi, Chemical Physics Letters 431 (2006) 190.

Rodriguez 2008: V. Rodriguez, Journal of Chemical Physics 128 (2008) 064707.

Rodriguez 2012: V. Rodriguez, Journal of Raman Spectroscopy 43 (2012) 627-636.

Savage 1971: C.M. Savage, P.D. Maker, Applied Optics 10 (1971) 965.

Schweppe 1970: H. Schweppe, Ultrasonics 8 (1970) 84.

Sekiya 1992: T. Sekiya, N. Mochida, A. Ohtsuka, M. Tonokawa, Journal of Non-Crystalline Solids 144 (1992) 128.

Shannon 1976: R.D. Shannon, Acta Crystallographica A32 (1976) 751.

Singj 1972: S. Singj, W.A. Bonner, L.G. Van Uitert, Physical Letters 38A(6) (1972) 407.

Smekal 1923: A. Smekal, Naturwissenschaften 11 (1923) 873.

Soobsch 1979: Kr. Soobsch. Fiz. FIAN 8 (1979) 31.

Stegeman 2003: R. Stegeman, L. Jankovic, H. Kim, C. Rivero, G. Stegeman, K. Richardson, P. Delfyett, Y. Guo, A. Schulte, T. Cardinal, Optics Letters 28 (2003) 1126.

Stern 1963: F. Stern, Solids State Phys. 15 (1963) 299.

Syrbu 1996: N.N. Syrbu, R.V. Cretu, Infrared Physics and Technology 37 (1996) 769.

Terhune 1965: R.W. Terhune, P.D. Maker, C.M. Savage, Physical Review Letters 14 (1965) 681.

Thomas 1988: P.A. Thomas, Journal of Physics C: Solid State Physics 21 (1988) 4611-4627.

Tincher 2010: B. Tincher, J. Massera, L. Petit, K. Richardson, Materials Research Bulletin 45 (2010) 1861-1865.

Turrel 1972: G. Turrel, "Infrared and Raman Spectra of Crystals", Academic Press, New York, 1972, Chap. 5.

Tzolov 2001: M. Tzolov, N. Tzenov, D. Dimova-Malinovska, M. Kalitzova, C. Pizzuto, G. Vitali, G. Zollo, I. Ivanov, Thin Solid Films 396 (2001) 274.

Uchida 1970: N. Uchida, Y. Ohmachi, Japanese Journal of Applied Physics 9 (1970) 155-156.

Uchino 1997: T. Uchino, S.-H. Kim, T. Yoko, T. Fukunaga, Journal of the Ceramic Society of Japan 105 (1997) 201.

Udoviv 2006: M. Udovic, P. Thomas, A. Mirgorodsky, O. Durand, M. Soulis, O. Masson, T. Merle-Mejean, J.C. Champarnaud-Mesjard, Journal of Solid State Chemistry 179 (2006) 3252.

Verbiest 2009: T. Verbiest, K. Clays, V. Rodriguez, "Second-order nonlinear optical characterizations techniques: An Introduction", CRC Press, New-York, (2009).

Vogt 1976: H. Vogt, G. Neumann, Optics Communications 19 (1976) 108.

Vogt 1978: H. Vogt, G. Neumann, Physica Status Solidi (b) 86 (1978) 615.

Vogt 1979: H. Vogt, G. Neumann, Physica Status Solidi (b) 92 (1979) 57.

Vogt 1981: H. Vogt and G. Rossbroich, Phys. Rev. B24 (1981) 3086.

Vogt 1982: H. Vogt, A. Sanjurjo and G. Rossbroich, Phys. Rev. B26 (1982) 5904.

Vogt 1984: H. Vogt, H. Uwe, Physical Review B 29 (1984) 1030.

Vogt 1985: H. Vogt, H. Presting, Physical Review B 31 (1985) 6731.

Vogt 1986: H. Vogt, M.D. Fontana, G.E. Kugel, P. Gunter, Physical Review B 34 (1986) 410.

Wada 2004: N. Wada, M. Kubo, N. Maeda, M. Akira, K. Kojima, Journal of Materials Research 19 [2] (2004) 667-75.

CHAPTER 4

NONLINEAR OPTICAL PROPERTIES IN TELLURITE-BASED GLASS

In the last chapters, we observed the impact of the glass modifier on the glass structure. In the TeO_2-$TaO_{5/2}$-ZnO glass network, we remarked that the introduction of ZnO was at the origin of a drastic drop of the linear refractive index and so on the polarizability in decreasing the first order electronic susceptibility $\chi^{(1)}$ (Chapter 2). Those marked changes were due to the rupture of the Te-O-Te chains' continuity with Zn addition and were responsible for the electronic delocalization and the changed polarizability of the TeO_2 glass network (Chapter 3).

In this chapter, we will review about the impact of these structural changes on the nonlinear optical properties, specifically the second and third order ($\chi^{(2)}$ and $\chi^{(3)}$). The effect on the short-range order will be discussed within the context of tellurite glass ceramics (GC) realized within the TeO_2-Bi_2O_3-ZnO glass matrix, previously discussed in Chapter 2. This chapter will finally conclude by answering to the main questions of the PhD study: *'What is the impact of the glass structure on the nonlinear optical properties? On Raman gain?"* Raman gain measurement (protocol and setup) from spontaneous Raman scattering, hyper-Rayleigh scattering (principles and setup) will be discussed to give i) the relationship between $\chi^{(2)}$ and $\chi^{(3)}$, and ii) to be informed about the evolutions of the Raman gain as function of the glass/glass ceramic structure.

1 Experimental techniques

1.1 Raman gain measurement

The theory regarding Stimulated Raman scattering (SRS), or Raman gain has been applied to bulk glass in details presented in the previous PhD dissertations of Clara Rivero and Robert Stegeman [**Rivero 2005-1][Stegeman 2006].** The objective in the present paragraph is not to develop those aspects in detail but to extend those findings by providing sufficient theoretical and experimental aspects of the Raman gain for the material's evaluation, offer by Rivero and Stegeman. Those aspects will be defined in the international system (SI) to facilitate the comprehension of the results. The stimulated Raman Scattering is a two-photon stimulated process that grows from spontaneous Raman emission **[Hellwarth 1963]**. Figure 4.1 shows a schematic representation of the Raman gain process.

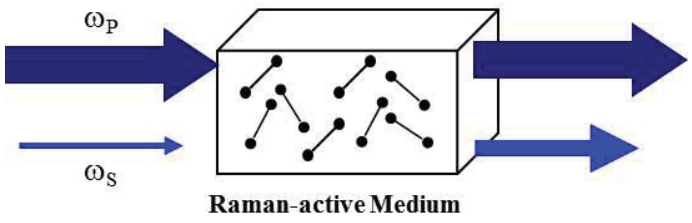

Figure 4.1 Schematic representation of the Raman gain process

This two-photon transition is a third-order nonlinear process that can be described as a third-order wave coupling between the pump and the Stokes waves. The nonlinear wave equations take the form.

$$\nabla\times(\nabla\times\vec{E}_P)-\frac{\omega_P^2}{c^2}\varepsilon_P\vec{E}_P=\frac{\omega_P^2}{c^2}\vec{P}^{(3)}(\omega_P) \qquad \textbf{Eq. 4.1}$$

$$\nabla\times(\nabla\times\vec{E}_S)-\frac{\omega_S^2}{c^2}\varepsilon_S\vec{E}_S=\frac{\omega_S^2}{c^2}\vec{P}^{(3)}(\omega_S) \qquad \textbf{Eq. 4.2}$$

Where $\overrightarrow{E_p}$ and $\overrightarrow{E_s}$ are the energy, ω_p and ω_s are the pump and signal frequency, $\overrightarrow{P^{(3)}}$ is the third order nonlinear polarization, ε_p and ε_s are the dielectric constant, and c is the speed of light in the vacuum.

In the case of an isotropic medium like glasses, taking E_P and E_S with the same polarization direction, the nonlinear polarizations can be expressed as

$$\vec{P}^{(3)}(\omega_P)=\varepsilon_0\left(\chi_P^{(3)}\left|E_P^2\right|+\chi_{R1}^{(3)}\left|E_S^2\right|\right)\vec{E}_P \qquad \textbf{Eq. 4.3}$$

$$\vec{P}^{(3)}(\omega_S)=\varepsilon_0\left(\chi_{R2}^{(3)}\left|E_P^2\right|+\chi_S^{(3)}\left|E_S^2\right|\right)\vec{E}_S \qquad \textbf{Eq. 4.4}$$

From Eq. 4.3 and 4.4, the quantities χ_{R1} and χ_{R2} are responsible for the coupling between E_P and E_S in Eq. 4.1 and 4.2 and correspond to the Raman gain process. The

terms $\chi_P^{(3)}$ and $\chi_S^{(3)}$ will be responsible for effects such as self-focusing, field-induced birefringence, self-phase modulation, etc. They are not considered since they do not participate to the Raman gain process **[Shen 1984]**.

For simplicity we assume plane waves and in this case the field can be written as

$$E_{Pi} = \frac{1}{2}\mathrm{E}_{Pi0}\exp(i\omega_p t - K_p z) + c.c. \qquad \textbf{Eq. 4.5}$$

Where E_{Pi} is the incident (pump) field of frequency ω_p and wave vector K_p. The Raman signal (or scattered) field takes the form

$$E_{Si} = \frac{1}{2}\mathrm{E}_{Si0}\exp(i\omega_s t - K_s.\vec{r}) + c.c. \qquad \textbf{Eq. 4.6}$$

Where in this case ω_s is the signal (scattered) frequency, K_s is the signal (or scattered) wave vector.

Assuming the slowly varying envelope approximation (SVEA) which considers that the magnitude of the electric fields varies slowly as compared to the wavelength, the nonlinear wave equations 4.1 and 4.2 can be solved using the following equations:

$$\left(\frac{\partial}{\partial z} + \frac{\alpha_P}{2}\right)E_{Pi0} = i\left(\frac{\omega_P}{4n_P C}\right)\chi_R^{(3)}\left|E_S\right|^2 E_{Pi0} \qquad \textbf{Eq. 4.7}$$

$$\left(\frac{\partial}{\partial z}+\frac{\alpha_S}{2}\right)E_{Si0}=i\left(\frac{\omega_S}{4n_S C}\right)\chi_R^{(3)}\left|E_P\right|^2 E_{Si0}\,, \qquad \textbf{Eq. 4.8}$$

Where α_P and α_S represent the attenuation coefficients, n_p and n_s are the refractive index at the pump and at the pump and Stokes wavelengths, respectively.

Let's assume a simple diatomic molecule to develop the classical equation monitoring the Raman scattering. If we assume a spring between its nuclei **[Boyd 1992]**, the simple harmonic oscillator model (SHO) the vibration of an electron with the nuclei around its equilibrium position can be described by

$$\frac{d^2 q_\beta}{dt^2}+\Gamma_\beta\frac{dq_\beta}{dt}+\Omega_\beta^2 q_\beta=\frac{F_q}{m_\beta}\,, \qquad \textbf{Eq. 4.9}$$

Where q_β represents the normal coordinate position around its equilibrium position, Γ_β represents the damping of the normal mode, Ω_β is the resonant vibrational frequency, and F_q is the force driving the mode vibration, m_β is the effective mass for the vibration.

The fundamental relation between the incoming electric field E, and the induced dipole moment P, is

$$\vec{P} = \alpha_{ij}^{\beta}\vec{E} = \left(\alpha_{0ij}^{\beta} + \frac{\partial \alpha_{ij}^{\beta}}{\partial q_{\beta}} |_{q_{\beta}=0}\, q_{\beta} \right)\vec{E} \,. \qquad \textbf{Eq. 4.10}$$

As given before, α_{ij}^{β} represents the polarizability tensor, and E is the total field. In the case of Raman gain, the perturbation of the molecular polarizability induces a nonlinear interaction, in which the driving force, F_q, takes the form

$$F_q = \frac{1}{2}\frac{\partial \alpha_{ij}^{\beta}}{\partial q_{\beta}}\bigg|_{q_{\beta}=0} E\,E \qquad \textbf{Eq. 4.11}$$

Hence, the solution of Eq. 4.9 is given by

$$q_{\beta} = \frac{1}{2m}\frac{\partial \alpha_{ij}^{\beta}}{\partial q_{\beta}}\bigg|_{q=0} EE\,\frac{1}{\Omega_{\beta}^{2} - \Omega^{2} - i\Omega\Gamma_{\beta}} + c.c \qquad \textbf{Eq. 4.12}$$

In the case of the stimulated Raman scattering process, the nonlinear polarization can be written as:

$$P^{NL} = N_{\beta}\frac{\partial \alpha_{ij}^{\beta}}{\partial q_{\beta}}\bigg|_{q=0} q_{\beta}\vec{E} \qquad \textbf{Eq. 4.13}$$

Using the Eq. 4.3, 4.4 and Eq. 4.13, the Raman contribution to the nonlinear susceptibility $\chi^{(3)}$ can be determined. One can formulate then an effective $\chi_{eff}^{(3)}$ that can be employed in the slowly varying envelope approximation (SVEA). Considering negligible absorption (α=0), SVEA gives the growing field at frequency ω_s as

$$\frac{d}{dz}\mathrm{E}_{\beta}(\omega_s) = i\frac{N_{\beta}\omega_s}{4n_s c\varepsilon_0}\frac{\partial\alpha_{ij}^{\beta}}{\partial q_{\beta}}|_{q_{\beta}=0}\, q_{\beta}^{*}\mathrm{E}(\omega_p) \qquad \textbf{Eq. 4.14}$$

Which leads to:

$$\frac{d}{dz}\mathrm{E}_{\beta}(\omega_s) = i\frac{N_{\beta}\omega_s}{8m_{\beta}n_s n_p c^2\varepsilon_0^2}|\frac{\partial\alpha_{\beta}}{\partial q_{\beta}}|_{q_{\beta}=0}|^2\,\frac{\Omega_{\beta}^2-\Omega^2-i\Omega\Gamma_{\beta\_HWHM}}{(\Omega_{\beta}^2-\Omega^2)^2+\Omega^2\Gamma_{\beta\_HWHM}^2}I(\omega_p)\mathrm{E}_{\beta}(\omega_s) \quad \textbf{Eq. 4.15}$$

The imaginary part of $\chi_{eff}^{(3)}$ corresponds to the Raman gain, and the real part the accompanying dispersion in the refractive index. Solving for the real part of Eq. 4.15 gives

$$\mathrm{E}_{\beta}(\omega_s, z) = \mathrm{E}(\omega_s,0)\exp[\frac{g_R(\Omega)}{2}I(\omega_p)z] \qquad \textbf{Eq. 4.16}$$

So that the Raman gain coefficient (defined by $I_{\beta}(\omega_s,z) = I(\omega_s,0)\exp[g_R I(\omega_p)z]$) is

$$g_R(\Omega) = \frac{N_\beta \omega_s \pi}{2 m_\beta n_s n_p c^2 \varepsilon_0^2} \left| \frac{\partial \alpha_\beta}{\partial q_\beta} \right|_{q_\beta = 0}^2 \frac{\Omega \Gamma_{\beta\_HWHW} / 2\pi}{(\Omega_\beta^2 - \Omega^2)^2 + \Omega^2 \Gamma_{\beta\_HWHM}^2} \qquad \textbf{Eq. 4.17}$$

Eq. 4.15 can be rewritten in terms of the pump intensity I_p and Stokes light intensity I_S

$$\frac{dI_S}{dz} = g'_R I_P I_S - \alpha_S I_S \qquad \textbf{Eq. 4.18}$$

In Eq. 4.18, the $1/\lambda$ dependence is factored out from the g'_R formulation. There is still dispersion dependence (excluding n_S and n_P) in the Raman gain coefficient, which is inherent to the hyperpolarizability tensor itself.

In the case of a Raman gain media, the gain must overcome the losses in the system, (i.e. the product of $g_R \cdot I_P$ needs to be greater than α_S). When this condition is satisfied the material can be used as an optical amplifier.

For the special case where pump depletion is neglected, assuming that $I_p(z) = I_p(0)\exp(-\alpha_p z)$, the solution of Eq. 4.18 is given by

$$I_S(L) = I_S(0)\exp(g_R I_P(0) L_{eff} - \alpha_S L), \qquad \textbf{Eq. 4.19}$$

Where L_{eff} is the fiber effective length defined as

$$L_{eff} = \frac{1-\exp(-\alpha_p L)}{\alpha_p}. \qquad \textbf{Eq. 4.20}$$

Assuming $\alpha_s=\alpha_p=0$, the Raman gain coefficient yields

$$g_R = \frac{1}{I_P(0)L}\ln\left(\frac{I_s(L)}{I_s(0)}\right). \qquad \textbf{Eq. 4.21}$$

The experimental experiment on Raman gain measurements is not an easy task and requires a dedicated experimental set up. Few experiments have been conducted to measure the Raman gain cross section on bulk glass. Stegeman et al. implemented a set up using picosecond pulses of high irradiance at 1064 nm for the pump source and a wavelength tunable source from an Optical Parametric Generator/Optical Parametric Amplifier (OPG/OPA) as the amplified probe. Since Raman gain is primarily a polarization-sensitive process, the probe was linearly polarized at 45^o with respect to the linear pump polarization. The polarization of the probe beam parallel to the pump beam polarization was used to detect approximately 10% gain, while the polarization of the probe beam orthogonal to the pump beam polarization was the "effective" input energy. The depolarization ratio (VV/VH) - obtained from spontaneous Raman scattering experiments on the same glasses - was used as a correction factor since the probe beam polarization orthogonal to the pump beam polarization did experience minor Raman excitations in these glasses. After propagation through the sample a monochromator was

used to filter the pump from the probe wavelength, and the two probe polarizations enter two identical, calibrated germanium detectors via a polarizing beam splitter. In concert with a calibrated silicon detector for the 1064 nm pump, Raman gain can be measured on a shot-to-shot basis, and averaging was done over hundreds of shots. The experimental apparatus was calibrated on a 3.18 mm thick Corning 7980-2F fused silica sample (peak Raman gain = 1.1 x 10^{-13} m/W) **[Stegeman 2006]**.

1.2 Raman gain estimation from spontaneous Raman scattering cross-section measurements

Hellwarth in 1963 predicted that there is a relation between spontaneous and stimulated Raman scattering processes **[Hellwarth 1963][Hellwarth 1975][Boyd 1992].** The Raman gain coefficient (g_R [cm/W]) can be given as:

$$g_R \ [cm/W] = \frac{4\pi^3 NC^2}{\hbar\omega_S^2\omega_P n_S^2}\left(\frac{\partial^2\sigma}{\partial\omega\partial\Omega}\right), \qquad \textbf{Eq. 4.22}$$

N is the number density of molecules, ω_S and ω_P are the Stokes (signal) and pump (laser) frequencies respectively, n_S is the refractive index at the Stokes wavelength, and $\frac{\partial^2\sigma}{\partial\omega\partial\Omega}$ is defined as the differential spontaneous Raman scattering cross-section.

G. Dai et al and later C. Rivero et al **[Dai 2004][Rivero 2005-2]** developed a method to calculate the Raman gain of glasses. Their work show that the Raman gain, g_R ($m.W^{-1}$) can be calculated from the differential spontaneous Raman scattering cross-section measured in the spontaneous Raman scattering spectra in vertically polarized.

Hence, taking into account the Fresnel transmission coefficient at the air-glass boundary and the effect of refraction on the solid angle subtended at the detector for a typical Raman scattering experiment, the ratio of the peak intensity of a Raman scattered line $I_{\beta}^{k,r}(\omega_P - \Omega_{\beta}^{k})$ in air (at the detector) due to the β'th normal mode of the k'th species (in the glass) to the incident intensity $I_{inc}(\omega_P)$ in air, at frequency ω_P is given by **[Rivero 2005-2].**

$$\frac{I_{\beta}^{k,r}(\omega_P - \Omega_{\beta}^{k})}{I_{inc}(\omega_P)\Delta\Omega} = K_{SR}^{k,r}(\omega_P - \Omega_{\beta}^{k})^4 \frac{[1 - R(\omega_P)][1 - R(\omega_P - \Omega_{\beta}^{k})]}{[n(\omega_P - \Omega_{\beta}^{k})]^2} \left| \frac{\partial \alpha_{ij}^{k,r}(\omega_P - \omega_{k,r})}{\partial q_{\beta}^{k}} \right|^2 \quad \textbf{Eq. 4.23}$$

Here $\Delta\Omega$ is the solid angle, Ω_{β}^{k} is the frequency shift of the Raman peak from the laser frequency, R is the reflectance coefficient $\left(R(\omega) = \frac{[n(\omega) - 1]^2}{[n(\omega) + 1]^2} \right)$ at normal incidence, and the $[n(\omega_P - \Omega_{\beta})]^2$ in the denominator is a consequence of the solid angle correction. Eq. 4.23 shows all of the explicit dependence on frequency, and all of the phonon and electromagnetic parameters, including the Bose-Einstein thermal population

factor, are contained in the constant $K_{SR}^{k,r}$. The dependence of the Raman gain coefficient (defined for the pump intensity) on frequency is given by

$$g_{R\beta}^{k,r}(\omega_P - \Omega_\beta^k) = K_{RG}^{k,r} \frac{\left(\omega_P - \Omega_\beta^r\right)}{n(\omega_P - \Omega_\beta^r) n(\omega_P)} \left| \frac{\partial \alpha_{ij}^{k,r}(\omega_P - \omega_{k,r})}{\partial q_\beta^k} \right|^2 \quad \textbf{Eq. 4.24}$$

Where $K_{RG}^{k,r}$ is a constant that contains all the phonon and electromagnetic constant parameters and is different from $K_{SR}^{k,r}$. When all of the experimental details are taken into account, it is therefore possible to evaluate the Raman gain coefficient from the spontaneous Raman spectrum, at the *same excitation frequency*. The detailed relationship is

$$g_{R\beta}^{k,r}(\omega_P - \Omega_\beta^r) = \frac{K_{RG}^{k,r}}{K_{SR}^{k,r}} \frac{n(\omega_P - \Omega_\beta^r)}{\left(\omega_P - \Omega_\beta^r\right)^3 n(\omega_P)\left[1 - R(\omega_P)\right]\left[1 - R(\omega_P - \Omega_\beta^r)\right]} \frac{I_\beta^{k,r}(\omega_P - \Omega_\beta^r)}{I_{inc}(\omega_P)\Delta\Omega} \quad \textbf{Eq. 4.25}$$

The Raman susceptibility exhibits dispersion with frequency, it is the same as the refractive index dispersion because not all of the vibrational modes couple (modulate) equally to the molecular polarizability **[Rivero 2005-2]**. Thus, standard spontaneous Raman spectroscopy can be deployed to estimate the strength of the Raman gain response of the material, using the relationship derived in Eq. 4.25. Finally, the Raman gain

spectrum parallels the spontaneous Raman spectrum after the correction of the spontaneous Raman spectrum by the Bose-Einstein correction factor **[Stolen 1973]**.

The Bose-Einstein correction to the spontaneous Raman scattering intensity can be written as

$$g_R \propto \frac{I_S}{[n_{BE}(\upsilon,T)+1]} \qquad \textbf{Eq. 4.26}$$

Where $n_{BE}(\upsilon,T)=\left[\exp\left(\frac{h\upsilon}{kT}\right)-1\right]^{-1}$ is the Bose-Einstein population factor which accounts for the thermal statistical fluctuation for each individual mode.

By measuring the Raman spectra of a test glass under the same experimental conditions as for fused silica at a laser wavelength for which the peak Raman gain for fused silica is known, the peak Raman gain of the test glass at that frequency for a Raman active mode can be deduced:

$$\frac{g_{R\beta}^{r,k}(\omega_{P1}-\Omega_{\beta}^{r})}{g_{R\beta'}^{r',k'}(\omega_{P1}-\Omega_{\beta'}^{r'})}=$$

$$\frac{(\omega_{P1}-\Omega_{\beta'}^{r'})^3}{(\omega_{P1}-\Omega_{\beta}^{r})^3}\frac{n(\omega_{P1}-\Omega_{\beta}^{r})n'(\omega_{P1})}{n'(\omega_{P1}-\Omega_{\beta'}^{r'})n(\omega_{P1})}\frac{\left[1-R'(\omega_{P1}-\Omega_{\beta'}^{r'})\right]\left[1-R'(\omega_{P1})\right]}{\left[1-R(\omega_{P1}-\Omega_{\beta}^{r})\right]\left[1-R(\omega_{P1})\right]}\frac{I_{\beta}^{k,r}(\omega_{P1}-\Omega_{\beta}^{r})}{I_{inc}(\omega_{P1})}\frac{I_{inc}'(\omega_{P1})}{I_{\beta'}^{r',k'}(\omega_{P1}-\Omega_{\beta'}^{r'})}, \qquad \textbf{Eq. 4.27}$$

Where the prime parameters belong to fused silica. Explicitly, $\Omega_{\beta}^{r'}$ is the peak Raman frequency shift at 440 cm^{-1} in fused silica, and Ω_{β}^{r} is the Raman active mode of for instance the most intense band in tellurite at around 665 cm^{-1}. Then the spectra can be compared to reference spectra such as SiO_2 or Schott SF6 glasses which have been measured in the literature. The procedure is then the following:

i. The glass spectrum of interest has to be measured under the same conditions as then the reference spectrum of SiO_2,

ii. Reflection loss has to be taken into account using the factor $F_{R\text{-}SO,}$ to correct for the reflection loss and variation in the internal solid angle:

$$F_{R-SO} = \frac{(1+n_{sam})^4}{(1+n_{SiO_2})^4}, \qquad \textbf{Eq. 4.28}$$

Where n_{sam}=refractive index of sample at the pump wavelength and n_{SiO_2}=1.46.

iii. To eliminate low wavenumber thermal effects due to the dispersion at the pump, the spectra has to be divided by the Bose-Einstein factor F_{BE} given by:

$$F_{BE}(\nu, T) = 1 + \left[exp\left(\frac{h\nu}{kT}\right) - 1\right]^{-1}, \qquad \textbf{Eq. 4.29}$$

Where ν=frequency of the Raman shift relative to the pump, k=Boltzmann constant (1.381×10^{-23} $J.K^{-1}$).

iv. Then we can approximate the Raman gain by multiplying the corrected spectral intensity I_{corr} by:

$$g_R = I_{corr} \times \left(\frac{n_{SiO_2}}{n_{sam}}\right)^2 \times g_{R_{SiO_2}}, \qquad \textbf{Eq. 4.30}$$

Where $g_{R_{SiO_2}}$=Raman gain of fused silica (0.89×10^{-13} m.W^{-1}) measured at λ=1064 nm for a Stokes shift of 440 cm^{-1}.

Following this procedure, Stegeman et al have demonstrated that the Raman gain cross section can be estimated by the measurement of spontaneous Raman cross section using MicroRaman apparatus. Due to the different corrections and the sensitivity of the measurements (reflection loss, variation of the internal solid angle, refractive index measurement, thermal effect), the calculated Raman gain owns a high error bar at ±15%. Raman gain measurements of thallium-tellurium oxide glasses are showed in Figure 4.2 **[Stegeman 2005]**.

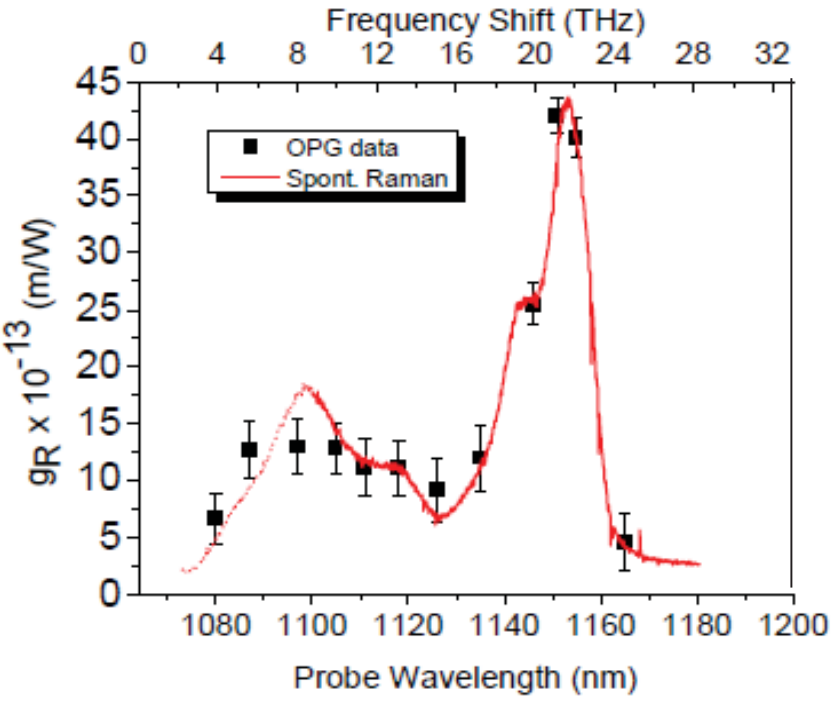

Figure 4.2 Raman gain curve obtained from spontaneous Raman measurement and Raman gain Coefficient obtained by using pump on the glass composition $59.5TeO_2$–$25.5TlO_{1/2}$–15PbO taken [Stegeman 2006]

Figure 4.2 clearly shows the good agreement between the data obtained by the experiemental Raman gain set up based on the Optical Parametric Generator (OPG) and the calculated spontaneous Raman scattering approaches employed in the former and present study.

Spontaneous Raman scattering can be measured on different spectral region depending about the wavelength of the laser. The impact of the laser wavelength has been investigated by Rivero and Stegeman **[Rivero 2005-1][Stegeman 2006]** and the dispersion effect has been quantified.

1.3 Dispersion effect on Spontaneous Raman cross-section

Rivero et al. have demonstrated the importance for accurate comparison of Raman gain cross section and spontaneous Raman cross section to allow the measurement at comparable wavelength. The ratio in the relation Eq. 4.27 only cancels out the $1/\lambda^4$ dependence of the Raman scattering. As described in the Figure 4.3 the relative Raman gain as compared to silica shows that the relation Eq. 4.27 does not take into account the dispersion of the Raman susceptibility sensor which is different from the studied glasses and the SiO_2 reference silica. **[Rivero 2005-1][Rivero 2005-2][Stegeman 2006]**.

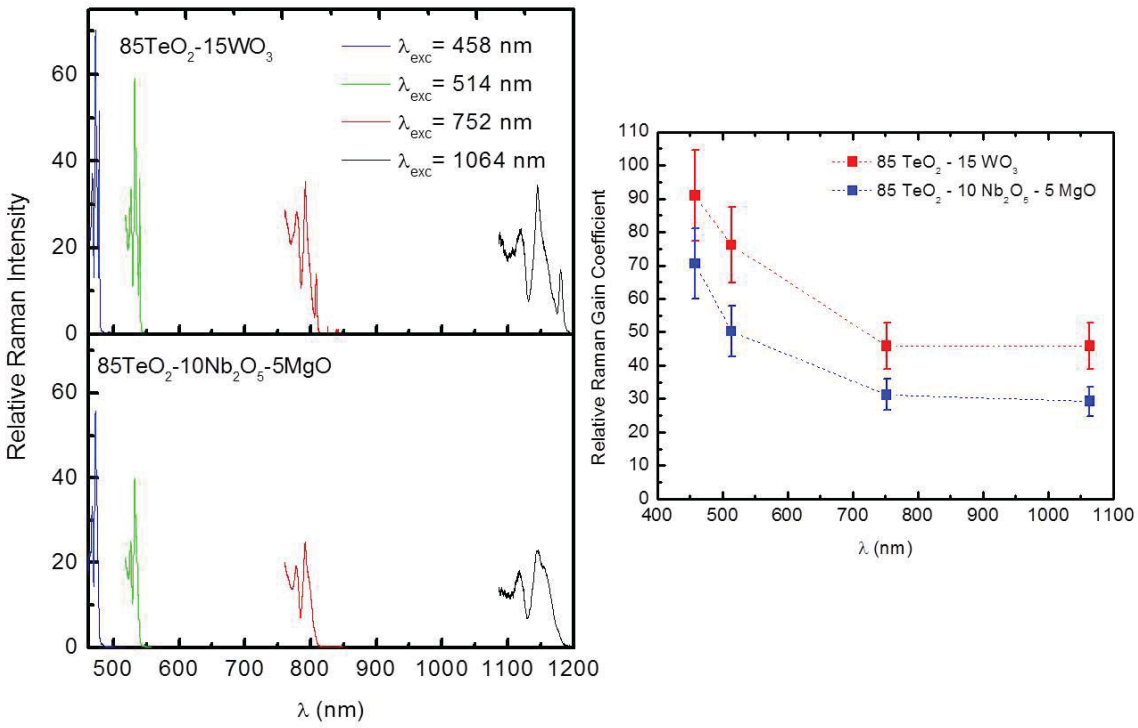

Figure 4.3 VV Polarized Experimental Spontaneous Raman Spectrum of samples $85TeO_2$-$15WO_3$ and $85TeO_2$-$10Nb_2O_5$-5MgO, normalized to SiO_2 measured at different wavelength (left) and Relative Raman gain coefficient calculated at $665cm^{-1}$ versus the wavelength (right) [Rivero 2005-1][Rivero 2005-2]

An overlap between the measurement of the spontaneous Raman cross section at 514 nm, and the absorption tail of the tellurite glasses appears, leading to an inherent dispersion of the spectrum. Rivero et al. showed a direct relationship between the differences of the spontaneous Raman cross section intensities and the wavelength dispersion **[Stolen 2000]**.

In the case of multi-component materials, a change of the shape of the spontaneous Raman spectra due to a potential resonance between the laser wavelength and a specific electronic transition of a molecule can appear **[Kato 1971][Hellwarth 1975][Boling 1978][Yoshino 2003][Lisinetskii 2005]**.

To avoid any dispersion effect on the Spontaneous Raman spectrum, Raman measurements are collected in the non-resonant regime. Tellurite-based glasses owns a multiphonon edge at < 400 nm.

1.4 Spontaneous Raman scattering cross-section measurements

In order to estimate the spontaneous Raman cross section of the different tellurite glasses studied in the present work, polarized (VV) spontaneous Raman spectra of the vitreous materials were measured using a micro-Raman setup with an excitation wavelength of 752 nm. The measurements have been conducted far from the resonance in the UV to avoid dispersion effects

A 100X microscope objective, with a numerical aperture of 0.75, was used to focus the light on the front polished surface of the sample. A combination of polarizers was used to select the polarization direction (vertical V and/or horizontal H) of the backscattered light. The scattered light was collected and spectrally analyzed with a CCD detector mounted on the exit port of a single grating spectrograph, with a typical resolution of about 6 cm^{-1}. The Rayleigh line was suppressed with a holographic notch fiber. The Raman gain coefficient g_R (m/W) was calculated from spontaneous Raman scattering spectra in vertically polarized (VV) scattering geometry after application of corrective factors and by scaling the Raman response to well-characterized standards i.e. fused-silica and Schott SF6 glasses as described by O'Donnell et al. **[O'Donnell 2008].**

1.5 Hyper-Rayleigh Scattering of glasses: principles

Hyper-Rayleigh scattering (HRS), also called harmonic light scattering (HLS), is an elastic nonlinear three-photons process, where we detect the scattered light at the optical frequency 2ω from an intense incident laser pulsed at ω **[Verbiest 2009]**. In contrast to second harmonic generation (SHG) where light propagates in a material, HRS is a spontaneous emission of one photon after a biphotonic excitation, where no phase relation occurs between the scatterers. HRS has become a popular and well adapted technique to quantify hyperpolarizability of molecules, i.e. molecular nonlinearities. The HLS signal is indicative of the structure **[Verbiest 2009]** (in terms of intensity) and of the dynamics **[Maker 1970][Kaatz 1996]**, (in terms of width and profile) of the molecules or elementary structural units (ESU) that constitute the material. In particular, one of us has

recently shown that HLS is a unique tool to probe the multipolar symmetry structure of ESU in isotropic materials, like ionic liquids **[Rodriguez 2010]** and even silica glass **[Rodriguez 2012]**.

Historically, inorganic glasses are generally discussed as a continuous network of polyhedral connected by common atoms of polyhedral **[Zachariasen 1932]**. Warren confirmed this affirmation of a structural model of glass by X-ray studies **[Warren 1936]**. Glasses are defined by a short-range order and a long-range disorder. This topological disorder and the absence of translational symmetry occur the molecules an arbitrary orientation. The short-range order cannot be extended to the long-scale, leading to a spatial homogeneity and a loss of the structural correlations (occurring for scale bigger than 30 -50 Å). This scale value is less than the wavelength of vibrational excitations, investigated by optical methods in vibrational spectroscopy **[Denisov 1987].**

The experimental setup is configured as explained in Chapter 3, session 2.4.2, namely a classical 90° scattering geometry (Figure 4.4), and it is based on a previous setup **[Rodriguez 2006]** that has been upgraded from nanosecond to picosecond pulse and also used for hyper-Raman and Raman studies of several liquids **[Quinet 2004][Quinet 2006]** and solids **[Rodriguez 2012][Rodriguez 2013]**. The incident radiation at 1064nm is obtained from a passively mode-locked Nd : YVO4 laser (EKSPLA) producing trains of 65 ps, ≤50 μJ pulses at a repetition rate of 2 kHz, avoiding any photostructural modification. The vertically polarized scattered HRS response, $I_{\Psi V}$, is collected using a general elliptical polarization of the incident light, denoted by the angle

ψ of a rotating half-wave plate upstream of a fixed quarter-wave plate as reported in Figure 4.4. With this setup, it is also possible to use linear polarization excitation to obtain the standard vertical-vertical (VV or //) response with ψ = 90° or the horizontal-vertical (HV or ⊥) response with ψ = 0.

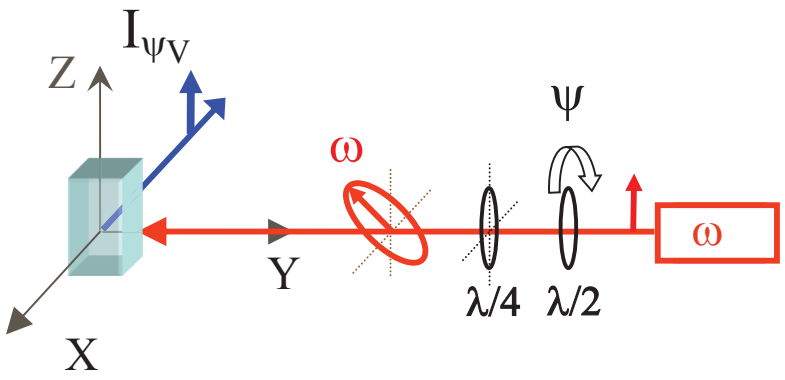

Figure 4.4 Sketch of the HRS experimental setup with different polarization capabilities: ψ = 0, 90 degree corresponding respectively to a horizontal (H) and linear vertical (V) incident polarization; and ψ=±45 degree correspond to left and right circular polarization

For low-symmetry structures of ESU expected in glasses, it is more convenient to discuss the HRS measurements in terms of multipolar components. The use of spherical invariants allows the β tensor to be decomposed as a sum of dipolar (J=1) and octupolar (J=3) tensorial β_J components and we define a nonlinear anisotropy parameter $r_{AP} = |\beta_3| / |\beta_1|$. In this way, the two standard HRS invariants can be expressed as:

$$I_{VV} \propto \left\langle \beta_{ZZZ}^2 \right\rangle = \frac{9}{45}|\beta_1|^2 + \frac{6}{105}|\beta_3|^2 = \left(\frac{9}{45} + \frac{6}{105} r_{AP}^2\right)|\beta_1|^2 \qquad \textbf{Eq. 4.31}$$

$$I_{HV} \propto \left\langle \beta_{ZXX}^2 \right\rangle = \frac{1}{45}\left|\beta_1\right|^2 + \frac{4}{105}\left|\beta_3\right|^2 = \left(\frac{1}{45} + \frac{4}{105} r_{AP}^2\right)\left|\beta_1\right|^2 \quad \textbf{Eq. 4.32}$$

In this multipolar description previously introduced **[Rodriguez 2010]**, the general HRS response of an isotropic material (including glass materials) is given by:

$$I_{\Psi V} = G f_L^2 \frac{\rho}{M}\left[C_{\Psi V}\left|\beta_1\right|^2\right] I_\omega^2 \quad \textbf{Eq. 4.33}$$

Where G is a constant taking into account geometrical, optical and electrical factors of the experiment setup; $f_L{}^2$ is described as the local field correction approximated using the high frequency Lorentz-Lorenz spherical cavity expression $f_L = f(\omega)^2 f(2\omega)$ with $f(\omega) = \left(n_\omega^2 + 2\right)/3$ including refractive indices at the optical frequencies ω and 2ω (measured by the Brewster angle method **[Rodriguez 2008]**); ρ is the volumetric weight (g.cm^{-3}) (measured by Archimedes' method), M is the molecular weight (g.mol^{-1}); $C_{\Psi V}$ is the factor accounting for the orientational average of the ESU spherical components of the hyperpolarizability given by:

$$C_{\Psi V} = \left\{\left(\frac{9}{45} + \frac{6}{105} r_{AP}{}^2\right) + \left(-\frac{20}{45} + \frac{10}{105} r_{AP}{}^2\right)\cos^2\Psi + \left(\frac{12}{45} - \frac{12}{105} r_{AP}{}^2\right)\cos^4\Psi\right\} \quad \textbf{Eq. 4.34}$$

For a non-polarized scattered signal, since both polarizations are detected with equal sensitivity, the orientational average over β is the sum of equations Eq. 4.31 and Eq. 4.32:

$$\left|\beta_{HRS}\right| = \sqrt{\left\langle \beta_{HRS}^2 \right\rangle} = \sqrt{\left\langle \beta_{ZZZ}^2 \right\rangle + \left\langle \beta_{ZXX}^2 \right\rangle} \qquad \textbf{Eq. 4.35}$$

The associated depolarization ratio is defined as:

$$DR = \frac{I_{VV}}{I_{HV}} = \frac{\left\langle \beta_{ZZZ}^2 \right\rangle}{\left\langle \beta_{ZXX}^2 \right\rangle} = 9\left(1 + \frac{2}{7} {r_{AP}}^2\right) \Big/ \left(1 + \frac{12}{7} {r_{AP}}^2\right) \qquad \textbf{Eq. 4.36}$$

Note the nonlinear anisotropy parameter r_{AP} provides a quantitative classification of the studied ESU in terms of their more or less pronounced octupolar/dipolar character. More straightforwardly, according to the symmetry of the ESU, the experimental depolarization ratio *DR* varies between typical values of octupolar-like structures ($r_{AP} \to \infty$) where DR = 3/2 and those of dipolar-like structures ($r_{AP} = 0$) where DR = 9.

To summarize, a polarization scan, obtained by varying ψ keeping a constant incident power, is a key experimental curve (Eq. 4.34) that gives directly the anisotropic parameter r_{AP} and also the depolarization ratio *DR*. Second, the quadratic dependence of I_{VV} (power scan), obtained by varying the incident power, scales the HRS response of the

ESU (Eq. 4.33) to obtain finally the dipolar $|\beta_1|$ and octupolar $|\beta_3|$ components as well as the commonly used term $|\beta_{HRS}|$ which gives an average-type response of the ESU.

2 Results

2.1 Raman gain measurement: TeO_2-$TaO_{5/2}$-ZnO, TeO_2-$NbO_{5/2}$, TeO_2-$BiO_{3/2}$-ZnO

Figure 4.5 shows the VV polarized Raman spectra of TeO_2-$TaO_{5/2}$-ZnO glasses obtained with an excitation at 785 nm. Spontaneous Raman spectroscopy and vibrational signatures have been extensively described in Chapter 3. As explained previously, the maximum of the Raman gain coefficient is corresponding to the peak **5** around 660 cm-1 (see Table 3.3 in chapter 3) assigned to a symmetric stretching of TeO_4 trigonal bipyramidal units, which exhibit the most intense magnitude. Calculated Raman gain values are reported in Table 4.1.

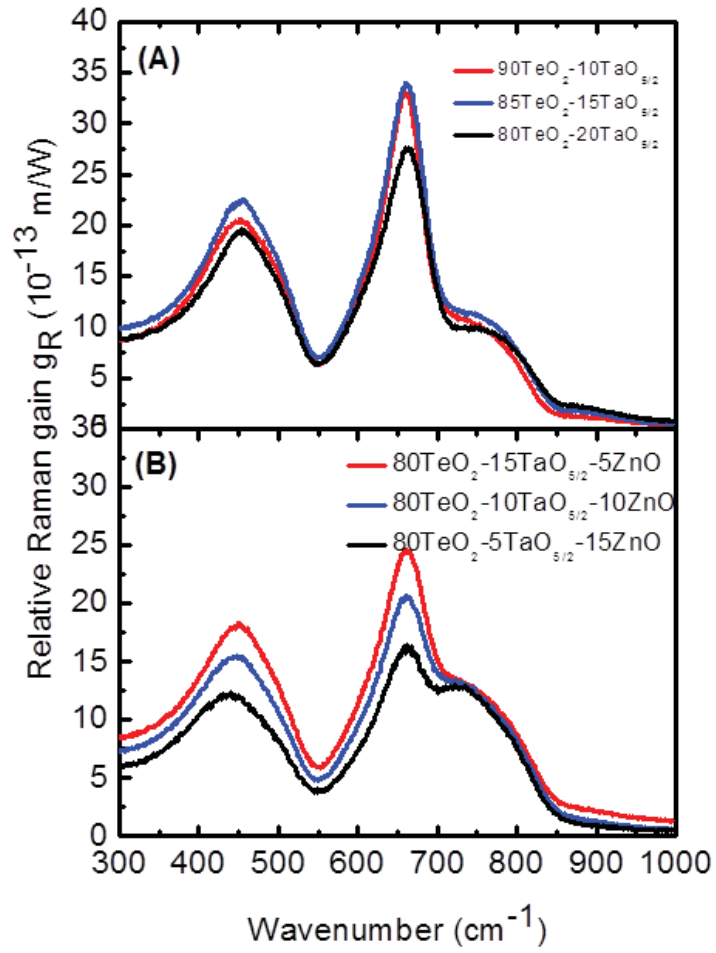

Figure 4.5 Raman spectra of bulk glass systems (100-x)TeO_2-x$TaO_{5/2}$ in (A) and 80TeO_2-(20-x)$TaO_{5/2}$-xZnO in (B) depicted in the form of relative Raman gain using pure SiO_2 as reference

The magnitude of the Raman gain taken at 660 cm^{-1} in the binary glass system is fairly constant, whereas in the ternary glass system, a drastic decrease of 50% is observed. This effect is mainly driven by the decrease of the Raman response associated to the TeO_4 disphenoids and the Te-O-Te bridges. As seen by Soulis and Mirgorodsky from ab initio studies **[Soulis 2008][Mirgorodsky 2006]**, the introduction of a glass

modifier reduces the $(TeO_2)_p$ chain structure of the glass, modifying the polarizability and hyperpolarizability responses. As observed in Chapter 3, the introduction of zinc oxide leads to a partial degree of depolymerization of the TeO_4 chain-like structure as revealed by spectral modifications but also it reduces both the Raman and hyper-Raman cross-sections. Zinc oxide is preferentially introduced into Te-O-Te tellurite chains, leading to a depolymerization of the glass network. Since the polymerization of the tellurite chains affects the linear and nonlinear susceptibilities, one observes a drastic decrease of the Raman cross sections and intrinsically a decrease of the Raman gain.

Glass Composition	**n (752 nm) [± 0.01]**	**Number density of Te atoms ($x10^{27}$ mol/m^3)**	**Area of relative Raman gain deconvoluted peak ($x10^{-16}$ m/W.cm^{-1})**	**Relative Raman gain to SiO_2 measured at 660 cm^{-1} with λ=752 nm (10^{-13} m/W) ±15%**
$90TeO_2$-$10TaO_{5/2}$	2.15	18.99	1.794	37.2
$85TeO_2$-$15TaO_{5/2}$	2.15	17.92	1.868	38.2
$80TeO_2$-$20TaO_{5/2}$	2.14	16.79	1.698	31.1
$80TeO_2$-$15TaO_{5/2}$-5ZnO	2.12	17.21	1.388	27.8
$80TeO_2$-$10TaO_{5/2}$-10ZnO	2.08	17.63	1.177	23.3
$80TeO_2$-$5TaO_{5/2}$-15ZnO	2.06	18.10	0.902	18.5

Table 4.1 n linear refractive indices, number density of Te atoms, area of relative Raman gain peak and relative Raman gain as a function of $TaO_{5/2}$ and ZnO contents

These important experimental observations added to the theoretical knowledge permit one to clarify the rule of each glass components into a glass matrix, and depending on the desired applications, it will permit to well-chosen glass modifiers to be used to engineer the glass structure.

Figure 4.6 shows the VV polarized Raman spectra of TeO_2-$NbO_{5/2}$ glasses obtained with an excitation at 785 nm. Spontaneous Raman spectroscopy and vibrational signatures have been extensively described in Chapter 3. As explained previously, the Raman gain coefficient is based on the symmetric stretching of TeO_4 trigonal bipyramidal units, which exhibit the most intense magnitude. Calculated Raman gain values are reported in Table 4.2.

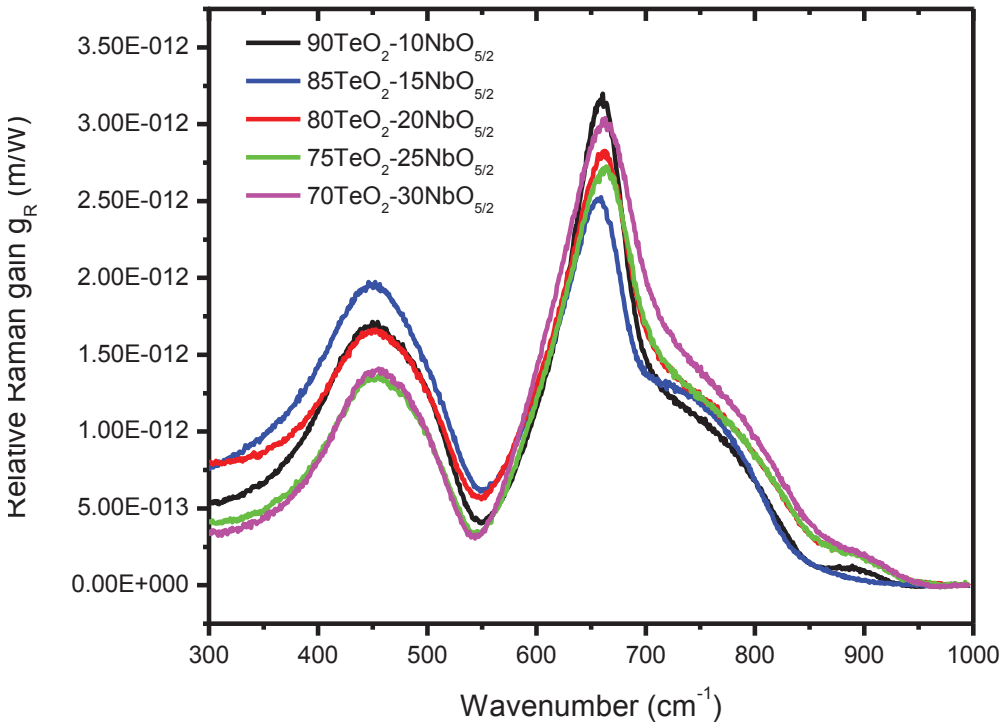

Figure 4.6 Raman spectra of bulk glass systems (100-x)TeO_2-x$NbO_{5/2}$ depicted in the form of relative Raman gain using pure SiO_2 as reference

Glass Composition	n (752 nm) [± 0.01]	Number density of Te atoms ($x10^{27}$ mol/m^3)	Relative Raman gain to SiO_2 measured at 660 cm^{-1} with λ=752 nm (10^{-13} m/W) ±15%
$90TeO_2$-$10NbO_{5/2}$	2.14	18.20	31.6
$85TeO_2$-$15NbO_{5/2}$	2.15	17.87	25.2
$80TeO_2$-$20NbO_{5/2}$	2.13	17.24	28.2
$75TeO_2$-$25NbO_{5/2}$	2.16	16.48	27.1
$70TeO_2$-$30NbO_{5/2}$	2.16	15.57	30.1

Table 4.2 n linear refractive index and relative Raman gain as function of $NbO_{5/2}$ content

As explained in Chapter 3, the introduction of a glass modifier changes the structural network with a transformation of the tellurite elementary structural units from a trigonal bipyramidal TeO_4 to a trigonal pyramidal unit TeO_3. In the TeO_2-$NbO_{5/2}$ glass system, the introduction of niobium oxide does not change linearly the magnitude of the Raman gain spectra. Indeed, it is observed firstly a decrease of the Raman gain with the decrease of TeO_2 mol% from 31.6 to 25.2 in glasses following the compositions (90:10) and (85:15) respectively; and then an increase of the Raman gain from 25.2 to 30.1 in glasses following the compositions (85:15) to (70:30). The hypothesis can be confirmed: the variation of the Raman gain takes place within the error bar [± 15%] of the measurement and so there is a fairly constant evolution of the coefficient as function of the glass composition.

Regarding the glass system TeO_2-$BiO_{3/2}$-ZnO following the glass composition (66:21:13) the Raman gain maximum has been measured at 730 cm^{-1} (compared to the usually 660 cm^{-1}) which is the most intense peak of the spectrum and represents g_R = 25.10^{-13} m/W. This glass composition owns high glass modifier content, i.e. a lower TeO_2 content, which leads to a higher TeO_3/TeO_{3+1} content than TeO_4 entities. One has to notice the high Raman cross section associated to the TeO_3/TeO_{3+1} units. The introduction of zinc oxide leads (as explained in Chapter 3) to a strong depolymerization of the tellurium network. The number density of tellurium ions [Te] (mol/m^3) for the composition 66%(TeO_2)-21%($BiO_{3/2}$)-13%(ZnO) is smaller [14.97 $x10^{27}$ mol/m^3] than for instance for the composition 80%(TeO_2)-10%($TaO_{5/2}$)–10%(ZnO) [17.64 $x10^{27}$ mol/m^3], but shows a comparable Raman gain value ($25x10^{-13}$ m/W and $23x10^{-13}$ m/W respectively). As the number density of tellurium is much smaller, we can conclude to a larger Raman cross section of the TeO_3/TeO_{3+1} in the tellurium bismuth zinc glass network than in the TeO_2-$TaO_{5/2}$-ZnO glass system. This phenomenon is indicating that the presence of bismuth leads to modified TeO_3/TeO_{3+1} units with high Raman gain values. The same effect has been observed by Rivero **[Rivero 2005-1]** in $xTeO_2$–(100-x)$TlO_{1/2}$ glass system for composition containing 50%(TeO_2)–50%($TlO_{1/2}$). We remark that bismuth has the same effect than thallium, by creating a special network where the TeO_3/TeO_{3+1} are more polarizable/hyper-polarizable than the TeO_4 entities. The presence of the zinc in the glass network is most likely compensating the benefit effect of the bismuth introduction by lowering the whole Raman response of the tellurite network.

The effect of the crystallization on the Raman has been investigated in the glass system TeO_2-$BiO_{3/2}$-ZnO for the following glass composition (66:21:13) for which a single crystalline phase β-$Bi_2Te_4O_{11}$ can be obtained (Chapter 2). The elaboration of glass ceramics (GC) has been described by Hu et al. **[Hu 2011]**, results are summarized in Table 4.3.

$66TeO_2$-$21BiO_{3/2}$-13ZnO	**First treatment**	**Second treatment**	**Crystal volume fraction**	**Average crystal size**	**Number density of Te atoms ($x10^{27}$ mol/m^3)**	**Relative Raman gain to SiO_2 measured at 660 cm^{-1} with λ=752 nm (10^{-13} m/W) ±15%**
$66TeO_2$-$21BiO_{3/2}$-13ZnO Based glass	-	-	0 %	-	14.97	25
Glass Ceramic 1 (GC1)	17 h at 340 °C	18 h at 345 °C	~ 1 %	~ 20 µm	14.97	19
Glass Ceramic 2 (GC2)	18 h at 330 °C	18 h at 350 °C	~ 5 %	~ 50 µm	14.97	29

Table 4.3 Evolution of the Raman gain coefficient of $66TeO_2$-$21BiO_{3/2}$-13ZnO as function of the crystallization (crystal volume fraction and average crystal size)

We can remark a constant value of the Raman gain by considering the error bar of the measurement [± 15%], as shown in Figure 4.7.

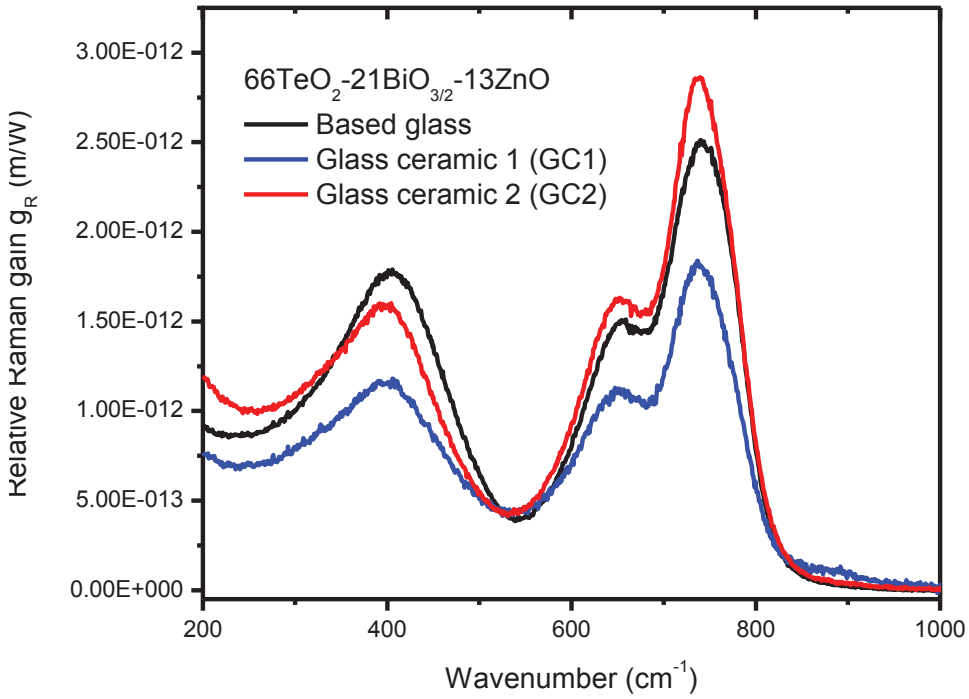

Figure 4.7 Raman spectra of bulk glass and glass ceramic systems $66TeO_2$-$21BiO_{3/2}$-13ZnO depicted in the form of relative Raman gain using pure SiO_2 as reference

The Raman spectra remain similar after crystallization. This effect is due most probably to the strong similarity of the local environment around the tellurium ions in the glass and in the crystalline structure. The β-$Bi_2Te_4O_{11}$ metastable cubic crystal phase has been defined in Chapter 2 as a layout of a $Bi_2Te_2O_7$-like crystal phase between two TeO_2-chain arrangements. The presence of TeO_2 chain-like structure allows us to postulate as to an enhancement of the ability to delocalize electrons and thus improve Raman gain in increasing the polarizability.

The resulting Raman cross section measured on the glass ceramic does not show significant modification in terms of absolute magnitude but the formation of a secondary crystalline phase definitely imparts changes to the glass structure as evident in the Raman spectra. This phenomenon could be related to the increase of the ZnO loading in the remaining (uncrystallized) glassy phase and thus its much larger decrease in localized Raman response. Most likely, it is an averaging of various contributions that we are observing that leads to a small difference in term of Raman cross-section between the virgin glass and the crystalline phase. Additionally, the small variation could also be related to the homogeneity of the crystallization as compared to the measured volume. Note that these glass samples were made in small volumes and thus would exhibit some local compositional variation/inhomogeneity. Subsequent crystallization of these regions would thereby transfer to the glass ceramic. Additionally, precise measurements of crystal volume fraction has not been made, rather, the data in Table 4.3 are results from microscopic investigatiosn that yielded estimates which were correlated with spectroscopic (IR data which illustrated variations in Fresnel losses associated with a changed refractive index in the glass ceramic). Despite these uncertainties, clearly the Raman responses of these infrared transparent glass ceramic materials are unique and offer promise to the ability to engineer glass physical properties (i.e. thermal/mechanical stability) through the creation of a second phase, without degradation to the material's optical quality.

The questions raised here indicate that a deeper, more thorough investigation is definitely necessary to evaluate the crystalline phase Raman response and its impact on the glass

ceramic response. An effort has to be made on the correlation between the crystal's Raman response, average crystal size and crystal volume density to more accurately define how and to what extent, crystallization could locally be used to tailor nonlinear and Raman gain, response.

The crystal phase β-$Bi_2Te_4O_{11}$ is a Bismuth-rich zone. The remaining glass is then a zinc-rich area It has been explained previously **[Guery 2012]** that introduction of zinc oxide into the tellurite network leads to discontinuity of the TeO_2-chains, and so on the decrease of the Raman gain in reducing the global polarizability. In average, no fluctuation of the Raman gain could be observed according to such a hypothesis.

The hyperpolarizability and the Raman gain response can be related by a hyper-Rayleigh scattering measurements, leading to the direct measurement of both hyperpolarizability parameter and depolymerization ratio.

2.2 Hyper-Rayleigh Scattering measurements

Polarization and power scans for TeO_2-$TaO_{5/2}$-ZnO glass samples have been recorded. Acetonitrile (MeCN) has been used as an external reference **[Verbiest 2009]**. Typical power and polarization scan curves obtained with $90TeO_2$-$10TaO_{5/2}$ are reported in Figure 4.8. The different results and parameters from HRS experiments are gathered in Table 4.4.

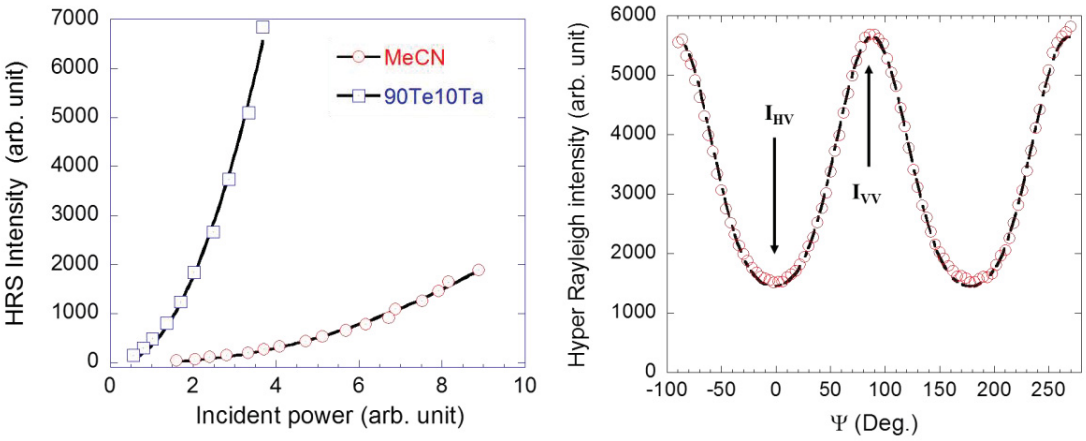

Figure 4.8 Left: Quadratic dependence of the HRS scattered intensity in $90TeO_2$-$10TaO_{5/2}$ (90Te10Ta) glass and acetonitrile (MeCN). Right: Experimental (circles) polarization curve of $90TeO_2$-$10TaO_{5/2}$ and best fit (solid line) according to Eq. 4.34

	$\|\beta_{HRS}\|^2$	β_1	β_3	r_{AP}	Refractive index (n)		ρ (g.cm^{-3})
					532 nm	1064 nm	
Acetonitrile	-	34.3	7.7	0.23	1.34	1.33	0.7822
$90TeO_2$-$10TaO_{5/2}$	131	19.6	21.9	1.12	2.15	2.00	5.81
$85TeO_2$-$15TaO_{5/2}$	120	18.8	20.9	1.11	2.15	2.00	5.91
$80TeO_2$-$20TaO_{5/2}$	117	17.9	21.8	1.22	2.14	1.99	5.99
$80TeO_2$-$15TaO_{5/2}$-5ZnO	94	16.7	18.1	1.08	2.12	1.97	5.89
$80TeO_2$-$10TaO_{5/2}$-10ZnO	66	14.0	15.4	1.11	2.08	1.93	5.78
$80TeO_2$-$5TaO_{5/2}$-15ZnO	71	14.4	15.9	1.11	2.06	1.91	5.67

Table 4.4 HRS intensity $|\beta_{HRS}|^2$, dipolar and octupolar β_J values (in atomic units*#) and anisotropic parameters (r_{AP}) deduced from HRS measurements. Measured refractive indices at optical frequencies ω and 2ω as well as volumetric weight of TeO_2-$TaO_{5/2}$-ZnO glasses are reported

*** 1 a.u. = 3.62×10^{-42} $m^4.V^{-1}$ = 8.641×10^{-33} esu**

 # Values have to be multiplied by a factor of two to refer to the T (Taylor series expansion) convention [Willetts 1992]

It is clearly observed that the depolymerization of tellurite glasses has a severe effect on the hyperpolarizability parameters $|\beta_{HRS}|^2$, as expected. These new results confirm the impact of the tellurite chains on the linear and nonlinear electronic susceptibilities. Figure 4.9 now details the general trends of the second-order intensity, which is proportional to $|\beta_{HRS}|^2$, with Te content.

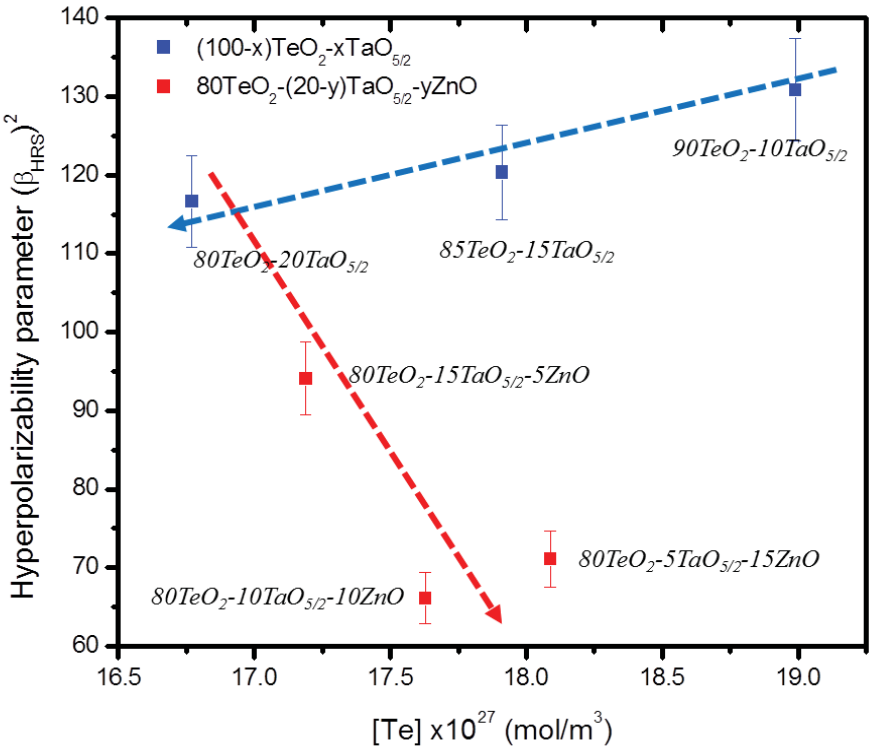

Figure 4.9 Evolution of the second-order intensity $|\beta_{HRS}|^2$ with Tellurium content. Dotted lines are guide for the eyes

A weak decrease of the hyperpolarizability during the exchange of TeO_2 by $TaO_{5/2}$ in the binary system is observed. However, it can be discerned a drastic decrease during the introduction of ZnO in the glass matrix. Again, it is observed that i) in the binary glass

system TeO_2-$TaO_{5/2}$, the introduction of octahedra [TaO_6] breaks the TeO_4 chain-like, reducing partially the hyperpolarizability, and ii) in the ternary glass system TeO_2-$TaO_{5/2}$-ZnO, exchanging octahedral [TaO_6] by tetrahedral [ZnO_4] has a great impact on the network, breaking TeO_4 chain-like (i.e. increase of the free volume fraction), leading to a reduction of the degree of polymerization of the glass. An important consequence of the depolymerization process is the drastic decrease of the hyperpolarizability.

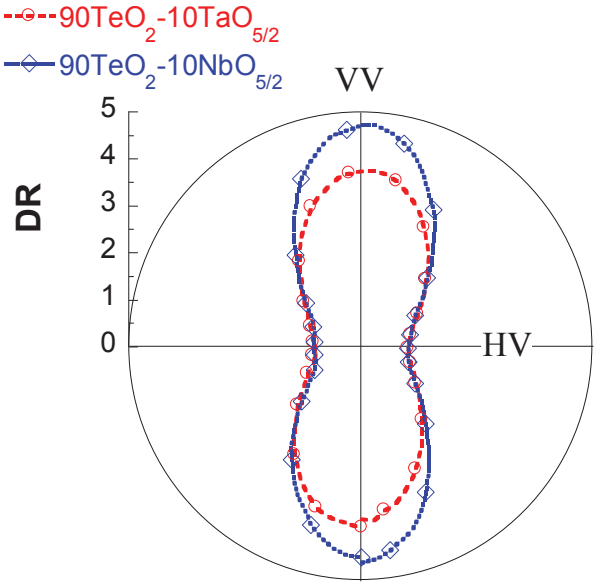

Figure 4.10 Experimental Normalized polarization curve $I_{\Psi V}/I_{HV}$ of $90TeO_2$-$10TaO_{5/2}$ and $90TeO_2$-$10NbO_{5/2}$

Figure 4.10 reports the experimental Normalized polarization curve $I_{\Psi V}/I_{HV}$ of $90TeO_2$-$10TaO_{5/2}$ and $90TeO_2$-$10NbO_{5/2}$for comparison purpose. We clearly see that the depolarization ratio $DR = I_{VV}/I_{HV} = 3.83$ (r_{ap} = 1.12, see Table 4.4) with 10% Ta

increases to $DR = I_{VV} / I_{HV} = 4.73$ giving an anisotropy parameter r_{ap} = 0.88 with 10% Nb. This indicate i) the Te-Nb glass network becomes more dipolar, ii) that even a small amount of 10% Nb has a great impact on the dipolar/octupolar nature of the glass network indicating that Nb is clearly embedded in the Te-O-Te network. In addition, this quite impressive shift to a dipolar HRS response is in good accordance with a distorted NbO_6 octahedron which is known to give a strong dipolar second order NLO response.

This vibrational information is in accordance with our understanding from the different vibrational analyses (IR, Raman and hyper-Raman) and can be related to the Raman gain property.

3 Relationship between hyperpolarizability and Raman gain in TeO_2-$TaO_{5/2}$-ZnO glasses

The Raman gain is strongly dependent of the glass network polymerization **[Guery 2012]**. In the TeO_2-$TaO_{5/2}$-ZnO glass system, it was shown that the introduction of ZnO in the glass matrix leads to a decrease of the Raman cross section of the TeO_4 molecular entities (responsible of the Raman gain), voicing the hypothesis that ZnO changes the network layout and breaks the TeO_n chain-like which are at the origin of the hyperpolarizability. Interestingly, Figure 4.11 details now the general trends of Raman gain with Te content. First we observe a significant decrease of the relative Raman gain when decreasing the Te content by introducing Ta. Second, the decrease of the Raman gain is much pronounced when substituting Tantalum with Zinc. Actually, the same

trends is observed if we consider the linear optical intensity at 1064 nm given by $\left|\chi^{(1)}\right|^2 = (n^2 - 1)^2$ where n is the index of refraction at 1064 nm given in Table 4.4.

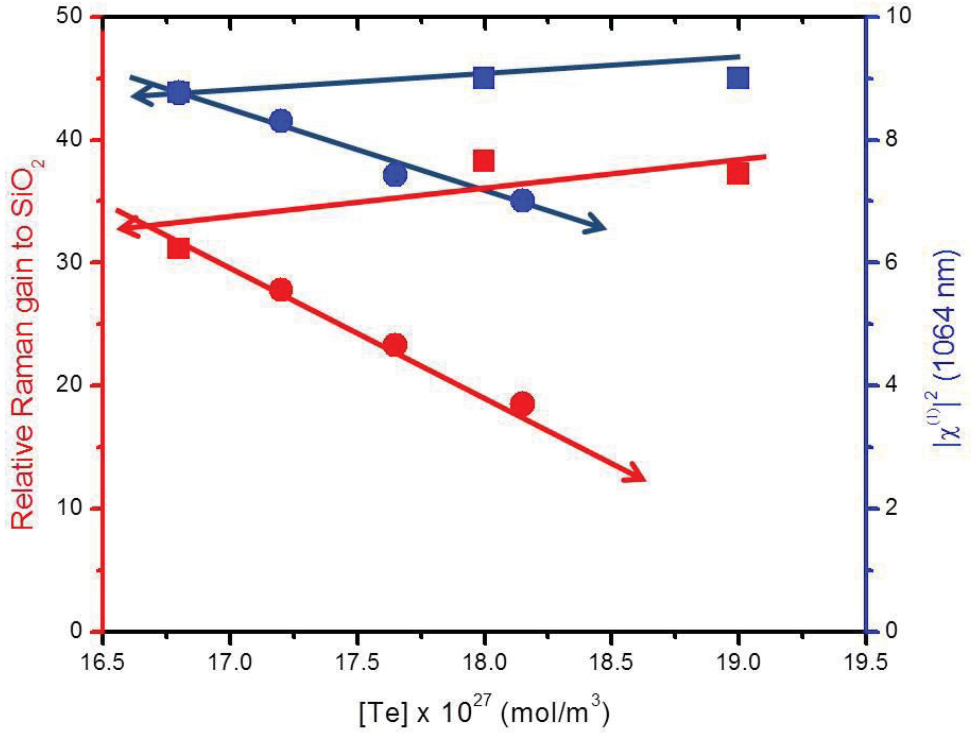

Figure 4.11 Evolution of the relative Raman gain to $Si0_2$ (red squares and full circles) and the linear optical intensity $|\chi^{(1)}|^2$ at 1064 nm (blue squares and full cercles) with Tellurium content. Full lines are guide for the eye

Clearly, Figures 4.9 and 4.11 both indicate a deep correlation of the optical response intensity, whatever the order of the response (linear, 2nd and 3rd order nonlinear responses), when changing the glass composition, i.e. with the Te content. This point is well summarized in Figure 4.12 that nicely demonstrates a linear correlation between the

two NLO responses when changing the glass composition. In addition, Figure 4.12 also nicely points out a linear relationship between the linear optical intensity and the second-order intensity.

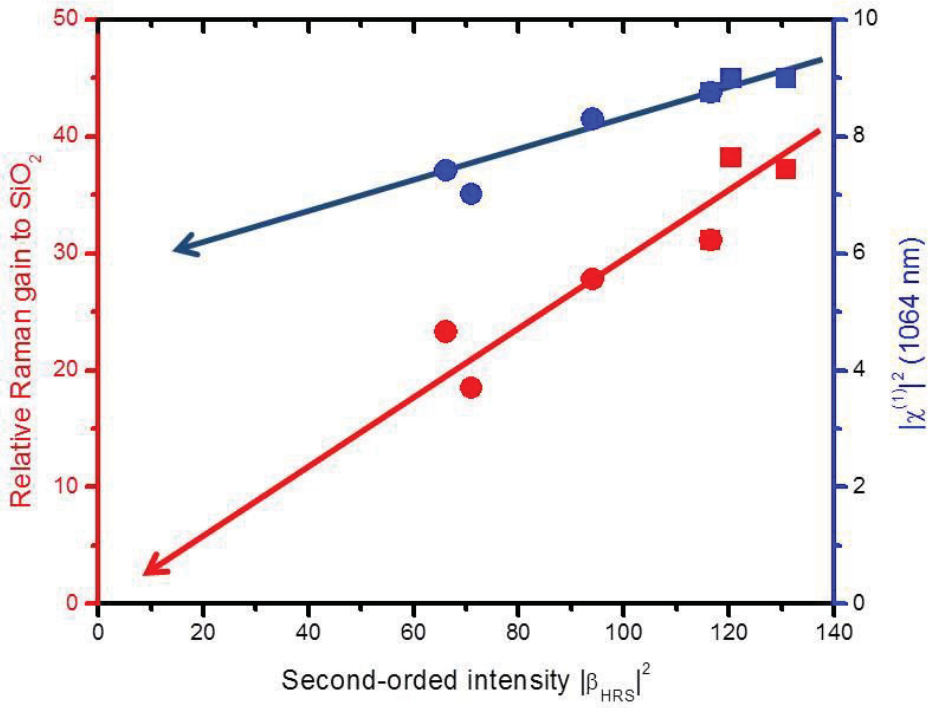

Figure 4.12 Relative Raman gain and first-order intensity versus second-order intensity $|\beta_{HRS}|^2$. Solid lines are guide for the eye

These linear correlations of intensity with Te content are typical of an incoherent signal, i.e. each ESU gives a response with no phase relation between the other ones. In that case, the intensity response from each ESU follows an adding scheme. Hence, **Eq. 4.33** introduced in section 1.5 can be generalized to Raman gain, hyper-Rayleigh scattering and linear intensity as:

$$I_{Glass} \propto N_{ESU} \left| \chi_{ESU}^{(n)} \right|^2 \qquad \textbf{Eq. 4.37}$$

Where N_{ESU} is the number density of ESU and $\chi_{ESU}^{(n)}$ is the nth order susceptibility of an ESU. However, inside each Te-based oligomer (ESU) that is responsible of this intensity adding scheme, it is expected an efficient coherent structure factor response $\chi_{ESU}^{(n)}$ that must be in consequence very sensitive to any modification of the glass composition as illustrated by previous IR and Raman analyses **[Guery 2012]**. In particular, looking at Figures 4.9 and 4.11, we note that the substitution of Te by Ta seems to give a linear soft decrease of intensity for any susceptibilities (Raman gain, linear optical response and HRS). This linear correlation is consistent with the change of the vibrational response which has been related to a decrease of Te–O–Te bridges associated to a depolymerization of the tellurite glass network and finally for the largest content of ZnO to the decrease of TeO_4 units and to the formation of TeO_{3+1} or TeO_3. The introduction of the zinc oxide results in a more pronounced but still linear decrease of intensity for all susceptibilities (Figures 4.9 and 4.11).

Here we finally establish a clear linear relationship between Raman gain, HRS and even linear polarizability of the glass and its level of polymerization of the TeO_4 chain-like structure.

4 Conclusion

The purpose of this chapter is to answer to the following question: *"What is the impact of the glass structure on the Raman gain?"*

A clear relationship between the polarizability of the material and the Raman response has been established. Adding $TaO_{5/2}$ and/or $NbO_{5/2}$ does not lead to a significant decrease of the glass polarizability because those entities do not break the tellurite glass network, in particular the Te-O-Te chain's continuity. Thus, the resulting Raman gain of TeO_2-$TaO_{5/2}$ and TeO_2-$NbO_{5/2}$ binary glass systems has been shown to remain fairly constant.

The introduction of zinc oxide in the TeO_2-$TaO_{5/2}$ glass network leads to the break down of the Te-O-Te chain's continuity and thus, to the concurrent decrease in the glass' polarizability and the Raman gain response. The disruption of the Te-O-Te chains has been shown to directly impact the glass' Raman cross-sections and thus, reduces its potential for amplification as a candidate compared to other TeO_2-based glasses.

The hyper-Rayleigh measurements permit us to obtain the hyper-polarizability parameter $|\beta_{HRS}|^2$, representing the nonlinear polarizability of the medium. It reinforces the observations of the evolution of the Raman gain as function of the glass composition. Through HRS measurements of the TeO_2-$TaO_{5/2}$-ZnO glass system, we observe a dramatic decrease in the hyper-polarizability of the glass accompanying ZnO introduction. The decrease of the hyper-polarizability is directly linked to the depolymerization (DR parameter) of the glass system, as would be expected, in

accordance, with the decrease of Te-O-Te chain content that results from the ZnO addition that causes chain continuity to be disrupted.

The hyper-polarizability $\chi^{(2)}$ measured by hyper-Rayleigh scattering is proportionally related to the Raman gain.

Chapter 4 – References

Boling 1978: N.L. Boling, A.J. Glass, and A. Owyoung, IEEE J. Quantum Electron. 14 (1978) 601-608.

Boyd 1992: W. Boyd, "Nonlinear Optics", Academic Press, Elsevier Science, USA (1992).

Dai 2004: G. Dai, F. Tassone, A. Li Bassi, V. Russo, C.E. Bottani, F. D'Amore, IEEE Photonics Technology Letters 16 (2004) 1011.

Denisov 1987: V.N. Denisov, B.N. Mavrin, V.B. Podobedov, Physics Report 151 (1987) 1-92.

Guery 2012: G. Guery, A. Fargues, T. Cardinal, M. Dussauze, F. Adamietz, V. Rodriguez, J.D. Musgraves, K. Richardson, P. Thomas, Chemical Physics Letters 554 (2012) 123.

Hellwarth 1963: R.W. Hellwarth, Physical Review 130 (1963) 1850-1852.

Hellwarth 1975: R. Hellwarth, J. Cherlow, T.T. Yang, Physical Review B 11 (1975) 964-967.

Hu 2011: X. Hu, G. Guery, J.D. Musgraves, D. VanDerveer, J. Boerstler, N. Carlie, P. Wachtel, S. Raffy, R. Stolen, K. Richardson, Journal of Non-Crystalline Solids 21 (2011) 3648-3653.

Kaatz 1996: P. Kaatz, D. P. Shelton, Molocular Physics 88 (1996) 683.

Kato 1971: Y. Kato, H. Takuma, Journal of Chemical Physics 54 (1971) 5398-5402.

Lisinetskii 2005: V.A. Lisinetskii, I.I. Mishkel, R.V. Chulkov, A.S. Grabtchikov, P.A. Apanasevich, H.J. Eichler, and V.A. Orlovich, Journal of Nonlinear Optical Physics and Materials 14 (2005)107-114.

Maker 1970: P. D. Maker, Physical Review A 1 (1970) 923.

Mirgorodsky 2006: A.P. Mirgorodsky, M. Soulis, P. Thomas, T. Merle-Mejean, Physical Review B 73 (2006) 134206.

O'Donnell 2008: M.D. O'Donnell, K. Richardson, R. Stolen, C. Rivero, T. Cardinal, M. Couzi, D. Furniss, A.b. Seddon, Optical Materials 30 (2008) 946-951.

Quinet 2004: O. Quinet, B. Champagne, V. Rodriguez, Journal of Chemical Physics 121 (2004) 4705.

Quinet 2006: O. Quinet, B. Champagne, V. Rodriguez, Journal of Chemical Physics 124 (2006) 244312.

Rivero 2005-1: C. Rivero, PhD thesis "High gain/Broadband oxide glasses for next generation Raman amplifiers" (2005) University of Central Florida, USA/University of Bordeaux, France.

Rivero 2005-2: C. Rivero, R. Stegeman, M. Couzi, D. Talaga, T. Cardinal, K. Richardson, G. Stegeman, Optics Express 13 (2005) 4759.

Rodriguez 2006: V. Rodriguez, D. Talaga, F. Adamietz, J.L. Bruneel, M. Couzi, Chemical Physics Letters 431 (2006) 190.

Rodriguez 2008: V. Rodriguez, Journal of Chemical Physics 128 (2008) 064707.

Rodriguez 2010: V. Rodriguez, J. Grondin, F. Adamietz, Y. Danten, Journal of Physical Chemistry B 114 (2010) 15057.

Rodriguez 2012: V. Rodriguez, Journal of Raman Spectroscopy 43 (2012) 627-636.

Rodriguez 2013: V. Rodriguez, M. Couzi, F. Adamietz, M. Dussauze, G. Guery, T. Cardinal, P. Veber, K. Richardson, P. Thomas, J. Raman Spectrosc. 2013, DOI: 10.1002/jrs.4251.

Shen 1984: Y.R. Shen, "The Principles of Nonlinear Optics", John Wiley & Sons, Inc. (1984).

Soulis 2008: M. Soulis, T. Merle-Mejean, A.P. Mirgorodsky, O. Masson, E. Orhan, P. Thomas, M.B. Smirnov, Journal of Non-Crystalline Solids 354 (2008) 199-202.

Stegeman 2005: R. Stegeman, C. Rivero, K. Richardson, G. Stegeman, P. Delfyett, Y. Guo, A. Pope, A. Schulte, T. Cardinal, P. Thomas, J-C Champarnaud-Mesjard, Optics Express, 13 (2005) 1144-1149.

Stegeman 2006: R. Stegeman "Direct nonlinear optics measurements of Raman gain in bulk glasses and estimates of fiber performance" (2006) University of Central Florida, USA.

Stolen 1973: R.H. Stolen, E.P. Ippen, Applied Physics Letters 22 (1973) 276-278.

Stolen 2000: R. H. Stolen, “Issues in Raman gain measurements”, in Tech. Dig. Symp. Optical Fiber Measurements, NIST Special Publication 953 (National Institute of Standards and Technology), Gaithersburg, MD, 139-142 (2000).

Verbiest 2009: T. Verbiest, K. Clays, V. Rodriguez, “Second-Order Nonlinear Optical Characterization Technique”, CRC Press (2009).

Warren 1936: BE. Warren, H. Krutter, O. Morningstar, Journal of the American Ceramic Society 19 (1936) 202.

Willets 1992: A. Willetts, J. E. Rice, D. M. Burland, D. P. Shelton, Journal of Chemical Physics 97 (1992) 7590.

Yoshino 2003: F. Yoshino, S. Polyakov, G.I. Stegeman, M. Liu, “Nonlinear Refraction and Absorption from 1300 to 2200 nm in Single Crystal Polymer poly [bis (p-toluene sulfonate)] of 2, 4-hexadiyne-1, 6-diol (PTS)”, Quantum Electronics and Laser Science QELS Prostconference Digest, QTuG43 (2003).

Zachariasen 1932: WI-I. Zachariasen. Journal of the American Chemical Society 54 (1932) 3841.

CONCLUSION AND FUTURE WORK

Our society is focused on the development and production of new technologies: smaller computers, larger data storage capacities, better performance with a faster internet connection.

This PhD thesis addresses an issue related to use of optical fibers for telecommunication applications. The ability to transmit and amplify over broad frequency ranges remains a challenge due to the limits of existing amplifier media. The Raman gain effect is presented as a tunable amplification method, able to enlarge a signal over a range imposed by a pump excitation. This effort has examined new candidate glasses that offer the potential as new Raman gain media. The underlying structural relationship between their nonlinear optical response has been correlated to glass chemistry and structure and key tools have been developed which enable prediction of physical and optical properties and performance of these interesting nonlinear optical materials.

We have investigated the potential of using tellurite glasses for Raman gain by bringing in new insights regarding the relationship between composition, glass structure, and Raman gain response. With an understanding of the critical criteria that such a glass must meet for the application, we have studied the potential of these materials to form stable glasses, resistant to crystallization with low levels of (OH^-) moisture impurities with high nonlinear reponse and Raman gain.

Glass compositions including TeO_2-$TaO_{5/2}$-ZnO, TeO_2-$NbO_{5/2}$ and TeO_2-$BiO_{3/2}$-ZnO have been optimized for nonlinear optical and fiber fabrication. The vibrational response of TeO_2 glasses was initially unclear and the present work offers a better comprehension of the relation between structure and those properties. The main question which has led this research can be summarized as *"What is the impact of the glass structure on Raman gain properties of tellurite glasses?"*

For answering, the effects of each glass modifier on the glass properties in the three different glass systems have been investigated. We have chosen to focus on few of them, namely tantalum, zinc, niobium and bismuth.

Regarding the material processing point of view, it has been shown that:

- The introduction of tantalum oxide or zinc oxide allows increasing the glass stability toward crystallization. The introduction of ZnO into tellurite glass matrix permits to obtain the largest $\Delta T = T_x - T_g$ and induces an important decrease of the refractive index,
- The development of high purity materials exhibiting limited or no absorption in the transmission bandwidth in the near infrared (NIR) is possible by melting under dried air atmosphere, showing a reduction of 90 % of the OH content in tellurite glasses,
- Optical losses measured on monolithic $80TeO_2$-$10TaO_{5/2}$-10ZnO glass materials without core and cladding represent 8.2 dB/m at 1.55 μm.

This purification process was performed on a glass rod and substquently drawn into a core-only optical fiber, and demonstrated optical losses lower than 10 dB/m (either at 1.55 μm or 2.0 μm). This encouraging result can be significantly optimized by designing appropriate core and cladding fiber structures, which may permit to have optical losses lower than 0.1 dB/m.

$TaO_{5/2}$, $NbO_{5/2}$ and $BiO_{3/2}$ have been chosen as glass modifiers for their nonlinear optical properties, while ZnO is known for improving the fiber fabrication processing. Those glass modifiers have an important impact on the glass structure. The structural evolutions have been investigated by using a combination of vibrational spectroscopic methods: IR absorption, as well as Raman and hyper-Raman scatterings. The selection rules are complementary and reveal new structural information, which permits to have a better understanding of the structure of the materials. Obtaining a detailed understanding of spectroscopic methods in the glassy state is always a difficult task, due to the existence of broadened spectral bands. We have proposed to base our work on the fundamental vibrations present in the paratellurite crystal α-TeO_2 (33 optical phonon branches). The result has been extrapolated to the case of tellurite glasses. This approach has demonstrated:

- A drastic decrease of the tellurite chains during the introduction of the zinc oxide in the tellurite glass matrix,
- A decrease of the glass polymerization observed with an experimental normalized polarization curve ($I_{\Psi V}/I_{HV}$), allowed by the measurement of the

depolymerization ratio (DR) curve $I_{\Psi V}/I_{HV}$, permitting to measure the depolymerization ratio DR.

Those structural analyses may be combined with other different techniques such as the Extended X-ray Absorption Fine Structure (EXAFS), X-ray Absorption Near Edge Structure (XANES) or Nuclear Magnetic Resonance (NMR).

An important consequence of the depolymerization process is the drastic decrease of the polarizability/hyperpolarizability**.** The reduction of polarizability in the material translates to a decrease of the nonlinear optical properties and in particular the Raman gain response; because of a linear correlation between hyperpolarizability and Raman gain. Both indicate a deep correlation of the optical response intensity, whatever the order of the response (linear, 2nd and 3rd order nonlinear responses), when changing the glass structure, the glass polymerization. So we can conclude on:

- The importance of Te-O-Te content into tellurite glasses for the nonlinear optical properties,
- The drastic impact of the short-range and medium order on the nonlinear optical response.

The effects of the TeO_4 molecular units and the Te-O-Te chains on the nonlinear optical response have been well defined and discussed. Regarding the effect of the specific TeO_{3+1}/TeO_3 associated with heavy ions (such as $BiO_{3/2}$, $TlO_{1/2}$, PbO), similar

investigations need to be carried out in order to understand the origin of the nonlinearity. It has been shown that the introduction of zinc oxide leads to a decrease of the Raman gain response but with an ease for fiber fabrication by decreasing the glass polymerization. It is obvious that for optimizing optical fibers for nonlinear optics, a different oxide has to be introduced.

The present work offers for the first time, a concrete understanding on the relationship between the vibrational response and the glass structure that allows for a definition of the best glass candidate for this specific application. In terms of application for developing compact system based on Raman gain, an order of magnitude more reduction in loss in the spectral window of use, is needed. At this time the study of a glass-ceramic nanocomposite structure offers numerous possibilities; additionally, combining the optimal Raman response of tellurite with the plasmon resonances of metal or a high response crystallite, might enable further opportunities for creating novel, tunable materials for the near- and mid-infrared.